ANL-88-49

Nuclear Technology Programs Semiannual Progress Report

April-September 1987

Argonne National Laboratory, Argonne, Illinois 60439
operated by The University of Chicago
for the United States Department of Energy under Contract W-31-109-Eng-38

This report has been reproduced from the best available copy.

Available from the
National Technical Information Service
U.S. Department of Commerce
5285 Port Royal Road
Springfield, VA 22161

Price: Printed Copy A09
Microfiche A01

Distribution Categories:
Light Water Reactor Technology (UC-523)
Chemical Separation Processes for
Plutonium and Uranium (UC-711)
Nuclear Waste Management (UC-510)
Magnetic Fusion Energy (UC-516)

ANL-88-49

ARGONNE NATIONAL LABORATORY
9700 South Cass Avenue
Argonne, IL 60439

NUCLEAR TECHNOLOGY PROGRAMS SEMIANNUAL PROGRESS REPORT

April-September 1987

Chemical Technology Division

M. J. Steindler, Director
J. E. Harmon, Editor

July 1989

TABLE OF CONTENTS

TABLE OF CONTENTS (CONTD)

LIST OF FIGURES

LIST OF FIGURES (CONTD)

LIST OF FIGURES (CONTD)

LIST OF FIGURES (CONTD)

LIST OF TABLES

LIST OF TABLES

LIST OF TABLES (CONTD)

NUCLEAR TECHNOLOGY PROGRAMS
SEMIANNUAL PROGRESS REPORT
April-September 1987

ABSTRACT

This document reports on the work done by the Nuclear Technology Programs of the Chemical Technology Division, Argonne National Laboratory, in the period April-September 1987. Work in applied physical chemistry included investigations into the processes that control the release and transport of fission products under accident-like conditions, the thermophysical properties of metal fuel and blanket materials of the Integral Fast Reactor, and the properties of selected materials in environments simulating those of fusion energy systems. In the area of separation science and technology, the bulk of the effort is concerned with developing and implementing processes for the removal and concentration of actinides from waste streams contaminated by transuranic elements. Another effort is concerned with examining the feasibility of substituting low-enriched for high-enriched uranium in the production of fission product ^{99}Mo. In the area of waste management, investigations are underway on the performance of materials in projected nuclear repository conditions to provide input to the licensing of the nation's high-level waste repositories.

SUMMARY

Applied Physical Chemistry

Source Term Studies. The Division is engaged in calculational and experimental efforts to investigate fission product release and transport from a light water reactor (LWR) under accident conditions.

In one such effort, the chemical form and rate of release of volatile fission products (Xe, Kr, Cs, Te, and I) effused from an irradiated LWR fuel pin sample were studied using quadrupole mass spectrometry. Experiments, up to a temperature of 2120 K, have identified Kr, Xe, Cs, and Te as the species released from the fuel. A weak signal was observed for atomic iodine at 1325 K. The source of the atomic iodine, e.g., dissociation of cesium iodine or dissociation of molecular iodine, has yet to be resolved. The observed rate of xenon release was several orders of magnitude lower than previously reported. The xenon release rate, however, increased significantly after the fuel was oxidized. A most significant finding is the lack of observation of molecular cesium iodine. In complementary experiments on nonradioactive material, it was found that tellurium release was hindered by reaction with Zircaloy cladding. Above 1300 K, gaseous SnTe was observed; its formation is attributed to reaction of the tin with tellurium all dissolved in the cladding.

Critical to understanding the behavior of fission products from reactor accidents is determining the nature and properties of the vapor phase species. In this experimental effort, we investigated the CsI·CsOH vapor species over a

liquid solution of CsI and CsOH. Vapor pressures were measured with a mass spectrometer. This required heating above the CsI melting point of 907 K. Thermodynamic data were obtained for CsOH(g), $Cs_2(OH)_2(g)$, CsI(g), $Cs_2I_2(g)$, and CsI·CsOH(g). Activity coefficients were derived for the CsI-CsOH system. The relative ionization cross section of CsOH was found to be about ten times the cross section of CsI(g). Our results also suggested that CsI·CsOH fragments to Cs_2OH^+ and an iodine atom.

Another effort involves investigation into the release of refractory fission products from the molten core-concrete mixtures that would form if a molten core penetrated the bottom of a reactor vessel in a severe accident. The vaporization of core-concrete mixtures is being measured using a transpiration method. Mixtures of stainless steel, concrete (limestone or basaltic), and urania (doped with La_2O_3, SrO, BaO, and ZrO_2) are vaporized at 2150-2400 K from a zirconia crucible into flowing He-6% H_2 gas. Up to 600 ppm H_2O is added to the gas to fix the partial molar free energy of oxygen in the range -420 kJ to -550 kJ. The fraction of the sample vaporized is determined by weight change and by chemical analyses on the condensates that are collected in an Mo condenser tube. The results are being used to test the thermodynamic data base and the underlying assumptions of computer codes used for prediction of release during a severe accident.

Analytical results, which are now complete for the two runs with mixtures of stainless steel, limestone concrete, and doped urania, are presented in the report. The amount of material transported at flow rates of 100 and 200 cm^3/min was nearly the same (98 and 129 mg, respectively), suggesting that gas saturation had been achieved. The analytical-chemistry data from the two runs showed that the major limestone-concrete components had achieved saturation. However, the major steel components showed less transport than in earlier runs with steel alone. When a sample was cross-sectioned, the steel was found embedded within the solidified mass of concrete and doped urania, suggesting that transport of steel components to the gas phase was hindered. Extensive dissolution of the zirconia beaker wall in the oxide melt was also noted. When this effect was taken into account, good agreement was achieved between experiments and calculations.

Thermophysical Properties of Metal Fuels. Renewed interest in metallic fuel for nuclear reactors has prompted study of the solidus and liquidus for the U-Pu-Zr system. These temperatures are of importance in assessing the possibility of fuel melting during abnormal reactor conditions. Data obtained in previous work were found to be inadequate for the needs of the current reactor development effort. A dual effort was undertaken to provide the needed data: (1) thermodynamic phase diagram analysis and calculation of the ternary solidus and liquidus surfaces and (2) experimental determination of solidus and liquidus temperatures for selected alloys. Solidus and liquidus temperatures were calculated for U-13 at. % Pu-15 at. % Zr, U-12 at. % Pu-29 at. % Zr, U-19.3 at. % Zr, U-19.5 at. % Pu-3.3 at. % Zr, and U-19.3 at. % Pu-14.5 at. % Zr. The calculated results agreed reasonably well with experimental data in the literature (first two alloys) and from our own experimental work (final three alloys).

The Thermodynamics of Pyrochemical Processes for Liquid Metal Reactor Fuel Cycles. The thermodynamic basis for pyrochemical processes for the recovery and purification of fuel for the liquid metal reactor fuel cycle is

described. These processes involve the transport of the uranium and plutonium from one liquid alloy to another through a molten salt. The processes discussed use liquid alloys of cadmium, zinc, and magnesium and molten chloride salts. The oxidation-reduction steps are done either chemically by the use of an auxiliary redox couple or electrochemically by the use of an external electrical supply. The same basic thermodynamics apply to both the salt transport and electrotransport processes. Large deviations from ideal solution behavior of the actinides and lanthanides in the liquid alloys have a major influence on the solubilities and the performance of both the salt transport and electrotransport processes. Separation of plutonium and uranium from each other and decontamination from the more noble fission product elements can be achieved using both transport processes. The thermodynamic analysis is used to make process design computations for different process conditions.

Fusion-Related Research. A critical element in the development of the fusion reactor is the blanket for breeding tritium fuel. Several studies are underway with the objective of determining the feasibility of using lithium-containing ceramics as breeder material.

The objective of one such study is to provide measured thermodynamic and kinetic data related to tritium retention and release from ceramic tritium breeder materials. The information will enable (1) comparison of candidate breeder materials, (2) calculation of operating conditions, and (3) elucidation of the phenomena underlying the behavior of tritium in breeder materials.

Isotherms at 673 and 773 K are presented for surface adsorption of $H_2O(g)$ and for solubility of OH^- in $LiAlO_2$ as a function of $H_2O(g)$ partial pressure. The Freundlich adsorption isotherms for 673 and 773 K, respectively, are:

$$\log(\theta) = (-1.590 \pm 0.691) + (0.497 \pm 0.064)\log(p_{H2O})$$

$$\log(\theta) = (-1.112 \pm 0.061) + (0.497 \pm 0.052)\log(p_{H2O})$$

where θ is the fraction of surface covered, and p_{H2O} is the partial pressure of $H_2O(g)$ in pascals. Hydroxide dissolution is exothermic. Depending on conditions, $LiAl_5O_8$ can be a second phase or a solute to give isotherms with slopes of 0.5 or 0.4, respectively. The hydroxide solubility isotherms for 673 and 773 K, respectively, are:

$$\log(x_{OH}) = (-4.667 \pm 0.096) + (0.399 \pm 0.088)\log(p_{H2O})$$

$$\log(x_{OH}) = (-4.899 \pm 0.079) + (0.499 \pm 0.063)\log(p_{H2O})$$

where x_{OH} is the mole fraction OH^-. The rate of $H_2O(g)$ evolution from $LiAlO_2$ showed the kinetics of the process to be second order in hydroxide with an activation energy of 14.7 ± 1.9 kcal (61.5 ± 7.9 kJ), a value less than that reported for $H_2O(g)$ evolution from Li_2O or from LiOH.

In another effort, we have developed a computer model to predict tritium release from a ceramic breeder, which considers diffusion and desorption as

the rate-controlling mechanisms. This model performed much better than a pure diffusion model when predicting the tritium release under pure helium purge gas for Li_2SiO_3 samples from the LISA tritium release experiment. Work is now in progress to develop a more sophisticated model, which will also include transport in the gas phase. Plans have also been made to investigate the effects of processes which currently are regarded as secondary (grain boundary diffusion, trapping, etc.) to determine their importance in developing an overall model for tritium transport and release.

In neutron dosimetry and damage analysis, neutron facilities are being characterized in terms of neutron flux and energy spectrum, which can be used to calculate atomic displacements and transmutations. These damage parameters can also be used to correlate properties changes and to predict materials performance in fusion reactors. In this report period, neutron production cross sections were measured near 14 MeV following high-fluence irradiations at the Rotating Target Neutron Source II facility. New results are reported for the production of ^{91}Nb, ^{93}Mo, and ^{93}Nb from natural Mo and ^{94}Mo enriched targets. Our data suggest that the half-life of ^{91}Nb may be shorter than previous estimates. Results are also presented for the JP4, JP5, and JP8 United States/Japan experiments in the High Flux Isotopes Reactor (HFIR) at Oak Ridge National Laboratory. All three experiments had similar exposures of about 58,000 MWD, resulting in 55 dpa and 3313 ppm helium at midplane for Type 316 stainless steel. Analyses of iron samples irradiated up to neutron fluences of 10^{27} n/m^2 in HFIR found more helium than was expected from fast neutron reactions at high fluences. The helium excess increased systematically with neutron exposure, suggesting a transmutation-driven process. The extra helium could be produced in two different ways: either by fast neutron reactions on the transmuted isotopes of iron or by a thermal neutron reaction with the radioactive isotope ^{55}Fe. Radiometric and mass spectrometric measurements of the iron isotopes composing the irradiated samples have been used to determine limits on the cross sections for each process. Either of these processes can be used to enhance helium production in ferritic materials during irradiations in mixed-spectrum reactors by isotopically enriching the samples. Further work is needed to clarify the reaction mechanisms and to determine helium-production cross sections. Our measurements determined the thermal neutron total absorption cross section of ^{55}Fe to be 13.2 ± 2.1 barns.

Since permeation losses from thermally hot blanket systems can be severe, methods are needed to reduce the molecular tritium partial pressure in these systems. A method that has been proposed involves oxidation of tritium to tritiated water. Experiments are in progress to study tritium oxidation in a stainless steel apparatus. For fusion blanket systems, tritium oxidation must be >99% complete if oxidation is to be considered an effective method to manage the transport of tritium. Results to date indicate that the yield of tritiated water increases with oxygen concentration in a helium sweep gas. The completeness of oxidation increased from 52% at 10^{-3} ppm oxygen to 98% at 2000 ppm oxygen.

Separation Science and Technology

The Division's work in separation science and technology consists of four projects. Three of these projects are concerned with removing and concentrating actinides from waste streams contaminated with transuranic (TRU) elements by use of the TRUEX solvent extraction process. The extractant found most

satisfactory for the TRUEX process is octyl (phenyl)-N,N-diisobutylcarbamoylmethylphosphine oxide, which is abbreviated CMPO. This extractant is combined with tributyl phosphate (TBP) and a diluent to formulate the TRUEX process solvent. The diluent is typically a normal paraffinic hydrocarbon (NPH) or a nonflammable chlorocarbon such as tetrachloroethylene (TCE). The fourth project, which is unrelated to the first three, is concerned with examining the feasibility of substituting low-enriched uranium for the high-enriched uranium currently used in the production of ^{99}Mo.

TRUEX Technology Base Development. This effort involves development of a generic data base and modeling capability for the TRUEX solvent extraction process. This capability will allow us to design flowsheets for specific waste streams and to predict the cost and space requirements for implementing a site- and feed-specific TRUEX process. Work in this report period was chiefly concerned with collection of batch distribution-ratio data to be used in modeling the partitioning behavior of actinides and important components of nuclear waste. The distribution ratios for Am, Tc, Ru, U, Pu, Np, and Fe were determined as a function of TRUEX solvent composition, aqueous phase composition, and temperature (25-50°C). A model has been developed for HNO_3 extraction by TBP at concentrations of 5-100 vol %, as well as extraction of Am and Fe by TRUEX-TCE solvent.

PUREX-TRUEX Processing of Chloride Salt Wastes. The objective of this effort is the development of a solvent extraction process to remove Pu and Am from chloride salt wastes being stored at Los Alamos National Laboratory (LANL). The process involves two parts: Pu(IV) is recovered in a PUREX-TCE cycle, then the Am and other transuranic elements are removed from the salt wastes in a TRUEX-TCE cycle.

Distribution ratios were measured for Pu(IV), Fe(III), Zn(II), and HCl between PUREX-TCE solutions and either HCl or acidic chloride solutions. The Pu(IV) results suggested that protonated Pu(IV)-chloride species, such as $HPuCl_6$ and H_2PuCl_6, are being extracted. The Fe(III) results indicate that 25% TBP in TCE extracts Fe(III) very well from acidic chloride solutions, and that three or four TBP molecules are involved in this extraction. The Zn(II) results indicate that the recovery of Pu(IV) from an acidic chloride solution containing Zn(II) should be possible, and that Zn(II)-chloride complexes are extracted with three or four TBP molecules.

Distribution ratios were also measured for Am(III) between TRUEX-TCE and acidic chloride solutions. Extraction of Am(III) as a complex with two or three CMPO molecules was indicated by the data. The Am(III) distribution ratios could be predicted using chloride ion activities for $NaCl/KCl/MgCl_2$ solutions, but chloride activities for solutions containing $CaCl_2$ were calculated to be higher than realized. The presence of $CaCl_2$ may decrease the extraction of Am(III) by CMPO.

Processing Waste from Plutonium Finishing Plant. In this effort, the Division is providing Westinghouse Hanford Operations with the technical support that is required to implement TRUEX processing of the waste streams in its Plutonium Finishing Plant (PFP).

As a first step in identifying key points for process monitoring and control, an electronic worksheet (spreadsheet) is being developed to perform stagewise solvent extraction calculations. This worksheet, called SASSE

(Spreadsheet Algorithm for Stagewise Solvent Extraction), is now able to determine the effect of varying flow rates for all currently designated PFP flowsheet streams as well as the effect of varying the extractant concentration between 0.1 M and 0.4 M. The SASSE worksheet was used to identify key parameters for monitoring and controlling the TRUEX process as it runs in a centrifugal contactor. One of the key parameters was found to be CMPO concentration in the solvent. Because of the high density of the diluent, the solvent density can be used to maintain control of the CMPO concentration. To facilitate this, the solvent density was correlated with temperature and concentrations of TCE, TBP, and CMPO. Excellent agreement was obtained between the measured and calculated densities (dry and wet).

A reference flowsheet for TRUEX processing of PFP waste has been given to Westinghouse Hanford, and countercurrent testing of this flowsheet with a 4-cm ANL centrifugal contactor has begun. In addition, Westinghouse Hanford is testing an ANL prototype 10-cm centrifugal contactor.

Production and Separation of ^{99}Mo from LEU Targets. The effect of low-enriched uranium (LEU) substitution for high-enriched uranium (HEU) in ^{99}Mo production was studied. The use of uranium silicide fuels for uranium aluminide requires changes in current chemical processing, especially during the initial basic dissolution step. The process envisioned now entails dissolution of the cladding in basic solution, followed by dissolution of the uranium silicide in a basic peroxide solution. The peroxide is then destroyed by heating, resulting in the precipitation of uranium. After separation of the uranium precipitate, the molybdenum-containing solution is diluted, acidified, and loaded onto a alumina column. The adsorbed ^{99}Mo is eluted with ammonium hydroxide and further purified.

High Level Waste/Repository Interactions

The Nevada Nuclear Waste Storage Investigation (NNWSI) Project is investigating the tuff beds of Yucca Mountain, Nevada, as a potential location for a high-level radioactive waste repository. As part of the waste package development portion of this project, which is directed by Lawrence Livermore National Laboratory, we are performing experiments to study the behavior of the waste form under anticipated repository conditions. This effort includes (1) the development and performance of a test to measure waste form behavior in unsaturated conditions, (2) the performance of experiments designed to study the behavior of waste package components in an irradiated environment, and (3) the performance of experiments to investigate the reaction of glass with water.

Efforts this period have focused on analyzing components from the N2 Unsaturated Test series and performing the N3 Unsaturated Test series using ATM-10 glass. The test apparatus provides for collection and containment of liquid and support of the waste package. The waste package consists of the glass waste form and a metallic holder presensitized by heat treatment. A solution feed system injects rock-equilibrated well water into the test apparatus at 90°C.

The N3 test was started July 6, 1987, according to the standard Unsaturated Test matrix and has been completed through the 26-week sampling period. The test results to date indicate that ATM-10 glass is reacting at about the same rate as the SRL 165 glass (tested in N2 test series) when

accelerated stainless steel/glass breakdown occurs for the SRL glass, but at a faster rate than when no accelerated reaction occurs in the SRL glass.

Because the NNWSI Unsaturated Test rigidly sets many of the test parameters, the effect that each parameter may have on the final radionuclide release needs to be studied. This is being done in parametric experiments. These parametric tests include determination of the effect of waste form surface area, test duration and temperature, water injection rate, presensitising of the waste form holder, and degree of water saturation. Results will be given in future reports.

Studies are in progress to determine the effect of relative humidity on the nuclear waste glasses SRL 131, SRL 165, and PNL 76-68 along with the natural glasses obsidian and basalt. All samples have been reacted at a temperature of 75°C in a relative humidity of 60%, 95%, or 100%. The vapor hydration experiments are now in their second year, with samples removed after 157 days and 365 days for analyses.

To understand the repository environment after waste emplacement, it is necessary to first understand how the groundwater is affected by the radiation fields. Experiments were performed using EJ-13 groundwater and synthetic nuclear waste glass formulations SRL 165, ATM-1c, and ATM-8 under the influence of penetrating gamma irradiation at 90°C. Exposure rates of about 0, 1×10^3, 1×10^4, and 2×10^5 R/h were used in an effort to elucidate the effects of the total gamma radiation exposure on the reaction. The major influence of penetrating gamma radiation appeared to be through acidification of the leachate and lowering of the Eh. Our results showed the extent of glass reaction to be similar in irradiated and nonirradiated experiments, probably because the release of highly leachable components such as Li, Na, B, or Mo from the glass is not strongly dependent on pH in the range 6.5-9.5. The behavior of some species released from the glass during reaction was influenced by the leachate pH and Eh differences; most noticeably affected were the actinide elements. The solubilities and speciation of the actinides are known to be very pH and Eh sensitive. The distribution of the released actinides between dissolved, suspended, and adsorbed phases was seen to vary slightly at different pH's.

A laser Raman microprobe (LRM) system is being developed to analyze microcrystalline precipitates which form during the hydration of nuclear waste glass. By use of standard microscope objectives, an argon ion laser can be focused to a beam diameter less than 2 μm. This allows spectra to be collected from very small samples without interference from the surrounding substrate. X-ray emission spectroscopy (both energy dispersive and wavelength dispersive), available on the SEM, can be used to analyze the sample. The Raman spectra of compounds having compositions consistent with the unknown can then be consulted for comparative identification. The LRM should be particularly useful in analyzing samples that are too small to be removed from the glass surface and studied by X-ray diffraction.

Hydrothermal leaching and vapor phase hydration experiments have been performed using two synthetic basalts and one SRL glass and deionized water. The reacted glasses are being quantitatively analyzed with respect to the layer composition and growth kinetics of the layer.

A study has been initiated to determine radionuclide release rates from spent fuels immersed in site-specific groundwater at the ambient hot cell temperature. Leaching tests will be conducted at room temperature in 304 L stainless steel vessels on bare fuel specimens submerged in 250 mL of J-13 water.

Two ultrasensitive laser techniques, laser photoacoustic spectroscopy (LPAS) and laser-induced fluorescence (LIF), are being developed for the detection and speciation of trace levels of actinides in solutions typical of those expected in a repository. These studies have been in progress for about 1-1/2 years and extend spectroscopic techniques into the nanomolar and sub-nanomolar regime. Once developed, these techniques will provide a powerful investigative tool for monitoring and investigating the chemistry of actinides in typical groundwaters. In this report period, the sensitivity of the LPAS system was pushed to 3×10^{-7} absorbance units per centimeter at a signal-to-noise ratio (S/N) of one. This exceeds published limits by a factor of 10.

I. APPLIED PHYSICAL CHEMISTRY
(C. E. Johnson)

The program in applied physical chemistry involves studies of the thermochemical, thermophysical, and transport behavior of selected materials in environments simulating those of fission and fusion energy systems.

A. Source Term Studies

The objective of this effort is to understand the release and transport of fission products from light water reactor (LWR) fuel so that accurate predictions can be made of the "source term." We are investigating (1) the transport, condensation, revaporization, and deposition of fission products in the primary reactor system, (2) the release of fission products during the interaction of molten fuel with the concrete basemat, and (3) the reactions between fission product compounds under the conditions expected in the primary system.

1. Fission Product Release from Irradiated Fuel
(I. Johnson)

The chemical form and the rate of release of volatile fission product species released from a defected irradiated light water reactor (LWR) fuel pin are being studied using quadrupole mass spectrometry. After release from the defected fuel pin, the gaseous species immediately enters the ionizer of the mass spectrometer, thus ensuring that its chemical form is not changed prior to identification and measurement. Our studies differ from prior studies in that (1) the chemical form of the volatile fission product is determined, and (2) the detection and measurement method does not depend on the radioactivity of the fission product element. Information on the chemical form of the released fission product species will permit a more accurate description of their transport and reaction in the primary reactor system. Also, these studies will yield information on the reaction of fission products with the Zircaloy cladding. The results of these studies will increase our understanding of the first step in the release of fission products from irradiated fuel and, therefore, assist in the development of an accurate source term.

Previous studies[1] of irradiated fuel samples have established the importance of two temperature ranges, below and above 1275 K. At temperatures below 1275 K, the easily released fission products are detected. These originate from gases that have migrated to cracks in the fuel and to the fuel-cladding gap during the irradiation. If a significant amount of CsI is present in these locations, it is very likely to be detected. Our experimental temperature was selected so that the vapor pressure of CsI would be high enough to give a measurable signal but not so high that all of the CsI would escape before the signal could be found. Above 1275 K, most of the species observed are fission products that escaped from very small cracks or diffused out of the fuel matrix. Previous studies[1] have indicated that the major species released in this temperature region are the rare gases Kr and Xe. Under some conditions, Cs, Te, and I have also been observed, although the signal intensity from these latter fission products has been very much lower than that of the rare gases.

a. Experimental

In these experiments, a section of an irradiated LWR fuel pin was inductively heated in a vacuum chamber. The volatile fission products that escape from the fuel are directed into the ionizer of a quadrupole mass spectrometer located adjacent to the fuel pin and separated by a radiation shield within the vacuum chamber (see Fig. I-1 for schematic of apparatus). The chamber was evacuated using a mechanical pump and a Cryotorr pump. The chamber is rough pumped to about 3 torr (400 Pa) before the Cryotorr pump is activated. Electropneumatically operated valves are used between the vacuum chamber and the pumps. A vacuum of $<10^{-7}$ atm is attained before the filament in the mass spectrometer is turned on. The sample is continuously heated as long as the pressure does not exceed 10^{-5} atm. The Knudsen effusion cell containing the fuel sample sits on a pedestal that is capable of axial and azimuthal (Z,ϕ) motion. The (Z,ϕ) motion is used to align the orifice of the sample cell with the entry hole to the cross-beam ionizer.

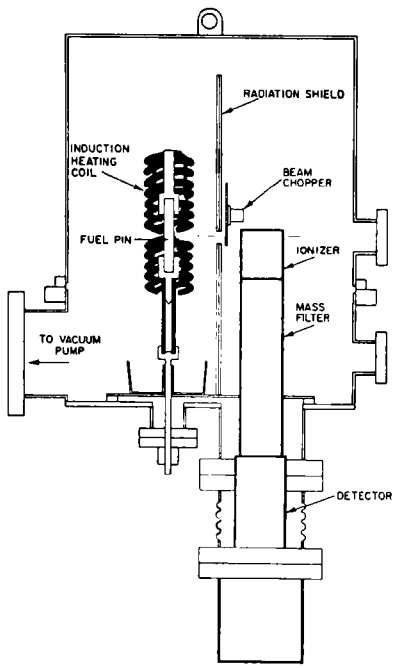

Fig. I-1.

Experimental Apparatus for Characterization of Volatile Fission Products Released from an Irradiated Fuel Sample

It is necessary to distinguish mass peaks due to fission product species from those due to background gases. For condensable species (such as CsI, Cs, and Te), this is usually done by placing a shutter between the sample and the ionizer of the mass spectrometer. Peaks that disappear when the shutter is closed are presumed to be due to species which originate in the sample. As the temperature of the system increases, the condensable species begin to act more like noncondensable gases, and these species can, therefore, contribute to the general background. Under these conditions, a mass peak due to species emitted from the sample is identified by a decrease in the magnitude of that mass peak when the shutter is closed. These conditions tend to decrease the sensitivity of the system. To maintain maximum sensitivity of the system, the molecular beam can be modulated (chopped) and

the modulated signal detected and amplified using phase-lock techniques. Figure I-2 shows the improvement in signal-to-noise ratio obtained with modulation and phase-lock amplification. The lower traces were taken without beam modulation; the peaks due to the various tellurium isotopic molecules are barely seen above the background noise. The upper traces display the same signal using beam modulation and phase-lock amplification.

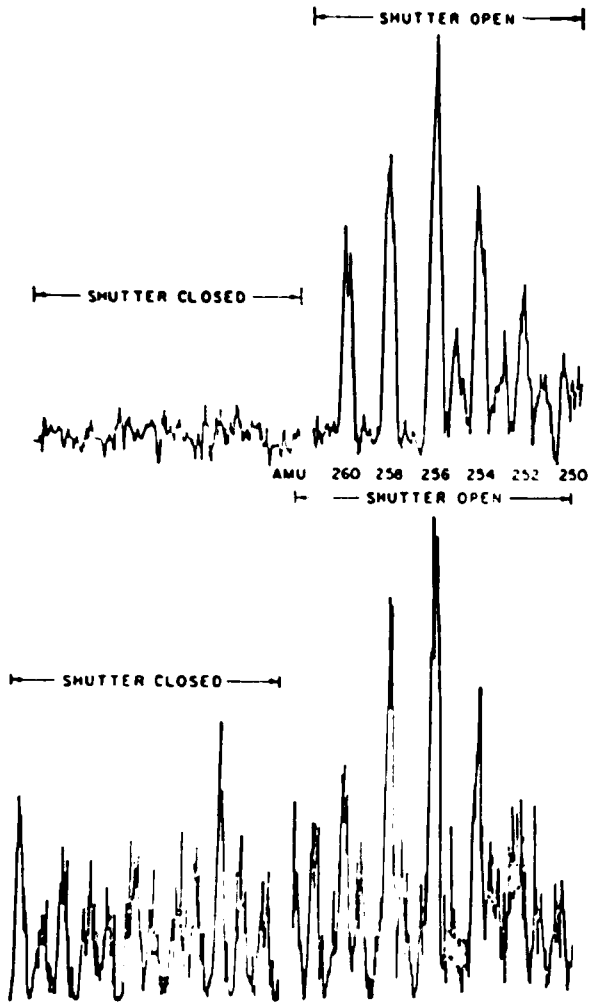

Fig. I-2.

Comparison of Mass Spectrometer Performance on Tellurium Spectra. The upper spectra are taken with modulation and phase-lock amplification and the lower spectra without.

Two fuel sample configurations were used in our studies. In the first, a 10-cm length of a fuel pin was sealed at both ends, a hole was drilled in the cladding to simulate a defect, and the pin was inductively heated in a vertical orientation. In the second sample configuration, a 1-cm long irradiated fuel segment was heated inside a tungsten or nickel Knudsen effusion cell. The hole in the cladding of the first sample and the orifice of the effusion cell of the second sample were aligned with the ionizer aperture. Each sample was heated to a selected temperature and held at that temperature for 15 to 60 min. While at the selected temperature, mass spectrometric observations of the released gaseous species were made. Between heating periods, the sample was allowed to remain at room temperature in the vacuum chamber.

Two irradiated samples were studied. The first sample was prepared from a 10-cm length of fuel cut from a Consumers Power Big Rock Point Reactor fuel rod. The average burnup of this sample was 31,250 MWD/T.* The second sample was a 1-cm long section from a second Big Rock Point fuel rod that had an average burnup of 39,150 MWD/T. Both samples were cut from a location near the axial center of the rod. The burnup for each sample was determined from scaling of gamma scans of the fuel rod, assuming the average burnup was as given above.

The gaseous species that enter the ionizer are partially ionized by an electron beam. The mass of the ion is determined using the quadrupole mass filter and an electron multiplier detector. The magnitude of the ion current is proportional to the rate of release of the gaseous species through the orifice. The proportionality factor is specific for each gaseous species and must be experimentally determined. Proportionality factors were determined in separate experiments using a Knudsen cell containing pure chemical compounds whose vapor pressure and ionization characteristics were known. For example, with pure CsI in the Knudsen cell, gaseous CsI is ionized by two mechanisms:[2]

$$CsI + e^- = CsI^+ + 2e^- \qquad \text{(I-1)}$$

and

$$CsI + e^- = Cs^+ + I + 2e^- \qquad \text{(I-2)}$$

For the range of electron energies used in these studies (20 eV and below), no iodine ions, positive or negative, were produced by the electron impact ionization of gaseous CsI. Cesium ions produced by Eq. I-2 can be distinguished from ions produced by the ionization of gaseous cesium by the value of the appearance potential. The appearance potential for Cs^+ in Eq. I-2 is 7.5 eV, while the value for Cs^+ from Cs (g) is 3.9 eV.[3]

In the case of xenon and krypton, the mass spectrometer was calibrated by separately leaking the pure gases into the vacuum chamber at a known rate. A gas manifold was attached to the vacuum chamber so that this calibration could be done when an irradiated fuel sample was in place. Tests of the apparatus with pure cesium iodide indicate that pressures of CsI as low as 3×10^{-9} atm are readily detected and measured.

The sample temperature was determined by an automatic optical pyrometer. The automatic pyrometer was calibrated in place using heated samples of Zircaloy or tungsten and a calibrated visual optical pyrometer. Below the range of the optical pyrometer (~1000 K), the temperature was

*MWD/T = megawatt days per ton.

estimated from the power output of the induction heater. A linear relation was found to exist between the logarithm of the temperature and the logarithm of the power output of the induction heater.

b. Studies of a Synthetic Mixture of Urania and Fission Product Compounds

As a final test of the experimental procedure and a means to gain an understanding of the behavior of known fission product species, we fabricated a mockup of a fuel pin section by filling a section of Zircaloy tubing with a powdered mixture of inactive fission product compounds and urania. Cesium was added as CsI and Cs_2CO_3, iodine as CsI, and tellurium as metallic tellurium. The urania-fissia mixture was prepared[4] using powdered urania and thirteen different elements to simulate the irradiated fuel. The urania-fission mixture was ball milled for several hours and then mixed with a mortar and pestle. The mixture was "sintered" at low temperature so as to minimize loss of simulants. The composition was the same as reported by Schreibmaier et al.[4] This sample was heated stepwise to a maximum temperature of ~1600 K over a total heating time of about 32 h.

At temperatures below 1170 K, only CsI^+ and Cs^+ ions were observed. The Cs^+ ion was found to originate from both the fragmentation of CsI and from atomic cesium arising from the decomposition of Cs_2CO_3 and/or Cs_2UO_4. (It is likely that the Cs_2CO_3 reacted with the UO_2 to produce cesium uranates, which decompose on heating above ~1000 K to yield gaseous cesium.) At ~1300 K, gaseous SnTe was observed (see Fig. I-3). The formation of this gas was attributed to a reaction between tin in the Zircaloy cladding and tellurium that had dissolved in the cladding at lower temperatures. After continued heating at ~1275 K, the SnTe signals disappeared, presumably because of the depletion of the readily available tin on the inner surface of the Zircaloy cladding (Zircaloy contains about 1.5% tin). Gaseous CsTe was also observed. This molecule was probably formed by the reaction of gaseous cesium (whose signal was very strong) with the $ZrTe_2$ layer on the inner surface of the Zircaloy cladding. The CsTe signal gradually decreased as the heating was continued, probably due to the depletion of the $ZrTe_2$ layer. At a temperature of 1325 K evidence for atomic iodine was first noted; at the highest temperature studied (1575 K), the existence of atomic iodine was verified. This iodine is believed to form from the thermal decomposition of CsI. At high temperatures CsI is expected to dissociate into Cs and I atoms. At 1500 K, the equilibrium constant for the dissociation reaction calculated from the thermodynamic data is about 5.7×10^{-8} atm. Thus, for an assumed background pressure of 1×10^{-6} atm, the degree of dissociation is 0.2. The results of SOLGAS[5,6] equilibrium calculations for the Zr-Sn-Te-Cs-I system are in qualitative agreement with the mass spectrometric results. The following chemical reactions are involved in these processes:

$$Te + Zr\ (cladding) = ZrTe(sol)$$

$$ZrTe(sol) + Sn\ (cladding) = Zr + SnTe(g)$$

$$ZrTe(sol) + Cs(g) = Zr + CsTe(g)$$

$$CsI(g) = Cs(g) + I(g)$$

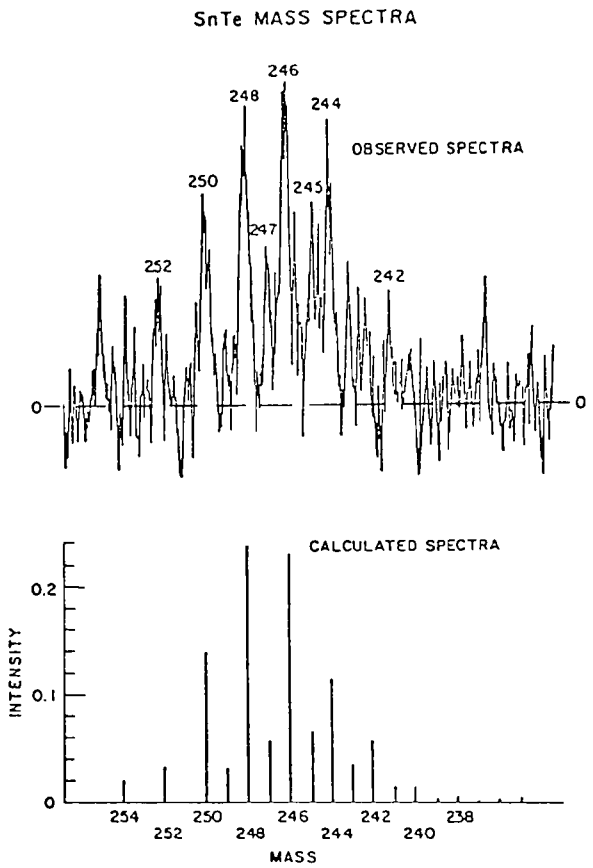

Fig. I-3.

Observed and Calculated SnTe Mass Spectra for the 238-254 Mass Region at ~1300 K

The ion currents observed for CsI^+ from the synthetic fuel/fission product mixture were considerably lower than would be expected from pure CsI in a Knudsen cell at the same temperature. For example, at 975 K, the vapor pressure of pure CsI is 1.6×10^{-3} atm. This pressure would yield a rate of escape of 1.1×10^{-2} g/min through the 1-mm dia hole in the cladding. From the observed ion current for CsI^+, the release rate was calculated to be 2.9×10^{-9} g/min. This very low release rate is believed due to the tortuous path that gaseous CsI must traverse through the porous bed of urania. To examine this question further, a small layer of the synthetic mixture was packed into the bottom of a Knudsen cell, and the CsI pressure was monitored as a function of time. The pressure decreased as the sample was depleted in CsI. The observed data were in agreement with the assumption that the decrease in pressure was due to the development of a depleted layer on the surface of the sample. Therefore, the observed low rate of escape of CsI(g) from the simulated fuel pin was likely due to the depletion of CsI near the orifice and the slow effusion of CsI (g) through the urania bed.

c. Studies of Irradiated Fuel Samples

The first irradiated fuel sample was heated stepwise to 1775 K over a total heating period of about 28 hours. The gaseous species observed were xenon, krypton, cesium, and tellurium. Xenon and krypton were observed

at all temperatures. The release rates of xenon and krypton were equal when corrected for their expected fission yield. Cesium was observed during the first six hours of heating (maximum temperature, 815 K). As the cesium signal disappeared shortly after being observed, it is believed that the cesium most likely originated from the fuel-cladding gap. Cesium release was not observed again until the sample temperature was above 1125 K. These observations are in striking contrast to those made on the simulated urania-fissia mixture, where the cesium emission increased as temperature increased. Measurement of the cesium activity from a deposit on the induction coil located near the hole in the cladding indicated that less than one percent of the total cesium in the fuel sample had been released during the total time of sample heating. Tellurium was not observed until the temperature was increased to about 1570 K. Its measured appearance potential was 9.4 eV, which is in agreement with the first ionization potential for Te of 9.0 eV.

The second irradiated fuel sample was heated to 2120 K during a period of 18 h. The gaseous species observed were xenon, krypton, cesium, tellurium, and iodine. Xenon and krypton were found at all temperatures. Cesium was not observed when the sample was initially heated, as in the case of the first sample, but was observed when the temperature reached about 1260 K, after which the cesium signal increased as the temperature increased. Tellurium was first observed at 1435 K, this signal also increased as the temperature increased. Iodine was first observed at 1535 K; this signal also appeared to be increasing as the temperature increased. Quantitative release rates were obtained for Kr and Xe but were not obtained for Cs, Te, or I.

The most prominent peak observed for both samples were those due to xenon (masses 131, 132, 134, and 136). The mass 136 peak was used for quantitative studies. The release rates for xenon and krypton, when corrected for fission yield, were equal within the uncertainty of the measurements. The xenon release rate was found to be a function of the temperature and the total time that the sample had been heated.

During the first 1100 min of heating of the first sample, when the temperature had been raised stepwise to 1225 K, the rate of release of xenon decreased. Above 1455 K, the rate increased. On subsequent heating of the sample, the rate was approximately an exponential function of temperature. On reheating the sample at low temperatures, the rate was much lower than observed initially. The initial high rates of xenon emission are believed due to the release of the relatively "free" xenon in cracks and fissures within the fuel oxide. The release of this xenon occurred in the first 1000 min of heating. The temperature increase during this period probably had only a minor effect on the release rate. Subsequent heating, which was at high temperatures, led to the release of xenon from within the grains. A plot of the logarithm of the rate of emission vs. the reciprocal of the absolute temperature gave a curved line, which could be resolved into a double exponential relation. If these two exponentials are interpreted as resulting from two activation-controlled processes, then the activation energy is calculated to be 19 kcal/mol at low temperatures and 97 kcal/mol at high temperatures. These values suggest pore diffusion at low temperatures and bulk or surface diffusion at high temperatures. Similar breaks in the rate of release of the rare gases have been previously reported.[7]

The rate of release of xenon in these studies is significantly lower than that given as the "best" estimate in a recent review by the Nuclear Regulatory Commission (NRC) of fission-product release rates.[3] At ~945 K the xenon fractional release rate observed in our studies (during the early part of the heating cycle) was 2 x 10^{-7}/min, while the NRC value is 4 x 10^{-8} /min. At ~1475 K, the observed fractional release rate was 1.7 x 10^{-6}/min, which is much lower than the NRC value of 2 x 10^{-3}/min. However, it should be noted that the NRC rates apply to an unclad fuel in the presence of steam. Our results suggest that the release rate is not a simple function of temperature but also depends on the previous irradiation history of the fuel. Our results also indicate that the release of other fission products is lower than suggested by the NRC report.

d. Effect of Fuel Oxidation on Xenon Release

Another test was performed to determine the effect of fuel oxidation on xenon release. In this test, a 10.4 g sample of irradiated fuel (burnup about 4.16%) was heated in a platinum-lined nickel Knudsen cell. Oxygen at low pressure could be leaked into the cell at a known rate from an external supply (Fig. I-4). The easily released fission gases were removed by

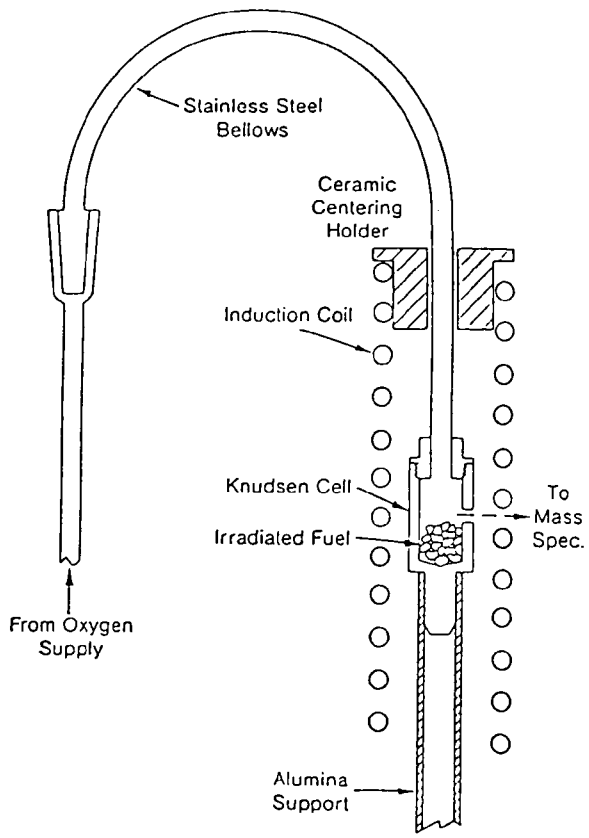

Fig. I-4.

Apparatus Used for Supplying Oxygen to Sample during Fuel Oxidation Studies

heating the sample (to about 1375 K) until very low release rates of xenon were detected. During subsequent heating cycles, oxygen was leaked into the cell when the sample was at constant temperature and the release of xenon had

reached a steady rate. For the first nine heating cycles in which oxygen was leaked into the cell, there was no significant change in the very low rate of release of xenon during the time that oxygen was leaked into the cell. However, CO_2 and CO pressures in the system increased when the oxygen flow started. Thus, the sample contained a carboniferous impurity, which was reacting with the oxygen to form CO and CO_2 that escaped from the cell. It was not possible to relate the water peak in the mass spectrum to a hydrogenous impurity in the sample; the water peak was dependent on the time at temperature and not noticeably related to the oxygen flow rate. The mass spectrometer had been calibrated for CO_2 and CO so that the observed ion currents were converted to rate of escape of these species from the cell. From the trend of the escape rates with time for CO_2 and CO, it was possible to estimate their escape rate in the first nine heating cycles and compute the amount of oxygen retained within the cell. When these corrections are applied, the calculated O/M ratio (where M = metal) at the end of the ninth heating cycle (if all of the oxygen retained in the cell oxidized the sample) is about 2.003. When the fuel was further oxidized, a significant increase in the rate of release of xenon was observed.

The total amount of xenon released for each heating cycle was obtained by a numerical integration of the rate of release data. The cumulative release of xenon as a function of the O/M ratio for the fuel sample is shown in Fig. I-5. It is seen that the release increases rapidly as soon as the O/M ratio increases above about 2.006. Above this stoichiometry, the release is essentially a linear function of the O/M ratio. The release appears to level off near an O/M ratio of 2.03. We believe this effect to be due more to the physical nature of the fuel, i.e., surface-to-volume ratio, than to stoichiometry. While at high temperature, the fuel is in a single-phase regime. However, the daily return to room temperature brings the

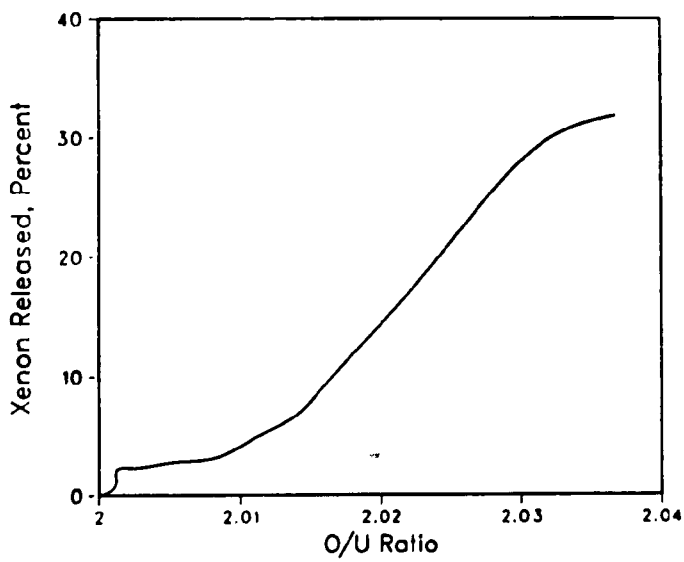

Fig. I-5. Effect of Change in Irradiated Fuel Stoichiometry on Xenon Release

material into a two-phase regime and strain is certain to develop. The strain/stress is relieved by cracking, each cycle transforming the fuel to a finer powder. If the estimated oxygen retentions are correct, the final O/M ratio of the fuel was about 2.02. These calculations imply that the fuel need not be completely oxidized to U_4O_9 to release all of the xenon. A 4.1% conversion to U_4O_9 corresponds to an O/M ratio of 2.036. The total amount of oxygen leaked into the fuel, not corrected for reaction with the carbon impurity, would have raised the O/M ratio to 2.08. Most of the heating cycles in which the effect of oxygen was studied were carried out at about 1425-1455 K.

e. Conclusions

Our laboratory experience indicated that the mass spectrometer exhibited no degradation in performance while in the β-γ radiation field. There was an increased background signal, which slightly decreased instrument sensitivity. Calibration checks were performed using pure cesium iodide, and over a four-year period the resolution and sensitivity of the quadrupole have remained constant.

Our synthetic fuel studies indicated the importance of the SnTe and CsTe species. Tellurium dissolution in the Zircaloy cladding with subsequent release as SnTe at high temperatures is an important mechanism for delaying release of tellurium. This reaction may have less importance in operating fuels because of an inner zirconium oxide layer that reduces the potential for tellurium to reach and dissolve in the Zircaloy.

Our studies with irradiated fuel yielded information on the release of xenon, krypton, cesium, tellurium, and iodine. Most important was the finding that the rare gases are released at a rate that is lower than given in Ref. 3. Further, the release of cesium differs from that of krypton and xenon release and is suggestive of retention within the fuel, probably as cesium uranate. Our oxidation studies showed that as the fuel is oxidized the xenon release rate increases significantly.

Probably our most significant finding is the lack of observation of molecular cesium iodide. This molecule should be readily observed based on Ref. 3. With our much lower measured ($\sim 10^3$) values for xenon release rate, we are near the detection limit for cesium iodide and background noise becomes a problem. Further, molecular cesium iodide may also diffuse very slowly through the fuel, thereby reducing its release rate even further.

2. Gas Phase Species in CsI-CsOH System
(P. E. Blackburn)

The revolatilization of fission products from reactor system surfaces due to self-heating of the deposits by radioactive decay has become a complicating factor in the source-term definition effort. Further, revaporization has had a major impact on calculating the fission product distribution during degraded core accidents. As currently modeled in pressurized water reactor (PWR) systems, revaporization will result in the delayed evolution of volatile fission products from the primary coolant system, thus increasing the containment airborne inventory at times when containment integrity may be uncertain. In some boiling water reactor (BWR) accidents, this process will

cause eventual transport of most of the volatile fission products out of the dry-well containment volume. In an earlier experimental program focused on the characterisation of vapor and aerosol transport, CsI and CsOH vapors were studied separately and together in flowing steam under a temperature gradient (from 1273 to 500 K). Analysis of the condensate revealed that the dew point of the iodine-carrying species was lower than expected when both CsI(g) and CsOH(g) were present in the gas mixture.[8] In order to explain this result, we postulated that CsI and CsOH formed a more volatile complex, i.e., CsI·CsOH(g), thereby reducing the partial pressure of CsI(g) in the vapor.

In the current experimental effort, we investigated the iodide-hydroxide (CsI·CsOH) vapor species over a liquid solution of CsI and CsOH. For these studies, baseline data for CsI and CsOH were established separately and then the CsI-CsOH mixture was studied. A review of the literature showed fairly good agreement for the thermodynamic properties of CsI(g) and $Cs_2I_2(g)$.[9-13] The JANAF tables showed a moderate uncertainty for the thermodynamic properties of the CsOH(g) monomer and a large uncertainty for those of the $Cs_2(OH)_2(g)$ dimer.[14] No data were found for CsI·CsOH(g).

a. Experimental

We used an Extranuclear quadrupole mass spectrometer to measure the partial pressures of vapor species over liquid CsOH held in a silver Knudsen cell. The Knudsen cell was heated in a tungsten resistance furnace. Temperatures were measured with a Chromel-Alumel thermocouple inserted in a well in the Knudsen cell. The ion current for each of the positive ions was measured, multiplied by the absolute temperature, and plotted in Fig. I-6.

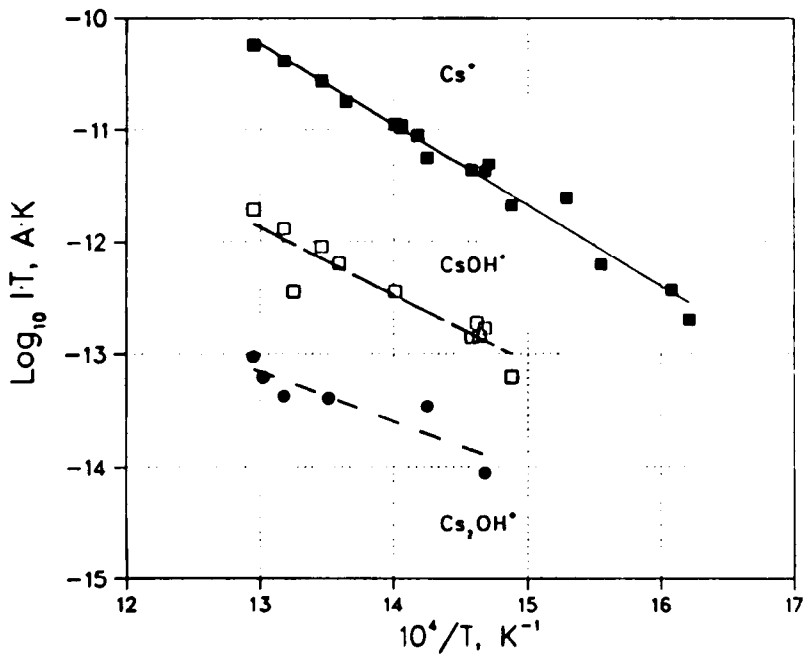

Fig. I-6. Product of CsOH Vapor Ion Currents and Temperatures Measured with a Mass Spectrometer vs. 1/T

The top curve is for Cs^+, which is believed to be a fragment of the CsOH(g) monomer; the next-lower curve is for the parent ion $CsOH^+$; and the bottom curve is for Cs_2OH^+, a fragment of $Cs_2(OH)_2(g)$. The CsOH(g) and $Cs_2(OH)_2(g)$ pressures were calculated from the $CsOH^+$ and Cs_2OH^+ ion peaks in the mass spectra. Schoonmaker and Porter[15] showed that formation of MOH^+ and M_2OH^+ (where M is Na, K, Rb, and Cs) arises from the dissociative ionization of MOH(g) and $M_2(OH)_2(g)$, respectively, when silver Knudsen cells are used. These authors also showed that M^+ is the product of dissociative ionization of MOH(g).

We also used a silver Knudsen cell in the mass spectrometric study of cesium iodide vapor, where Cs^+, CsI^+, and Cs_2I^+ ion intensities were measured. The Cs^+ ion is a fragment of the CsI(g) monomer, and Cs_2I^+ is a fragment of $Cs_2I_2(g)$. The CsI^+ and Cs_2I^+ ion intensities were then used to calculate CsI(g) and $Cs_2I_2(g)$ pressures. Lelik et al.[16] analyzed (with a mass spectrometer) NaI vapors yielding Na^+, NaI^+, Na_2I^+, $Na_3I_2^+$, and $Na_4I_3^+$ ions, and CsI vapors yielding Cs^+, CsI^+, Cs_2I^+, $Cs_3I_2^+$, and $Cs_4I_3^+$ ions. The ionization efficiency curves for both iodides showed no break points to indicate further fragmentation. Lelik et al. assumed the latter ions in each case resulted from dimer, trimer, and tetramer fragmentation during ionization with the formation of a free iodine atom.

We produced liquid solutions of cesium iodide and cesium hydroxide by adding weighed amounts of these two salts to the Knudsen cell, dehydrating at 450°C, and heating above the liquidus temperature in the mass spectrometer vacuum system. Reproducible partial pressures were taken as an indication of thorough mixing. This required heating above the CsI melting point of 907 K.

Following calibration of the mass spectrometer with the pure components, we measured the partial pressures of CsI(g), $Cs_2I_2(g)$, CsOH(g), and $Cs_2(OH)_2(g)$ over solutions of CsOH in CsI. In these measurements, the ion intensities of the four gases were measured continuously with time and temperature. The ions detected were CsI^+, Cs_2I^+, $CsOH^+$, and Cs_2OH^+; the dimers lost either I or OH during the ionization process. When the samples were loaded into the silver Knudsen cell, the initial amounts of CsI and CsOH were determined by weighing the cell before and after each addition. The CsOH used in the experiments contained about one mole of water per mole of CsOH. To remove the water of hydration, the loaded Knudsen cell was placed in a silver tube inside a quartz tube surrounded by a resistance furnace. Helium was flowed over the cell while the temperature was slowly increased to about 450°C. The temperature was held there for at least two hours. The Knudsen cell was cooled in flowing helium and then weighed to determine water loss, then it was immediately placed in the vacuum chamber of the mass spectrometer. This procedure allowed determination of the initial composition of the CsI-CsOH sample. The final composition was determined by weighing the sample residue and chemically analyzing the residue after a series of pressure measurements.

b. Calculational

To convert ion intensities obtained from the mass spectrometry studies to pressures, it is necessary to determine the constant K in the formula,

$$P = K\ I\ T \tag{I-3}$$

where P is the pressure in atmospheres, I is the ion intensity, and T is the temperature in Kelvin. For this purpose the Langmuir equation is used:

$$P = \frac{\Delta w\ T^{1/2}}{44.33\ A\ t\ M^{1/2}} \tag{I-4}$$

where Δw is the weight lost, M is the molecular weight of the gas, A is the area of the Knudsen cell orifice corrected for the Clausing factor,[17] and t is the time in seconds. The reciprocal of the constant K is calculated by combining the two equations:

$$\frac{1}{K} = \frac{44.33\ A\ M^{1/2} \int I\ T^{1/2}\ dt}{w} \tag{I-5}$$

where w is the weight of CsI or CsOH vaporized as CsI(g) or CsOH(g). The fraction of CsI or CsOH vaporizing as monomer was computed from the total CsI or CsOH by apportioning the weight to the monomer and dimer by $\sqrt{2}$ times the intensity ratio of monomer to dimer for each system. Equation I-5 is numerically integrated over the total time, corresponding to the weight loss as monomer, to obtain the constant K. Pressures are then calculated from Eq. I-3. The constant for the dimer is one-half that of the monomer (assuming that the ionization cross section for the dimer is twice that for the monomer). The pressure is inversely proportional to the ionization cross section. The constant was determined for each set of measurements to minimize the effects of misalignment of the molecular beam from the Knudsen cell or other possible nonreproducible effects. For the conditions of our experiments, the values of the constants were approximately $K_{CsOH} = 10^8$ and $K_{CsI} = 10^9$ atm/A/K. This means that the ionization cross section of CsOH(g) is about ten times higher than the cross section of CsI(g). Although the sensitivity of the mass spectrometer was checked using perfluorotripentylamine for the mass range between 50 and 602, there is some uncertainty about these tests. We believe the measurements are accurate within a factor of two for the dimers. The cesium iodide and hydroxide molecules were ionized with 30 eV electrons.

c. Results and Discussion

(1) Partial Pressures over CsOH and over CsI

Equations I-3 to I-5 were used to calculate the pressures of CsOH, $Cs_2(OH)_2$, CsI, and Cs_2I_2 gas over liquid CsOH and CsI. Third-law calculations were carried out using JANAF free energy functions for CsOH(c), CsOH(l), CsOH(g), and $Cs_2(OH)_2$(g).[14] Estimated free energy functions for CsI(c), CsI(l), CsI(g), and Cs_2I_2(g) were used to calculate the heats of vaporization of CsI(g) and Cs_2I_2(g).[18] These values were based on thermodynamic properties listed in NBS Technical Note 270-8[19] and the heat content

of the solid and liquid from Kaylor et al.[20] Values for cesium and iodine were taken from JANAF.[21] The free energy functions for gaseous CsI and Cs_2I_2 were also estimated[17] using the data of Welch et al.[22] and Rusk and Gordy.[23]

Third-law calculations for the heat of vaporization ($\Delta H_{vap\ 298}$) yielded 36.330 ± 0.448 kcal/mol for CsOH(g), 37.199 ± 0.727 kcal/mol for $Cs_2(OH)_2$(g), 45.039 ± 0.315 kcal/mol for CsI(g), and 55.931 ± 0.519 kcal/mol for Cs_2I_2(g), where the uncertainty is one standard deviation. The experimental data and the resulting heats of vaporization are presented in Tables I-1 to I-4.

Table I-1. CsOH(g) Pressure over Liquid CsOH

T, K	P_{CsOH}, atm x 10^5	$-(G^\circ - H_{298})/T$, cal/deg mol		ΔH_{vap},[a] kcal/mol
		Gas	Liquid	
654	0.782	63.83	33.03	35.429
684	1.68	64.14	33.51	35.903
684	1.28	64.14	33.51	36.270
686	1.24	64.16	33.54	36.403
714	3.23	64.44	33.99	36.419
622	0.0560	63.50	32.50	37.074
672	0.553	64.02	33.32	36.797
736	5.70	64.67	34.33	36.621
759	11.6	64.90	34.69	36.592
702	3.19	64.32	33.80	35.875
681	1.49	64.11	33.46	35.914
743	8.04	64.74	34.44	36.431
772	17.1	65.03	34.89	36.573

[a]Average $\Delta H^\circ_{vap\ 298}$ = 36.330 ± 0.448 kcal/mol.

Table I-2. $Cs_2(OH)_2$(g) Pressure over Liquid CsOH

T, K	P_{CsOH}, atm x 10^5	$-(G^\circ - H_{298})/T$, cal/deg mol		ΔH_{vap},[a] kcal/mol
		Gas	Liquid	
759	1.88	93.25	34.69	38.003
702	1.53	92.21	33.80	35.958
681	0.394	91.82	33.46	36.916
743	1.81	92.90	34.39	37.289
768	2.81	93.41	34.83	37.747
772	4.21	93.48	34.89	37.283

[a]Average $\Delta H^\circ_{vap\ 298}$ = 37.199 ± 0.727 kcal/mol.

Table I-3. CsI(g) Pressure over Liquid CsI

T, K	P_{CsOH}, atm x 10^5	$-(G^\circ - H_{298})/T$, cal/deg mol		ΔH_{vap},[a] kcal/mol
		Gas	Liquid	
917	0.634	69.72	35.39	44.894
942	0.935	69.88	35.81	45.146
949	1.78	69.92	35.93	45.202
955	1.77	69.95	36.03	44.435
977	1.96	70.09	36.38	45.043
993	2.46	70.19	36.64	45.180
1003	2.67	70.25	36.79	45.374
1017	3.74	70.34	37.01	45.191
1029	4.82	70.41	37.19	45.093
1035	5.08	70.45	37.28	45.191
1032	5.06	70.43	37.24	45.094
997	2.83	70.22	36.70	45.042
972	1.78	70.06	36.30	45.038
945	1.11	69.90	35.86	44.945
922	0.771	69.75	35.48	44.732

[a]Average $\Delta H^\circ_{vap\ 298}$ = 45.039 ± 0.315 kcal/mol.

Table I-4. Cs_2I_2(g) Pressure over Liquid CsI

T, K	P_{CsOH}, atm x 10^5	$-(G^\circ - H_{298})/T$, cal/deg mol		ΔH_{vap},[a] kcal/mol
		Gas	Liquid	
924	0.515	111.57	35.51	55.594
944	0.789	111.85	35.84	55.632
950	1.28	111.93	35.94	54.980
968	1.35	112.18	36.24	55.582
984	1.70	112.40	36.49	55.760
997	1.87	112.58	36.70	56.079
1004	1.96	112.68	36.81	56.253
1022	2.59	112.92	37.09	56.368
1033	3.05	113.07	37.25	56.449
1041	3.25	113.18	37.38	56.615

[a]Average $\Delta H^\circ_{vap\ 298}$ = 55.931 ± 0.519 kcal/mol.

Figure I-7 shows, as a function of temperature, the measured and calculated concentrations of CsOH vapor species (monomer and dimer) over liquid CsOH. These curves were determined from the JANAF tables[14] and our mass spectrometric work. The JANAF tables predict that the dimer will be more abundant than the monomer below 800 K, and that the monomer will be the dominant species above 800 K. Our data (labeled "CMT") show CsOH monomer pressures about one-third of those calculated with the JANAF values. The largest difference was found for the dimer, where the values are 100-fold lower than the JANAF values at 800 K. When both sets of CsOH species (monomer

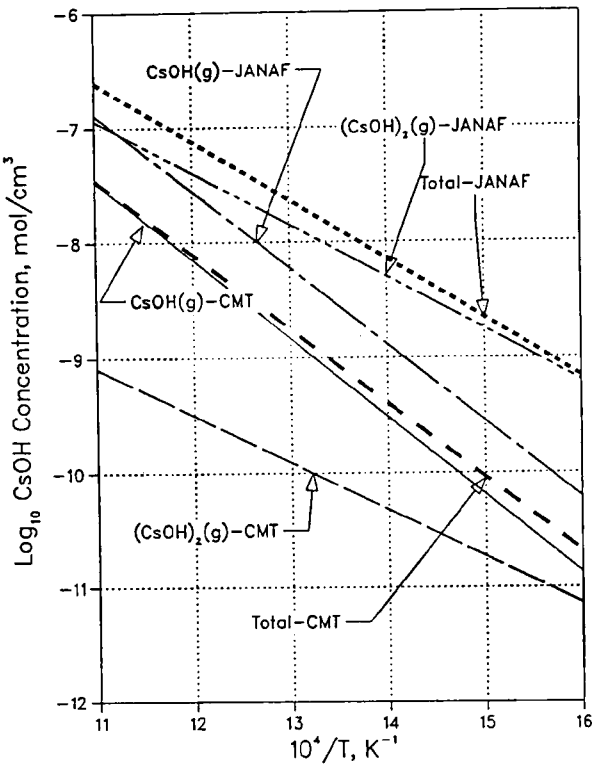

Fig. I-7.

Measured CsOH Gas Concentrations (designated by "CMT") and Calculated CsOH Concentration (designated by "JANAF") in Equilibrium with Liquid CsOH

and dimer) are added, our CsOH concentrations are a factor of ten lower than those calculated with JANAF data, but are in general agreement with the transpiration results of Cummings et al.[24]

A heat of formation at 298.15 K of -62.0 ± 3.0 kcal/mol was calculated for CsOH(g) based on atomic absorption spectroscopy of hydrogen-oxygen flames reacting with cesium gas.[14] Our heat of formation is -60.7 ± 0.5 kcal/mol CsOH(g). The JANAF heat of formation for dimeric cesium hydroxide, $Cs_2(OH)_2(g)$, based on mass spectrometric measurements, is -164.4 ± 10.0 kcal/mol. A much smaller value of -156.9 ± 0.7 kcal/mol for $Cs_2(OH)_2(g)$ was found here. The much lower pressure of dimeric cesium hydroxide gas accounts for the lower total concentration of cesium hydroxide measured in the Cummings et al. transpiration measurements and our unpublished transpiration measurements.

Our data for the heats of formation of the cesium iodide monomer and dimer gases are in reasonably good agreement with the NBS selected values of chemical thermodynamic properties.[19] We found heats of formation at 298.15 K of -37.8 ± 0.7 and -109.8 ± 0.6 kcal/mol for CsI(g) and $Cs_2I_2(g)$, respectively. The NBS selected values are -36.3 and -109.6 kcal/mol, respectively.

(2) Gases over Solutions of Cesium Iodide in Cesium Hydroxide

In the mass spectrometry measurements, we attempted to measure the $CsI \cdot CsOH^+$ ion at mass 410 without success. Since the alkali halide polymers lose a halide atom and alkali hydroxide polymers lose OH

during ionisation to produce fragments of the parent molecules, $CsI \cdot CsOH(g)$ should lose either I or OH during ionisation. The problem here is that the two possible fragments are indistinguishable from those of $Cs_2I_2(g)$ or $Cs_2(OH)_2(g)$, i.e., Cs_2I^+ or Cs_2OH^+, respectively. Furthermore, we do not know which fragment to look for.

By taking advantage of the relation between the CsOH or CsI concentration in liquid solution and its partial pressure and the relation between the monomer and dimer pressures, one can establish conditions where the concentration of the fragment of the $CsI \cdot CsOH$ complex is larger than either fragments of the dimer [Cs_2I_2 or $Cs_2(OH)_2$] to be detected. Since the fragment of $CsI \cdot CsOH(g)$ has not been established, it is necessary to try both conditions (i.e., low concentrations of CsOH or low concentrations of CsI). The procedure outlined here will work only if the mixed anion complex ($CsI \cdot CsOH$) is stable enough to produce an ion fragment in sufficient quantities to be detected when added to the dimer fragment.

Figure I-8 may help to explain the process we used to measure the partial pressure of $CsI \cdot CsOH(g)$. Figure I-8 shows the partial pressures of $Cs_2I_2(g)$, and $Cs_2(OH)_2(g)$, and $CsI \cdot CsOH(g)$ calculated from our measurements. The calculated pressures at 925 K illustrate the effect of the

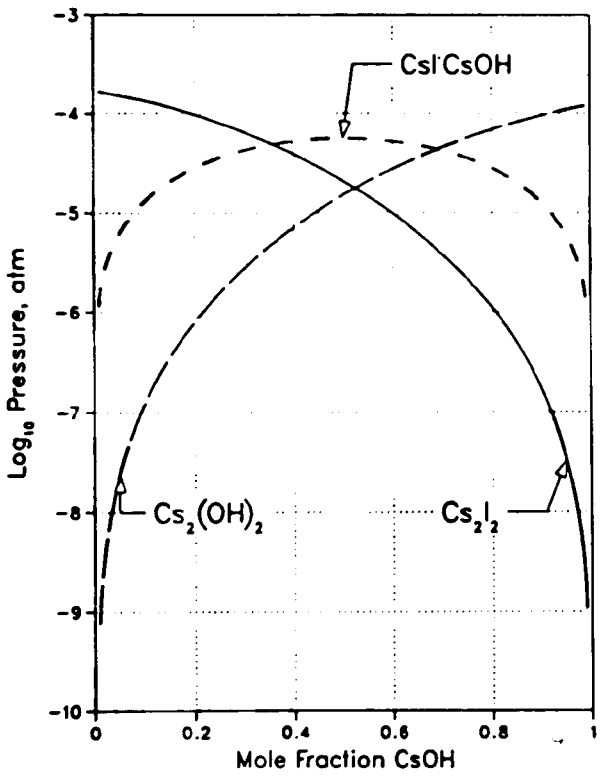

Fig. I-8.

Pressure Variation of Cs_2I_2, $Cs_2(OH)_2$, and $CsI \cdot CsOH$ at 925 K vs. CsOH Concentration in Liquid CsI

activity changes of CsI and CsOH on the partial pressures. The ratio of $CsI \cdot CsOH(g)$ to $Cs_2(OH)_2(g)$ increases as the concentration of CsOH decreases, changing from about 10 at 50% CsOH to 1000 at 1% CsOH. A similar effect is seen as the concentration of CsI in the solution decreases. It is apparent in Fig. I-8 that, if $Cs_2(OH)_2(g)$ and $CsI \cdot CsOH(g)$ species both produce Cs_2OH^+

fragments, the majority of the fragment will represent the CsI·CsOH molecule for lower CsOH concentrations. If the complex were less stable, the curve representing CsI·CsOH would be lower and the fraction of ion fragment lower. Therefore, we investigated the low CsOH concentrations to improve our chances of finding the complex.

By making measurements with solutions poor in CsOH or poor in CsI, we can lower the activity and partial pressure of CsOH or CsI, respectively. Since the dimer pressures are proportional to the square of the monomer pressures, the partial pressures of the dimers for the low activity species will be substantially reduced, while those for the complex will be reduced much less (see Fig. I-8). The CsI·CsOH pressures are proportional to the product of the CsI and CsOH pressures; the low activity species will have a low partial pressure, whereas the other species will have a high partial pressure. From our previous measurements of CsI(g) and $Cs_2I_2(g)$ pressures over CsI(1), we calculated the relation between the two gases for dimerization, 2 CsI(g) = $Cs_2I_2(g)$, where the dimer pressure may be calculated from

$$P_{Cs_2I_2} = P^2_{CsI} \exp(17915/T - 13.34) \qquad \text{(I-6)}$$

For dimerization of CsOH, $2CsOH(g) = Cs_2(OH)_2(g)$, the dimer pressure is calculated from,

$$P_{Cs_2(OH)_2} = P^2_{CsOH} \exp(18574/T - 19.08) \qquad \text{(I-7)}$$

Measurements of the Cs_2I^+ ion over CsI-CsOH solutions with low CsI concentrations produced intensities expected for fragments of $Cs_2I_2(g)$. This eliminated Cs_2I^+ from consideration as a fragment of CsI·CsOH. Calculations using measurements of CsI-CsOH solutions with an initial mole fraction of 0.135 CsOH showed that the fragmentation of the CsI·CsOH produces Cs_2OH^+ rather than Cs_2I^+. The ion intensity of the Cs_2OH^+ was more than 18-fold higher than calculations suggested it would be if it were only a fragment of $Cs_2(OH)_2(g)$. The results of analysis of this set of experiments are given in Table I-5.

In Table I-5, the first column gives the time of the experiment in minutes. Earlier measurements in this series did not include measurements of Cs_2OH^+ because temperatures were too low for its detection. The mole fraction of CsOH in the loaded Knudsen cell was computed from initial and final analysis and numerical integration of the pressures of CsOH and CsI with time. The CsOH mole fraction is tabulated in the second column. The temperature (column 3) was also changing as the composition changed. The pressure of Cs_2OH^+, calculated as $Cs_2(OH)_2(g)$, is given in the next column. [The Cs_2OH^+ ion intensity is the sum of the ion fragments from $Cs_2(OH)_2(g)$ and CsI·CsOH(g).] Pressures of CsOH and CsI, given in the next two columns, were interpolated from their ion intensities at intermediate times and temperatures. Equation I-7 was used to calculate the expected Cs_2OH^+ ion intensity for a fragment of $Cs_2(OH)_2(g)$ for the corresponding CsOH pressure (column 7). The ratio of the measured Cs_2OH^+ to the calculated Cs_2OH^+ ion intensity is

Table I-5. Pressures of CsI·CsOH Complex in Equilibrium with CsI and CsOH Gas

Time, min	CsOH Mole Fraction	T, K	Pressure, atm Cs_2OH^+ x 10^6	CsOH x 10^5	CsI x 10^5	$Cs_2O_2H_2$ (calc.) x 10^8	Ratio Col 4 / Col 7	Pressure of CsI·CsOH, atm x 10^6	K_{eq}
142	0.122	809	4.05	7.52	2.97	23.1	17.5	7.15	3198
151	0.114	839	6.47	9.43	11.8	16.0	40.3	11.8	1063
162	0.105	876	5.06	9.70	23.2	6.67	76.0	9.33	414
166	0.102	888	6.16	11.2	29.9	6.64	92.7	11.4	341
173	0.093	918	7.78	16.0	42.7	6.89	113.0	14.4	211
179	0.085	925	9.63	15.9	59.8	5.81	166.0	17.9	188
189	0.071	926	9.99	14.6	77.9	4.83	207.0	18.6	163
196	0.062	927	7.86	12.2	81.7	3.25	242.0	14.6	147
205	0.053	927	6.08	8.54	68.8	1.60	378.0	11.3	193

given in the next column. The total Cs_2OH^+ ion intensity varies from 17 to 378 times the fragment concentration expected if only $Cs_2(OH)_2(g)$ were present. The partial pressure of the CsI·CsOH complex is calculated from the total ion fragment intensity minus that computed from the calculated pressure of $Cs_2(OH)_2(g)$. The ion fragment intensity attributed to CsI·CsOH is converted to pressure with the constants in Eq. I-3 and the relative ionization cross sections. The ionization cross section for the complex is assumed to be the sum of the cross sections for CsI(g) and CsOH(g). The last column gives the equilibrium constant K_{eq} for the reaction of CsI(g) and CsOH(g) to form the complex. For the reaction CsI(g) + CsOH(g) = CsI·CsOH(g):

$$K_{eq} = \exp(17713/T - 14.02) \qquad \text{(I-8)}$$

This equation was calculated from a least squares fit to the data. Equation I-8 can also be derived from the measured free energy change and an estimated entropy for the complex. The entropy of the complex was estimated from the entropies of $Cs_2I_2(g)$ and $Cs_2(OH)_2(g)$. From the entropy change (31.4 e.u.) and the free energy at 900 K (-10350 cal), we calculated an enthalpy change of -38590 cal for the reaction to form the complex CsI·CsOH(g). This gives the following equation for the equilibrium constant:

$$K_{eq} = \exp(19420/T - 15.79) \qquad \text{(I-9)}$$

Pressures of CsI and CsOH over the mixture were measured to establish activities of CsI and CsOH in the solution. A mixture with an initial composition of 0.135 CsOH-0.865 CsI was heated to a maximum temperature of 927 K, while the ion intensities were measured for $CsOH^+$, Cs_2OH^+,

CsI^+, and Cs_2I^+. During the measurements almost all of the CsOH was vaporized and over half of the CsI was lost. The final composition of the sample was found to be 0.018 CsOH-0.982 CsI. The data were numerically integrated to obtain the constants to use in Eq. I-3 for the pressure calculations. The pressures were used with those for pure CsI and CsOH to calculate the activities of CsI and CsOH. The pressures were also used to calculate the change in composition between the initial and final values. From these activities and compositions, we calculated the formula for the activity coefficient for CsOH:[25]

$$RT \ln \gamma_{CsOH} = (-2600 \pm 280) N^2_{CsI} \qquad (I\text{-}10)$$

where R is the gas constant, T is the absolute temperature, γ_{CsOH} is the CsOH activity coefficient, and N_{CsI} is the mole fraction of CsI. The constant in Eq. I-10 (-2600 cal) was calculated from the last seven experimental points in Table I-5. Lumsden[25] reported a value of -2600 cal for the constant for a similar system, KI-KOH.

Equation I-10 was used to calculate the activities of CsOH and CsI at 925 K. The CsOH(g) and CsI(g) pressures were calculated with these activities and the pressures of pure CsOH(1) and CsI(1) described earlier. The pressures are the product of the activity and pressure of the pure substance. The pressures of $Cs_2I_2(g)$, $Cs_2(OH)_2(g)$, and CsI·CsOH(g) were calculated with Eqs. I-6 to I-8. These pressures (at 925 K) are plotted as a function of the mole fraction of CsOH in the CsOH-CsI solution in Fig. I-8.

Calculated pressures of CsOH(g), CsI(g), and CsI·CsOH(g) as a function of the CsI mole fraction at 800 K are presented in Table I-6. The percentage of iodine present as CsI·CsOH(g) is given in the last column; the rest of the iodine is present as CsI(g). The CsI·CsOH accounts for almost

Table I-6. Calculated CsI·CsOH Pressure over CsI-CsOH Liquid Solutions

	Pressures at 800 K, atm			
N_{CsI}	CsI·CsOH	CsI	CsOH	CsI·CsOH, %
0.00	0.00	0.00	4.24E-4	0.00
0.10	4.53E-7	5.63E-7	3.75E-4	44.6
0.20	1.01e-6	1.49E-6	3.17E-4	40.4
0.30	1.56E-6	2.85E-6	2.56E-4	35.4
0.40	1.97E-6	4.70E-6	1.96E-4	29.5
0.50	2.12E-6	7.03E-6	1.41E-4	23.2
0.60	1.97E-6	9.78E-6	9.40E-5	16.8
0.70	1.56E-6	1.28E-5	5.70E-5	10.9
0.80	1.01E-6	1.59E-5	2.98E-5	5.97
0.90	4.53E-7	1.87E-5	1.13E-5	2.36
1.00	0.00	2.12E-5	0.00	0.00

half of the gaseous iodine when the condensed CsI constitutes one-tenth of the CsI-CsOH solution, in agreement with the work of Johnson et al.[8] Table I-6 also gives the pressures of CsI(g), CsOH(g), and CsI·CsOH(g) as functions of CsI concentration dissolved in liquid CsOH.

Figure I-9 plots the pressures of CsOH(g), CsI(g), and CsI·CsOH(g) over a solution containing 0.1 CsI-0.9 CsOH at temperatures from 600 to 1300 K. The ratio of CsI·CsOH(g) to CsI(g) is close to one at low temperatures and decreases slightly with increasing temperature. The presence of the complex nearly doubles the amount of volatile iodine in the gas compared to that as CsI(g).

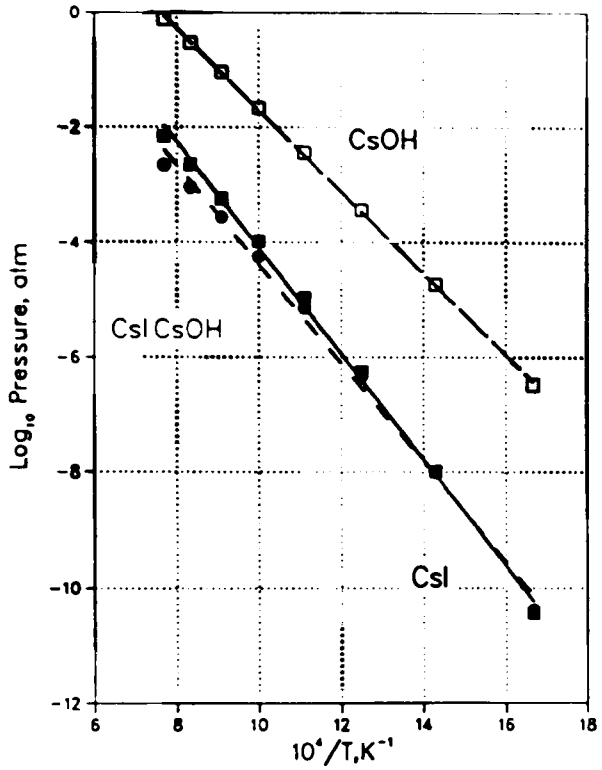

Fig. I-9.

CsI, CsOH, and CsI·CsOH Pressures over 0.1 CsI-0.9 CsOH Solution vs. 1/T

The results of this investigation are significant in understanding iodine and cesium release in a reactor accident. It was established that CsOH(g) properties measured here agree reasonably well with literature data. However, the partial pressures of the dimer, $Cs_2(OH)_2(g)$, are nearly 100 fold lower than those calculated from JANAF. Thus, the total pressure of CsOH in the gas should be much less than that calculated from the JANAF tables at low temperatures. For example, at 800 K the CsOH concentration in the gas at equilibrium with condensed CsOH obtained from our data is about one-tenth as high as that obtained from JANAF data (see Fig. I-7). The existence of the complex molecule CsI·CsOH(g), established here, should increase the amount of iodine in the gas phase at moderate temperatures. Since the fission yield of ^{235}U produces about 16 times as much CsOH as CsI, the presence of CsI·CsOH(g) will nearly double the concentration of iodine in the gas during revaporization. This could double the amount of iodine

released from the containment building. In the duct experiments by Johnson et al.,[8] CsOH and CsI deposited on the wall, formed aerosols which deposit or are carried out of the duct, and/or revaporized from deposits because of fission product decay heat. Our equilibrium pressures of CsI(g), $Cs_2I_2(g)$, CsOH(g), $Cs_2(OH)_2(g)$, and Cs·CsOH(g) may be used in analyzing and predicting the release behavior of cesium and iodine fission products under accident conditions.

3. Fission Product Release from Core-Concrete Melts
(M. F. Roche, J. L. Settle, and L. Leibowitz)

The objective of this study is prediction of the release of refractory fission products--strontium, barium and the rare earths--from the molten core-concrete mixtures that would form if a molten core penetrated the bottom of a reactor vessel in a severe accident. The vaporization of the core-concrete mixtures is being measured using a transpiration method. The materials tested are stainless steel, concrete (limestone or basaltic), and urania doped with 1 mol % La_2O_3 and SrO, 0.4 mol % BaO, and 2 mol % ZrO_2. These materials (alone or mixtures of all three) are vaporized at 2150-2400 K from a zirconia crucible into He-6% H_2 gas flowing at a rate of 100 cm^3/min or 200 cm^3/min over the sample surface. Up to 600 ppm H_2O is added to the gas in order to fix the partial molar free energy of oxygen in the range -420 to -550 kJ. The fraction of the sample that is vaporized is determined by weight change and by chemical analyses (inductively coupled plasma/atomic emission spectroscopy and fluorescence spectroscopy) of the condensates, which are collected in a molybdenum condenser tube.

The data obtained from the experimental runs are being compared with calculations made with the SOLGASMIX computer code. This computer code is used to calculate equilibrium conditions for 17 elements in the gas, the liquid, and the solid phases of the core-concrete melts. The number of gas-phase species (elements, oxides, hydroxides) included in the calculations is 100. There are also 74 solid or liquid species included in metallic and oxide phases. The thermodynamic data are obtained from the literature. Computer codes similar to SOLGASMIX are being used for prediction of refractory fission-product release from core-concrete mixtures in a severe reactor accident. Comparison of the experimental results and the calculations provides a test of the thermodynamic data base and the underlying assumptions of the computer codes.

In the runs with a mixture of stainless steel, limestone concrete, and doped urania, the amount of material transported was 98 mg at 100 cm^3/min and 129 mg at 200 cm^3/min. The closeness of these two amounts suggests that gas saturation had been achieved. Analytical chemistry data from the two runs (Table I-7) indicated that the major limestone-concrete components (Mg and Ca) had achieved saturation. However, the major steel components (Fe, Cr, and Ni) showed less transport (by factors of three to ten) than in earlier runs with steel alone.

To search for the cause of the low transport rate for the steel components, we cross-sectioned the zirconia crucible from the run at 100 cm^3/min. The solidified mass of concrete, urania, and steel occupied the bottom third of the crucible and had evidently been liquid during the run. The concrete-urania phase, which had wet the zirconia crucible, had a pronounced meniscus. In addition, the thickness of the zirconia-crucible wall had been reduced by

Table I-7. Calculated and Measured Transport by He-6% H_2-0.006% H_2O Gas (15.2 L) in Runs at 2150 K with Stainless Steel, Limestone Concrete, and Doped Urania

	Amount Added, mg	Calculated Transport, mg	Measured Transport, mg	
			200 cm^3/min	100 cm^3/min
La	33	0.013	<0.002	<0.005
Ba	6	0.006	0.018	0.028
Sr	12	0.003	0.006	0.012
U	2848	0.062	0.047	0.028
Fe	2470	44.0	1.26	1.52
Cr	628	32.0	1.64	1.36
Ni	277	3.0	0.08	0.04
Mn	50	30.0	15.4	9.7
Zr	2056	0.0	0.009	<0.005
Ca	974	0.29	0.2	0.22
Mg	143	17.0	40.0	39.0
Si	118	1.1	2.9	—
Al	32	31.0	0.0	0.2
Mo[a]	—	—	314.0	371.0

[a]The molybdenum is from the condenser tube.

roughly 40% in the wetted area (the bottom third of the crucible). The steel phase was approximately spherical and was embedded within the solidified concrete-urania mixture. Evidently, the steel could not equilibrate with the gas phase in this geometry. We plan to eliminate the steel phase from future runs since we cannot obtain good measurements with two-phase mixtures of this type. With the steel omitted, a tungsten or molybdenum crucible can be used and the problem of zirconia dissolution can also be circumvented.

The "amount added" column in Table I-7 includes our estimate of zirconia dissolution from the beaker. This amount is a factor of 100 higher than was added as a dopant to the urania. According to our SOLGASMIX calculations, the zirconia suppresses vaporization of the alkaline earth oxides by forming zirconates. With the zirconia addition, reasonable agreement was obtained between the calculations and the measurements for transport of Ba, Sr, Ca, and Mg (see Table I-7). We were less successful in modeling the very low vaporization of lanthanum. It is likely that zirconia is suppressing the lanthanum vaporization by forming the compound $La_2Zr_2O_7$ (mp, 2573 K). However, thermodynamic data are not available for this compound, so we are not yet able to include its effects in the SOLGASMIX code.

The transpiration experiments appear to be capable of yielding useful data with which to check the computer codes now being used to predict release during a severe accident. However, the experiments are difficult to

interpret due to complex chemical and physical effects. The results obtained to date have indicated a need for inclusion of more complex species, such as the alkaline earth zirconates, in the calculations. With additional work, we hope to be able to derive activity coefficients for the elements of interest (Ba, Sr, and the rare earths).

B. Thermophysical Properties of Metal Fuels

(L. Leibowitz, E. Veleckis, R. A. Blomquist, and A. D. Pelton*)

Development of the Integral Fast Reactor (IFR) requires understanding of fuel behavior for wide temperature and composition ranges. Much of the needed information is not available, and our ongoing program is designed to provide the essential thermophysical property data. These efforts are coordinated with R&D efforts on fuel performance, design, and safety to be certain that fuel properties of primary concern are examined. Our effort involves experimental and calculational work.

1. Calculation of U-Pu-Zr Solidus and Liquidus Temperatures

(L. Leibowitz, E. Veleckis, R. A. Blomquist, and A. D. Pelton*)

The techniques involved in thermodynamic phase diagram analysis have been well documented.[26-30] When applied to the computation of an unknown ternary phase diagram, these techniques involve the critical evaluation and analysis of all relevant phase diagram and thermodynamic data for the three binary sub-systems with a view to obtaining mathematical expressions for the thermodynamic properties of all binary phases as functions of composition and temperature. Following this, interpolation techniques based upon solution models are used to estimate the thermodynamic properties of the ternary phases from the properties of the binary phases. The ternary phase diagram is then calculated from the estimated ternary Gibbs energy surfaces. All calculations are performed with programs of the F*A*C*T (Facility for the Analysis of Chemical Thermodynamics) computer system based in Montreal.[27] For the Pu-U-Zr system, a liquid solution and, as the highest-temperature solid phase, a body-centered-cubic (bcc) solid solution exist at all compositions within the ternary system. Liquidus and solidus curves have been reported for all three binary subsystems, but virtually no data on the ternary liquidus or solidus are available.

For solutions in which deviations from ideal behavior are not large, polynomial expansions of the excess Gibbs energy (G^E) in terms of the molar fractions are commonly used. In a binary system with components A and B, the excess Gibbs energy is given by:

$$G^E = X_A X_B (a_o + a_1 X_B + a_2 X_B^2 + \ldots) \qquad \text{(I-11)}$$

where X_A and X_B are the molar fractions, and a_o, a_1, a_2, ... are empirical coefficients to be determined. It should be noted that, because the Gibbs energy of mixing can be written as the sum of an ideal Raoultian term,

*Ecole Polytechnique, Montreal, Quebec, Canada.

$RT(X_A \ln X_A + X_B \ln X_B)$, and an "excess" term, G^E, the excess free energy for a binary system can be written as

$$G^E = RT(X_A \ln\gamma_A + X_B \ln\gamma_B) \qquad \text{(I-12)}$$

where γ_A and γ_B are the activity coefficients. In general, G^E varies with T, but for the Pu-U-Zr system the available data are insufficient to determine the temperature dependence. Thus, it is assumed that G^E (and, hence, all coefficients a_o, a_1, a_2, ...) is independent of temperature. This is equivalent to assuming zero excess entropy.

If all coefficients a_o, a_1, a_2 ... are zero, then the solution is ideal. If only a_o is nonzero, then the solution is "regular." If a_o and a_1 are nonzero, then the solution is "subregular." In the present case, no more than three coefficients (a_o, a_1, and a_2) were ever required in any solution for a binary system.

a. Melting Points, Enthalpies, and Gibbs Energies of Melting

The Gibbs energies of melting for all three elements of the alloy are required in the present analysis. In the equations which follow, the Gibbs energy of melting (ΔG°_{fusion}) is in cal/mol and the temperature (T) is in K.

Data for plutonium have been reviewed by Oetting et al.[31] A melting point of 640 ± 2°C and an enthalpy of melting of 680 ± 25 cal/mol are given. Heat capacities of the solid and liquid are also known with reasonable accuracy. The resultant expression for the Gibbs energy of melting is

$$\Delta G^\circ_{fusion(Pu)} = -786 + 11.768\ T - 1.600\ T \ln T \qquad \text{(I-13)}$$

For zirconium, data are available in the JANAF tables.[21] The melting point is 1852 ± 5°C and the enthalpy of fusion is 5000 ± 7% cal/mol. Solid and liquid heat capacities are also given in the JANAF tables.[21] The resultant Gibbs energy of melting expression is

$$\Delta G^\circ_{fusion(Zr)} = 2308 + 16.474\ T + 5.550 \times 10^{-4}\ T^2 - 2.446\ T \ln T \qquad \text{(I-14)}$$

The data for uranium have been reviewed by Oetting et al.[31] The melting point is 1132 ± 3°C. Oetting et al. discussed two determinations of the enthalpy of fusion of uranium[32,33] and selected the more-recent calorimetric value,[32] 2185 cal/mol. There is a third experimental value[34] of 2.9 kcal/mol, as well as estimates of 3.25 kcal/mol[35] from vapor pressure data and 2.5 kcal/mol[36] from an assessment of uranium alloy phase diagrams. As shown later, the value of 2185 cal/mol gives poor agreement with the measured phase diagram. The Savage and Seibel[34] value of 2900 cal/mol, while not recommended by Oetting et al., gives much better agreement with the Pu-U phase diagram. This presented a significant problem in that, on the one hand, two independent determinations of the Pu-U solidus were available and, on the

other hand, the recommended enthalpy of fusion of 2185 cal/mol seemed to be quite reliable. We resolved this dilemma in favor of the recommended enthalpy of fusion of uranium because it gave better agreement with our measurements and it seemed unlikely that the experimental enthalpy measurement would be so much in error. The equation used for the Gibbs energy of melting of uranium is

$$\Delta G^{\circ}_{fusion(U)} = -1299 + 18.899\ T - 2.48\ T\ \ln T \qquad \text{(I-15)}$$

b. Analysis of Binary Systems

We analyzed the available data on the three binary systems to obtain excess Gibbs energy equations, which are required for ternary system calculations. In addition, we estimated the uncertainties in binary solidus and liquidus temperatures based on the available data and thermodynamic consistency. One source of difficulty in achieving consistency among the studies assessed is the influence of impurity content. Oxygen, nitrogen, and carbon impurities can have important effects on phase behavior, especially for zirconium-containing systems. In the earlier literature, in particular, such variables were not well controlled. Some of the discrepancies found in the assessment given below may be a result of impurity effects, for which we did not attempt to correct. As is shown below, our estimated uncertainties differed considerably among the three binary sub-systems.

(1) Pu-Zr System

The liquidus and solidus for Pu-Zr have been measured up to about 50 mol % Zr by Marples[37] and Bochvar et al.[38] These two studies disagree by as much as 50°C in the liquidus and 100°C in the solidus. A study by Taylor[39] for Zr concentrations up to 10 mol % gave a solidus close to that of Bochvar et al.[38] but a liquidus 40°C higher than either Marples[37] or Bochvar et al.[38] at 10% Zr. In a fourth study,[40] liquidus temperatures 200°C higher than those of all other authors were reported at Zr concentrations near 15 mol %. Because of this very large discrepancy, this study can probably be discounted. The work of Marples[37] appears to be the most extensive, and so more weight was given to the results of this study in the analysis. This was also the opinion of Shunk[41] in his compilation.

Under the assumption of ideal liquid behavior and regular solution behavior for the solid with

$$G^{E}_{(sol)} = 1600\ X_{Pu}X_{Zr} \qquad \text{(I-16)}$$

the diagram shown in Fig. I-10 was calculated. This figure shows that the calculated diagram is a compromise between the various reported diagrams, but that more weight is given to the diagram of Marples.[37] The existence of small positive deviations in the solid phase[42,43] is supported by the shape of the two-phase ϵ/δ region, which passes through a maximum at 640°C. For this binary system, error limits are estimated as ±50°C for the liquidus and ±100°C for the solidus.

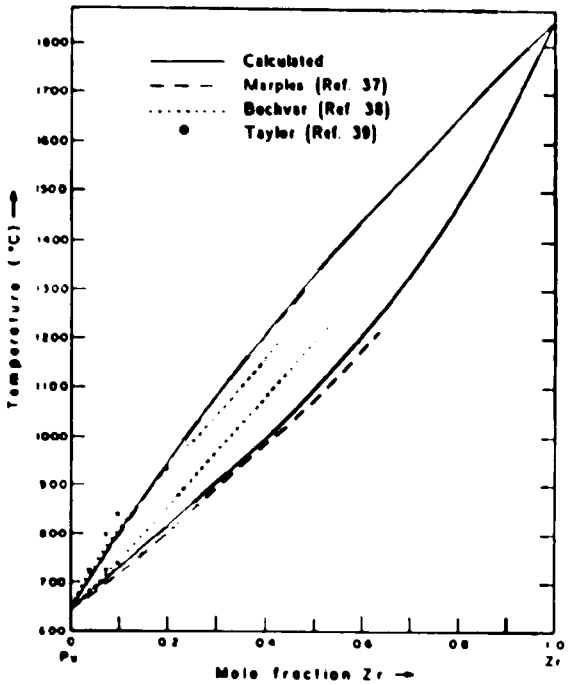

Fig. I-10.

Pu-Zr Phase Diagram

(2) Pu-U System

The liquidus and solidus for Pu-U have been measured by Ellinger et al.[44] and by Mound Laboratory.[45] The liquidus curves of these two studies agree to within better than 15°C, but the solidus curves diverge by up to 40°C. Ellinger et al.[44] state that they experienced difficulty in obtaining reproducible solidus measurements. They reported the minimum to be at 610°C and 12 mol % U on the basis of their solidus points. However, their liquidus measurements place the minimum closer to 620°C, which is the minimum temperature reported by Mound Laboratory.[45] Another author[46] reports a minimum at 624°C and 9 mol % U.

Activity measurements in the liquid phase were reviewed by Chiotti et al.[47] Although the results suggest negative deviations in the liquid, they are so imprecise and their interpretation involves so many assumptions that they should be viewed cautiously. It is simpler, and also more concordant with experience in other alloy systems, to assume that the solidus/liquidus minimum is the result of small positive deviations in the solid. This contention is supported by the shape of the two-phase ϵ/η region, which passes through a maximum.

The liquidus in this system seems to be relatively accurately known. Under the assumption that the liquidus is correct, it can be shown[48] that the solidus, as well as $G^E_{(sol)}$, can be calculated if the enthalpies of fusion of the components and $G^E_{(liq)}$ are known. We performed such calculations assuming ideal liquid behavior, using Eq. I-13 for the enthalpy of fusion of plutonium and taking the enthalpy of fusion of uranium to be 2185 cal/mol.[31] The resulting $G^E_{(sol)}$ was small, subregular, and behaved as expected, but the calculated solidus was up to 25°C above that reported by Mound Laboratory[45] and 65°C above that reported by Ellinger et al.[44] Reasonable agreement with the published solidus data may be obtained, however, if

the enthalpy of fusion of uranium is set at 2900 cal/mol, the value of Savage and Seibel.[34] Assuming a negative $G^E_{(liq)}$ as suggested by Chiotti et al.[47] makes things worse. Fair agreement can be obtained if quite large positive excess Gibbs energies in both solid and liquid phases, which nearly compensate each other, are assumed. However, this seems improbable. It is more likely that either the reported solidus curves are in error, or the enthalpy of fusion of uranium is higher than 2185 cal/mol. The former seems more attractive in view of the experimental results reported below and the precision of the enthalpy data of Stephens.[32] The excess Gibbs energy is thus given by

$$G^E_{(SOL)} = X_{Pu}X_U\ (730 - 390\ X_U) \qquad \text{(I-17)}$$

The resulting calculated phase diagram is shown in Fig. I-11. Because of the discrepancies discussed above, error limits are set at ±15°C for the liquidus and ±40°C for the solidus.

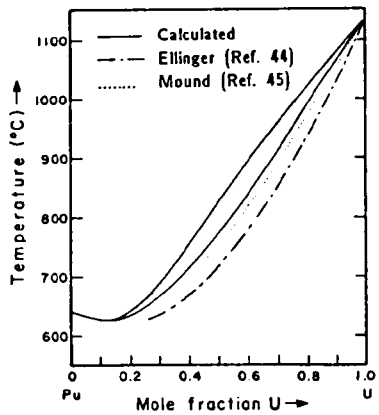

Fig. I-11.

Pu-U Phase Diagram

(3) Zr-U System

The solidus and liquidus for Zr-U have been measured in only one study.[49] Another study[40] gives no data but reports that "solidus and liquidus temperatures are in agreement" with those of Summers-Smith[49] up to 50% Zr. A "lens-shaped" two-phase region in the phase diagram of Summers-Smith[49] is indicative of close-to-ideal behavior in both solid and liquid phases. However, the existence of a solid-solid miscibility gap at lower temperatures indicates quite strong positive deviations in the solid phase. Furthermore, the fact that the consolute composition of the gap is displaced toward higher uranium concentrations indicates that the positive deviations are quite asymmetric (nonregular). These positive deviations in the solid are expected to give rise to a minimum in the liquidus/solidus. That there is no such minimum can only be explained if the liquid phase also exhibits non-regular and nearly compensating positive deviations. Such behavior is unusual, and these observations thus add to the uncertainty surrounding the liquidus/solidus of this system. Activity measurements in the solid solution as reviewed by Chiotti et al.[47] are so imprecise as to be of little value in the analysis.

More recent measurements[50] of the solid-solid miscibility gap place the consolute point at 772°C and $X_U = 0.70$, with boundaries at the eutectoid temperature of 693°C at $X_U = 0.576$ and $X_U = 0.89$. These results, although quite different from those of Summers-Smith,[49] are preferred by Shunk[41] in his compilation on the basis of better experimental technique. We calculated the following equation to reproduce the eutectoid compositions:

$$G^E_{(SOL)} = X_{Zr}X_U\ (-688 + 5123\ X_U) \qquad \text{(I-18)}$$

Under the assumption of subregular behavior for the liquid, the following equation was computed in order to give a reasonable reproduction of the measured liquidus and solidus points:

$$G^E_{(LIQ)} = X_{Zr}X_U\ (0 + 3800\ X_U) \qquad \text{(I-19)}$$

The calculated diagram is shown in Fig. I-12. The S-shape of the solidus at high U concentrations is a direct result of the positive deviations in the solid. The narrowness of the two-phase (liquid + solid) region at high Zr concentrations is a consequence of the enthalpy of fusion of Zr and should be reasonably correct. This system is not well characterized. Error limits should probably be set at ±75°C for the liquidus and ±75°C for the solidus.

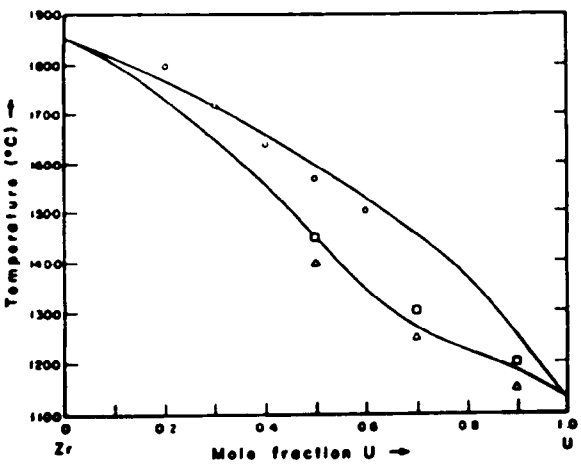

Fig. I-12.

Zr-U Phase Diagram. (Data points are from Summers-Smith;[49] the curve was calculated by us.)

c. Calculation of Ternary Phase Diagram

Excess Gibbs energies in the ternary liquid and solid phases were calculated from the values for the three binary systems by means of the "Kohler interpolation equations"[51]:

$$G^E = (1 - X_{Pu})^2\ G^E_{U/Zr} + (1 - X_U)^2\ G^E_{Zr/Pu} + (1 - X_{Zr})^2\ G^E_{U/Pu} \qquad \text{(I-20)}$$

At a ternary composition point, G^E is calculated from the values $G^E_{U/Zr}$, $G^E_{Zr/Pu}$, and $G^E_{U/Pu}$ in the three binary systems at the same values of the ratios X_U/X_{Zr}, X_{Zr}/X_{Pu}, and X_U/X_{Pu} as at the ternary point. This equation has been used extensively for ternary alloy systems.[28,29]

Representative calculated ternary solidus and liquidus curves are shown in Fig. I-13. Error limits for ternary compositions lying near a binary edge of the ternary composition triangle are approximately the same as the error limits at adjacent compositions in that binary, as given earlier.

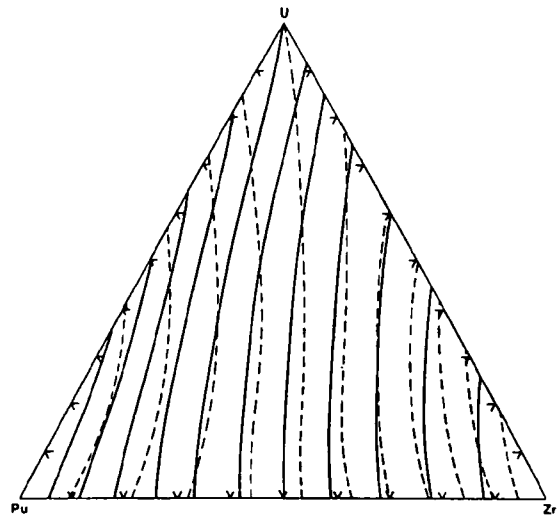

Fig. I-13.

Calculated Projection of Liquidus (solid curves) and Solidus (dashed curves) for the U-Pu-Zr System. Temperatures range from 700°C at the Pu corner to 1700°C at the Zr corner (inclusive) in 100°C intervals.

For compositions near the center of the ternary composition triangle, an additional uncertainty due to the approximate nature of the Kohler interpolation technique must be included. Near the median of the composition triangle ($X_{Pu} = X_U = X_{Zr} = 1/3$) error limits are estimated as ±75°C for the liquidus and ±125°C for the solidus.

Ternary isotherms in the Pu corner of the diagram have been reported by the Mound Laboratory.[40] However, that study gives liquidus temperatures in the Pu-Zr binary which are 200°C higher near 15 mol % Zr than those reported by any other source. Hence, these results should be discounted. Nevertheless, the general shape of the reported isotherms is the same as that of the calculated isotherms.

We calculated activity coefficients in both ternary phases by differentiation of the Kohler equation. The calculated activity coefficients were referred to the pure bcc solids as standard states for the solid solution and to the pure liquids for the liquid solution.

In the following expressions for activity coefficients, the components are numbered Pu = 1, U = 2, and Zr = 3 with mole fractions X_1, X_2, and X_3. In addition, the temperature (T) is in K and R = 1.987.

Liquid Solution

$$RT \ln\gamma_1 = -3800X_2^2 X_3/(1 - X_1) \quad \text{(I-21)}$$

$$RT \ln\gamma_2 = 3800X_2X_3 (X_1X_2 + 2X_3)/(1 - X_1)^2 \quad \text{(I-22)}$$

$$RT \ln\gamma_3 = 3800X_2^2 (X_2 - X_3 + X_1X_3)/(1 - X_1)^2 \quad \text{(I-23)}$$

Solid Solution

$$RT \ln\gamma_k = -(1 - X_k)^2 f_{ij} + (1 - X_i)(f_{k(kj)} + X_i f_{kj}) + (1 - X_j)(f_{k(ki)} + X_j f_{ki}) \quad \text{(I-24)}$$

$$f_{13} = 1600(1 - t_{13})t_{13}$$

$$f_{1(13)} = 1600t_{13}^2 \qquad \text{where } t_{13} = X_3/(X_1 + X_3) \quad \text{(I-25)}$$

$$f_{3(13)} = 1600(1 - t_{13})^2$$

$$f_{23} = (1 - t_{23})t_{23}(-688 + 5123t_{23})$$

$$f_{2(23)} = (1 - t_{23})^2(-688 + 10246t_{23}) \qquad \text{where } t_{23} = X_2/(X_2 + X_3) \quad \text{(I-26)}$$

$$f_{3(23)} = 5811t_{23}^2 + 10246t_{23}^3$$

$$f_{12} = (1 - t_{12})t_{12}(730 - 390t_{12})$$

$$f_{1(12)} = 1120t_{12}^2 - 780t_{12}^2 \qquad \text{where } t_{12} = X_2/(X_1 + X_2) \quad \text{(I-27)}$$

$$f_{2(12)} = (1 - t_{12})^2(730 - 780t_{12})$$

If one of the mole fractions is set equal to zero in Eqs. I-21 to I-27, activity coefficients in any of the three binary subsystems can also be calculated. In view of the many approximations which have been made, computed values of $\ln\gamma$ should be considered accurate to within a factor of two.

This model was used to calculate solidus and liquidus temperatures for the alloys reported by Harbur et al. (U-13 Pu-15 Zr and U-12 Pu-29 Zr with composition in at. %).[52] Table I-8 gives their

Table I-8. Solidus and Liquidus Temperatures of U-Pu-Zr Alloys Obtained by Calculation and from Experimental Data in the Literature[52]

Alloy, at. %	Temp., °C	
	Solidus	Liquidus
U-13 Pu-15 Zr[a]	1105	1240
	1121 (calc.)	1268 (calc.)
U-12 Pu-29 Zr[a]	1195	1425
	1187 (calc.)	1394 (calc.)
U-19.3 Zr[b]	1216 ± 7	1358 ± 10
	1221 (calc.)	1371 (calc.)
U-19.5 Pu-3.3 Zr[b]	996 ± 5	1050 ± 4
	1012 (calc.)	1060 (calc.)
U-19.3 Pu-14.5 Zr[b]	1093 ± 8	1321 ± 23
	1071 (calc.)	1216 (calc.)

[a]Solidus and liquidus obtained by calculation and from experimental data in the literature.[52]

[b]Solidus and liquidus obtained by calculation and from our experimental work.

experimental results along with our model calculations, indicated by "(calc.)". This agreement is reasonably good and tends to support the model assumptions.

2. Measurement of U-Pu-Zr Solidus and Liquidus Temperatures

a. Methods

Solidus and liquidus temperatures were measured with differential thermal analysis (DTA) methods. For this work, a Netzsch, Inc. Model STA 409 instrument was installed in a helium-atmosphere glove box suitable for work with plutonium-containing materials. The melting points of high purity aluminum and gold were measured periodically to ensure that temperatures were being accurately determined. Melting points within ±1-2 K of literature values were regularly obtained. Solidus and liquidus temperatures were measured on U-Pu-Zr alloys at heating and cooling rates ranging from 1 to 20 K/min. At low rates, detection of the solidus and liquidus was very difficult. At high rates, shifts in the indicated temperatures were found. Generally, rates between 5 and 10 K/min were employed for the data reported.

Crucibles fabricated of beryllia (National Beryllia Corp.) and yttria (prepared by R. Poeppel, Materials and Components Technology Division, Argonne National Laboratory) were heated at 1500°C for several hours and tested for compatibility with U-Pu-Zr alloys. Samples of ternary alloys melted in the beryllia and yttria crucibles were examined by scanning electron microscopy (SEM)/energy dispersive X-ray spectroscopy (EDS) (all such examinations

were performed by R. V. Strain, EBR II, Argonne National Laboratory). The samples heated in a yttria crucible (U-19 wt % Pu-10 wt % Zr and U-20 wt % Pu-2 wt % Zr) showed no significant composition gradients within the matrix of the sample and no evidence of interaction with the crucible. The sample melted in a beryllia crucible (U-19 wt % Pu-10 wt % Zr), in contrast, showed clear evidence of reaction with the crucible and reduced zirconium concentration in the alloy matrix. It was also found that the zirconium concentration was lower near the edges and bottom than at the center and top. Low solidus and liquidus temperatures for the alloy were found in the beryllia crucible and evidently resulted from a reduced zirconium concentration caused by reaction with the beryllia crucible. All subsequent measurements were performed in yttria DTA crucibles.

Alloys for this study were parts of batches prepared by injection casting for irradiation exposure in the EBR-II reactor. The procedure used has already been described.[53] Impurity content for a U-10 wt % Zr alloy, typical of those used, is as follows (in ppm): Ta, 39; C, 171; Co, 7; Si, 282; Y, 39; Al, 41; Cr, 23; Ni, 21; Fe, 111; Mn, 11; Cu, 7; N, 13; O, 21.

In a typical DTA measurement, a cylindrical sample of alloy about 5 mm high and 5 mm in diameter was cleaned and placed in the DTA crucible and mounted on the sample thermocouple in the DTA system. An identical crucible containing platinum was mounted on the reference thermocouple. The furnace was lowered into position and the system was pumped and flushed several times with high-purity helium. The system was finally filled with high-purity helium (reported as 99.9999%) to a pressure slightly above ambient. Samples were heated to 1500°C and data from the initial heating/cooling cycle were discarded. The desired number of heating and cooling cycles was then completed and data were recorded. The STA 409 instrument includes thermogravimetry capability, and weight changes were frequently followed during the DTA runs. No significant weight changes were ever detected.

b. Results

(1) Sample Morphology

The as-cast fuel of overall composition U-19 wt % Pu-10 wt % Zr, shown in Fig. I-14, contained small, nearly spherical particles about 5-10 μm diameter, referred to as the "globular phase." The only metal detectable within this phase by SEM/EDS is zirconium, which is presumed to be α-Zr stabilized by oxygen or nitrogen. A similar phase was reported by O'Boyle and Dwight,[54] who mention "a small volume fraction of an oxygen-stabilized α-zirconium solid-solution phase" in their samples, whose volume fraction varied directly with oxygen concentration. They report this phase to dissolve up to 4.0 wt % uranium and 2.5 wt % plutonium. In our samples, uranium and plutonium were found in this phase, but as discrete inclusions rather than in solution as implied by O'Boyle and Dwight. Phase behavior can be significantly influenced by impurities, and these effects have been discussed in a recent review of the U-Zr system by Sheldon and Peterson.[55]

Following our measurements of solidus and liquidus temperatures, this globular Zr phase was found almost entirely at the top of the sample, evidently having floated to the top while the alloy was molten. The remainder of the alloy was virtually free of this material with the exception

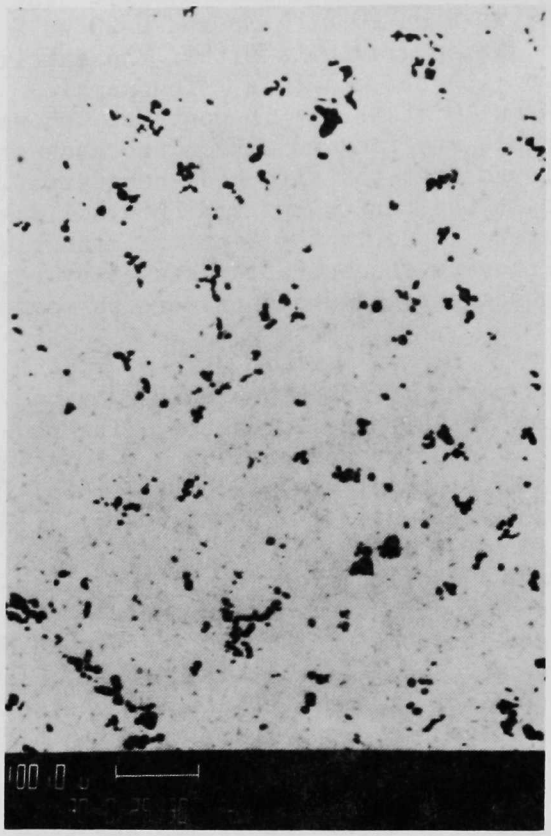

Fig. I-14.

As-cast U-19.3 at. % Pu-14.5 at. % Zr Showing Globular Zr Inclusions

of a small amount at the very bottom. This material may be mechanically removed from the frozen ingot and a very clean alloy sample obtained. The zirconium concentration of the globule-free ternary-alloy phase was quite uniform and had a concentration of about 7 wt %. Alloy compositions obtained from gross chemical analysis can be quite misleading because of this globular phase, which can contain significant quantities of zirconium, oxygen, nitrogen, and carbon.

The Zr-rich globular phase appeared in a layer at the surface in globules about 50-100 μm in diameter (Fig. I-15). This size is about ten times larger than was seen in the as-cast fuel. In addition, very small U-Pu-containing inclusions (Fig. I-16), about 1 μm in diameter or less, were seen uniformly distributed within the large Zr-rich globules. The large globules may have resulted from simple agglomeration of the smaller ones with some of the matrix alloy trapped within it. The Zr-rich phase, however, appears to have formed from a liquid. There may be a previously unknown multi-component Zr-rich phase, which is liquid below 1500°C and is immiscible in the U-Pu-Zr matrix alloy. No liquid phases exist in either the Zr-O or Zr-N systems below the melting point of pure Zr. Investigation of this phenomenon is continuing.

(2) Solidus/Liquidus Temperatures

Results of our measurements of solidus and liquidus temperatures on three alloys (U-19.3 Zr, U-19.5 Pu-3.3 Zr, and U-19.3 Pu-14.5 Zr,

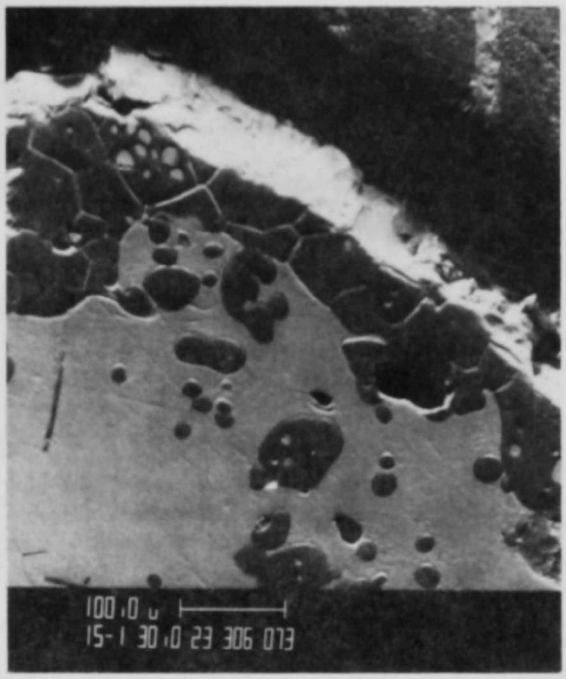

Fig. I-15.

Thick Zr-Rich Layer on Top of Sample Following Melting

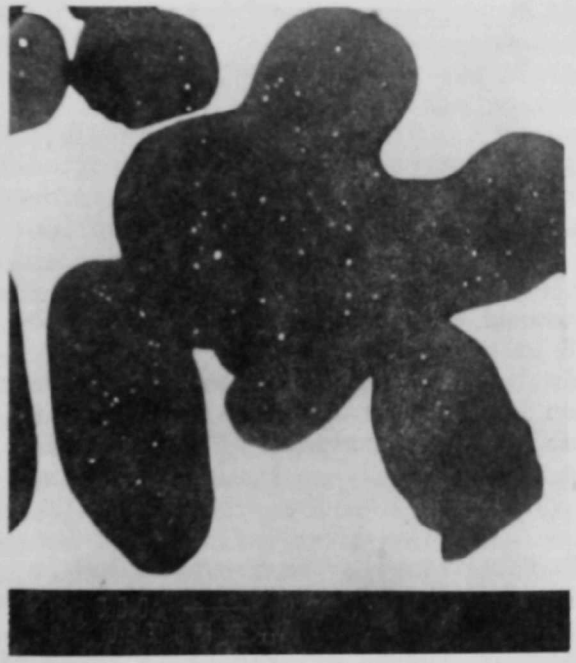

Fig. I-16.

Small U-Pu-Rich Inclusions (bright areas) in (dark) Zr-Rich Globular Phase

composition in at. %) are presented in Table I-8. The three compositions were determined by SEM/EDS following the melting measurements. Measurements made before and after removal of the Zr-rich surface layer gave the same values. Generally solidus temperatures were determined on heating, and liquidus temperatures were determined on cooling. A sample DTA curve is shown in

Fig. I-17, which gives a portion of a heating and cooling cycle run at 10 K/min for U-19.5 at. % Pu-3.3 at. % Zr. Note some evidence of subcooling in the cooling curve.

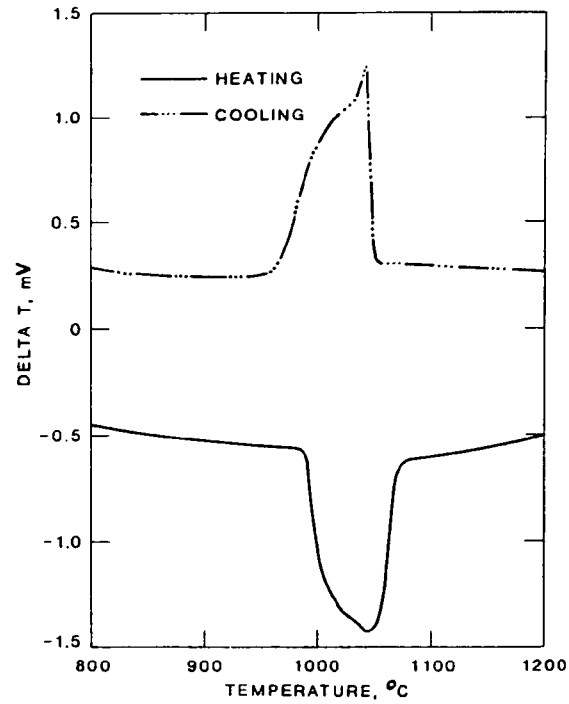

Fig. I-17.

Heating and Cooling DTA Curves at 10 K/min for U-19.5 at. % Pu-3.3 at. % Zr

The uncertainties given for the measurements reported in Table I-8 are standard deviations (σ) calculated from measurements performed at heating/cooling rates of 5-10 K/min. Calculated values for the solidus and liquidus are also given in Table I-8.

A comparison of measured and calculated values for the bottom three alloys listed in Table I-8 is quite instructive. For the U-19.3 Zr alloy, a U-Zr binary, the calculated values agree well with those measured. Although only one composition has been examined, this agreement, to some extent, lends support to the thermodynamic assessment of that system given above. The uncertainty estimates, based solely on our thermodynamic evaluation, may be too large.

For the U-19.5 Pu-3.3 Zr alloy, a ternary with low Zr content, we find good agreement between measured and calculated values. This agreement supports our choices for this system as discussed above. Had we elected to reject the recommended enthalpy of fusion of uranium in favor of the published Pu-U solidus, agreement would have been poorer. This suggests to us that the published binary solidus data[45,46] rather than the enthalpy of fusion of uranium are in error. This possibility is still under study.

For the U-19.3 Pu-14.5 Zr alloy, we find reasonable agreement with the calculations for the solidus but poor agreement for the liquidus. This liquidus also has the largest experimental uncertainty, a reflection of the difficulty we had in making this measurement.

Overall, we believe that the model reasonably describes the solidus-liquidus surface for this system. The agreement with the experimental values, moreover, supports our belief that it is the published Pu-U solidus which is in error, rather than the enthalpy of fusion of uranium.

C. The Thermodynamics of Pyrochemical Processes for Liquid Metal Reactor Fuel Cycles
(I. Johnson)

The development of fast breeder reactors is justified by the greatly increased utilization of uranium. Recent improvement in the performance of metallic fuels[56] has made feasible a safe and highly efficient reactor if an on-site fuel reprocessing method can be developed. Pyrochemical processes are ideally suited for metallic-fueled fast breeder reactors. Such processes are compact and, therefore, can be readily integrated with the reactor.[57] The fuel cycle can be designed so that no fissile material leaves the plant, therefore greatly decreasing the possibility of diversion of fissile material. This section describes the thermodynamic basis for the pyrochemical processes for recovering and purifying the fuel in a liquid metal reactor. The basis for design computations is described and illustrated for different process conditions.

1. Chemical Basis of Processes

The pyrochemical processes being considered for metallic-fueled fast reactors involve the dissolution of the metallic fuel in a liquid metal solvent, the oxidation of the uranium and plutonium into a molten salt solvent, the reduction of the uranium and plutonium from the molten salt solution into a liquid metal solvent, and the separation of the metal solvent (by retorting) from the uranium and plutonium. The separations are obtained by control of the conditions during the oxidation and reduction steps of the process.[58]

The processes considered involve the use of molten mixtures of chloride salts and low-melting liquid metals, such as liquid alloys of zinc, cadmium, and magnesium. The early work on these processes was done in connection with the development of a process for the recovery of plutonium and uranium from oxide fast reactor fuels.[59] The first step of these processes involved the reduction of the oxide to metal so that the main separations were achieved by molten salt-liquid metal extraction processes.[60]

The oxidation step, $U(alloy) = U^{3+}(salt) + 3e^-$, requires a sink for the electrons. This sink can be either an electronic conductance path to the second liquid alloy or a reduction reaction such as $Mg^{2+}(salt) + 2e^- = Mg(alloy)$. Likewise at the second alloy, a source of electrons is required for the reduction reaction, $U^{3+}(salt) + 3e^- = U(alloy)$. This electron source can be furnished by an external electrical power source or an oxidation reaction. The use of an auxiliary redox couple for the oxidation-reduction steps can be traced to the pioneering work of Chiotti and Parry.[58] It has been extensively developed by Knighton et al.[60] and is known as the salt transport process. The use of an external power source[61] for the oxidation-reduction steps was suggested by the success of the electrorefining process for plutonium developed by Mullins and Leary[62] and various molten salt processes for the electrolytic preparation of high purity uranium[63] and will be referred to as the electrotransport process. Both processes depend on equilibrium between molten salts and liquid alloys.

2. Distribution between Molten Salts and Liquid Alloys

The thermodynamic basis for the separation processes will be derived by calculating the distribution of uranium between a molten chloride salt and liquid magnesium-zinc alloys. The chemical equilibrium is

$$UCl_3(salt) + 3/2\ Mg(alloy) = U(alloy) + 3/2\ MgCl_2(salt) \qquad (I\text{-}28)$$

The equilibrium constant for this reaction can be written as follows:

$$\frac{a_U(a_{MgCl_2})^{3/2}}{a_{UCl_3}(a_{Mg})^{3/2}} = K_a \qquad (I\text{-}29)$$

where the a's are activities and K_a is the activity equilibrium constant. By substituting the activities with the product of the mole (atom) fractions, χ, and the activity coefficients, γ, and defining the distribution coefficient, D, of uranium as the ratio χ_{UCl_3}/χ_U, one obtains the following expression:

$$\log D = \Delta G^\circ/2.3RT - 3/2 \log a_{Mg} + \log\gamma_U + 3/2\log a_{MgCl_2} - \log\gamma_{UCl_3} \qquad (I\text{-}30)$$

It is convenient to separate the right-hand side of Eq. I-30 into three components.[64] The first term, which depends only on the free energies of formation of the two chlorides, represents the reaction potential. The next two terms, which depend only on the composition of the liquid alloy, represent the reduction potential. The last two terms, which depend only on the composition of the molten salt phase, represent the oxidation potential.

The reaction potential can be considered in terms of the free energies of formation of the chlorides; a short table of numerical values is given in Table I-9. The entries in this table are the free energies of formation (at 1000 K) for one gram-atom of chlorine divided by 2.3RT. Differences in Table I-9, after correction for the number of gram-atoms per mole, can be used to determine the distribution coefficients. Thus, if this term were the only one of importance, the distribution coefficient of $CeCl_3$ would be $10^{1.34} \times 3$ (about 1.05×10^4) greater than that for $PuCl_3$. If the redox potential of the system is controlled by the Mg-$MgCl_2$ couple, then all of the chlorides above $MgCl_2$ would favor the salt phase and all below $MgCl_2$, the metallic alloy phase. Thus, a separation of uranium and plutonium from the more noble fission products and cladding metals would expect to be achieved by oxidizing U and Pu into the molten salt with $MgCl_2$. However, when such simple schemes are attempted for the separation of U and Pu from each other and the rare earth fission products, the large effect of the oxidation and reduction potentials on the distribution coefficient must be considered. The difficulty of separating plutonium from the rare earth fission products stymied the development of a high-decontamination pyrochemical process for many years.

Table I-9. Relative Stabilities of Chlorides at 1000 K (values from Pankratz[65]). Values are $\Delta G^{\circ}_{f}/2.3RT$, per g-atom of Cl.

$BaCl_2$	-18.28	$MgCl_2$	-12.68
CsCl	-18.08	UCl_3	-11.68
KCl	-17.84	$ZrCl_4$	-9.85
LiCl	-17.23	$ZnCl_2$	-7.13
$CaCl_2$	-16.77	$CdCl_2$	-6.33
NaCl	-16.66	$CrCl_2$	-7.09
$PrCl_3$	-14.19	$FeCl_2$	-5.73
$CeCl_3$	-14.09	$NbCl_5$	-5.42
$NdCl_3$	-13.95	$NiCl_2$	-4.09
$PuCl_3$	-12.75	MoCl3	-2.81

The discovery of copper-magnesium alloys as a metallic solvent system by Knighton et al.[60] led to the development of a high-decontamination pyrochemical process. The favorable reduction potentials for U, Pu, and the rare earth metals in copper-magnesium alloys made the high separations possible.

To illustrate the application of Eq. I-30, we will discuss the computation of the distribution coefficient of uranium between molten $MgCl_2$ and liquid Mg-Zn alloys. The numerical details are given in Table I-10.

Table I-10. Computation of Distribution of Uranium between Molten $MgCl_2$ and Liquid Zn-Mg (1073 K). (See text for reference to data.)

$\Delta G^{\circ}/2.3\ RT = -3.999$

X_{Mg}	log D_{Obs}	3/2 log a_{Mg}	log γ_U	log D_{calc}[a]	Calc - Obs[b]
0.0063	-0.502	-4.482	-0.771	-0.288	0.214
0.0592	-1.972	-2.871	-0.452	-1.579	0.292
0.1438	-2.075	-2.077	0.048	-1.874	0.201
0.2355	-2.151	-1.565	0.563	-1.871	0.280
0.2907	-2.026	-1.313	0.885	-1.801	0.225
0.4650	-1.656	-0.750	1.831	-1.418	0.238
0.6056	-1.297	-0.295	3.026	-0.678	0.312
0.7789	-0.626	-0.190	3.428	-0.308	0.246
0.8018	-0.506	-0.165	3.540	-0.294	0.212
				Avg.:	0.252

[a]Assumes that log $\gamma_{UCl_3} = 0$.

[b]Equal to log γ_{UCl_3}.

The reaction potential was computed from the free energy of formation data selected by Pankratz[65] for $MgCl_2$ and by Fuger et al.[66] for UCl_3. Since the temperature, 1073 K, was below the melting point of UCl_3 (1110 K), the free energy of UCl_3 had to be corrected for the free energy of fusion. For the molten salt phase, values of the free energies for the liquid (supercooled if necessary) salts should be used so that published molten salt activity data for the constituents can be used. The value of the reaction potential at 1073 K was found to be -3.999.

The reduction potential was computed from the activity of magnesium in liquid Mg-Zn alloys reported by Chiotti and Stevens[67] and the activity coefficients of uranium in liquid zinc[68] and magnesium alloys.[69] It was assumed that the small concentration of uranium in the liquid alloys had a negligible effect on the activities of magnesium, and the activity could be computed from the data on the binary alloys, shown in column 3 of Table I-10. The activity coefficient of uranium in the liquid binary Mg-Zn alloy solvent, column 4 in Table I-10, was computed using the Darkin[70]-Alcock-Richardson[71] approximation:

$$\log\gamma_U = \chi_{Mg}\log\gamma_{U(Mg)} + \chi_{Zn}\log\gamma_{U(Zn)} - \Delta G_{Mg-Zn}/2.3RT \qquad \text{(I-31)}$$

in which $\gamma_{U(Mg)}$ and $\gamma_{U(Zn)}$ are the activity coefficients of uranium in pure liquid magnesium and zinc, respectively, and ΔG_{Mg-Zn} is the excess free energy of mixing of the Mg-Zn alloy whose composition is given by the atom fractions χ_{Mg} and χ_{Zn}. At 1073 K the activity coefficients of uranium in liquid Zn and Mg are 0.155 and 3.131×10^4, respectively. The uranium-zinc system was studied using a high-temperature EMF method, while the activity coefficient of uranium in liquid magnesium can be computed from the uranium solubility in liquid magnesium since the equilibrium phase is solid uranium. Both of these activity coefficients use solid uranium as the reference state, even though it is used for an alloy in the liquid state. This unusual convention for uranium can be traced back to the use of high-temperature EMF methods for the study of the thermodynamics of liquid alloys of uranium and low melting metals.[72] The cell EMF was measured relative to a pure solid uranium electrode. Also, the free energy of formation of UCl_3 used to compute the reaction potential was referenced to solid uranium.

The oxidation potential for this system was computed by assuming that the activity of $MgCl_2$ in these dilute solutions was unity. There are no experimental data for the activity of UCl_3 in molten $MgCl_2$. The distribution coefficients for uranium were computed assuming that χ_{UCl_3} was unity, and this yielded the values given in column 5 of Table I-10. It was found that the computed values were larger than the experimental values[73] by a constant factor, as shown in column 6 of Table I-10 (0.252 ± 0.009). This leads to an activity coefficient of UCl_3 in molten $MgCl_2$ of 1.79. This value, which is equivalent to about 1500 cal, should be accepted with caution since it depends on the value used for the reaction potential. It is doubtful whether the individual values of the free energies of UCl_3 and $MgCl_2$ are known well enough to place much confidence in 1.79 for the activity coefficient. However, these data suggest that only small deviations, possibly positive, from ideal

behavior exist. This result is in sharp contrast with the large negative deviations from ideal behavior observed when a molten $LiF-BeF_2$ salt is used.[74,75] In these systems, the formation of stable complexes in the molten salt greatly reduces the activity coefficient.

The results of these computed values for the distribution coefficient of uranium between $MgCl_2$ and Mg-Zn are compared to the experimental data reported by Knighton and Steunenberg[73] in Fig. I-18. It is seen that the computed curve fits the experimental data very well.

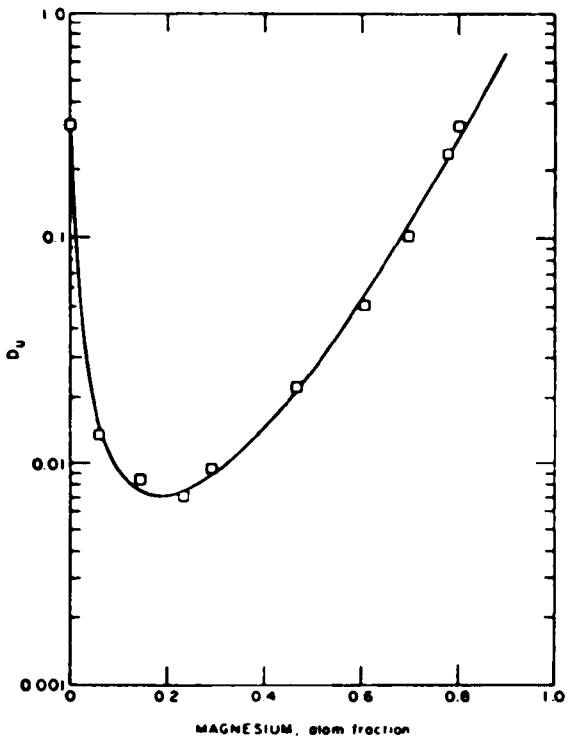

Fig. I-18.

Calculated and Observed[73] Distribution of Uranium between Molten $MgCl_2$ and Liquid Mg-Zn Alloys at 1073 K

Similar computations of the distribution of plutonium between molten $MgCl_2$ and liquid Zn-Mg alloys indicate that an activity coefficient for $PuCl_3$ in molten $MgCl_2$ of 6.68 ± 0.08 is required to fit the experimental data.

These illustrations of the computation of distribution coefficients are for systems in which the redox potential is controlled by an auxiliary redox couple, i.e., the $Mg-MgCl_2$ couple. However, the same procedure can be used to compute the distribution coefficients of systems where two or more different actinides or fission products are present in equilibrium. For example, if a mixture of uranium and plutonium is dissolved in a liquid metal (for example cadmium) and then placed in contact with a molten mixture of alkali metal chlorides containing a small amount of dissolved $CdCl_2$, the uranium and plutonium in the liquid metal would transfer (by oxidation) into the salt until the concentration of $CdCl_2$ in the salt was extremely small

(note the large differences in stability, Table I-9). The uranium and plutonium would exist in equilibrium according to the equation:

$$UCl_3(salt) + Pu(alloy) = PuCl_3(salt) + U(alloy) \qquad (I-32)$$

In this example, the ratio of the distribution coefficients of uranium and plutonium depends on the same three components used to analyze Eq. I-30. Thus, it is necessary to know the free energies of formation of UCl_3 and $PuCl_3$, the activities coefficients of Pu and U in liquid cadmium, and the activity coefficients of UCl_3 and $PuCl_3$ in the molten salt mixture. It would be expected that the free energies and the activity coefficients in liquid cadmium would be most important in determining the ratio of distribution coefficients. In this case, the ratio of distribution coefficients is equal to the mole (atom) fraction equilibrium constant, which could be used to compute the compositions of the liquid metal and molten salt phases.

3. Thermodynamics of Salt Transport Processes

Transfer from one liquid alloy through a molten salt to another liquid alloy is the main pyrochemical process used for the recovery and purification of uranium and plutonium. These two oxidation-reduction steps can be used to separate uranium and plutonium from the more noble fission product metals and the stainless steel (cladding) metals. By the use of more than one acceptor alloy, it is possible to prepare two product streams, one plutonium-rich and one uranium-rich. Only small separations from the rare-earth fission products are obtained in salt transport processes. If high decontaminations from the rare earths are required, then separate countercurrent extraction steps must be used prior to the salt transport step.[59]

The salt transport process will be considered first, but as will be seen, the same relations are applicable to the analysis of both the salt transport and the electrotransport. The liquid alloy in which the uranium and plutonium are initially dissolved is referred to as the donor while the liquid alloy to which uranium or plutonium are transferred is referred to as the acceptor(s). In the electrotransport process, these two liquid alloys are the anode and cathode(s), respectively. At the donor the following reaction occurs:

$$U(d) + \frac{3}{2} MgCl_2\ (s) = UC_3\ (s) + \frac{3}{2} Mg(d) \qquad (I-33)$$

while, at the acceptor, the reverse reaction occurs:

$$UCl_3\ (s) + \frac{3}{2} Mg(a) = U(a) + \frac{3}{2} MgCl_2\ (s) \qquad (I-34)$$

where d, s, and a refer to the donor, salt, and acceptor, respectively. The overall reaction is

$$U(d) + \frac{3}{2} Mg(a) = U(a) + \frac{3}{2} Mg(d) \qquad (I-35)$$

which leads to the equilibrium relation:

$$\frac{a_{U(a)}\ a_{Mg(d)}^{3/2}}{a_{U(d)}\ a_{Mg(a)}^{3/2}} = 1 \qquad \text{(I-36)}$$

When the activities are expressed as the product of the atom fraction and the activity coefficient, one obtains

$$\frac{\chi_{U(a)}}{\chi_{U(d)}} = \left(\frac{a_{Mg(a)}}{a_{Mg(d)}}\right)^{3/2} \frac{\gamma_{U(d)}}{\gamma_{U(a)}} \qquad \text{(I-37)}$$

Therefore, the ratio of the atom fractions in the two alloys when the transfer is complete depends on the activities of magnesium and the ratio of the activity coefficients in the two alloys. Since the activity coefficients can have very large or small values, the fraction transferred is very dependent on the compositions of the two alloys. When both uranium and plutonium are present, and equilibrium has been established among Pu, U, and Mg, the following relation is obtained:

$$\frac{a_{U(a)}}{a_{U(d)}} = \frac{a_{Pu(a)}}{a_{Pu(d)}} \qquad \text{(I-38)}$$

This equation indicates that the separations are dependent on the activity coefficients of U and Pu in the two alloys. If the activity coefficients have the same ratio in the two alloys, then the U/Pu ratio in the two alloys would be the same.

The analysis thus far has assumed that the two alloys were single phase, i.e., complete solubility of uranium and plutonium in each alloy. Since limited solubility in the alloys would have a large effect on the operation of practical processes, it will now be considered. It is convenient to use a different approach to describe the effect of limited solubility on the salt transport process. This approach uses the distribution coefficient and solubility data directly. The distribution data can be computed from thermodynamic data by the method described in Sec. I.C.2, while solubilities can be computed by methods described elsewhere.[76,77] The analysis also assumes that the transfer from the donor to the acceptor is carried out in a stepwise fashion, i.e., the salt is first contacted with the donor alloy, allowed to reach equilibrium, then moved to a separate vessel containing the acceptor alloy where equilibrium is established. The salt is then returned to the donor alloy vessel.

For this analysis, the distribution coefficient for the donor (K_D) and acceptor (K_A) is defined as w_S/w_D and w_S/w_A, respectively. Here, w_S, w_D, and w_A are the weight fractions of the solute in the salt, donor, and acceptor, respectively.

For the transport to occur or continue, the concentration of uranium or plutonium in the salt phase when in equilibrium with the donor must be greater than the concentration when in equilibrium with the acceptor; therefore, $K_D w_D > K_A w_A$. When the concentration in the salt returning from the acceptor is equal to the concentration in equilibrium with the donor, transfer will stop and the maximum transfer will be achieved; then, $K_D w_D = K_A w_A$. Therefore, when the maximum transfer has occurred,

$$\frac{w_A}{w_D} = \frac{K_D}{K_A} \tag{I-39}$$

This equation is equivalent to Eq. I-37. To model the stepwise transfer process, the fractional transfer must be calculated as a function of the distribution coefficients; the amount of donor (D), salt (S), and acceptor (A); and the number of transfer cycles.

From the mass balance and the definition of the distribution coefficient, the fraction, F_D, of the solute (U or Pu) in the donor and salt transferred to the acceptor is given by

$$F_D = \frac{K_D(S/D)\chi + z}{K_D(S/D) + 1} \tag{I-40}$$

where χ is the fraction of salt transferred, and z is the fraction of donor entrained with the salt. A similar expression is obtained for the fraction of solute back-transferred from the acceptor to the donor, except that K_D is replaced with K_A and D by A.

The fraction transferred after n cycles, Φ_n, is given by

$$\Phi_n = \left(1 - \frac{F_A}{1 - F}\right)(1 - F^n) \tag{I-41}$$

in which $F = (1 - F_A)(1 - F_D)$. Since F is less than unity, the maximum fractional transfer, Φ_{max}, is given by

$$\Phi_{max} = \left(1 - \frac{F_A}{1 - F}\right) \tag{I-42}$$

To a good approximation (~0.1%), $\Phi_{max} \approx 1 - f$, where $f = F_A/F_D$. If there is no entrainment of either alloy during the transfer (i.e., $z = 0$), then the maximum fractional transfer is given by

$$\phi_{max} = \frac{K_D A}{K_A D + K_D A + K_A K_D S} \qquad \text{(I-43)}$$

This relation shows that complete transfer would be possible if $K_A = 0$. This expression may also be derived from the mass balance, the definitions of the distribution coefficients, and Eq. I-39.

Since $1 - F^n$ varies from 0 to 1 as n varies from 0 to ∞, the number of cycles, n, required to obtain a given fraction, P, of the maximum possible transfer, ϕ_{max}, is given by

$$n = \frac{\ln(1 - P)}{\ln F} \qquad \text{(I-44)}$$

The value of n increases rapidly when F increases above 0.8.

The above equations were derived with the assumptions that all of the solute was initially present in solution in the donor and salt (none initially in the acceptor) and that all of the solute transferred to the acceptor was completely soluble. The amount of solute transferred to the acceptor, $\phi w_{d,i} (K_D S + D)$, is directly proportional to its initial concentration ($w_{d,i}$) in the donor. If that concentration is low, as would be the case if its solubility in the donor were low, then the amount transferred would be small even though the fraction transferred were large. With a low concentration of solute in the salt (this concentration is equal to $K_D w_d$), when in contact with the donor, a large number of cycles would be needed to transfer a small amount of solute. This would not yield a practical process.

The amount transferred can also be limited by ϕ_{max} when F_D is not much greater than F_A, as would be the case if K_D is not much greater than K_A. In this case, the amount transferred can be increased by beginning the salt transfer with a part of the initial charge as an insoluble metallic phase. This has two advantages: the total amount of solute available for transfer is larger, and the rate of transfer is greater. This latter follows from the fact that, as long as undissolved solid remains in the donor, the fraction transferred from the donor will remain constant and will be greater than the fraction obtained if the concentration in the donor decreased with each cycle. The fraction transferred after n cycles is given by

$$\phi_n = \frac{pF_D(1 - F_A)}{F_A} \left(1 - (1 - F_A)^n\right) \qquad \text{(I-45)}$$

where p is the fraction of the total solute initially in solution in the donor and salt. The value of p may be calculated from the total amount of solute in the donor initially, the distribution coefficient, and the solubility of the solute in the donor. This equation is valid only when excess solute is

present as an insoluble metallic phase. When all of the solid has dissolved, Eq. I-41 must be used to calculate the fractional transfer for the remaining part of the transfer. Starting the salt transfer with part of the solute as an insoluble metallic phase in the donor will increase the maximum transfer over the value that can be obtained starting with all of the solute in solution. This will decrease the number of cycles needed. We also found that there is an optimal value for p to achieve a given fractional transfer with the minimum number of cycles. These effects can be significant for practical processes. For example, a system for which the maximum fractional transfer was 97.3% (for an "infinite" number of cycles) would achieve a fractional transfer of 99% in 21 cycles if 20% of the initial charge was in solution, with the remaining 80% present as a solid metallic phase. It should be noted that the solubility of the solute in the donor was not low, even though only 20% of the initial charge was in solution. This case and the case discussed in the previous paragraph should not be confused.

If the solubility of the solute in the acceptor is low, then the back-transfer of solute to the donor will be decreased and the maximum fractional transfer will be increased. If the acceptor becomes saturated after the first transfer cycle, then the fraction transferred to the acceptor after n cycles is given by

$$\Phi_n = \left(1 - \frac{a}{F_D}\right)\left(1 - (1 - F_D)^n\right) \qquad \text{(I-46)}$$

where a is the fraction of the original charge that is returned each cycle to the donor from the acceptor after the acceptor has become saturated. This quantity will be constant throughout the transfer. The value of a can be computed from the total amount of solute initially present, the distribution coefficient (K_A), the solubility of the solute in the acceptor, and the amounts of salt and acceptor. A small value for the solubility of the solute in the acceptor can be used to compensate for a large value of K_A. The maximum fractional transfer is obtained from Eq. I-46 by setting the last factor equal to unity:

$$\Phi_{max} = 1 - \frac{a}{F_D} \qquad \text{(I-47)}$$

It is possible to combine an excess of solute in the donor with a low solubility in the acceptor to obtain a highly efficient process. An example of such a system is discussed by Knighton et al.[60] In this example uranium is recovered and purified by being salt-transported from a copper-magnesium alloy through a molten $MgCl_2$ salt to a magnesium-zinc alloy. Uranium has a moderate solubility (1%) in the Cu-Mg alloy but a low solubility (0.025%) in the Mg-Zn alloy. The distribution coefficients are 0.45 for the Cu-Mg donor and 0.3 for the Mg-Zn acceptor. The insoluble uranium forms an intermetallic phase, UCu_5, in the donor and is present as pure metallic uranium in the acceptor. In a kilogram-scale experiment, 99% of the uranium was recovered in 27 transfer cycles.[78] In addition, removals of over 99% were obtained for zirconium and other noble metal fission products.

The salt transport process can be used to separate uranium and plutonium from the more noble fission product elements. The decontamination factor, D.F., is defined as

$$D.F. = \frac{\Phi_{U \text{ or } Pu}}{\Phi_{impurity}} \tag{I-48}$$

For the purpose of this discussion, the fractional transfer of U or Pu can be set equal to one. The fractional transfer for the impurity can be shown to be approximately equal to $n(K_{Di}S/D\chi + z)$, where K_{Di} is the distribution coefficient of the impurity, and n is the number of cycles needed to obtain the required high recovery of uranium or plutonium. To obtain this result, it is assumed that $F_A = 0$ and that $K_{Di}S/D$ is small compared to one. Hence the D.F. is given by

$$D.F. = \frac{1}{n(K_{Di}S/D\chi + z)} \tag{I-49}$$

Since K_{Di} is be expected to be small, the amount of donor entrained with the salt becomes important and may, in some cases, limit the decontamination which can be achieved. Where very high decontaminations are required, it may be necessary to salt transport to an intermediate acceptor alloy, which then acts as the donor for the final acceptor. In a test case where a D.F. of 320 was obtained with no entrainment, the D.F. was reduced to 90 when 0.1% entrainment occurred.

The above analysis, Eqs. I-39 to I-49, is based on the assumption that the distribution coefficients are constant during the salt transport process. However, during the transfers, magnesium is sent from the acceptor to the donor. This will lead to a change in the activities of the solutes in the two alloys and change the distribution coefficients. For a more exact treatment, these changes must be considered. The treatment given above allows the computation of the overall performance of a proposed process configuration to the accuracy needed for process development. The treatment adds to the understanding of the salt transport process.

4. Thermodynamics of Electrotransport Processes

The analysis of the electrotransport processes is similar to that used for the salt transport process. In this case, the transfer is done by electrolyzing (i.e., oxidizing) U and Pu into the salt at the anode and electrodepositing an equivalent amount at the cathode. Some U and Pu must be present in the salt before the electrolysis is started. This could be obtained by adding a mild oxidizing agent, most likely a salt of the anode solvent metal. The composition of the mixture of Pu and U deposited at the cathode depends on the kinetic factors that control electrodeposition from molten salts into a liquid alloy electrode. However, after some U and Pu has been transferred to the cathode, there is a tendency for equilibrium to be maintained between the salt and the alloy at each electrode. Hence, at each electrode, the following equilibrium will exist:

$$UCl_3(salt) + Pu(alloy) = U(alloy) + PuCl_3(salt) \quad \text{(I-50)}$$

This reaction leads to the following equilibrium relation:

$$\frac{a_{U(alloy)}\, a_{PuCl_3(salt)}}{a_{Pu(alloy)}\, a_{UCl_3(salt)}} = K_a \quad \text{(I-51)}$$

If there are no large concentration differences in the salt, then the activities in the salt will be the same at each electrode, and one obtains the relation:

$$\left(\frac{a_U}{a_{Pu}}\right)_{anode} = \left(\frac{a_U}{a_{Pu}}\right)_{cathode} \quad \text{(I-52)}$$

which can be written in the same form as Eq. I-38 if one assumes that donor ≡ anode and acceptor ≡ cathode. This equation, when written in the same form as Eq. I-38, shows that the EMF for both possible cells is the same value:

$$-nFE = RT \ln \frac{a_{U(a)}}{a_{U(c)}} = RT \ln \frac{a_{Pu(a)}}{a_{Pu(c)}} \quad \text{(I-53)}$$

in which a and c refer to the anode and cathode, respectively. The condition expressed by Eq. I-52 is referred to as the "equal EMF condition" and is an important result for the understanding of the operation of the electrotransport process. This condition connects the two liquid alloy electrodes in the analysis of the system. During the operation of the electrotransport process, the total number of equivalents of solute in the salt (i.e., UCl_3 and $PuCl_3$) is constant. This was also true of the salt transport process, in which case $MgCl_2$ has to be included with the UCl_3 and the $PuCl_3$. The total number of equivalents of solute metals, at any given juncture of the transport process, in each liquid electrode is constant, although the composition will change as equilibrium is established.

To use Eqs. I-51 and I-52 in the analysis that follows, the activities are replaced by concentration units. The equilibrium relation, Eq. I-51, may be written in terms of atom (mole) fractions:

$$\frac{\chi_U \chi_{PuCl_3}}{\chi_{UCl_3} \chi_{Pu}} = K_a \frac{\gamma_{Pu} \gamma_{UCl_3}}{\gamma_U \gamma_{PuCl_3}} \quad \text{(I-54)}$$

The right-hand side of this equation is defined as K_χ, the atom fraction equilibrium constant. While the activity coefficients are functions of the solute concentrations in the alloys, the variation with concentration is not

large, and the γ's can be considered constant for most computations. If more accurate results are required, the γ values can be adjusted for the actual concentrations found, and the computation repeated as often as needed to obtain the required accuracy. The atom fraction of U is given by

$$\frac{n_U}{n_U + n_{Pu} + n_{Cd}}$$

where the n's are moles of the subscripted element and cadmium is assumed to be the solvent metal. A similar expression is obtained for the atom fraction of Pu. The denominators cancel when the ratio is taken. Similar expressions are obtained for the mole fractions of the salts; again the denominators cancel when the ratio is taken. This allows the equilibrium relation to be written as

$$\frac{PuCl_3}{n_{UCl_3}} \times \frac{n_U}{n_{Pu}} = K \qquad \text{(I-55)}$$

In a similar way, the equal EMF relation can be written as

$$\frac{n_{U,a}}{n_{Pu,a}} = \frac{n_{U,c}}{n_{Pu,c}} \qquad \text{(I-56)}$$

Equations I-54 and I-55 apply to the liquid phases of the two electrodes. To complete the description of the system, three mass balance relations are needed:

$$n_{U,a} + n_{U,c} + n_{UCl_3} = n_U \qquad \text{(I-57a)}$$

$$n_{Pu,a} + n_{Pu,c} + n_{PuCl_3} = n_{Pu} \qquad \text{(I-57b)}$$

$$n_{UCl_3} + n_{PuCl_3} = n_s \qquad \text{(I-57c)}$$

where n_U, n_{Pu}, and n_s are the total amounts of uranium, plutonium, and salts in the system. One additional condition is needed to specify the system, the total amount of solute transferred to the cathode. This can be stated in a variety of ways. For the case that all of the solute is in solution in the cathode, the following relation may be used:

$$n_{U,c} + n_{Pu,c} = n_c \qquad \text{(I-57d)}$$

where n_c is the total solute in the cathode. Determining the distribution of n_{PuCl_3} is done by calculating the first ratio with Eq. I-57c and the second ratio with Eqs. I-56, I-57a and b. The result, when both liquid electrodes are single (liquid) phases, is the following quadratic equation in which n_{PuCl_3} has been replaced by χ:

$$\frac{\chi}{n_s - \chi} \times \frac{n_U - n_s + \chi}{n_{Pu} - \chi} = K_\chi \qquad \text{(I-58)}$$

Once χ is known, the amount of U and Pu in the anode and cathode can be computed by substitution in Eq. I-57. Equation I-58 only needs to be solved once to obtain the ratio $n_{U,c}/n_{Pu,c}$. This ratio will be constant throughout the transfer (if the small variations in the activity coefficients with concentration are neglected). Values of $n_{U,c}$ and $n_{Pu,c}$ are obtained for different amounts of transfer to the cathode by changing the value of n_c in Eq. I-57d. If either of the liquid alloys is not a single phase, the procedure is similar but the manner in which the second factor in Eq. I-58 is calculated is changed to include the solubility of the solute(s) in the liquid alloy(s).

As the electrotransport proceeds, the EMF of the system varies due to the change in the ratio of the atom fractions of uranium (or plutonium) in the two liquid alloy electrodes. Since the atom fraction ratio is that of uranium (or plutonium) between two different liquid alloys, the value for the total moles in each alloy used to convert the moles of uranium to atom fraction does not cancel out; the ratio is given by the equation:

$$\frac{\chi_{U,a}}{\chi_{U,c}} = \frac{n_{U,a}}{n_{U,c}} \times \frac{n_{U,a} + n_{Pu,c} + n_{Cd,c}}{n_{U,a} + n_{Pu,a} + n_{Cd,a}} \qquad \text{(I-59)}$$

Since the number of moles of Cd in each alloy electrode is usually much larger than the moles of solute, the latter can often be neglected. The EMF, E, is given by the relation:

$$E = \frac{RT}{nF} \ln \frac{\chi_{U,a}}{\chi_{U,c}} \qquad \text{(I-60a)}$$

The recovery and separation of uranium and plutonium by electrotransport will be discussed by the use of two numerical examples. The electrotransport of a mixture of plutonium and uranium from one liquid cadmium alloy to another will be used in these examples. The first step is to estimate the value of K_χ, the atom fraction equilibrium constant for the distribution of uranium and plutonium between liquid cadmium and a molten salt. The value of K_a is computed from ΔG° using the relation:

$$-RT \ln K_a = \Delta G_{f_{PuCl_3}} - \Delta G_{f_{UCl_3}} \qquad \text{(I-60b)}$$

Values of the free energies of formation were obtained from Fuger.[66] At 773 K, ΔG° was found to be -21835 cal/mol, which gives a K_a value of 1.48×10^6. Values for γ_{Pu} and γ_U, Eq. I-54, were obtained from the EMF studies of the Cd-Pu[79] and Cd-U[80] systems. Both activity coefficients are dependent on the solute concentration in the liquid Cd alloy. At 773 K the γ_{Pu} values vary from 1.39×10^{-4} to 2.37×10^{-4} as the concentration varies from zero to the saturation value (1.805 at. %)[29], while the γ_U values vary from 81.3 to 88.7 as the concentration varies from zero to the saturation value (1.128 at. %).[81] The equilibrium solid phases are the intermetallic compound $PuCd_6$ and elemental uranium. The ratio γ_{Pu}/γ_U varies from 1.71×10^{-6} to 2.67×10^{-6} over the concentration range. The ratio of the γ's for $PuCl_3$ and UCl_3 in the molten salt phase depends on the composition of the molten salt. There is a paucity of such data. For the present example, the results reported in Sec. I.C.2 have been used. Hence, $\gamma_{UCl_3}/\gamma_{PuCl_3} = -0.267$. When these activity coefficients are combined with the value of K_a, the value of K_γ is found to vary from 0.68 to 0.93. A value of 0.8 was selected for the numerical examples. The very large effect of the activity coefficients in the liquid alloys should be noted.

For these examples, a mixture of 82.5% uranium and 17.5% plutonium was assumed. This is approximately the composition of spent core fuel. The anode was assumed to contain 100 moles of cadmium, while the cathode contained 50 moles of cadmium. These choices were selected to illustrate some of the characteristics of electrotransport and do not represent the optimum choices for a practical process. In the first example, the amount of the U-Pu mixture was selected so that the anode would be initially just saturated with respect to uranium, while in the second example the anode was initially just saturated with respect to plutonium. Thus, in the first example all of the uranium and plutonium are initially in solution in the anode, while in the second example a large fraction of the uranium is initially present as solid uranium. From the solubility data for uranium in liquid cadmium,[81] the initial charge in the first example contained 0.242 moles of Pu and 1.141 moles of U. Ten percent of the initial charge was transferred to the salt to furnish the solute chlorides needed for the electrotransport. In a practical process, the molten salt may contain UCl_3 and $PuCl_3$ from the previous batch.

The results of the numerical computations are shown in Table I-11. Column 1 is the percent of the U and Pu initially in the anode (after 10% was oxidized into the salt) but then transferred to the cathode. The compositions of the anode and cathode are given in moles. At 55.7% transfer, the cathode becomes saturated in uranium. As more uranium is transferred to the cathode, the amount in solution in the cathode does not change; the excess adds to the metallic uranium precipitate. The Pu/U ratio in the anode and cathode up to 55.7% transfer is constant and equal for the two liquid electrodes. This is what is expected (Eq. I-52) if the activity coefficients are equal in the two alloys and do not change with concentration. Once the cathode becomes saturated with uranium, these ratios are no longer constant. The transfer of uranium to the cathode, after saturation is achieved, results in less uranium in solution. The Pu/U ratio in solution will increase for both liquid electrodes, as is seen for the anode. In the cathode, some of the uranium is not in solution and the overall Pu/U ratio, which is shown in Table I-11, will be

Table I-11. Computation of Anode and Cathode Composition during Electrotransport of Uranium and Plutonium

Anode: 100 mol Cd; Cathode: 50 mol Cd
U = 1.141 mol; Pu = 0.242 mol
10% [U+Pu] in salt; 773 K

$[U + Pu]_c$, %	Anode, mol			Cathode, mol		
	Pu	U	[Pu/U]	Pu	U	[Pu/U]
8.0	0.204	0.941	0.217	0.018	0.082	0.217
16.0	0.186	0.859	0.217	0.036	0.164	0.217
32.1	0.150	0.694	0.217	0.071	0.329	0.217
40.1	0.133	0.612	0.217	0.107	0.493	0.217
55.7	0.098	0.453	0.217	0.123	0.570	0.217
59.5	0.092	0.410	0.225	0.128	0.613[a]	0.209
69.8	0.075	0.300	0.252	0.143	0.726[a]	0.198
73.3	0.058	0.210	0.278	0.158	0.818[a]	0.194
85.6	0.042	0.137	0.304	0.173	0.893[a]	0.194
91.1	0.025	0.075	0.331	0.188	0.957[a]	0.197
95.7	0.013	0.039	0.348	0.198	0.994[a]	0.199

[a]Cathode contains 0.57 mol U in solution.

increased by the amount present as an insoluble solid phase. The Pu/U ratio in the cathode remains almost constant because the effect of the increase in the Pu/U ratio caused by the decrease of the U in solution is almost balanced by the decrease caused by the additional uranium present as solid. The Pu/U ratio in solution in the cathode increases as the amount of solid increases, as would be seen if the amount of Pu in solution is divided by 0.57 moles, the amount of uranium in solution. Equation I-56 applies only to the uranium and plutonium in solution.

From the solubility of Pu in Cd,[79] the initial charge in the second example contains 2.19 moles of Pu and 12.35 moles of uranium. One percent of this charge was transferred to the salt to furnish the $PuCl_3$ and UCl_3 required for the electrolysis. The anode initially contains solid uranium as an insoluble phase. The numerical details of the computation are given in Table I-12. As the solute is moved from the anode to the cathode, the total amount of uranium in solution increases due to the dissolution of some of the uranium at the anode.

This will decrease the Pu/U ratio in solution, as is seen for both the anode and the cathode in Table I-12. The decrease in the overall Pu/U ratio in the anode as the transfer takes place will be reduced by the dissolution of solid uranium. At 10.33% transfer, the cathode becomes saturated with respect to uranium. Further transfers of solute from the anode to the

Table I-12. Computation of Anode and Cathode Composition during Electrotransport of Uranium and Plutonium

Anode: 100 mol Cd; Cathode: 50 mol Cd
U = 12.35 mol; Pu = 2.19 mol
1% [U+Pu] in salt; 773 K

$[U + Pu]_c$, %	Anode, mol			Cathode, mol		
	Pu	U	[Pu/U]	Pu	U	[Pu/U]
0.63	2.066	10.24	0.202	0.050	0.028	1.18
2.58	1.918	10.15	0.184	0.200	0.119	1.68
5.37	1.722	10.00	0.172	0.400	0.265	1.51
8.47	1.525	9.81	0.155	0.600	0.449	1.34
10.33	1.418	9.69	0.146	0.709	0.570	1.24
16.15	1.418	8.97	0.158	0.709	1.291[a]	0.549
32.30	1.418	6.97	0.204	0.709	3.291[a]	0.216
48.45	1.418	4.97	0.286	0.709	5.291[a]	0.134
64.59	1.418	2.97	0.478	0.709	7.291[a]	0.097
79.33	1.418	1.141	1.243	0.709	9.12[a]	0.078

[a]Cathode contains 0.57 mol U in solution.

cathode simply move solid uranium from the anode to the uranium solid phase in the cathode. The total amount of Pu and U in solution does not change; hence, the composition of the two liquid phases is constant. The overall Pu/U ratio increases in the anode and decreases in the cathode. Since no additional Pu is transferred to the cathode during this phase of the transfer, a Pu-rich solution can be obtained in the anode. In a practical process, this Pu could be recovered by transfer to a second cathode. This is similar to the way that Pu and U are separated in the salt transport process where two different acceptors are used.

The EMF as a function of [U + Pu] transferred was computed for the two examples given in Tables I-11 and I-12 using Eqs. I-59 and I-60a. The results are shown in Fig. I-19. A positive EMF is based on the assumption that the anode would be negative in the conventional sense, i.e., electrons would leave the system at the anode. This assumes that U and Pu are oxidized at the anode and reduced at the cathode. The two curves indicate that the EMF's for both systems are positive initially, and that both systems would spontaneously transfer U and Pu from the anode to the cathode if the two electrodes were connected with an electronic conductor. This is expected since the activities of both Pu and U are initially greater in the anode. As the electrolysis continues, the EMF will decrease since the transfer of Pu and U to the cathode will increase their activities and eventually reach zero when the activities are equal. Further transfer to the cathode requires an external electrical power source.

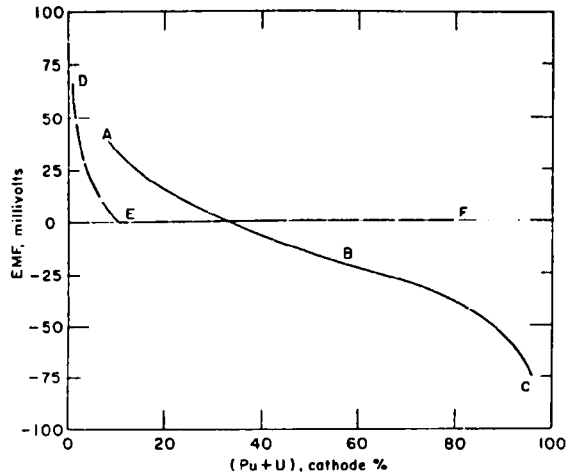

Fig. I-19. Calculated EMF during Electrotransport of Uranium and Plutonium at 773 K. Curve ABC is calculated from data in Table I-11. Curve DEF is calculated from data in Table I-12. Segment AB: both anode and cathode, single (liquid) phase. Segment BC: anode, single phase; cathode, two phase (liquid alloy and solid U). Segment DE: anode, two phases; cathode, single phase. Segment EF: both anode and cathode, two phase (liquid alloy and solid U).

For the ABC curve from the first example (Table I-11), additional transfer after the zero EMF is achieved results in a system that spontaneously transfers U and Pu in the opposite direction if the two electrodes are connected with an electronic conductor. The rapid decrease in the Pu and U in solution after the cathode becomes saturated increases the rate of decrease of the EMF, as seen in the BC segment. Once the cathode becomes saturated with uranium, its activity will be constant and further transfers of uranium to the cathode will not increase its activity. This is the reason for the difference in curvature of the two segments of curve ABC.

The curve DEF for the second example (Table I-12) has two segments. The first segment corresponds to the transfer from the saturated (with respect to U) anode to the unsaturated cathode. The activities in the cathode increase and the EMF decreases. At point E, both electrodes become saturated with respect to uranium, and hence the activities are equal and the EMF is zero. To move additional U to the cathode, an external source of electrical power must be applied. If the EMF is computed on the basis of the Pu contents of the two electrodes using the data in Table I-12 and Eqs. I-59 and I-60a, a zero value is obtained. If the small concentration dependence of the activity coefficients is included in the computation of the EMF, then the Pu contents of the two electrodes would have to be slightly adjusted. The concentration would be decreased in the anode and increased in the cathode.

5. Comparison of Salt Transport and Electrotransport

This analysis treats both the salt transport and electrotransport as equilibrium processes. Both processes involve the establishment of equilibrium between two (or more) liquid alloy phases and a common molten salt phase, with the restriction that the number of equivalents of solute in each phase is constant. This restriction is due to the fact that the transfer of solutes between a liquid alloy and a molten salt is an oxidation-reduction process, and the equivalents of solute oxidized (transferred to the molten salt) must be balanced by the equivalents reduced (transferred to the liquid alloy). The number of equivalents of solute in each phase is fixed by the initial composition of the system, i.e., the number of moles of solute in each alloy and in the salt. In the case of salt transport, U, Pu and Mg must be considered solutes since all three are involved in the oxidation-reduction reactions. Hence at the end of the salt transfer, the sum of the number of equivalents of U, Pu, and Mg in the donor alloy is the same as it was initially, except that the proportions of each has changed since U and Pu have been transferred to the acceptor. The same is true of the acceptor except that the amount of U and Pu is greater and balanced exactly by less Mg. In the case of electrotransport, the number of equivalents of U and Pu in the anode and cathode changes as the electrolysis occurs. However, the total number of equivalents of U and Pu in the two alloys is constant, as is the number of equivalents of U and Pu in the salt. The tendency to establish equilibrium during electrotransport can be considered as a series of salt transport steps in which the initial compositions of the liquid alloy phases are being changed stepwise by the electrolysis. The composition of the liquid alloys is determined by the equilibrium relation and the condition that the activities in the molten salt are equal at both alloys. This latter condition yields the equal EMF relation in electrotransport (Eq. I-52) and a similar relation (Eqs. I-36 to I-38) for salt transport.

In using these relations for practical computations, one must convert to relations between composition variables. This is done by using either the atom (mole) fraction equilibrium constants or the distribution coefficients and the solubilities in the liquid alloys. The analysis presented in this paper can be used as the starting point for more detailed computations involving other solutes and other initial conditions. The effect of changing alloy composition on the activity coefficients must be computed using iterative methods, since the equations obtained when the dependence of the equilibrium constants or distribution coefficients on alloy composition is explicitly included are too complex to solve analytically.

D. Fusion-Related Research

A critical element in the development of the fusion reactor is the blanket for breeding tritium fuel. We are conducting several studies with the objective of determining the feasibility of using lithium-containing ceramics as breeder material. We are also conducting design studies of methods for improving fusion reactor performance and neutron dosimetry and damage analysis of fusion materials in neutron facilities.

1. Adsorption, Dissolution, and Desorption Characteristics of the $LiAlO_2$-H_2O System

(A. K. Fischer)

Accounting for the tritium inventory in the tritium breeding blanket of a fusion reactor requires, among other things, knowledge of several properties: (1) the adsorption-desorption characteristics of tritium-containing species on the breeder surface, (2) the solubility of tritoxide and tritide in the bulk breeder, and (3) the kinetics of various processes that transport tritium out of the breeder. An experimental study on $LiAlO_2$ was initiated to obtain information for the thermodynamics of adsorption of $H_2O(g)$ and dissolution of OH^-, as well as for the kinetics of the evolution of $H_2O(g)$. Detailed thermodynamic calculations performed earlier[82] indicated that the solubility of hydroxide in a breeder is, in general, dependent on the oxygen activity. For low oxygen activities (below about 10^{-15}) the dependence is significant, but for oxygen activities above this level, such as in high purity helium, the dependence is slight. Although the effect of low oxygen activity on the measured values was not addressed, the question will be examined experimentally by the use of gases with fixed ratios of H_2O:H_2. Effects related to low oxygen activities are the subject of future reports.

a. Experimental

Adsorption measurements with γ-$LiAlO_2$ were made by the frontal analysis technique of gas chromatography,[83] also known as the breakthrough technique. The method is to introduce a gas stream with a known flow rate and partial pressure of $H_2O(g)$ into the inlet of a packed column of the sample at a known time. A Beckman H_2O analyzer measures the $H_2O(g)$ level in the effluent gas. Because the adsorption process is rapid, the response of the analyzer remains at the preinjection baseline level until the surface of the sample reaches the degree of coverage that is thermodynamically required by the prevailing temperature and partial pressure of $H_2O(g)$. At that time, water vapor emerges at the end of the column (breakthrough occurs), and the analyzer records a sharp rise in water level in the effluent gas. A similar technique was used by Yoshida et al.[84] to study surface adsorption of H_2O on Li_2O.

Figure I-20 is a schematic representation of typical data from an experimental run. The area "ADS" indicates the amount of water vapor adsorbed on the surface. Reaction and dissolution of hydroxide is a slower process than adsorption and was recorded in the next part of the curve, which measures the uptake of $H_2O(g)$. In this region of increasing H_2O content in the effluent gas, the area after the breakthrough point and before the level of the plateau is a measure of the solubility of hydroxide and is labeled "SOL" in Fig. I-20. Establishment of the plateau level of the water concentration in the gas phase indicates equilibrium of the solid with the hydroxide reaction product at an activity corresponding to p_{H_2O}. After this plateau, the gas phase composition was switched back to pure helium and evolution of $H_2O(g)$ was recorded. Integration under this curve, area "EV" in Fig. I-20, provided data for the kinetic analysis of the water evolution process.

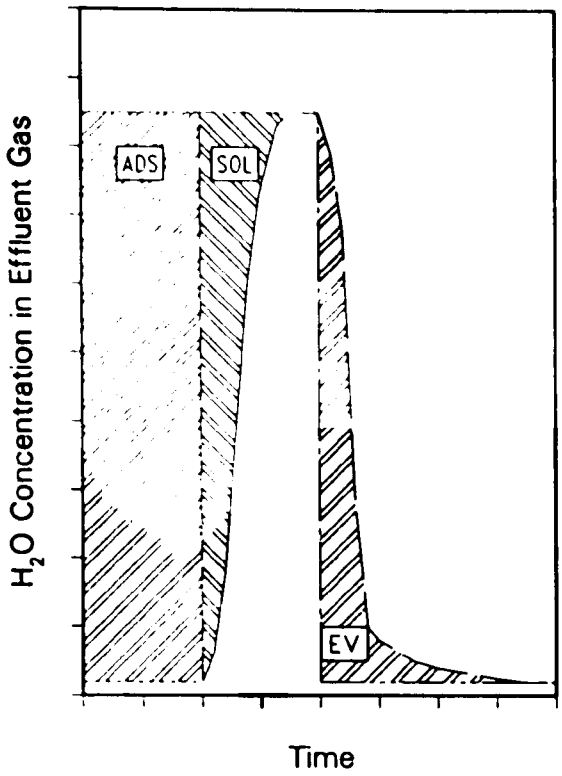

Fig. I-20.

General Form of Data from an Experimental Run Showing the Regions Characterizing Adsorption of $H_2O(g)$ (ADS), Solubility of OH^- in $LiAlO_2$ (SOL), and Rate of Evolution of $H_2O(g)$ (EV)

The γ-$LiAlO_2$ particles were used as-purchased from Cerac, Inc. They had a particle size range of 150 to 300 μm and a surface area of 0.16 ± 0.02 m^2/g (BET analysis). A sample column was loaded with 0.333 mol of this material. Its purity was 99.9%, with Na, Fe, Ca, Mg, Cu, and Si accounting for the 0.1% impurity content.

b. Results

(1) Baseline Corrections

Because the baseline conditions always involve a small partial pressure of $H_2O(g)$, there will always exist some residual hydroxide, both on the surface and in the bulk. These amounts of residual hydroxide must be added to the amounts measured on the surface and in the bulk in order to obtain corrected data. The amount of this residual hydroxide was estimated for the adsorption and the solubility measurements to provide the necessary corrections. The estimate involved an experimental and a calculational part. Experimentally, after the water evolution had run its course and the baseline was reestablished, the sample was heated to 939 K (666°C). This temperature was selected to avoid sintering of the surface. Under these conditions, the additional $H_2O(g)$ evolution provided a partial measure of the amount of residual hydroxide remaining in the sample in equilibrium with the partial pressure of $H_2O(g)$ in the helium sweep gas. The difference between the amounts of water evolved in heatings from 673 to 939 K and from 773 to 939 K was (8.32 ± 4.6) x 10^{-7} mol (one standard deviation).

The total amount of residual hydroxide had to be estimated and apportioned between that to be ascribed to the surface and that to be ascribed to the bulk. This estimation was approached in the following way. The slope of $\log(\theta)$ or $\log(x_{OH})$ vs. $\log(p)$ curves obtained from the raw data for adsorption and solubility had values greater than 0.5, where θ is the fraction of surface covered, x_{OH} is the mole fraction of hydroxide in the bulk, and p is the partial pressure of $H_2O(g)$. At 673 K the raw values of the slopes were 0.550 and 1.032 for the adsorption and solubility curves, respectively. These values were 0.673 and 0.606, respectively, for 773 K. However, a value 0.5 would be expected for the slope of the adsorption isotherm for dissociative adsorption of H_2O. Furthermore, a value of 0.5 is expected for the hydroxide dissolution process if it produces insoluble $LiAl_5O_8$ (activity, a, is equal to 1) according to the reaction,

$$5LiAlO_2 + 2H_2O(g) \rightleftharpoons 4LiOH(soln.) + LiAl_5O_8(a = 1) \qquad (I\text{-}61)$$

However, if $LiAl_5O_8$ is soluble in $LiAlO_2$ so that the reaction is

$$5LiAlO_2 + 2H_2O(g) \rightleftharpoons 4LiOH(soln.) + LiAl_5O_8(soln.) \qquad (I\text{-}62)$$

the slope would be 0.4. Applying additive corrections for the residual quantities to each measured value of θ or x_{OH} would reduce the slopes of the respective curves. By an iterative process, the incremental values needed to produce curves with slopes of 0.5 were determined. The values at 673 K are 7×10^{-3} for θ and 1.95×10^{-5} for x_{OH}. At 773 K, they are 6×10^{-2} for θ and 8.4×10^{-6} for x_{OH}. The incremental values of mole fraction hydroxide needed to produce curves with slopes of 0.4 for the solubility data were also determined. They are 3.0×10^{-5} and 2.0×10^{-5} for 673 and 773 K, respectively. The selection of these values is explained in Sec. I.D.1.c.

(2) Surface Adsorption

Figure I-21 presents the surface adsorption isotherms for adsorption of $H_2O(g)$ on $LiAlO_2$ at 673 K and 773 K. The value of θ is based on the measured surface area and on the approximation that the size of one adsorption site is 10^{-15} cm^2. This assumption is based on observations by DeBoer et al.[85] that the water monolayer capacity on alumina corresponds to 1.1×10^{15} sites/cm^2. Also, the crystallographic surface density of aluminum atoms on alumina has been reported to be $1.02 \times 10^{15}/cm^2$.[86] Possibly, a maximum value for site density could be set because there are 1.7×10^{15} oxide ions in a close-packed sheet.[87] However, all exposed faces of the $LiAlO_2$ sample are not necessarily such crystallographic planes.

Both isotherms are of the Freundlich type and include the additive corrections for residual surface OH groups to produce a slope of 0.5. The linear regression equations representing the adsorption isotherms are

$$\log(\theta) = (-1.590 \pm 0.691) + (0.497 \pm 0.064)\log(p_{H_2O}) \qquad (I\text{-}63)$$

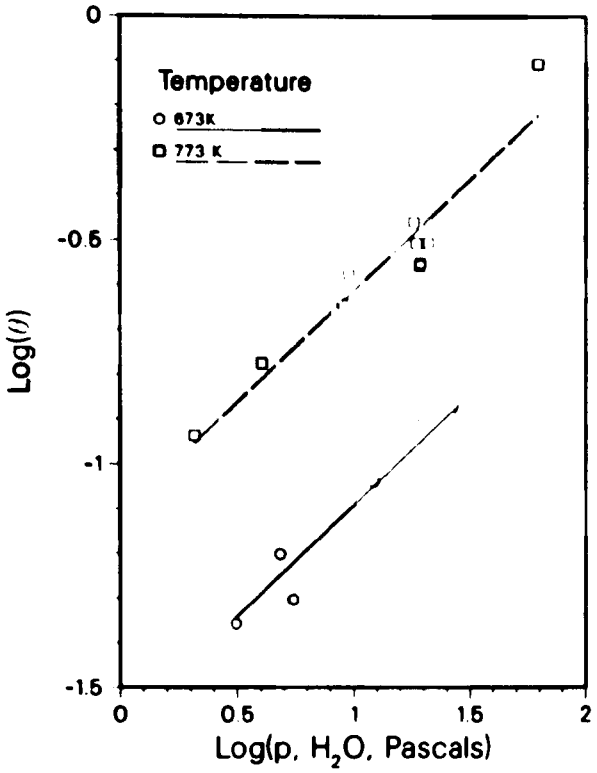

Fig. I-21.

Surface Adsorption Isotherms for $LiAlO_2$-H_2O(g) System at 673 and 773 K

$$\log(\theta) = (-1.112 \pm 0.061) + (0.497 \pm 0.052)\log(p_{H_2O}) \qquad \text{(I-64)}$$

where p_{H_2O} is the partial pressure of H_2O(g) in Pascals.

(3) Solubility

Figure I-22 presents the isotherms for the solubility of OH^- in $LiAlO_2$ at 673 K and 773 K. These isotherms include the additive corrections for residual hydroxide and give a slope of 0.4 for 673 K and 0.5 for 773 K. The reasons for these values of slopes are presented in Sec. I.D.1.c. The linear regression equations for 673 K and 773 K, respectively, are

$$\log(x_{OH}) = (-4.867 \pm 0.096) + (0.399 \pm 0.088)\log(p_{H_2O}) \qquad \text{(I-65)}$$

$$\log(x_{OH}) = (-4.899 \pm 0.079) + (0.499 \pm 0.063)\log(p_{H_2O}) \qquad \text{(I-66)}$$

Based on a reference state of LiOH for unit activity at the temperatures of the measurements and Tetenbaum and Johnson's data[88] for the LiOH-Li_2O-H_2O(g) equilibrium, activity coefficients were calculated for LiOH as a solute in $LiAlO_2$. Within the precision and range of the measurements, the activity coefficients are independent of composition and are $1.4 \times 10^4 \pm 2 \times 10^3$ and $4.3 \times 10^3 \pm 3 \times 10^2$ at 673 and 773 K, respectively.

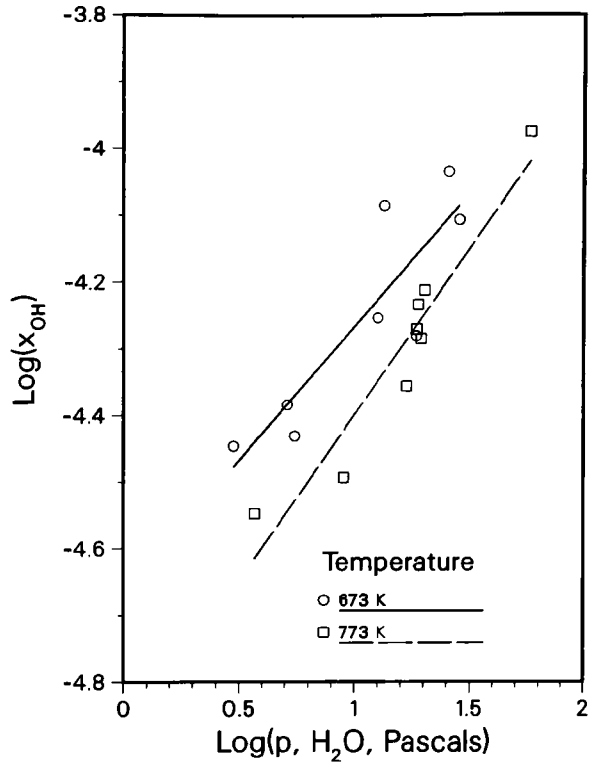

Fig. I-22.

Isotherms for Solubility of Hydroxide in $LiAlO_2$ at 673 and 773 K

(4) Kinetics of $H_2O(g)$ Evolution

Kinetic data for the $H_2O(g)$ evolution process were obtained by stepwise integration under the curves corresponding to the EV area of Fig. I-20. To determine the reaction order, a generalized rate equation was used:

$$dx_{OH}/dt = k_g(a - m_{OH})^n \qquad \text{(I-67)}$$

where dx_{OH}/dt is the rate of water loss expressed in terms of hydroxide, k_g is the generalized rate constant, a is the amount of hydroxide present in the system at zero time for the start of the kinetic analysis, m_{OH} is the amount of hydroxide that has been lost (as H_2O) at time, t, and n is the kinetic order of the process. The values of a and m_{OH} were also corrected for residual hydroxide by the same amounts as discussed above. The reaction order was found to be 2.22 ± 0.17 for 673 K and 1.95 ± 0.17 for 773 K. The reaction appears to be essentially second order. This result justified plotting the data as $m/a(a - m)$ vs. kt, for which a linear fit is characteristic of second-order kinetics. General conformance to linear behavior was found. The second-order rate constants derived in terms of evolved $H_2O(g)$ in units of $(\text{mol min})^{-1}$ were 995 ± 130 for 673 K and 4118 ± 538 for 773 K. The activation energy derived from these second-order rate constants is 14.7 ± 1.9 kcal (61.5 ± 7.9 kJ).

(5) Post-run Heatup Results

For several cases, following completion of $H_2O(g)$ evolution at the temperature of a run, the temperature was raised to about 923 K. The curve for the subsequent $H_2O(g)$ evolution under these conditions often showed up to three peaks. The relative heights of these peaks were variable. A detailed interpretation of them has not been made yet. However, their occurrence is consistent with the Freundlich view that the adsorption process involves sites of different properties and energies.

c. Discussion and Conclusions

The choice of increments of mole fraction hydroxide needed to correct the raw data for residual hydroxide to give slopes of 0.4 or 0.5 for the $\log(x_{OH})$ vs. $\log(p_{H_2O})$ curves was based on the following considerations. First, in heating the sample under a constant low partial pressure of $H_2O(g)$, the baseline helium flow conditions, evolution of $H_2O(g)$ was observed. On cooling, uptake of $H_2O(g)$ was observed. This is a direct observation that, under conditions of constant partial pressure of $H_2O(g)$, the overall adsorption/solubility decreases as temperature rises. The overall process is, therefore, exothermic. (Endothermic behavior for solubility was observed for Li_2O by Tetenbaum et al.[89] and by Norman and Hightower.[90]) If the solubility data points had been adjusted so that both isotherms had slopes of either 0.4 or 0.5, the isotherms would have been essentially identical. This would indicate that solubility is independent of temperature, which is not consistent with the observations made when the samples were heated. The assignment of slope to the isotherms was thus based on a comparison between (1) the observed difference in evolved H_2O on heating to 939 K from 673 and from 773 K and (2) the difference between the total moles of H_2O equivalent to the increments of hydroxide required to produce the 0.4 and 0.5 slopes for the two temperatures. Within experimental error, the slope assignment of 0.4 to the 673 K isotherm and 0.5 to the 773 K isotherm was consistent with the difference in water evolved in the heating from these temperatures to 939 K.

For the $H_2O(g)$ partial pressure range of these measurements, comparison of the slopes of the solubility curves suggests that $LiAl_5O_8$ is soluble in $LiAlO_2$ at 673 K but not at 773 K, an example of retrograde solubility. In terms of the ternary phase diagram for the $LiAlO_2$-LiOH-$LiAl_5O_8$ system, the relevant portion is a minute region around the $LiAlO_2$ corner. In general, one would expect a single-phase region of solubility at the corner. Adjacent to it, there would be two-phase regions, one involving LiOH as a second phase, and one involving $LiAl_5O_8$ as a second phase. The latter is the one under consideration. The p_{H_2O} values in the measurements are below the values that would be required for a LiOH phase to exist, namely, 30 Pa at 673 K and 376 Pa at 773 K.[91] Also, the two temperatures, 673 and 773 K, bracket the melting point of LiOH, 744 K. It is possible that the behavior of OH^- would be different below and above this temperature. If so, then isotherms for both adsorption and solubility would reflect different processes. It becomes necessary, therefore, to measure additional, more closely spaced isotherms to separate the effects clearly.

To provide a benchmark for reactor blanket conditions, the solubility of tritium as tritons in the form of tritoxide is: ppmW T = $4.5 \times 10^4 x_{OH}$ (assuming no isotope effect). Extrapolation to 1 ppmV $H_2O(g)$ in the sweep gas at 10^5 Pa total pressure gives 0.39 and 0.18 ppmW T in $LiAlO_2$ at 673 and 773 K, respectively. For the Li_2O system, the hydroxide activity coefficients in the present p_{H_2O} range are 3.2×10^5 and 3.0×10^4 for 673 and 773 K, respectively.[89] The ratio of hydroxide activity coefficient in Li_2O to that in $LiAlO_2$ is about 23 and 7 for 673 and 773 K, respectively. Nonideal behavior appears to be stronger in Li_2O than in $LiAlO_2$.

Freundlich adsorption isotherms are generally indicative of surface heterogeneity, such as the presence of more than one kind of surface site for adsorption.[92] This heterogeneity arises from differences among O^{2-}, Li^+, and Al^{3+} sites as well as from dislocations, ledges, etc., on the surface. Different energies of adsorption are expected from such chemical and physical differences. Different kinds of sites can dominate in different measurements involving different ranges of surface coverage. Evidence for this was found in the heatings that were performed after some of the runs.

Although the hydroxide solubility for a given water partial pressure appears to decrease at higher temperature, the fractional surface coverage between 673 and 773 K appears to increase. However, preliminary results from a few measurements at 873 K indicate that the degree of surface adsorption decreases at this higher temperature. Low temperature chemisorption that becomes reversed at higher temperature is one way to understand the results. Without more closely spaced isotherms, it is impossible to determine at which temperature the maximum adsorption occurs. It is, therefore, premature to attempt calculations of heats of adsorption.

If the equations for θ are nevertheless extrapolated to a p_{H_2O} value corresponding to a condition of 1 ppmV $H_2O(g)$ in a sweep gas of 10^5 Pa total pressure, then $\theta = 0.0082$ and 0.025 for 673 and 773 K, respectively. Reactor blanket conditions might fall into such a range.

Adherence to a rate equation that is second order in the hydroxide content of the system is consistent with a rate-determining bimolecular process. This process is taken to be the combination of two surface OH^- groups to split out a molecule of $H_2O(g)$ with an activation energy of 14.7 kcal (61.5 kJ). (An intervening, but faster, desorption step, $H_2O(ads) \rightarrow H_2O(g)$, is possible.) For a system containing small amounts of tritium and relatively large amounts of protium, as in a reactor, the kinetic behavior would be pseudo-first order in tritoxide. A report by Kudo[93] on the kinetics of thermal decomposition of LiOH [$H_2O(g)$ evolution] indicated that the rate-limiting step follows first-order kinetics and that the activation energy is 29.5 ± 1.1 kcal (123.4 ± 4.6 kJ). Kudo suggested that desorption of H_2O molecules was the first-order rate-limiting step in that system. An alternative view is that the first-order rate-limiting step is proton diffusion through the bulk to the surface.

Removal of H_2O from LiOH results in a two-phase system of LiOH-Li_2O. If the main processes to consider for the surface are desorption from the surface and surface combination of OH^-, then a comparison of the present results for $LiAlO_2$ with those of Kudo for LiOH-Li_2O suggests some

differences for the two systems. Because the slow step on $LiAlO_2$ is bimolecular combination of OH^-, it appears that unimolecular desorption is faster than combination of OH^- groups on $LiAlO_2$. For $LiOH$-Li_2O, the reverse relationship between the two processes is suggested by Kudo's results. Furthermore, the overall evolution process is easier from $LiAlO_2$ because the activation energy is lower. Kudo et al. also reported that the evolution of HTO from neutron irradiated Li_2O followed first-order kinetics with an activation energy of 18.8 ± 1.3 kcal (78.7 ± 5.4 kJ).[94] A conclusive explanation for the difference in his values was not given. However, the activation energy for $H_2O(g)$ release from $LiAlO_2$ for the present work is lower than either of the values for the Li_2O or LiOH systems. On this basis, tritium release from $LiAlO_2$ would be expected to be easier than from Li_2O.

2. Modeling of Tritium Transport in Ceramic Breeders (J. P. Kopasz)

The objective of this work is to develop a computer model that will predict tritium behavior in ceramic breeder materials. When complete, the model will enable one to compare the relative contributions of the different transport processes (such as bulk diffusion, grain boundary diffusion, desorption, permeation, and trapping) to the total tritium inventory and to the tritium release kinetics.

Until recently, the tritium release from ceramic breeder materials was interpreted as controlled by either diffusion[95-97] or desorption.[98,99] Models based on these processes were unable to satisfactorily account for much of the data obtained in tritium release experiments. In addition, the inappropriate use of the simple diffusional release model has resulted in a large variation in reported tritium diffusivities, especially for ceramics such as $LiAlO_2$. We have developed a diffusion-desorption model that is a significant improvement over previous models.

Our diffusion-desorption model leads to the following expression for the tritium flux (R_t) as a function of time for a spherical grain after a temperature change occurs:

$$R_t = \left(1 - \frac{3}{Ga} K_d C_1\right)\left[\frac{Ga}{3} - 2h^2 aG \sum_{n=1}^{\infty} \frac{\exp(-D\alpha_n^2 t)}{\alpha_n^2[a^2\alpha_n^2 + ah(ah-1)]}\right] + K_d C_1 \qquad \text{(I-68)}$$

where

G = generation rate/unit volume
a = grain radius
K_d = effective desorption rate constant
C_1 = concentration of tritium at the surface prior to the temperature change
D = tritium diffusivity
h = K_d/D
α_n = roots of $a\alpha \cot(a\alpha) = 1 - ah$

Using this equation and previously determined values, we calculated the in situ tritium release from a sample of Li_2SiO_3. As shown in Fig. I-23, the results are in good agreement with experimentally observed release for the

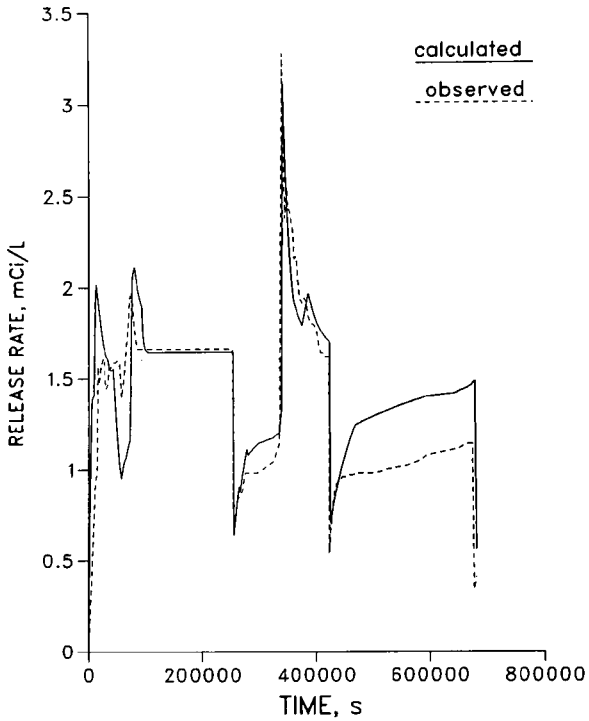

Fig. I-23.

Calculated and Observed Tritium Release from First Li_2SiO_3 Sample. Calculated curve obtained from diffusion-desorption model.

LISA experiment under conditions of pure helium purge gas.[100] Next, tritium release was calculated using both a pure-diffusion model and our diffusion-desorption model for a second Li_2SiO_3 sample from the LISA experiment. The diffusion model did a very poor job of predicting the observed tritium release behavior when the diffusion coefficients calculated by Werle et al.[100] were used. When the diffusion coefficients were optimized to fit the data, the fit was fair (Fig. I-24) but not as good as that for our diffusion-desorption model.

Predictions of the tritium release for two other samples of Li_2SiO_3 were calculated with the diffusion-desorption model and were also in good agreement with the experimental data. There were some regions in the observed tritium release profiles where the diffusion-desorption model did not accurately predict the tritium release. This indicates that the values used for the diffusivity and the desorption rate constant in the calculations may be in error, or that a third mechanism may be important in determining tritium release in these regions.

Work is in progress to develop a more-sophisticated model that will take into account other processes that affect tritium release besides diffusion and desorption. Processes under investigation include grain boundary diffusion, surface reactions, and permeation.

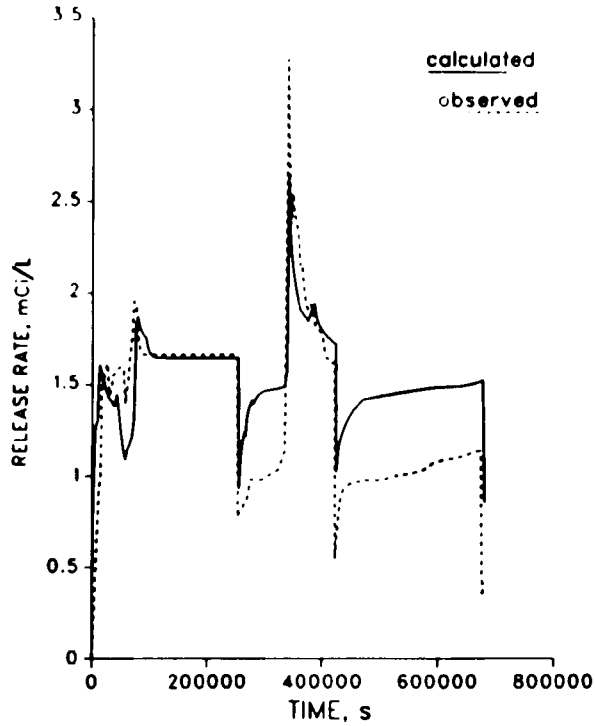

Fig. I-24.

Calculated and Observed Tritium Release from Second Li_2SiO_3 Sample. Calculated curve obtained from pure-diffusion model with optimized diffusional parameters.

3. Dosimetry and Damage Analysis

Fusion materials are being irradiated in a variety of facilities, including fission reactors, 14 MeV d-t neutron sources, and higher energy accelerator-based neutron sources. We are determining the neutron energy spectrum, flux levels, and damage parameters for the materials irradiated in these facilities, along with exposure parameters for each irradiation.

a. Cross-Section Measurements for Long-Lived Isotopes near 14 MeV (L. R. Greenwood and D. L. Bowers)

We are engaged in an effort to measure production cross sections near 14 MeV for long-lived radioisotopes in fusion reactor materials. We have previously published results for ^{26}Al, ^{55}Fe, ^{63}Ni, and ^{94}Nb.[101-108] These production rates are needed to determine the activity levels in fusion waste materials, and the data are also useful for dosimetry, plasma diagnostics, and reactor maintenance applications.

In the present case, results are reported for the measurement of ^{91}Nb, ^{93}Mo, and ^{93m}Nb. For these measurements, natural Mo and enriched ^{94}Mo samples were irradiated at the Rotating Target Neutron Source II to neutron fluences of 0.5-1.5 x 10^{18} n/cm^2. Details concerning fluences were published previously[101] along with our results for the $^{94}Mo(n,p)^{94}Nb$ (20,000 y) reaction since the same samples were used for both measurements.

After the irradiation samples were dissolved in a mixture of HCl and HNO_3. Small aliquots were then flame dried on tantalum discs and covered with a thin layer of tape for X-ray counting. The deposits generally

measured about 1 mg of Mo spread over an area of about 0.5 cm^2. In this way, self-absorption corrections were less than 1% for X-rays in the 15-19 keV region. Absolute calibration of the detector was determined with a ^{93m}Nb X-ray standard (NBS-SRM4267). The isotope ^{93m}Nb has a half-life of 16.1 ± 0.3 y, and the K X-ray (16.5-19.1 keV) intensity is 10.57 ± 0.54%. The half-life of ^{93}Mo is 3500 ± 700 y, and it has the same X-rays as ^{93m}Nb except that the intensity is 73.0 ± 2.7%. The isotope ^{91g}Nb decays with a lifetime of 680 ± 130 y and the K X-rays (15.7-18.1 keV) have an intensity of 63.6 ± 2.2%. All of the above decay data are taken from Ref. 107.

Since we irradiated both natural Mo and ^{94}Mo-enriched samples, measurements of the K X-ray activity can be used to determine the fraction of the activity in each sample which is due to either ^{92}Mo or ^{94}Mo. At the long decay times of our measurement (1090 d), there are no other known sources of Nb or Zr K X-rays from the other Mo isotopes, except for very long-lived isotopes such as ^{92}Nb (3.7×10^6y). Four samples were counted (two natural, two enriched), and a simultaneous fit to the data yielded the cross-section values listed in Table I-13. In the case of ^{92}Mo, the only known activity with X-rays in this energy region is ^{91g}Nb. The 62-day isomer of ^{91m}Nb has already decayed away in these samples. Moreover, ^{91g}Nb can be made by several reactions, primarily ^{92}Mo(n,2n)^{91}Mo, which rapidly decays to ^{91}Nb. Although there is an isomer in ^{91}Mo and in ^{91}Nb, all of these reaction products eventually decay to ^{91g}Nb; ^{91}Nb can also be made by the ^{92}Mo(n,d + np + pn) reactions. Hence, our cross-section value represents the net production of ^{91g}Nb from ^{92}Mo.

Table I-13. Results of Mo Cross-Section Measurements

Reaction	Energy,[a] MeV	σ,mb
^{92}Mo(n,2n)^{91g}Nb	14.7	603 ± 119[b]
^{94}Mo(n,x)^{93}Mo	14.7	<810[c]
^{94}Mo(n,x)^{93m}Nb	14.7	<26[d]

[a]Mean energy; width ~0.5 MeV.
[b]Uncertainty: stat. 1%, std. 2.4%, $T_{1/2}$ 19%, fluence 5%, net 20%.
[c]Uncertainty: stat. 1%, std. 2.4%, $T_{1/2}$ 20%, fluence 5%, net 21%.
[d]Uncertainty: stat. 1%, std. 2.4%, $T_{1/2}$ 2.2%, fluence 5%, net 6%.

In the case of ^{94}Mo, we can make ^{93}Mo from the (n,2n) reaction and ^{93m}Nb from the (n,d + np + pn) reactions. In addition, ^{93m}Nb can be made from the (n,t + nd + nnp) reactions on ^{95}Mo; however, ^{95}Mo is only 5.18% of the enriched sample and thus can only make a minor contribution (<1%). The situation is further complicated by the fact that ^{93}Mo decays to ^{93m}Nb. We plan to perform a radiochemical separation of Nb and Mo so that we can determine the cross sections for both species. However, at present, we can only

place limits on the cross sections for both reactions. The decay of ^{93}Mo to ^{93m}Nb is rather slow due to the long half-life of 3500 y, and we calculate that at least 2% of the present activity must be due to ^{93m}Nb. Hence, we can place upper limits on both cross sections, as is done in Table I-13. It is, however, most probable that we produced more ^{93}Mo than ^{93m}Nb during the irradiation, as discussed below.

There are no known previous measurements of the ^{94}Mo(n,2n)^{93g}Mo cross section. The cross section to the 6.9-h isomeric state of ^{93}Mo is reported to be 2.4-6.4 mb; however, the reaction proceeds mainly to the ground state of ^{93}Mo and the total cross section should be much larger. Haight et al.[108] have reported a value of 9 ± 3 mb for the ^{94}Mo(n,d) cross section. This is consistent with our results; however, our measurements also include other possible reaction channels, such as ^{94}Mo(n,np + pn).

We have used the THRESH2 semiempirical computer code[109] to estimate the strength of various reaction cross sections in order to gain some insight concerning the relative importance of unobserved reactions. These calculations predict a relatively flat energy dependence near 14 MeV for the ^{94}Mo(n,2n) reaction with a cross section of about 1 barn. This calculation is close to our maximum value of 810 mb. In addition, THRESH2 predicts that the ^{94}Mo production cross section for ^{93m}Nb is 51 mb, and that the (n,np + pn) cross sections are about equal to the (n,d) value. However, these reaction cross sections steeply rise near 14 MeV. If the ratio of the production cross sections from THRESH2 for ^{93}Mo/^{93m}Nb is roughly correct, then we estimate that the ^{94}Mo(n,2n)^{93}Mo cross section is about 280 mb and that the ^{94}Mo(n,x)^{93m}Nb cross section is about 17 mb. This latter value agrees with the (n,d) measurement of Haight et al.,[108] assuming equal strength for the (n,np + pn) reactions.

There have been several measurements of the ^{92}Mo(n,2n)^{91}Mo reaction to both the ground and isomeric states. Unlike the ^{94}Mo(n,2n) reactions, the ^{92}Mo(n,2n) cross section steeply rises with energy near 14 MeV. Hence, some care must be taken in comparisons with our data since our energy resolution is about 0.4 MeV. Previous measurements give a value of about 200-250 mb in our energy region of 14.5-14.9 MeV. However, our measurements also include the production of ^{91g}Nb by the ^{92}Mo(n,d, + np + pn) reactions. Haight et al.[108] measured 22 ± 7 mb for the (n,d) reaction at 14.8 MeV. Using the THRESH2 computer code, we estimated that the (n,pn + np) reaction cross sections sum to about 70 mb. Thus, the total production cross section of ^{91g}Nb should be about 300 mb, much less than our measurement of 603 mb.

There are several possible explanations for the discrepancy between our measurements and previous data for the production of ^{91g}Nb from ^{92}Mo. Since our measurement is based on the strength of the Zr and K X-rays, it is possible that there are other contributing isotopes. However, because of the long decay time before analysis (1090 d), we are unable to identify any known interferences from other Mo isotopes or impurities in the material. It may also be that the unobserved ^{92}Mo(n,np + pn) reactions have a much larger cross section than predicted by THRESH2; however, this seems highly unlikely since we expect these reactions to be much weaker than the (n,2n) reaction. A more likely explanation is that our measurements could be reconciled with previous data if the half-life of ^{91}Nb were reduced to about 350 y. The present value of 680 ± 130 y has a rather large uncertainty (19%). Further measurements are needed to resolve this issue.

The present measurements can be used to calculate the production of these radioisotopes in a fusion reactor. Using the STARFIRE reactor design with a lifetime first-wall irradiation of 21.6 $MW \cdot y/m^2$ and 3000 d cooling, we calculate that Mo would produce 243 mCi/cm^3 of ^{91}Nb, <41 mCi/cm^3 of ^{93}Mo, and <140 mCi/cm^3 of ^{93m}Nb.

b. Dosimetry and Damage Calculations for the U.S./Japanese Experiments in HFIR
(L. R. Greenwood and C. A. Seils)

Results are reported for the JP4, JP5, and JP8 U.S./Japanese experiments in the High Flux Isotopes Reactor (HFIR) at Oak Ridge National Laboratory. These three irradiations were conducted in the target position as follows:

Experiment	Dates	Exposure
JP4	05/01/84-04/18/86	57,909 MWD*
JP5	09/11/84-08/12/86	58,217 MWD
JP8	10/05/84-09/07/86	58,214 MWD

Results for the JP1 and JP3 irradiations[110] and the JP2, JP6, and JP7 irradiations[111] were reported previously.

Dosimeters were located at three vertical positions in JP4 and JP8 and at six positions in JP5. The lowest dosimeter from JP5 was damaged during disassembly. All remaining eleven aluminum capsules measured about 0.25-in. (0.64-cm) long by 0.05-in. (0.13-cm) OD and contained small wires of 0.1% Co-Al, Fe, 80.2% Mn-Cu, and Ti. The Ti samples were totally destroyed in runs JP5 and JP8, presumably due to reactions with gaseous impurities in the helium cover gas. However, the Ti samples from JP4 were all recovered and showed no discoloration. This difference is probably due to the fact that the specimens were irradiated at 55°C for JP4 but 300-600°C for JP5 and JP8. The Ti could thus be reacting with H, O, or N outgassed from the assemblies.

All of the dosimeters were gamma counted and the corrected activities are listed in Table I-14. Close comparisons of the data from each run show only small (1-3%) differences. All of the data are well described by a simple polynomial:

$$f(z) = f(o)\ (1 + bz + cz^2) \qquad \text{(I-69)}$$

where z is the height in centimeters. For the thermal reactions, b~0 and $c = -8.71 \times 10^{-4}$, and for the three fast reactions $b = 7.42 \times 10^{-4}$ and $c = -9.80 \times 10^{-4}$.

*MWD = megawatt days.

Table I-14. Measured Activities for HFIR-JP4, JP5, and JP8 (Activities in atom/atom-sec at 100 MW; ±3%)

	$^{59}Co(n,\gamma)^{60}Co$			$^{58}Fe(n,\gamma)^{59}Fe$		
	($\times10^{-8}$)			($\times10^{-9}$)		
Height, cm	JP4	JP5	JP8	JP4	JP5	JP8
25.4	-	3.65	-	-	1.23	-
17.1	5.29	-	-	1.72	-	-
16.5	-	5.31	5.58	-	1.75	1.85
7.1	-	6.19	-	-	-	-
2.1	6.31	6.37	6.29	2.33	2.33	2.40
-12.1	-	5.56	-	-	1.96	-
-19.3	4.69	-	-	1.55	-	-
-21.0	-	-	4.38	-	-	1.40

	$^{54}Fe(n,p)^{54}Mn$			$^{46}Ti(n,p)^{46}Sc$	$^{55}Mn(n,2n)^{54}Mn$		
	($\times10^{-11}$)			($\times10^{-12}$)	($\times10^{-14}$)		
Height, cm	JP4	JP5	JP8	JP4	JP4	JP5	JP8
25.4	-	2.75	-	-	-	7.91	-
17.1	5.07	-	-	7.34	1.55	-	-
16.5	-	5.21	5.47	-	-	1.66	1.61
7.1	-	-	-	-	-	1.99	-
2.1	6.95	7.39	6.76	9.84	1.98	2.08	1.92
-12.1	-	5.88	-	-	-	1.85	-
-19.3	4.59	-	-	6.14	1.39	-	-
-21.0	-	-	3.84	-	-	-	1.12

Since the three runs have the same exposure within ±0.3%, and the activities at each position agree within ±3%, we decided to report all three runs jointly, with identical neutron fluence and damage parameters.

The neutron energy spectra were determined with the STAY'SL computer code using midplane activities determined from a global fit to the data in Table I-14 and Eq. I-69. The spectral adjustments were small (~10%), and the spectrum is quite similar to previous results.[110,111] The resultant neutron fluences are given in Table I-15.

Damage parameters were calculated with the SPECTER computer code,[112] and displacements-per-atom (dpa) and amount of helium (atom parts per million) are reported in Table I-16. Thermal effects are included for Ni and Cu, as discussed in recent publications.[113,114] It should be noted that the recently discovered thermal helium effect in copper produced 9.4 times more helium than expected from fast neutron reactions. For Ni, these irradiations produced about 0.25 at. % helium or 3313 appm in 316 stainless steel. The nonlinear gradients for stainless steel are listed in Table I-17. Gradients

Table I-15. Neutron Fluence for HFIR-JP4, JP5, and JP8

Energy	Neutron Fluence, 10^{22} n/cm^2
Total	24.45
Thermal (<0.5eV)[a]	10.00
0.5 eV-0.1 MeV	7.82
>0.1 MeV	6.63
>1 MeV	3.36

[a]Total neutrons <0.5 eV; for 2200 m/s value multiply by 0.886.

Table I-16. Damage Parameters for HFIR-JP4, JP5, and JP8 (Values at Midplane; for Gradients use Eq. I-69)

Element		dpa	He, appm
Al		86.3	41.8
Ti		54.8	28.0
V		61.4	1.41
Cr		54.1	9.60
Mn[a]		59.5	8.46
Fe		47.9	17.1
Co[a]		60.0	8.38
Ni	Fast	51.5	226.2
	^{59}Ni	44.4	25,160.0
	Total	95.9	25,386.0
Cu[b]	Fast	46.7	12.4
	^{65}Zn	0.2	116.6
	Total	46.9	129.0
Nb		46.3	3.12
Mo		34.5	-
316 SS[c]		55.2	3313.0

[a]Thermal neutron self-shielding may reduce dpa value.

[b]Cu values reported in Ref. 114.

[c]316 SS: Fe(0.645), Ni(0.13), Cr(0.18), Mn(0.019), Mo(0.026).

Table I-17. Damage Gradients for 316 Stainless Steel in HFIR-JP4, JP5, and JP8

Height, cm	He,[a] appm	dpa[b]
0	3313	55.2
3	3285	54.7
6	3198	53.2
9	3053	50.7
12	2844	47.2
15	2566	42.7
18	2218	37.2
21	1791	30.7
24	1277	23.1

[a]Includes ^{59}Ni and fast reactions.
[b]Includes thermal effect from ^{59}Ni.

for all other damage parameters (except helium in copper) can be obtained using Eq. I-69 and the midplane values in Table I-16. All of these results are nearly identical to those reported previously for the JP2 experiment.[111]

c. Enhanced Helium Production in Ferritic Materials
(L. R. Greenwood and D. G. Graczyk)

High-purity (99.99%) iron samples were irradiated at three locations in three separate fusion materials experiments in the Peripheral Target Position of HFIR. These nine iron samples were used for both activation (Argonne) and helium measurements (Rockwell International). Other radiometric dosimeters were also included, and the activation measurements were used to determine the neutron energy spectra by spectral adjustment procedures.[115] The iron helium measurements have been reported previously[116] along with results for other elements, and details of the procedures are reported in that work.

The neutron fluences and measured helium levels are listed in columns 1 and 2 of Table I-18. Helium production from fast neutrons (column 3 of Table I-18) can be readily calculated from the adjusted neutron energy spectra by using the evaluated helium cross sections given in the ENDF/B-V Gas Production File.[117] Comparison of the measured and calculated helium indicated a systematic trend with increased neutron exposure, as shown in Table I-18 (column 4) and Fig. I-25 (circles).

The rate of helium production from fast neutrons will change during the course of irradiation due to transmutation of the iron isotopes. We have used two techniques to measure the various iron isotopes in the

Table I-18. Helium Measurements and Fast Neutron Calculations for Iron

Total Fluence, 10^{26} n/m^2	Measured He, appm	ENDF[a] He, appm	C/E[b]	THRESH2[c] He, appm	C/E[b]
3.48	2.24	3.38	1.06	2.48	1.11
4.60	2.99	3.14	1.05	3.31	1.11
4.81	3.12	3.25	1.04	3.47	1.11
5.57	3.66	3.68	1.01	4.04	1.10
8.30	5.73	5.64	0.98	6.14	1.07
9.67	6.76	6.39	0.95	7.22	1.07
11.05	8.17	7.64	0.94	8.33	1.02
16.45	12.36	10.99	0.89	12.81	1.04
19.16	14.69	12.95	0.88	15.13	1.03

[a]Fast helium from ENDF/B-V Gas File 533[112] and natural iron.

[b]Calculated-to-experimental helium ratio.

[c]Fast helium using THRESH2[109] and ratios of transmuted iron isotopes.

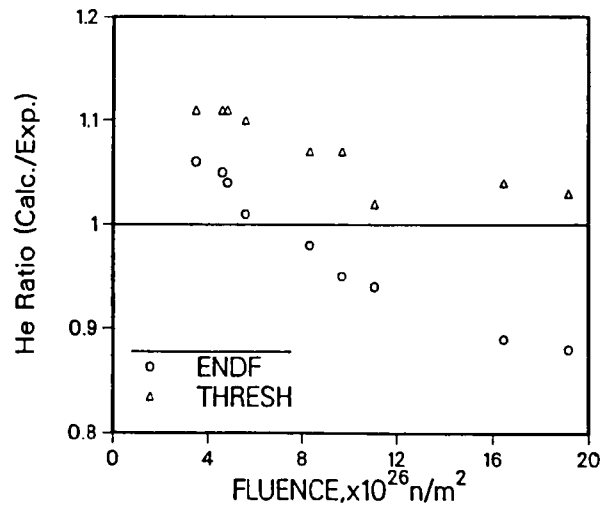

Fig. I-25. Ratio of Calculated-to-Experimental Helium Production for Iron Samples in HFIR as Function of Total Neutron Fluence. Calculations are compared for ENDF/B-V (no transmutation) and THRESH2 (with calculated isotopic transmutation).

irradiated samples. Thermal ionization mass spectrometry was performed on three samples to measure the ratios of all iron isotopes, and the results are given in Tables I-19 and I-20. In addition ^{55}Fe was measured by liquid scintillation spectrometry,[118] and those results are given in Table I-20. Both types of analyses were performed using dissolutions of the same three samples, and chemical separations were performed to remove the possibility of interferences. Since ^{55}Fe decays to ^{55}Mn and Mn is more volatile than Fe in the

Table I-19. Iron Isotopic Mass Spectrometry Measurements[a] (calculations based on ENDF/B-V[119])

Thermal Fluence, 10^{26} n/m^2	Isotope Atomic Percent							
	^{54}Fe		^{56}Fe		^{57}Fe		^{58}Fe	
	Exp.	Calc.	Exp.	Calc.	Exp.	Calc.	Exp.	Calc.
6.37	5.02	5.02	78.36	77.81	14.84	15.02	1.28	1.68
3.48	5.33	5.35	83.54	83.80	10.12	9.74	0.70	0.80
3.21	5.41	5.39	84.83	84.37	8.86	9.22	0.59	0.74
Mean(C/E)		0.999		0.997		1.003		1.23

[a]Relative uncertainties: ^{54}Fe, 0.4%; ^{56}Fe, 0.07%; ^{57}Fe, 0.3%; ^{58}Fe,1.2%.

Table I-20. ^{55}Fe Measurements and Total Absorption Cross Section

Thermal Fluence, 10^{26} n/m^2	^{55}Fe Atomic Percent			
	LIQS[a]	TIMS[b]	Calc.[c]	C/E[d]
6.37	0.460	0.451	0.463	1.02
3.48	0.317	0.323	0.309	0.97
3.21	0.314	0.302	0.313	1.02
			Mean = 1.00 ± 0.3	

[a]Liquid scintillation measurements (±5%).

[b]Thermal ionization mass spectrometry (±4%).

[c]^{55}Fe total absorption cross section = 13.2 b; ^{54}Fe capture cross section from ENDF/B-V (Ref. 119).

[d]Ratio of calc./exp. (average of LIQS and TIMS).

thermal ionization mass spectrometry technique, Fe-Mn separations were performed within a day of the measurements. All data in Tables I-19 and I-20 have been corrected for decay of ^{55}Fe since irradiation.

A computer program was developed to calculate the isotopic ratios and helium production in each sample. These calculations consider all contributing and competing reaction channels, including thermal (n,γ), total absorption, and (n,α) for ^{55}Fe. Thermal neutron cross sections were adopted from ENDF/B-V.[119] An epithermal neutron correction of about 7% was also made based on previous measurements of the neutron energy spectrum in HFIR.[115] In all subsequent discussion, references to thermal cross sections will be

understood to include this effect. The amount of ^{55}Fe in each sample depends on the production from ^{54}Fe, losses by radioactive decay, and the burnup of ^{55}Fe. The neutron fluence levels were taken from our radiometric dosimetry data, which included measurements of the $^{54}Fe(n,p)^{54}Mn$ and $^{58}Fe(n,\gamma)^{59}Fe$ reactions for each sample. As shown in Table I-19, the ^{54}Fe atomic fractions are very well fit by the data (C/E = 0.999 ± 0.004), thus confirming our calculation of the production of ^{55}Fe. The total thermal burnup cross section of ^{55}Fe can thus be determined since the decay rate is also well known (2.73 ± 0.03 y).[120] A total absorption cross section for ^{55}Fe of 13.2 ± 2.1 b provides an excellent fit to the ^{55}Fe data (C/E = 1.00 ± 0.03), as shown in Table I-20. The only previous estimate of this cross section gave a value less than 170 b.[121]

Our calculations for the higher mass isotopes of iron are also given in Table I-19. As can be seen, the agreement is quite good for ^{56}Fe and ^{57}Fe (C/E = 0.997 and 1.003, respectively); however, the calculations overpredict the amount of ^{58}Fe (C/E = 1.23). The thermal cross sections and resonance integrals from ENDF/B-V have uncertainties of about 5% for $^{54,56,58}Fe$ and 12% for ^{57}Fe. To fit our iron isotopic data for ^{58}Fe, it is necessary to lower the thermal neutron capture cross section for ^{57}Fe by about 20%--from 2.48 ± 0.30 b (ENDF/B-V)[119] to about 2.0 b.

Because calculations of helium production from fast neutrons using ENDF/B-V underpredicted the helium at high fluences, we completed a more detailed calculation with the above transmutation rates. Unfortunately, the energy-dependent helium cross section for each isotope is not well known. Cross sections were thus calculated for each iron isotope using the THRESH2 computer code.[109] The abundance-weighted results for iron appear to be in reasonable agreement with the cross section in the ENDF/B-V Gas Production File.[117] We also note that the iron isotopic helium cross sections are in reasonable agreement with our published results at 14 MeV. Helium calculations using THRESH2 cross sections and calculated transmutation rates of the iron isotopes are also given in Table I-18 (column 5) and shown in Fig. I-25 (triangles).

Although the isotopic helium calculations improve the fit to the data, there is still an increasing deviation with neutron exposure, as shown in Fig. I-25 and Table I-18 (column 6). Such a trend is similar to the situation with nickel and copper, where thermal neutrons produce a significant amount of helium from transmutants. Consequently, we investigated the thermal, two-step reaction $^{54}Fe(n,\gamma)^{55}Fe(n,\alpha)$. It is very unlikely that thermal neutron helium production could be significant for any other isotope in our samples. Thermal helium production is energetically allowed from ^{55}Fe, whose Q-value of +3.58 MeV is much larger than the other iron isotopes. We have also looked at impurities in the iron which might produce helium; however, the only known candidate, boron, is far too low (0.2 appb) in these samples to account for the helium excess.

As seen in Table I-18, at the lowest neutron fluences the calculations exceed the measurements. Hence, to examine any possible thermal effects, we first readjusted the fast neutron helium cross sections. Based on the data, the calculated fast helium should be reduced by a factor of at least 0.94 (ENDF) or 0.90 (THRESH) simply to fit the measurements at the lowest fluences. Data from iron measurements in other mixed-spectrum reactors at lower fluences give a C/E ratio of 0.92-1.01, and measurements in fast

reactors give a value of about 0.84. These differences are compatible with the estimated uncertainties of about 10% in the neutron spectral analyses; however, spectral differences between facilities may also be significant. In the present work, we have assumed that the fast helium production in HFIR must be reduced by a factor between 0.84 and 0.88.

The data in Table I-18 from the ENDF/B-V Gas Production File clearly indicate that the helium levels exceed the fast helium production from natural iron. If we instead use the isotopic values in THRESH2 for the transmuted iron isotopes, the fit is clearly improved and the difference or excess helium is cut about in half. We are thus faced with three possibilities. Firstly, the THRESH2 helium values with C/E of 1.08 (Table I-18, column 6) could be improved to 1.00 ± 0.04 if we reduce the fast helium cross sections by 0.92. It is further possible that by varying the isotopic fast (n,α) cross sections we could fit the data more precisely; however, we have not attempted to do this. In this case, there would be no effect from thermal neutrons. Secondly, the THRESH2 values may be entirely misleading and thus should be ignored. In this case, we should use the ENDF values for natural iron, and the entire helium excess is due to a thermal neutron effect from ^{55}Fe. Finally, it is possible that the THRESH2 values are about right. In this case, about half the excess is due to fast transmutation and half is due to thermal neutron effects from ^{55}Fe.

If we assume that the calculated helium excess is indeed due to thermal helium production from ^{55}Fe, then we can use the previously described computer code to determine the cross section. Unfortunately, we do not know exactly how to adjust the fast helium calculations. If we use the ENDF fast helium values, reduced by a factor of 0.84-0.88, and assume that the entire helium excess is due to thermal production from ^{55}Fe, then the cross section is 18 ± 3 mb. If we instead use the THRESH2 helium production, similarly reduced, then we deduce that the thermal helium production cross section is 9 ± 4 mb. The uncertainties are determined from the uncertainties in the helium measurements (1%), neutron fluences (5%), and a sensitivity analysis of the uncertainties in the other parameters. Both cases are illustrated in Fig. I-26.

Simulations of fusion reactor damage and gas production in fission reactor irradiations are not generally possible, since the low helium rates do not produce the correct helium-to-dpa ratios. This problem has been solved for nickel-bearing materials by using the thermal helium production from ^{59}Ni. However, this solution cannot be applied to ferritic alloys, and thus fusion simulations are more difficult.

Based on the present work, increased helium-to-displacement ratios can be readily achieved in iron or ferritic alloys irradiated in mixed-spectrum reactors by isotopic tailoring. If the observed helium excess is due to thermal neutron production from ^{55}Fe, then iron enriched in ^{54}Fe would increase the helium production from 10 appm to 30-60 appm for a one year irradiation in HFIR, depending on the thermal cross section. If we further dope the sample with about 30-60% ^{55}Fe, we would produce about 300 appm helium, thereby achieving a fusion-like 10:1 helium-to-dpa ratio. It is also interesting to note that, with initial ^{55}Fe doping, the helium-to-dpa ratio for iron does not change very much with neutron fluence and, hence, is always close to the fusion ratio.

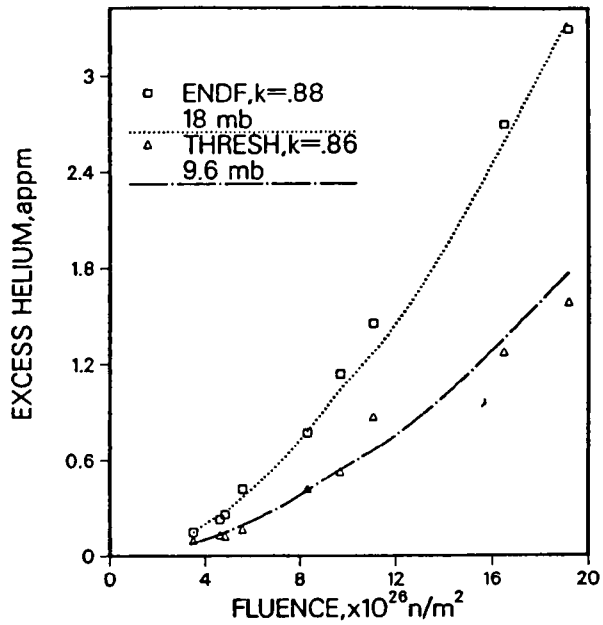

Fig. I-26. Excess Helium as Derived from Difference between Measurements and Fast Neutron Calculations with either ENDF/B-V or THRESH2. These differences are fit assuming thermal neutron helium production from ^{55}Fe with a cross section of about 18 mb (ENDF) or 9 mb (THRESH).

If no thermal effect is operative, then it would not be possible to achieve fusion-like helium-to-dpa ratios. Nevertheless, we note that there are large differences in the isotopic cross sections as predicted by THRESH2. Using samples enriched in ^{54}Fe or ^{57}Fe would increase the helium production by factors of two to three, respectively. Using ^{55}Fe would increase the helium production by a factor of six. This would be about a factor of five less than fusion; however, the variation might be enough to predict the influence of helium production on materials properties.

4. Tritium Oxidation Experiment
(P. A. Finn)

Tritium losses due to permeation from fusion breeder blanket systems can be severe. These permeation losses could be reduced if the tritium is retained in the oxidized (T_2O) rather than the reduced (T_2) form. We are undertaking a series of experiments to evaluate tritium oxidation as a means of converting the permeating tritium to tritiated water. The overall objective is to determine (1) if tritium permeating through a stainless steel component can be oxidized to tritiated water, (2) what conditions will optimize the yield of tritiated water, and (3) if competing reactions that use oxygen are important.

We are examining tritium oxidation in a double-walled tube made of stainless steel. A tritium/helium gas mixture is circulated through the inner tube, and an oxygen/helium gas mixture is circulated through the outer tube. An ethylene glycol trap collects the tritiated water formed by oxidation in the steel tube. The other reaction product, molecular tritium, is converted to tritiated water in a copper oxide bed and collected in another ethylene glycol trap. A metal oxide coating is produced on the steel surface in the course of an experiment.

The experimental parameters which we assumed to be important are oxygen concentration, temperature, presence of excess gaseous protium in the oxygen/helium gas, and tritium concentration. Four types of experiments were planned to study tritium oxidation. The first is a series of runs at <0.01 ppm oxygen and temperatures of 350-550°C. The second is a series of runs at 550°C with 15 ppm protium and an oxygen level up to ~1000 ppm. The third is a repeat of the second series but without the protium. The fourth is a series of runs in which temperature, tritium concentration, and oxygen concentration are randomly varied.

In the first series, the yield of tritiated water was <50%, ranging from 35.5% at 350°C to 41.9% at 550°C. At the low oxygen level used for these runs (<0.01 ppm), we expected competition between the oxidation of the stainless steel surface and the oxidation of the tritium. The respective free energies of formation of chromium oxide, iron oxide (FeO), and tritiated water for each mole of oxygen at 500°C are -920, -219, and -203 kJ/mol, respectively. Since the free energies of formation of iron oxide and tritiated water are similar, the reaction product could depend on the kinetics. For iron oxide, we calculated the need for oxygen assuming a metal oxide growth rate independent of the tritium present. Metal oxide growth could incorporate all the oxygen at a 10 ppm level. However, we found that up to 41.9% of the tritium was converted to tritiated water at <0.01 ppm oxygen. Therefore, tritium oxidation appears to be kinetically favored. Nevertheless, the water yield at this low oxygen level is not high enough to minimize permeation losses.

The second series of experiments consisted of runs at 10^{-3}, 40, and 912 ppm oxygen, all at 550°C with 15 ppm gaseous protium in the oxygen/helium gas. We hoped in this series to observe the combined effect of increased oxygen concentration and added protium on the tritiated water yield. We found a steady increase in the yield of tritiated water as we increased the oxygen level. The yield of tritiated water to molecular tritium was 52% at 10^{-3} ppm oxygen, 70.6% at 40 ppm, and 97.2% at 912 ppm. The maximum yield was 97.2% at 912 ppm oxygen.

The third series of experiments consisted of runs done at 550°C and oxygen levels in the range 10^{-3} to 2000 ppm (no protium). The yield of tritiated water increased from 52% to 98% with oxygen concentration. This represents an increase in the completeness of oxidation from 52% to 98%. The yield of 98% oxidation is the maximum that we have observed. The combination of the 98% oxidation and a factor of ~700 reduction in the tritium permeation due to the formation of an oxide film on the back surface of the stainless steel tube reduced the tritium partial pressure in the annulus of the double-wall tube to acceptable levels (<10^{-5} Pa). Preliminary analysis of the data indicated (Fig. I-27) that there are two distinct breaks in the plot of the

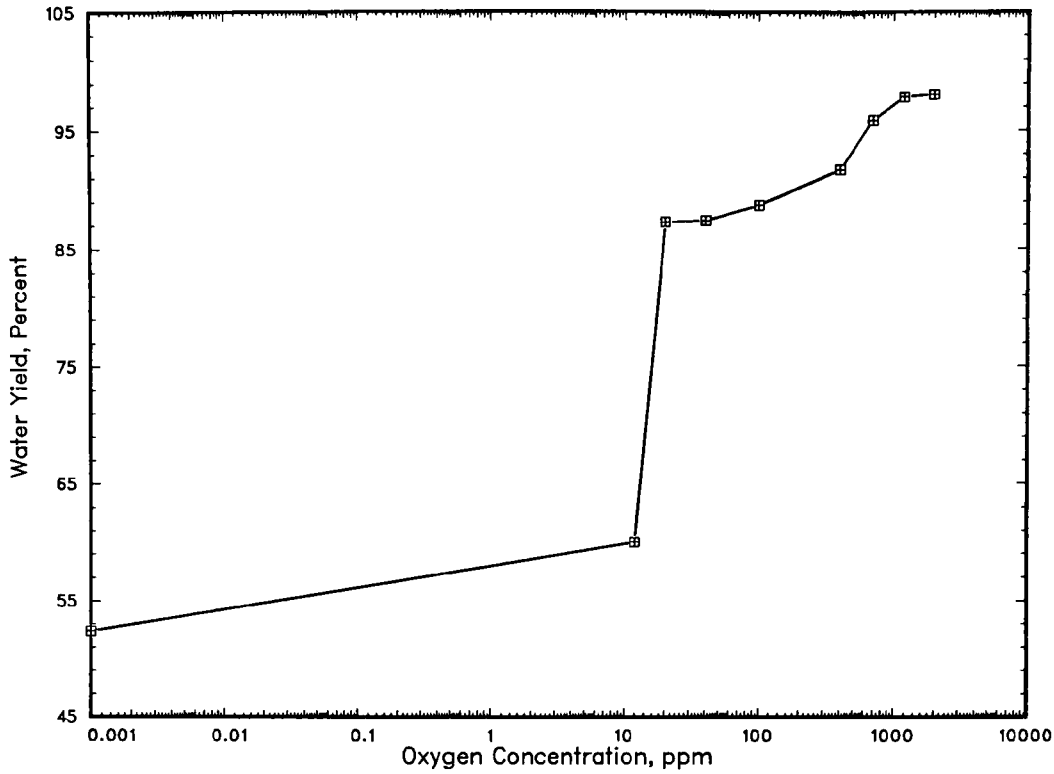

Fig. I-27. Yield of Tritiated Water as Function of Oxygen Concentration for Test Series Three (550°C, no protium)

amount of tritiated water formed versus oxygen concentration. These breaks occur at 20 and 400 ppm oxygen. The mechanism behind these shifts in yield with oxygen concentration is under investigation.

To determine the reproducibility of our results, we repeated the runs at oxygen concentrations of 10^{-3} ppm and 1200-2000 ppm. These results showed good agreement with our earlier ones. We noted a subtle effect when we did these runs. When we decreased the oxygen level from 2000 to 10^{-3} ppm, the tritium permeation rate increased from 0.08 to 0.10 μCi/min. When we increased the oxygen level to 1200 ppm, the permeation rate returned to a low permeation rate, 0.07 μCi/min. The initial increase in the permeation rate is probably due to a partial reduction of the oxide layer, producing a thinner oxide film. The later decrease in the permeation rate is due to the growth of a thicker oxide film on the stainless steel. These results seem to indicate that if one reduces and then reoxidizes the metal oxide, the ratio of tritiated water to molecular tritium can be reestablished.

Comparing the results from the second and third series at 40 ppm oxygen showed that the excess protium in the oxygen gas reduced the oxidation yield from 87.3% to 70.6%. The cause of this reduction in the yield is not

known. Two different possible mechanisms are (1) the occupation of active sites for oxygen adsorption by the protium species, thus reducing the availability of oxygen and (2) reduction of the iron oxide at the surface.

In the next quarter, we will examine the effect of temperature on tritium oxidation so that an energy of activation can be derived. We also plan to do destructive analysis of a test cell.

REFERENCES

1. M. F. Osborne, J. L. Collins, and R. A. Lorenz, Nucl. Tech. 78, 157 (1987).

2. Nuclear Regulatory Commission, Technical Basis for Estimating Fission Product Behavior During LWR Accidents, NUREG-0772 (June 1981).

3. J. Berkowits, J. Chem. Phys. 50, 3503 (1969).

4. J. Schreibmaier, V. Matschoss, H. Albrecht, and A. Mack, Herstellung von Erubrennstoff und Simulietern Abbrand (Fissium) an de Anlage FIFA, Kernforschungszentrum Karlsruhe, KfK 2991 (June 1980).

5. T. M. Besman, SOLGASMIX-PV, a Computer Program to Calculate Equilibrium Relationships in Complex Chemical Systems, Oak Ridge National Laboratory Report ORNL-TM-5775 (1977).

6. G. Eriksson, Acta. Chem. Scand. 25 2651 (1971).

7. G. W. Parker et al., Fission Gas Release from Reactor Grade UO_2 by Oxidation, Diffusion, and Melting, Oak Ridge National Laboratory Report ORNL-31/b (1961).

8. I. Johnson, C. E. Johnson, M. Farahat, and J. Settle, "Downstream Behavior of Fission Products," Proc. of Symp. on Chemical Phenomena Associated with Radioactive Releases During Severe Nuclear Accidents, Anaheim, CA, September 8-12, 1986, pp. 3-53.

9. P. A. Akishin, L. N. Gorokhov, and L. N. Sidorov, Doklady Akademii Nauk (SSSR) 135, 113 (1960).

10. K. Matsumoto, N. Kiba, and T. Takenchi, Talanta 22, 695-697 (1975).

11. P. Winchell, Nature 206, 1252 (1965).

12. V. Venugal, R. Prasad, and D. D. Sood, J. Nucl. Mater. 130, 115 (1985).

13. I. Barin and O. Knacke, Thermochemical Properties of Inorganic Substances, Springer-Verlag, Berlin, p. 254 (1977).

14. JANAF Thermochemical Tables, 1974 Supplement, J. Phys. Chem. Ref. Data 3, 311 (1974).

15. R. C. Schoonmaker and R. F. Porter, J. Chem. Phys. 30, 283 (1959); R. F. Porter and R. C. Schoonmaker, J. Phys. 62, 234 (1958).

16. L. Lelik, G. Sajo', K. Vass-Balthazar, and O. Kaposi, Acta Chim. Hung. 113, 61 (1983).

17. R. D. Freeman and J. G. Edwards, "Transmission Probabilities and Recoil Force Correction Factors for Conical Orifices," in The Characterization of High Temperature Vapors, J. L. Margrave, ed., John Wiley & Sons, New York, p. 508 (1967).

18. I. Johnson, Argonne National Laboratory, private communication (March 1987).

19. D. D. Wagman et al., "Compounds of Uranium, Protactinium, Thorium, Actinium, and the Alkali Metals," in Selected Values of Chemical Thermodynamic Properties, NBS Technical Note 270-8 (May 1981).

20. C. E. Kaylor, G. E. Walden, and D. F. Smith, J. Phys. Chem. 64, 276-278 (1960).

21. D. R. Stull and H. Prophet, JANAF Thermochemical Tables, Second Ed., National Bureau of Standards Report NSRD-NBS37, Washington, DC (June 1971).

22. D. O. Welch et al., J. Chem. Phys. 64, 835-839 (1976).

23. J. R. Rusk and W. Gordy, Phys. Rev. 127, 817-830 (1961).

24. J. C. Cummings, R. M. Elrich, and R. A. Sallach, Status Report on the Fission-Product Research Program, Sandia National Laboratories Report NUREG/CR-1820, SAND80-2662 R3 (March 1982).

25. J. Lumsden, Thermodynamics of Molten Salt Mixtures, Academic Press, New York, p. 149 (1966).

26. J. J. Van Laar, Z. Phys. Chem. 63, 216; 64, 257 (1908).

27. C. W. Bale, A. D. Pelton, and W. T. Thompson, F*A*C*T Users Instruction Manual, McGill University/Ecole Polytechnique, Montreal (1979-84).

28. P. J. Spencer and I. Barin, Mater. Eng. Appl. 1, 167 (1979).

29. I. Ansara, Int. Met. Rev., Review 238, No. 1, p. 20 (1979).

30. A. D. Pelton, Chapt. 7 in Physical Metallurgy, Third Ed., R. W. Cahn and P. Haasen, eds., North-Holland, New York (1984).

31. F. L. Oetting, M. H. Rand, and R. J. Ackermann, The Chemical Thermodynamics of Actinide Elements and Compounds - Part I, International Atomic Energy Agency, Vienna (1976).

32. H. P. Stephens, High Temp. Sci. 6, 156 (1974).

33. L. S. Levinson, J. Chem. Phys. 40, 3584 (1964).

34. H. Savage and R. D. Seibel, Heat Capacity Studies of Uranium and Uranium-Fissium Alloys, Argonne National Laboratory Report ANL-6702, (1963).

35. K. K. Kelley, U.S. Bur. Mines Bull., 584 (1960).

36. M. H. Rand and O. Kubaschewski, The Thermochemical Properties of Uranium Compounds, Oliver and Boyd, London (1963).

37. J. A. C. Marples, J. Less-Common Met. 2, 331 (1960).

38. A. A. Bochvar et al., Proc. U. N. Int. Conf. on Peaceful Uses of Atomic Energy, Geneva, Vol. 6, pp. 184-193 (1958).

39. J. M. Taylor, J. Nucl. Mater. 30, 346 (1969).

40. Reactor Fuels and Materials Development Plutonium Research: January-March 1966, Mound Laboratory Report MLM-1346 (1967).

41. F. A. Shunk, Constitution of Binary Alloys - Second Supplement, McGraw-Hill, New York (1969).

42. M. Hansen, Constitution of Binary Alloys, McGraw-Hill, New York (1958).

43. R. P. Elliott, Constitution of Binary Alloys - First Supplement, McGraw-Hill, New York (1965).

44. F. H. Ellinger, R. O. Elliott, and E. M. Cramer, J. Nucl. Mater. 3, 233 (1959).

45. Reactor Fuels and Materials Development Plutonium Research: 1966 Annual Report, Mound Laboratory Report MLM-1402 (1967).

46. S. Rosen, M.V. Nevitt, and J.J. Barker, J. Nucl. Mater. 9, 128 (1963).

47. P. Chiotti, V. V. Akhachinskij, I. Ansara, and M. H. Rand, The Chemical Thermodynamics of Actinide Elements and Compounds - Part 5, International Atomic Energy Agency, Vienna (1981).

48. A. D. Pelton, Ber. Bunsenges Phys. Chem. 84, 212 (1980).

49. D. Summers-Smith, J. Inst. Metals 83, 277 (1954-1955).

50. S. T. Zegler, The Uranium-Rich End of the Uranium-Zirconium System, Argonne National Laboratory Report ANL-6055 (1962).

51. F. Kohler, Monatsh. Chemie 91, 738 (1960).

52. D. R. Harbur, J. W. Anderson, and W. J. Mariman, Studies on the U-Pu-Zr Alloy System for Fast Breeder Reactor Applications, Los Alamos National Laboratory Report LA-4512 (1970).

53. J. H. Kittel, J. E. Ayer, W. N. Beck, M. B. Brodsky, D. R. O'Boyle, S. T. Zegler, F. H. Ellinger, W. N. Miner, F. W. Schonfeld, and R. D. Nelson, Nucl. Eng. 15, 373 (1971).

54. D. R. O'Boyle and A. E. Dwight, "The Uranium-Plutonium-Zirconium Ternary Alloy System," in Nuclear Metallurgy, Vol. 17, Plutonium 1970 and Other Actinides, W. N. Miner, ed., p. 720 (1970).

55. R. I. Sheldon and D. E. Peterson, "The U-Zr (Uranium--Zirconium) System," to be published in Bull. Alloy Phase Diagrams.

56. B. R. Seidel, D. L. Porter, L. C. Walters, and G. L. Hofman, Am. Nucl. Soc., Int. Conf. on Reliable Fuels for Liquid Metal Reactors, pp. 2-107 to 2-121 (September 1986).

57. R. K. Steunenberg, R. D. Pierce, and L. Burris, "Pyrometallurgical and Pyrochemical Fuel Processing Methods," Progress in Nuclear Energy, Series III, Process Chemistry, Vol. 4, pp. 461-504, Pergamon Press, Oxford (1969).

58. P. Chiotti and S. J. S. Parry, Separation of Various Components from Uranium by Oxidation-Reduction Reactions in a Liquid KCl-LiCl/Zinc System, Ames Laboratory Report IS-286 (April 19, 1961).

59. R. K. Steunenberg, R. D. Pierce, and I. Johnson, "Status of the Salt Transport Process for Fast Breeder Reactor Fuels," Symp. on Reprocessing of Nuclear Fuels, P. Chiotti, ed., Nuclear Metallurgy, Vol. 15, Conf-690801, pp. 325-335 (August 1969).

60. J. B. Knighton, I. Johnson, and R. K. Steunenberg, "Uranium and Plutonium Purification by the Salt Transport Process," ibid., pp. 337-362.

61. L. Burris, R. K. Steunenberg, and W. E. Miller, "The Application of Electrorefining for Recovery and Purification of Fuel Discharged from the Integral Fast Reactor," AIChE Symp. Series, No. 254, Vol. 82, pp. 135-142 (1987).

62. L. J. Mullins and J. A. Leary, I&EC Process Design and Development, 4, 394-400 (1965).

63. G. Chauvin, H. Coriou, P. Jabot, and A. Laroche, J. Nucl. Mater. 11, 183-192 (1964).

64. I. Johnson, "Partition of Metals Between Liquid Metal Solutions and Fused Salts," in Application of Fundamental Thermodynamics to Metallurgical Processes, G. R. Fitterer, ed., Gordon and Breach, New York, pp. 153-196 (1967).

65. L. B. Pankratz, Thermodynamic Properties of Halides, Bulletin 674, U.S. Bureau of Mines (1984).

66. J. Fuger, V. B. Parker, W. N. Hubbard, and F. L. Oetting, "The Chemical Thermodynamics of Actinide Elements and Compounds," Part 8, The Actinide Halides, International Atomic Energy Agency, Vienna, p. 248 (1983).

67. P. Chiotti and E. R. Stevens, Trans. Met. Soc. AIME 233, 198-209 (1965).

68. I. Johnson, "Thermodynamics of Plutonium, Thorium, and Uranium Metallic Systems," in Compounds of Interest in Nuclear Reactor Technology, J. T. Waber and P. Chiotti, eds., IMD Special Report No. 13, AIME, pp. 171-192 (1964).

69. P. Chiotti, Bull. Alloy Phase Diagrams 1, 108-109 (1980).

70. L. S. Darkin, J. Am. Chem. Soc. 72, 2909 (1959).

71. C. B. Alcock and F. D. Richardson, Acta Met. 8, 882 (1960).

72. I. Johnson and H. M. Feder, "Thermodynamics of Binary Systems of Uranium with Zn, Cd, Ga, In, Tl, Sn, and Pb," in Thermodynamics of Nuclear Materials, International Atomic Energy Agency, Vienna, pp. 319-329 (1962).

73. J. B. Knighton and R. K. Steunenberg, Trans. Am. Nucl. Soc. 5, 460 (1962).

74. H. Moriyama, K. Yajima, N. Nunogane, T. Ohmura, K. Moritani, and J. Oishi, J. Nucl. Sci. Tech. 21, 949-958 (1984).

75. L. M. Ferris, J. C. Mailen, J. J. Lawrence, F. J. Smith, and E. D. Noguera, J. Inorg. Nucl. Chem. 32, 2019 (1970).

76. I. Johnson, "The Solubility of Uranium and Plutonium in Liquid Alloys," Symp. Reprocessing of Nuclear Fuels, P. Chiotti, ed., Nuclear Metallurgy, Vol. 15, Conf.-690801, pp. 547-575 (August 1969).

77. I. Johnson, J. Nucl. Mater. 51, 163-177 (1974).

78. W. J. Walsh et al., "Engineering Studies of Salt Transport Separations," in Chemical Engineering Division Semiannual Report, July-December 1966, Argonne National Laboratory Report ANL-7325, p. 26 (April 1967).

79. I. Johnson, M. G. Chasanov, and R. M. Yonco, Trans. Met. Soc. AIME 233, 1408-1414 (1965).

80. I. Johnson and H. M. Feder, Trans. Met. Soc. AIME 224, 468-473 (1962).

81. A. E. Martin, I. Johnson, and H. M. Feder, Trans. Met. Soc. AIME 221, 789-791 (1961).

82. A. K. Fischer, J. A. McDaniel, and C. E. Johnson, J. Nucl. Mater. 141-143, 344 (1986) and references therein.

83. J. R. Conder and C. L. Young, Physicochemical Measurement by Gas Chromatography, John Wiley & Sons, New York, pp. 6, 124, 354 (1979).

84. H. Yoshida, S. Konishi, H. Takeshita, T. Kurasawa, H. Watanabe, and Y. Naruse, J. Nucl. Mater. 122-123, 934 (1984).

85. J. H. DeBoer, J. M. H. Fortuin, B. C. Lippens, and W. H. Meijs, J. Catal. 2, 1 (1963).

86. T. Morimoto, M. Nagao, and J. Imai, Bull. Chem. Soc. Japan 44, 1282 (1971).

87. W. S. Millman, F. H. Van Cauwelaert, and W. K. Hall, J. Phys. Chem. 83, 2764 (1979).

88. M. Tetenbaum and C. E. Johnson, J. Nucl. Mater. 126, 25 (1984).

89. M. Tetenbaum, A. K. Fischer, and C. E. Johnson, Fusion Tech. 7, 53 (1985).

90. J. H. Norman and G. R. Hightower, J. Nucl. Mater. 122-123, 913 (1984).

91. M. Tetenbaum and C. E. Johnson, J. Nucl. Mater. 126, 25 (1984).

92. D. O. Hayward and B. M. W. Trapnell, Chemisorption, Butterworths, London, p. 174 (1964).

93. H. Kudo, J. Nucl. Mater. 87, 185 (1979).

94. H. Kudo, K. Tanaka, and H. Amano, J. Inorg. Nucl. Chem. 40, 363 (1978).

95. R. G. Clemmer et al., The TRIO Experiment, Argonne National Laboratory Report ANL-84-55 (1984).

96. K. Okuno and H. Kudo, J. Nucl. Mater. 138, 210 (1986).

97. T. Kurasawa, H. Watanabe, G. W. Hollenberg, Y. Ishi, A. Nishimira, H. Yoshida, Y. Naruse, M. Aizawa, H. Ohno, and S. Konishi, J. Nucl. Mater. 141-143, 265 (1986).

98. M. Dalle Donne, Fusion Tech. 9, 503 (1986).

99. T. Tanifuji, K. Noda, S. Nasu, and K. Uchida, J. Nucl. Mater. 95, 108 (1980).

100. H. Werle, J.J. Abassin, M. Briec, R. G. Clemmer, H. Elbel, H. F. Hafner, M. Mason, P. Sciers, and H. Wedemeyer, J. Nucl. Mater. 141-143, 321 (1986) and unpublished data.

101. L. R. Greenwood, D. G. Doran, and H. L. Heinisch, Phys. Rev. C 34, 76-80 (1987).

102. R. K. Smither and L. R. Greenwood, J. Nucl. Mater. 122, 1071-1077 (1984).

103. R. K. Smither and L. R. Greenwood, Damage Analysis and Fundamental Studies Progress Report, DOE/ER-0046/17, pp. 11-13 (1984).

104. L. R. Greenwood, Symp. on Effects of Rad. on Materials, Seattle, June 1986, ASTM-STP 956, in press.

105. R. K. Smither, L. R. Greenwood, and H. Hendel, Rev. Sci. Intrum. 56, 1078-1080 (1985).

106. L. R. Greenwood and D. L. Bowers, "SPECOMP Calculations of Radiation Damage in Compounds," Proc. Sixth ASTM-EURATOM Symp. on Reactor Dosimetry, Jackson, WY, June 1-5, 1987, in press.

107. E. Browne and R. B. Firestone, Table of Radioactive Isotopes, V. S. Shirley, ed., John Wiley, New York (1986).

108. R. C. Haight, S. M. Grimes, R. G. Johnson, and H. H. Barschall, Phys. Rev. C 23, 700 (1981).

109. S. Pearlstein, Nuclear Cross Sections for Technology, National Bureau of Standards Report NBS-SP425, p. 332 (1975).

110. L. R. Greenwood, Damage Analysis and Fundamental Studies, Quarterly Progress Report, DOE/ER/0046/24, pp. 5-9 (February 1986).

111. L. R. Greenwood, "Measurements for the JP2, JP6, and JP7 U.S./Japanese Experiments in HFIR," Second Fusion Reactor Materials Semi-Annual Progress Report, DOE/ER-00313/2, in press.

112. L. R. Greenwood and R. K. Smither, SPECTER: Neutron Damage Calculations for Materials Irradiations, Argonne National Laboratory Report ANL/FPP-TM-197 (January 1985).

113. L. R. Greenwood, D. W. Kneff, and R. P. Skowronski, J. Nucl. Mater. 122-123, 1002-1010 (1984).

114. D. W. Kneff, L. R. Greenwood, B. M. Oliver, R. P. Skowronski, and E. L. Callis, Rad. Effects 92-96, 553-556 (1986).

115. L. R. Greenwood, Damage Analysis and Fundamental Studies Quarterly Progress Report, DOE/ER-0046/21, p. 9 (May 1985).

116. D. W. Kneff, L. R. Greenwood, B. M. Oliver, and R. P. Skowronski, J. Nucl. Mater. 141-143, 824-828 (1986).

117. Evaluated Neutron Data File (ENDF), Gas Production File 533, Brookhaven National Laboratory (1979).

118. D. L. Bowers and L. R. Greenwood, "Analysis of Long-Lived Isotopes by Liquid Scintillation Spectrometry," to be published in J. Radioanalytical Chem.

119. S. F. Mughabghab, M. Divadeenam, and N. E. Holden, Neutron Cross Sections, Vol. I, Academic Press, New York (1981).

120. E. Brown and R. B. Firestone, Table of Radioactive Isotopes, V. S. Shirley, ed., John Wiley, New York (1986).

121. A. Anufriev, Proc. Fifth All-Union Conf. on Neutron Physics, September 15-19, 1980, Kiev, USSR.

II. SEPARATION SCIENCE AND TECHNOLOGY
(G. F. Vandegrift)

A. TRUEX Technology-Base Development

(G. F. Vandegrift, D. J. Chaiko, D. R. Fredrickson, J. M. Copple, R. A. Leonard, L. Reichley-Yinger, P.-K. Tse, J. R. Shinn,* J. Sedlet,** and J. E. Stangel***)

The primary objective of this program is to develop a data base and computer model so that the TRUEX solvent extraction process can be designed for a variety of user needs. The computer model developed from this generic solvent extraction information will allow calculations of flowsheets for a variety of feed compositions, process capacities, purity requirements for products, and information pertinent to equipment requirements. The Generic TRUEX Model will also allow estimates to be made of the cost of establishing a TRUEX solvent extraction process using centrifugal contactors for a specific waste stream at a specific facility. These costs can be used by DOE and management at that facility to decide between this and other options for handling specific waste streams. If the TRUEX option is chosen by the facility, we will be available on a consultation basis to help in bringing the process on line.

The secondary objective of this program is to have facilities and expertise available at ANL to demonstrate at a pilot-plant level the specific TRUEX process flowsheets for simulated or actual waste streams. This capability would be useful to DOE contractors for (1) assuring the operability of TRUEX process flowsheets for their specific needs, (2) providing a source of consultation on specific process problem areas, and (3) training personnel in using the process and the equipment.

Other tasks to be performed in FY 1988 are:

- develop an analytical method for CMPO/TBP analysis by supercritical fluid chromatography
- study the hydrolytic and radiolytic degradation of the TRUEX-NPH solvent and develop solvent clean-up procedures
- verify the data base and model by countercurrent experiments in centrifugal contactors
- design and fabricate a 16-stage mini contactor
- test the use of a remote-handled centrifugal contactor for shielded-cell or glove box facilities.

1. Model Development

a. Acid Extraction

As part of the generic TRUEX modeling effort, it was necessary to model HNO_3 extraction by TBP. The model is based on the formation of the

*Co-op student from University of Illinois, Champaign-Urbana, IL.

**Consultant.

***Co-op student from Georgia Institute of Technology.

organic phase species TBP•HNO_3, 2TBP•HNO_3, and TBP•2HNO_3, with the last species becoming important at aqueous nitric acid concentrations of 6M or greater. The model (described further in Ref. 1) works successfully at TBP concentrations of 5 to 100 vol % and was effective at predicting the extraction of HNO_3 from $HNO_3/NaNO_3$ and $HNO_3/LiNO_3$ solutions. Within the TBP concentration range of 5-30%, a single set of extraction constants was sufficient to fit available extraction data.

Although a number of models for the PUREX/HNO_3 system have been presented in the literature,[2-7] a model was needed that could predict the extraction behavior of HNO_3 in the presence of high concentrations of inextractable nitrate salts. Recently, a thermodynamic model of HNO_3 extraction by TBP was presented by Ly.[6] However, aqueous-phase activity coefficients were included in an empirical expression, which must be evaluated from experimental extraction data. Our extraction model utilizes thermodynamic data available in the literature.

b. Americium Extraction

Work on the modeling of americium extraction by the TRUEX solvents is continuing. Initial efforts have been focused on the extraction behavior of 0.25M CMPO in TCE. This system will be used to determine the organic phase speciation of CMPO-metal complexes important in Am^{3+} extraction by the TRUEX solvent.

From Karl-Fisher titration data, it appears that americium is extracted by CMPO as an anhydrous complex.[8] Accordingly, Am^{3+} extraction by CMPO can be described by

$$Am(H_2O)_9^{3+} + 3NO_3^- + 3\overline{CMPO} \xrightleftharpoons{K_o} \overline{Am(NO_3)_3\ (CMPO)_3} + 9H_2O \qquad \text{(II-1)}$$

If the distribution ratio of Am is defined as $D_{Am} = [\overline{Am}]/[Am]_{aq}$, and the activity coefficients of all aqueous Am species are assumed to be constant, D_{Am} (following Eq. II-1) is given by

$$D_{Am} = \frac{K_o\ [\overline{CMPO}]_f^3\ \{NO_3^-\}^3}{\left[1 + \beta_1 \frac{\{NO_3^-\}}{\{H_2O\}} + \beta_2 \frac{\{NO_3^-\}^2}{\{H_2O\}^2}\right] \{H_2O\}^9} \qquad \text{(II-2)}$$

The symbols { } and [ ] refer to activity and molar concentration, respectively, and β_1 and β_2 are constants. The concentration of the free CMPO, $[\overline{CMPO}]_f$, can be calculated from the acid extraction model.[1] The denominator of Eq. II-2 takes into account the aqueous phase complexation of Am^{3+} by NO_3^-, which forms an inner sphere complex.[9] Equation II-2 can be rearranged to the form of a polynomial to give

$$\frac{[\overline{CMPO}]_f^3 \{NO_3^-\}^3}{D_{Am} \{H_2O\}^9} = \frac{1}{K_o} + \frac{\beta_1}{K_o} \frac{\{NO_3^-\}}{\{H_2O\}} + \frac{\beta_2}{K_o} \left(\frac{\{NO_3^-\}}{\{H_2O\}} \right)^2 \qquad \text{(II-3)}$$

The constants K_o, β_1, and β_2 were obtained by a least-squares fit of the Am extraction data for $[HNO_3] \leq 0.5\underline{M}$. The data analysis was restricted to low aqueous nitric acid concentrations, where the reaction in Eq. II-1 is presumably the only equilibrium of importance. The values of K_o, β_1, and β_2 were found to be 1.27×10^6, 58, and 67.7, respectively. Since these constants are based on activities, they are independent of ionic strength. Equation II-2 gives a good fit to the extraction data up to about $1\underline{M}$ HNO_3 (see Fig. II-1, curve A).

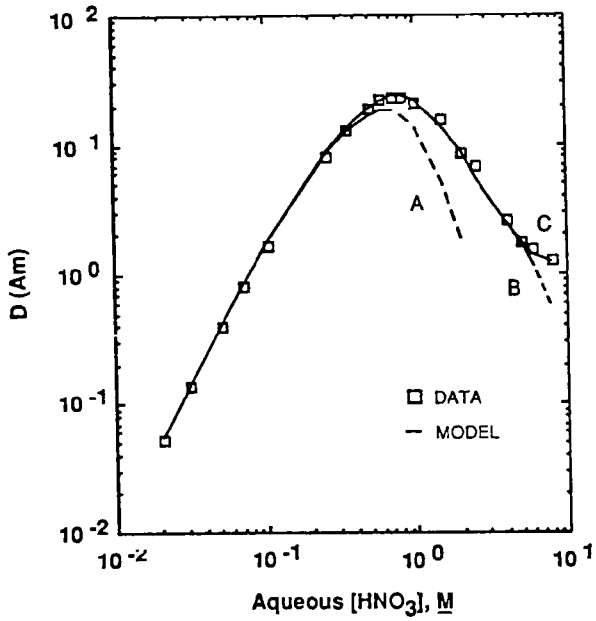

Fig. II-1.

Measured and Calculated Americium Extraction by $0.25\underline{M}$ CMPO in TCE at 25°C. Curve A was calculated from Eq. II-2; Curve B was calculated from Eq. II-7; Curve C was generated from the complete extraction model. Some of the data were obtained from Ref. 8.

For aqueous acid concentrations of $1\underline{M}$ or greater, Eq. II-2 must be modified to include the participation of the $\overline{CMPO} \cdot HNO_3$ species in Am^{3+} extraction. The model was modified to include the $CMPO \cdot HNO_3$ species in the extracted metal complex for extractions above $0.5\underline{M}$ aqueous HNO_3. Written in terms of the free CMPO species, the extraction equilibria are:

$$Am(H_2O)_9^{3+} + H^+ + 4NO_3^- + 3\overline{CMPO} \underset{\longleftarrow}{\xrightarrow{K_1}} \overline{Am(NO_3)_3(CMPO)_2(CMPO \cdot HNO_3)} + 9H_2O \qquad \text{(II-4)}$$

$$Am(H_2O)_9^{3+} + 2H^+ + 5NO_3^- + 3\overline{CMPO} \xrightleftharpoons{K_2} \overline{Am(NO_3)_3(CMPO)(CMPO{\cdot}HNO_3)_2} + 9H_2O \qquad \text{(II-5)}$$

$$Am(H_2O)_9^{3+} + 3H^+ + 6NO_3^- + 3\overline{CMPO} \xrightleftharpoons{K_3} \overline{Am(NO_3)_3(CMPO{\cdot}HNO_3)_3} + 9H_2O \qquad \text{(II-6)}$$

When the equilibria of Eqs. II-4 to II-6 are incorporated into Eq. II-2, the expression of D_{Am} becomes

$$D_{Am} = \frac{[\overline{CMPO}]_f^3 \{NO_3^-\}^3 \left(K_o + K_1\{H^+\}\{NO_3^-\} + K_2\{H^+\}^2\{NO_3^-\}^2 + K_3\{H^+\}^3\{NO_3^-\}^3 \right)}{\left(1 + \beta_1 \frac{\{NO_3^-\}}{\{H_2O\}} + \beta_2 \left(\frac{\{NO_3^-\}}{\{H_2O\}} \right)^2 \right) \{H_2O\}^9} \qquad \text{(II-7)}$$

The addition of the terms containing K_1, K_2, and K_3 extends the range of the model up to 5M HNO_3 (Fig. II-1, curve B). To model the remainder of the data (Fig. II-1, curve C), it was necessary to include an additional term ($K_4\{H^+\}^4\{NO_3^-\}^4$) in Eq. II-7, which may be explained in terms of the following extraction equilibrium:

$$Am(H_2O)_9^{3+} + 4H^+ + 7NO_3^- + 3\overline{CMPO} \xrightleftharpoons{K_4} \overline{Am(NO_3)_3(CMPO{\cdot}HNO_3)_2(CMPO{\cdot}2HNO_3)} + 9H_2O \qquad \text{(II-8)}$$

Preliminary data show that the model successfully predicts the effects of inextractable nitrate salts (i.e., $NaNO_3$) on Am^{3+} extraction. The calculated and experimental D_{Am} values are given in Table II-1 for the extraction of Am^{3+} from $HNO_3/NaNO_3$ solutions.

Table II-1. Americium Extraction by 0.25M CMPO in TCE from $HNO_3/NaNO_3$ Solutions at 25°C

$[HNO_3]$, M	$[NaNO_3]$, M	$[NO_3^-]$, M	D_{Am} Measd.	D_{Am} Calcd.
0.5	1	1.5	63.3	63.0
1.0	1	2	30.1	30.6
2.0	1	3	8.6	9.7
4.0	1	5	2.2	2.8

The use of Eq. II-3 for determining β_1 and β_2 is dependent upon there being only one metal-CMPO complex (i.e., $\overline{Am(NO_3)_3(CMPO)_3}$) at low acid concentrations. In future work, literature data for Am^{3+} extraction by the acidic extractant di[para(1,1,3,3-tetramethyl butyl)phenyl] phosphoric acid (HDoϕP)[10] will be used to evaluate β_1 and β_2 independently of the CMPO extraction data. Since it has been shown that only one Am-HDoϕP complex exists, the data of Peppard[10] should produce β values having a higher degree of confidence.

2. Metal Extraction Studies

The distribution ratios of Tc, Ru, U, Pu, and Fe have been measured with the TRUEX solvents. These ratios are being measured as a function of aqueous phase composition at 25 and 50°C. These data, together with the nitric acid extraction data collected earlier, will be used in developing metal extraction models.

a. Technetium

Figure II-2 shows the distribution ratio data of technetium in the presence of 0.01M neodymium originally present in either the organic or aqueous phases as a function of nitric acid concentration. The extractability

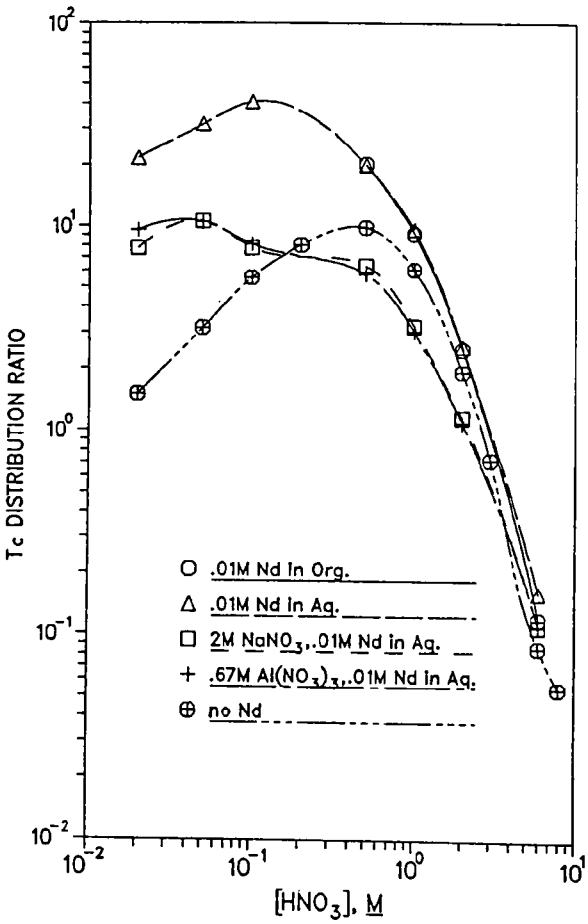

Fig. II-2.

Distribution Ratios for TcO_4^- with TRUEX-NPH at 25°C

of Tc into the TRUEX-NPH depends upon the concentration of neodymium ion present in the solution at nitric acid concentrations less than ~1M (compare "no Nd" curve with ".01M Nd" curves).

The presence of uranyl ion also increases the extraction of pertechnetate by the TRUEX solvent.[11] However, the distribution ratio values of Tc in the presence of uranium decrease continuously with increasing HNO_3 concentrations, while in the presence of neodymium, the D_{Tc} values increase gradually up to ~0.1M HNO_3 and then decrease continuously. This difference may be accounted for by the different extraction coefficients of uranium and neodymium. Uranium distribution ratios are all significantly greater than ten over the range of nitric acid concentrations shown in Fig. II-2, whereas the neodymium distribution ratios (which are very close to those of americium, see Fig. II-1) only exceed one for [HNO_3] above 0.1M. The amount of technetium present in the organic phase depends on the relative extractability of the metal salts. The difference in the extractability of uranium and neodymium pertechnetate salts causes the different amount of Tc extracted at low nitric acid concentration.

When non-extractable nitrate salts [$NaNO_3$ or $Al(NO_3)_3$] were present in the aqueous phase, the D_{Tc} values were lower due to the increased competition for the extractant by nitric acid that was forced into the organic solvent by the common-ion effect.

b. Ruthenium

Figure II-3 displays the forward and reverse distribution ratio results* of ruthenium between TRUEX-NPH and nitric acid. The forward and reverse distribution ratios of ruthenium are different by almost two orders of magnitude at HNO_3 ≤2M and even greater at higher HNO_3 concentrations. This result suggests that different ruthenium complexes are present in the aqueous and organic phases, and that the rate of exchange of these complexes is low when compared to the one-minute contact times. At 1M HNO_3, about 80% of the aqueous-phase ruthenium exists as a mononitrato complex, which has a low extractability, and less than 20% of ruthenium is in the trinitrato form, for which the extractability is higher.[12] Results show that the forward distribution ratio values of ruthenium are below 0.2 because the mononitrato ruthenium compound is the dominant species in the aqueous solution.

As the nitric acid concentration was increased, the forward distribution ratio of ruthenium decreased because of competition for CMPO between the ruthenium complexes and nitric acid. This can be explained by the D value being a function of the free CMPO concentration.

When radioactive ruthenium was combined with 0.028M of ruthenium carrier solution, the distribution ratio values changed slightly. When the solution was equilibrated in a water bath for four hours at 50°C and left over the weekend at room temperature, only a slightly higher distribution ratio value at 3M HNO_3 was found.

---

*A "forward" distribution ratio result is for ruthenium originally present in only the aqueous phase. In a "reverse" distribution ratio, the solvent containing the extracted ruthenium is equilibrated with a fresh aqueous phase, containing no ruthenium.

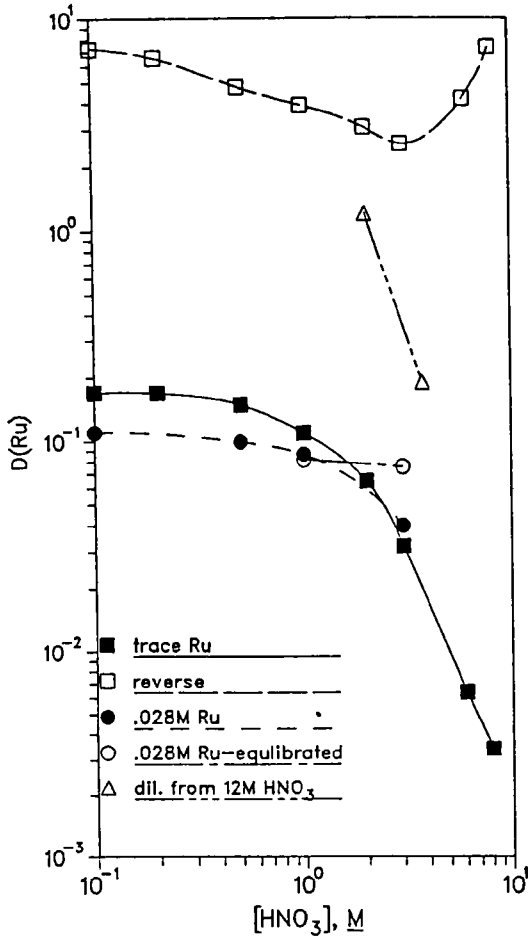

Fig. II-3.

Distribution Ratios for Ru with TRUEX-NPH at 25°C

Significant increases of the distribution ratio values of ruthenium were found when the measurements were performed within five minutes of the dilution of the ruthenium stock solution which contained 12M HNO_3. At 12M HNO_3, over 70% of ruthenium exists as trinitrato compound.[12] Dilution will decrease the percentage of the trinitrato complex over long periods as the trinitrato hydrolyzes to lower nitrato forms. In these experiments, the hydrolysis was not allowed to reach equilibrium, and more of the trinitrato complex was present than in the previously discussed experiments. Clearly, its hydrolysis affects the distribution ratio of ruthenium.

When fresh organic solution was added to the separated aqueous phase and a second extraction performed, the second forward distribution ratio value was significantly lower than the first value. In addition, the third one was lower than the second value (D_{f1} = 1.9, D_{f2} = 0.13, D_{f3} = 0.07). However, the opposite was found for the reverse extraction. These results imply that (1) in the aqueous phase, mono- and dinitrato ruthenium complexes become the predominant species as the trinitrato complex is extracted, and (2) the organic phase is enriched with trinitrato ruthenium compound. Therefore, the distribution ratio value of ruthenium is very sensitive to the nitrato species present in the solution.

Since TBP is a good extractant for ruthenium complexes, it is necessary to determine whether CMPO is the extractant for the ruthenium

complex in the TRUEX solvent. Under similar experimental conditions, the ruthenium distribution ratio between 2M HNO_3 and the TRUEX-TCE solvent was 0.69, compared to the value 0.74 when TBP was removed from the solvent. This result indicates that the TBP has little effect on the extraction of ruthenium complexes by the TRUEX solvent.

c. Uranium

As shown in Fig. II-4, the uranium distribution ratios with HNO_3 increase with increasing nitric acid concentration in the TRUEX-NPH system; an inflection point occurs between 0.5 and 2M HNO_3. Figure II-4 also displays the uranium distribution ratio values as a function of nitric acid concentration in 2M $NaNO_3$ and in 0.67M $Al(NO_3)_3$. The added nitrate salts enhanced the extractability of uranium, especially at lower nitric acid concentrations, but $Al(NO_3)_3$ is a better salting-out agent than $NaNO_3$ for uranium extraction in the TRUEX-NPH system. Temperature also affects the extraction of uranium from HNO_3 solutions by TRUEX-NPH; the distribution ratio decreased by a factor of two when the temperature was increased from 25°C to 50°C.

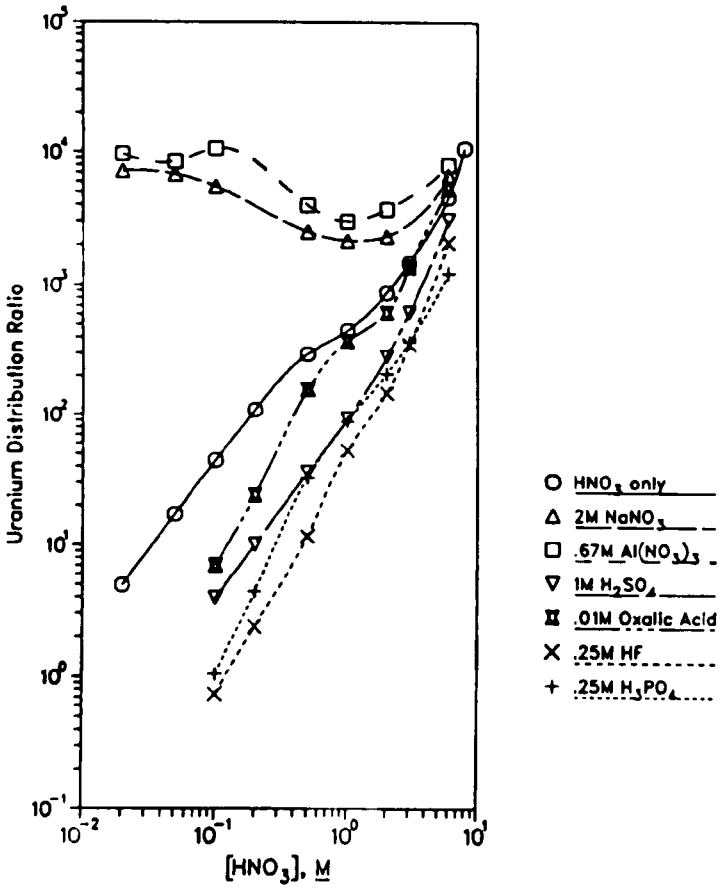

Fig. II-4. Distribution Ratios for Uranium with TRUEX-NPH at 25°C

The uranium distribution ratios between the TRUEX-NPH solvent and HNO_3 in the presence of different amounts of aqueous complexants (sulfuric acid, oxalic acid, hydrofluoric acid, or phosphoric acid) have been measured. Figure II-4 plots the uranium distribution ratios for these complexants, which suppress the extraction of uranyl ion from the aqueous phase. Literature values show that uranyl ion has higher stability constants with HSO_4^-, $C_2O_4^{2-}$, F^-, and $H_2PO_4^-$ anions [$K(HSO_4^-) = 6.4$, $K(C_2O_4^{2-}) = 10^6$, $K(F^-) = 26$, and $K(H_2PO_4^-) = 7.9$] than with nitrate ($K = 0.24$).[13,14]

d. Plutonium

The plutonium distribution ratios between the TRUEX-TCE solvent and HNO_3 are shown in Fig. II-5. The plutonium distribution ratios show a trend similar to the uranium distribution ratios. This suggests that a change in the composition of the extracted species is occurring. Figure II-5 also lists the distribution ratios of plutonium between TRUEX-TCE and HNO_3 solutions containing added salts. For 0.2 to 2M HNO_3, the addition of 2M $NaNO_3$ or 0.67M $Al(NO_3)_3$ resulted in a decrease in the D values. Above 2M HNO_3, the experimental results showed that the presence of salt increases plutonium extraction into the organic phase. The changing effect of these salts on plutonium extraction is surprising. Again, it suggests a change in the relative amounts of the different species present in the aqueous phase.

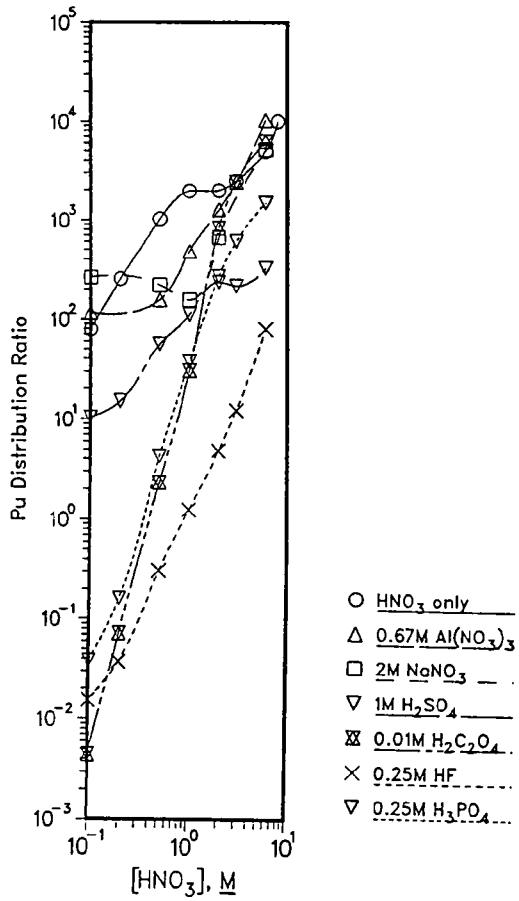

Fig. II-5.

Pu(IV) Extraction by TRUEX-TCE from Aqueous Nitrate Solutions Containing Complexants or Salts at 25°C

Temperature effects on the extraction of plutonium by TRUEX-TCE are complex. Aqueous phases studied at 50°C include 0.2 and 1.0M HNO_3 in the absence or presence of 1.0M H_2SO_4, 0.01M $H_2C_2O_4$, and 0.25M H_3PO_4. For these representative aqueous phases, the distribution ratios generally decreased with temperature. However, TBP extraction studies in nitrate[15] and chloride[16] media have shown that the distribution ratios for Pu(IV) increase with temperature. Further, measurements at 50°C are planned and should clarify the effect of temperature on the extraction of Pu(IV) by TRUEX solvents.

Plutonium distribution ratios have also been measured between TRUEX-TCE and HNO_3 in the presence of different amounts of aqueous complexants (sulfuric acid, oxalic acid, hydrofluoric acid, and phosphoric acid). The results are plotted in Fig. II-5. In data not shown in Fig. II-5, sodium nitrate was added to some aqueous phases to study the salt effect in these systems. The data indicate, as expected, that plutonium forms stronger complexes with these complexants than it does with nitrate. Literature values show the stability constants of HSO_4^-, $C_2O_4^{2-}$, F^-, and HPO_4^{2-} anions to be $K(HSO_4^-)$ = 740, 25.2, or 9.45*; $K(C_2O_4^{2-})$ = 5.6 x 10^8; $K(F^-)$ = 5.9 x 10^6; and $K(HPO_4^{2-})$ = 8.3 x 10^{12}),[17] which are higher than that of nitrate (K = 5.5).

e. Iron Extraction

(1) Iron Extraction by TRUEX-TCE

Both ^{55}Fe and ^{59}Fe were used to measure the distribution of iron between various nitric acid solutions and the TRUEX-TCE solvent at varying contact times. The TRUEX-TCE solvent contains 0.25M CMPO and 0.75M TBP diluted by tetrachloroethylene. In addition, 250 mL of the TRUEX solvent was prepared as follows:

1. Dissolve 25.86 g CMPO (assumed 98.5% pure) in 125 mL of TCE (in a 250 mL beaker).

2. Weigh 49.93 g of TBP in a 100 mL beaker (~50 mL) and add to the CMPO-TCE solution.

3. Place resulting solution in a 250 mL volumetric flask.

4. Rinse both beakers with TCE into the volumetric flask.

5. Prepare solvent to the exact volume with TCE.

The original ^{55}Fe or ^{59}Fe stock solution was converted from $FeCl_3$ to $Fe(NO_3)_3$ by successive evaporations with 1M nitric acid. The extractions were carried out from solutions containing the prepared $Fe(NO_3)_3$ at 0.1-6M nitric acid as follows.

The organic phase was pre-equilibrated with the appropriate fresh acid (three times; O/A** = 1) and the final organic phase was

*The three $K(HSO_4^-)$ values were measured under different conditions.[17]

**Organic-to-aqueous phase ratio.

used in equilibration with Fe tracer solutions. For the metal extraction, an aqueous solution spiked with radiotracer iron and the equilibrated organic solution were thermostated at 25°C, followed by vortex mixing (appropriate time) and centrifuging. The phases were separated using glass pipettes. Duplicate samples of each phase were taken and counted by liquid scintillation for ^{55}Fe (each in a 10-mL scintillation cocktail) and by gamma counting for ^{59}Fe.

This extraction rate study was done at six different contact times (2, 5, 15, 30, 60, and 300 s) and with eight different concentrations of nitric acid. The results tabulated in Table II-2 and plotted in Fig. II-6 show that D_{Fe} values for the forward extraction increase with nitric acid concentration and contact time. Also, differences in D_{Fe} values are less dependent on contact time at higher concentrations of nitric acid.

This study continued with determination of the effect of contact time on the back-extraction distribution ratios of Fe(III). This back extraction was done at four different contact times (5, 15, 60, and 300 s) and with eight different concentrations of nitric acid. The results are tabulated in Table II-3 and plotted in Fig. II-7 along with corresponding forward extractions.

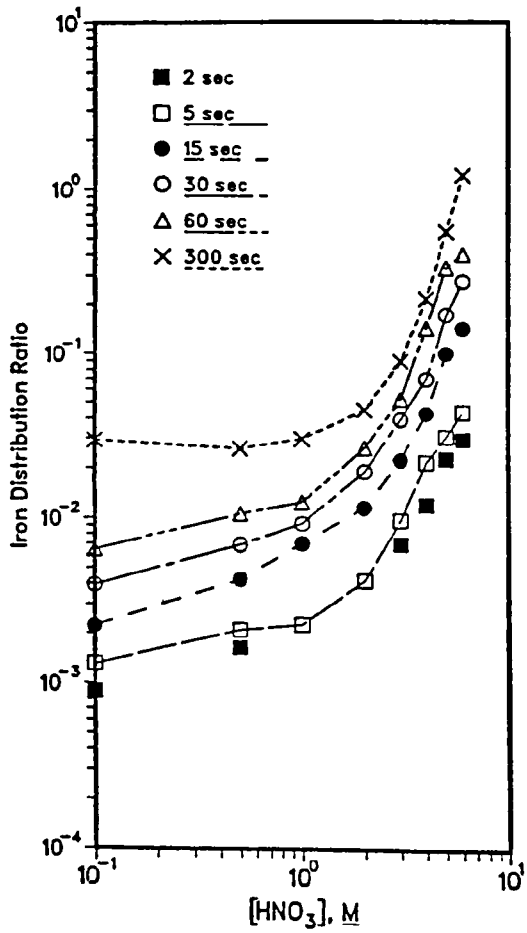

Fig. II-6.

Forward Iron Extraction by TRUEX-TCE at 25°C and Contact Times of 2-300 s

Table II-2. Distribution Ratios for the Forward Extraction of Iron between Nitric Acid and TRUEX-TCE at 25°C

HNO_3, M	Fe Distribution Ratios					
	2 s	5 s	15 s	30 s	60 s	300 s
0.1	8.98×10^{-4}	1.30×10^{-3}	2.23×10^{-3}	3.94×10^{-3}	6.46×10^{-3}	2.93×10^{-2}
0.5	1.64×10^{-3}	2.09×10^{-3}	4.24×10^{-3}	6.85×10^{-3}	1.05×10^{-2}	2.59×10^{-2}
1	---	2.25×10^{-3}	6.97×10^{-3}	9.19×10^{-3}	1.23×10^{-2}	2.96×10^{-2}
2	---	4.15×10^{-3}	1.14×10^{-2}	1.88×10^{-2}	2.61×10^{-2}	4.46×10^{-2}
3	6.90×10^{-3}	9.57×10^{-3}	2.21×10^{-2}	3.90×10^{-2}	5.20×10^{-2}	8.91×10^{-2}
4	1.19×10^{-2}	2.13×10^{-2}	4.25×10^{-2}	6.92×10^{-2}	0.143	0.215
5	2.25×10^{-2}	3.05×10^{-2}	9.95×10^{-2}	0.172	0.333	0.547
6	2.95×10^{-2}	4.33×10^{-2}	0.142	0.275	0.400	1.207

Table II-3. Distribution Ratios for Iron Extraction (Reverse) by TRUEX-TCE at 25°C vs. Nitric Acid Concentration and Contact Time

	Fe Dist. Ratios			
HNO_3, M	5 s	15 s	60 s	300 s
0.1	10.42	7.58	3.56	0.831
0.5	5.65	3.61	1.16	0.291
1.0	6.32	3.28	0.857	0.214
2.0	6.20	2.75	0.728	0.215
3.0	7.10	3.37	0.554	0.257
4.0	8.18	4.50	0.760	0.340
5.0	12.89	5.77	1.49	0.806
6.0	19.16	6.08	2.64	2.14

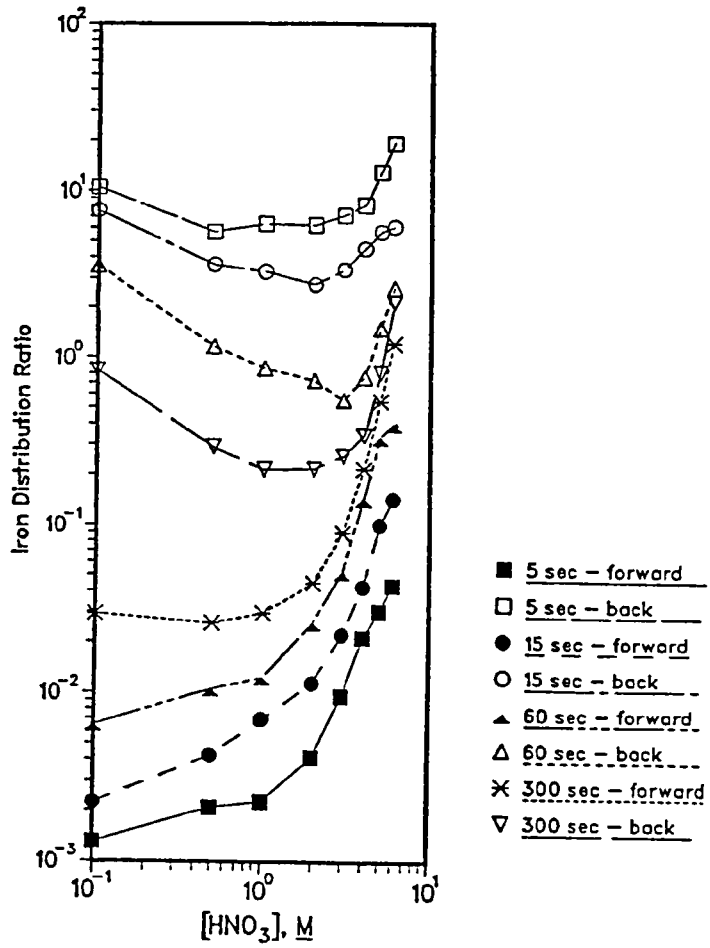

Fig. II-7. Iron Extraction by TRUEX-TCE at 25°C and Contact Times of 5-300 s

The effect of contact time (forward and reverse) on the extraction of iron by the TRUEX-TCE solvent covered times from 2 to 300 s. Iron distribution data were also obtained for long contact times, up to 20 days (forward and reverse). For this work, a roto-torque (heavy duty rotator) was assembled in the hood under ambient conditions (21°C ± 2), and two sets of eight centrifuge tubes were inserted into the roto-torque (eight per side). After spiking the aqueous phases with ^{59}Fe, Set I ($[HNO_3]$ = 0.1, 0.5, 1, 2, 3, 4, 5, and 6M) was rotated for nine days of forward extraction. Phases were separated and counted. The remaining organic phase was contacted with fresh aqueous (containing no iron) and rotated for 20 days; phases were separated and counted for measuring the back extraction. Set II (acid concentrations the same) was rotated for 19 days of forward extraction. After samples were taken, the remaining organic phase was contacted with fresh aqueous phase and rotated for 10 days, separated, and counted for the back extraction measurement. The results, tabulated in Table II-4, show that equilibration of iron is very slow and complex in that forward and back extraction do not appear to be moving toward the same equilibrium state.

Table II-4. Measured Distribution Ratios of Fe(III) for Iron Extraction by TRUEX-TCE vs. Nitric Acid Concentration and Contact Time (Long Term)

	Iron Dist. Ratio			
HNO_3, M	Forward 9 days	Back 20 days	Forward 19 days	Back 20 days
0.1	0.155	0.392	0.119	0.410
0.5	0.085	0.179	0.093	0.216
1.0	0.083	0.140	0.086	0.144
2.0	0.103	0.164	0.105	0.181
3.0	0.166	0.217	0.168	0.235
4.0	0.318	0.411	0.308	0.380
5.0	0.814	0.950	0.860	0.916
6.0	2.23	2.45	2.43	2.50

To determine the effect on distribution coefficients of iron levels comparable to those found in waste streams, further extractions were done. A stock solution of $Fe(NO_3)_3$ (1M in HNO_3) was prepared and used to spike each of eight nitric acid samples to a level of 0.1M in iron. In addition, ^{59}Fe was added and a series of forward extractions followed by back extractions (same sample) was completed. The results are shown in Table II-5, columns 3 and 5. Columns 2 and 4 are results given previously in this report (for comparison). Although forward extraction appears little affected by iron concentration, back extraction appears to be increased by increased iron concentrations at lower nitric acid concentrations.

Table II-5. Extraction of Fe(III) by TRUEX-TCE for Contact Time of 60 s and Temperature of 25°C

HNO_3, M	Iron Dist. Ratio			
	Forward ^{59}Fe	Forward ^{59}Fe + 0.01M Fe	Reverse ^{59}Fe	Reverse ^{59}Fe + 0.01M Fe
0.1	6.46×10^{-3}	5.18×10^{-3}	3.56	0.896
0.5	1.05×10^{-2}	8.40×10^{-3}	1.16	0.132
1.0	1.23×10^{-2}	1.36×10^{-2}	0.857	0.098
2.0	2.61×10^{-2}	2.49×10^{-2}	0.728	0.128
3.0	5.20×10^{-2}	5.67×10^{-2}	0.554	0.233
4.0	0.143	0.110	0.760	0.712
5.0	0.333	0.190	1.49	1.26
6.0	0.400	0.354	2.64	3.95

(2) Iron Extraction by TRUEX-NPH

The effect of contact time on the extraction of iron from aqueous nitric acid solution into TRUEX-NPH is reported here. The study is similar to the TRUEX-TCE work already reported. Distribution ratio data for the forward and back extraction of Fe(III) from nitric acid solutions in the range of 0.1 to 6M have been obtained at contact times of 15, 30, 60, and 300 s. Results are given in Table II-6 and Fig. II-8.

(3) Derivation of Rate Expression

The extent of the forward and back extraction of Fe(III) by the TRUEX-TCE solvent has been found to be dependent on the time of contact. The simplest treatment of this effect is to assume a simple first-order reversible reaction:

$$Fe(III)_{aq} \underset{k_2}{\overset{k_1}{\rightleftharpoons}} Fe(III)_{org} \qquad \text{(II-9)}$$

where k_1 and k_2 contain terms for the contact surface area and are, therefore, rate constants measured in inverse time units. The rate of Fe(III) buildup in the organic phase is given by the equation:

$$\frac{dy}{dt} = k_1 x - k_2 y \qquad \text{(II-10)}$$

where y is the fractional concentration of Fe(III) in the organic phase, and x is the fractional concentration of Fe(III) in the aqueous phase. With the volumes of both phases being the same,

$$x + y = 1 \qquad \text{(II-11)}$$

Table II-6. Extraction of Fe(III) by TRUEX-NPH for Contact Times of 15-300 s and Temperature of 25°C

Nitric Acid, M	Iron Dist. Ratio							
	Forward Extrac.				Reverse Extrac.			
	15 s	30 s	60 s	300 s	15 s	30 s	60 s	300 s
0.1	4.52×10^{-3}	4.58×10^{-3}	4.98×10^{-3}	6.89×10^{-3}	0.173	0.140	8.98×10^{-2}	5.70×10^{-2}
0.5	1.80×10^{-2}	2.43×10^{-2}	2.72×10^{-2}	3.25×10^{-2}	0.692	0.306	0.102	4.30×10^{-2}
1.0	2.03×10^{-2}	3.53×10^{-2}	4.42×10^{-2}	6.20×10^{-2}	2.43	1.12	0.277	7.21×10^{-2}
2.0	4.84×10^{-2}	7.62×10^{-2}	9.08×10^{-2}	0.170	7.52	2.84	1.13	0.265
3.0	0.119	0.126	0.164	0.409	10.96	5.84	2.85	0.694
4.0	0.165	0.188	0.261	0.878	21.38	11.04	5.13	1.86
5.0	0.295	0.306	0.493	2.34	42.5	28.1	16.1	4.42
6.0	0.489	0.546	0.870	8.01	77.5	45.6	27.4	12.0

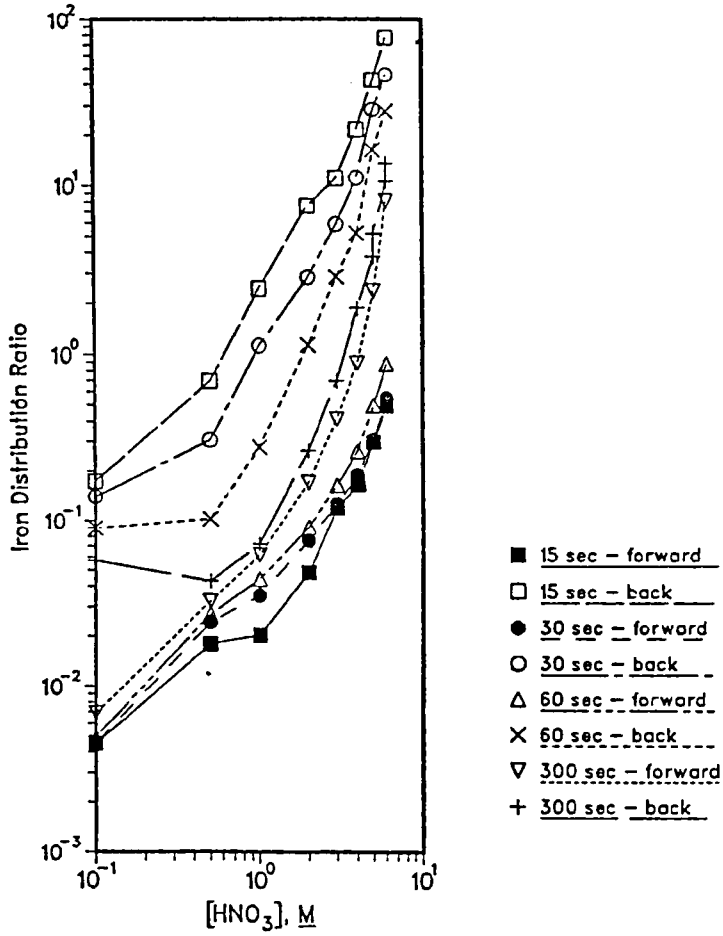

Fig. II-8. Iron Extraction by TRUEX-NPH at 25°C and Contact Times of 15-300 s

Substitution of Eq. II-11 into II-10 and rearrangement into an integrable form give:

$$\int_0^y \frac{dy}{k_1 - (k_1 + k_2)y} = \int_0^t dt \qquad \text{(II-12)}$$

where the initial concentration of Fe(III) in the organic phase was zero. The equation is in the form:

$$\int_0^u \frac{du}{a + bu} = \int_0^t dt \qquad \text{(II-13)}$$

Integrating this equation gives:

$$\frac{1}{b} \ln(a + bu) \Big|_{o}^{u} = t \qquad \text{(II-14)}$$

where $u = y$, $a = k_1$, and $b = -(k_1 + k_2)$. Thus,

$$\ln \left[\frac{k_1 - (k_1 + k_2)y}{k_1} \right] = -(k_1 + k_2)t \qquad \text{(II-15)}$$

This equation can be rearranged by the following steps. At equilibrium, the rates of the forward and reverse reactions must be equal, or

$$k_1 x_\infty = k_2 y_\infty \qquad \text{(II-16)}$$

Rearranging Eq. II-16 leads to

$$k_2 = k_1 \frac{x_\infty}{y_\infty} \qquad \text{(II-17)}$$

Substituting Eq. II-17 into Eq. II-15 leads to

$$\ln \left[\frac{k_1 - (k_1 + k_1 \frac{x_\infty}{y_\infty})y}{k_1} \right] = -(k_1 + k_2)t \qquad \text{(II-18)}$$

or

$$\ln \left[1 - (1 + \frac{x_\infty}{y_\infty})y \right] = -(k_1 + k_2)t \qquad \text{(II-19)}$$

or

$$\ln \left[1 - (\frac{y_\infty + x_\infty}{y_\infty})y \right] = -(k_1 + k_2)t \qquad \text{(II-20)}$$

Since $y_\infty + x_\infty = 1$,

$$\ln \left(1 - \frac{y}{y_\infty} \right) = -(k_1 + k_2)t \qquad \text{(II-21)}$$

Therefore, a plot of ln $(1 - y/y_\infty)$ vs. t should be linear with a slope of $-(k_1 + k_2)$. Since data were collected as distribution ratios of Fe(III), not as $Fe(III)_{org}$ concentrations, Eq. II-22 should be rearranged in terms of D_{Fe} values. This can be done by substitution using the two equations:

$$x + y = 1 \qquad \text{(II-22)}$$

and

$$D = y/x \qquad \text{(II-23)}$$

Substitution of the solution of these two equations:

$$y = D/(D + 1) \qquad \text{(II-24)}$$

and

$$y_\infty = \frac{D_\infty}{D_\infty + 1} \qquad \text{(II-24a)}$$

into Eq. II-21 yields

$$1 - \frac{y}{y_\infty} = 1 - \frac{D/(D + 1)}{D_\infty/(D_\infty + 1)} \qquad \text{(II-25)}$$

$$= \frac{\dfrac{D_\infty}{D_\infty + 1} - \dfrac{D}{D + 1}}{\dfrac{D_\infty}{D_\infty + 1}} \qquad \text{(II-25a)}$$

$$= \frac{\dfrac{D_\infty (D + 1) - D (D_\infty + 1)}{(D_\infty + 1)(D + 1)}}{\dfrac{D_\infty}{D_\infty + 1}} \qquad \text{(II-25b)}$$

$$= \frac{D_\infty - D}{D_\infty (D + 1)} \qquad \text{(II-25c)}$$

Therefore, a plot of ln $(D_\infty - D)/(D_\infty(D + 1))$ vs. time will have a slope of $-(k_1 + k_2)$. The slope of each plot and the equilibrium distribution ratio at a specific nitric acid concentration,

$$D_\infty = \frac{y_\infty}{x_\infty} = \frac{k_1}{k_2} \qquad \text{(II-26)}$$

can be used to calculate k_1 and k_2 for this condition. The slope of each plot (k_{obs}) can be used to calculate k_1,

$$k_1 = \frac{k_{obs}}{1 + D_\infty} \qquad \text{(II-27)}$$

The reverse extraction rate constant, k_2, can be calculated from the relationship

$$k_2 = k_1/D_\infty \qquad \text{(II-28)}$$

The back-extraction data can be calculated in the same manner for experiments where the Fe(III) begins in the organic phase, and the initial Fe(III) concentration in the aqueous phase is zero. In this case,

$$\frac{dx}{dt} = k_2 y - k_1 x \qquad \text{(II-29)}$$

and the final form is

$$\ln (1 - x/x_\infty) = -(k_1 + k_2)t \qquad \text{(II-30)}$$

Putting this equation into a form using the measure distribution ratios at time t gives the following relationship:

$$\ln \left(\frac{D - D_\infty}{D + 1} \right) = -(k_1 + k_2)t \qquad \text{(II-31)}$$

The treatment of the slope is exactly the same as that in the forward extraction.

3. Evaluation of Neptunium Distribution Ratio Data

a. Neptunium (IV)

The distribution ratio of Np(IV) in TRUEX-NPH solvent was measured using ^{239}Np and 0.33M ferrous sulfonate as a holding reductant. One forward and two back extractions were used in two separate experiments to verify $D_{Np(IV)}$ values over a series of nitric acid concentrations. The back-extraction results were more reproducible than the forward extractions, and the averages of the second back extractions are shown in Table II-7, together with the results obtained by Kolarik and Horwitz[18] for Np(IV) and by Reichley-Yinger for Pu(IV) (from Sec. II.A.2.d). The values in Table II-7 are also plotted in Fig. II-9. The ratios from Kolarik and Horwitz[18] were read from a graph; thus, individual points are not plotted in Fig. II-9, although those used to generate the graph are given in Table II-7. The agreement between the results obtained here and those reported by Kolarik and Horwitz appears reasonable, particularly in view of the differences in the laboratory techniques used and the instability of the Np(IV) state. The distribution ratios for neptunium are less than those for plutonium at the lower acid concentrations, but become greater than for plutonium about 0.5M HNO_3.

Only one run was performed to measure the Np(IV) distribution ratio for TRUEX-TCE. The results are given in Table II-7 and Fig. II-9. The back-extraction results seem reasonable compared with the TRUEX-NPH data. The TRUEX-NPH and TRUEX-TCE results are fairly close, except at the highest acidity used (5M). The differences between the Pu and Np results are obvious.

Table II-7. Distribution Ratios for Np(IV) and Pu(IV) vs. Nitric Acid Concentration at 25°C and an O/A Volume Ratio of 1

$[HNO_3]$, M	Dist. Ratios				
	TRUEX-NPH			TRUEX-TCE	
	Np(IV)[a]	Np(IV)[b]	Pu(IV)[c]	Np(IV)[d]	Pu(IV)[c]
0.05	3.9	-	-	2.3	-
0.10	17.7	-	81	16.2	78
0.20	185	63	203	113	253
0.50	2.9×10^3	4×10^3	450	1.2×10^3	1.0×10^3
1.0	7.3×10^3	1.3×10^4	763	4.2×10^3	2.0×10^3
2.0	2.0×10^4	-	1.0×10^3	6.3×10^3	2.0×10^3
3.0	5.6×10^4	-	1.4×10^3	2.1×10^4	2.5×10^3
5.0	1.7×10^5	-	-	1.1×10^4	-
6.0	-	-	2.7×10^3	-	5.0×10^3

[a]Average of second back extractions.

[b]Data read from graph; nitric acid concentrations range between 0.2M and 1M only.[18]

[c]From Sec. II.A.2.d.

[d]Second back extraction.

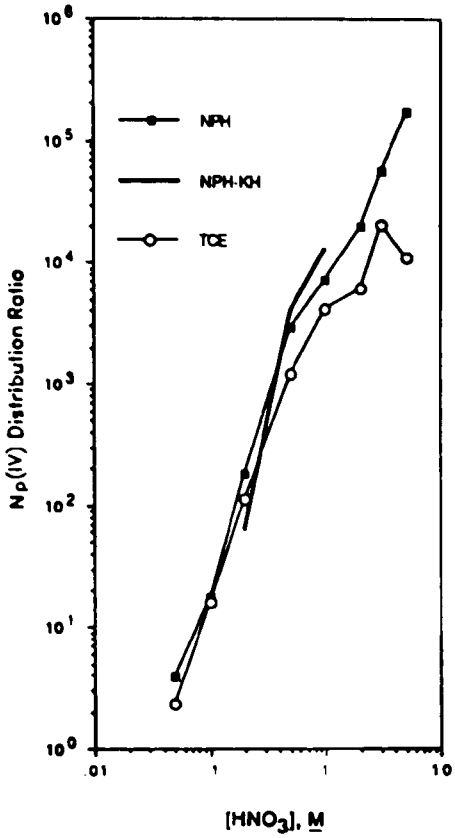

Fig. II-9.

Np(IV) Distribution Ratios between Nitric Acid and Two TRUEX Solvents. "NPH" is TRUEX-NPH and "TCE" is TRUEX-TCE, this study. "NPH-KH" is TRUEX-NPH (Ref. 18).

b. Neptunium (V)

Two experiments were performed to measure the Np(V) distribution ratio for TRUEX-NPH: one with sodium metabisulfite added to each aqueous phase to maintain the oxidation state, and one without the addition of a holding reductant. Four consecutive extractions of the aqueous phases were performed with fresh solvent. The first three were done to remove any Np(IV) and Np(VI) present, and the fourth to obtain the distribution ratio for Np(V). The presence of bisulfite made little difference, and the distribution ratios did not vary greatly between the four extractions, except at 5M HNO_3. At this concentration, the ratios for the four extractions varied from 3.6 to 57, but the counting rates in the aqueous phases were usually too low after the first or second extraction to give reliable results.

The best results are those from the fourth extraction, without bisulfite, since the points fall on a smooth curve and agree fairly well with those obtained by Kolarik and Horwitz.[18] These results are given in Table II-8 and Fig. II-10. Only one series of extractions was performed with Np(V) in TRUEX-TCE. These results are also given in Table II-8 and Fig. II-10.

c. Neptunium (VI)

The hexavalent state of neptunium was prepared by two methods: (1) oxidation with 0.01M $K_2Cr_2O_7$ at room temperature, and (2) oxidation with 5M HNO_3 in the presence of 0.05M $NaNO_2$, both reported to be fast reactions.[19,20] With the dichromate-produced Np(VI), the neptunium was added to

Table II-8. Distribution Ratios for Np(V) in TRUEX-NPH and TRUEX-TCE at 25°C

$[HNO_3]$, M	TRUEX-NPH[a]	TRUEX-TCE[a]	TRUEX-NPH[b]
0.05	0.017	0.023	-
0.10	0.038	0.039	0.0234
0.20	0.059	0.055	-
0.32	-	-	0.069
0.50	0.143	0.126	-
1.0	0.227	0.142	0.210
2.0	0.575	0.213	-
3.0	1.04	0.332	-
3.2	-	-	1.00
5.0	3.18	0.813	-
5.25	-	-	4.1

[a]Fourth extraction.
[b]From Ref. 18. .

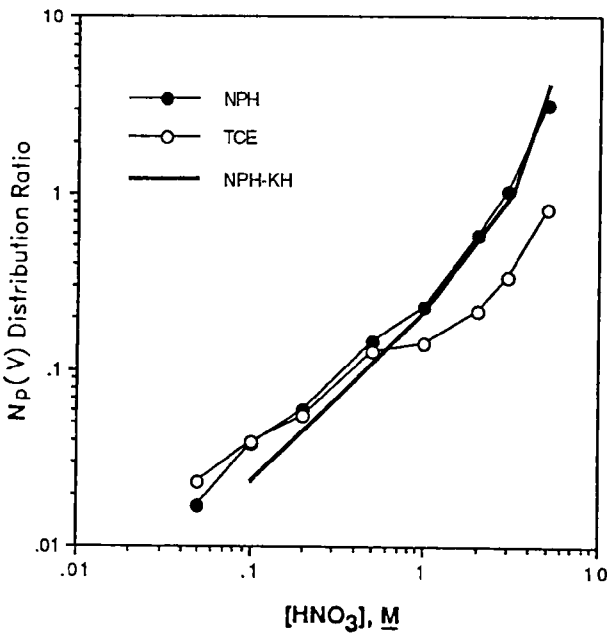

Fig. II-10.

Np(V) Distribution Ratios between Nitric Acid and Two TRUEX Solvents. "NPH" is TRUEX-NPH and "TCE" is TRUEX-TCE, this study. "NPH-KH" is TRUEX-NPH (Ref. 18).

the aqueous phase, and one forward and two back extractions were performed with TRUEX-NPH as the solvent. Each aqueous phase was also made with 0.01M in $K_2Cr_2O_7$ as a holding oxidant. Based on the colors of the phases, it was apparent that some dichromate extracted. At 0.05M to 0.5M HNO_3, the organic phase remained yellow. At 1M HNO_3 and above, the organic phase became progressively greener until at 5M HNO_3 the yellow dichromate color was no longer visible, and the color appeared to be all due to Cr(III). At 5M HNO_3,

in the first back extraction, and at 3M and 5M HNO_3 in the second back extraction, a green precipitate formed in the organic phase, making accurate sampling and counting impossible. Evidently, dichromate reacts very rapidly with the solvent (probably with CMPO), and distribution ratios measured by dichromate oxidation are unacceptable, particularly at high acidities. The Np(VI) tracer, prepared by HNO_3-HNO_2 oxidation, was extracted first into TRUEX-NPH solvent, and this solution was used to spike the organic phases for distribution ratio measurements that are considered reasonable. A first back extraction was followed by an equilibration of the aqueous phase with fresh organic (forward extraction) and the organic phase with fresh aqueous (second back extraction). The forward and second back extractions gave similar results, except at the two highest acidities (3 and 5M). The forward extraction results are considered more reliable since the high acidity distributions follow those obtained for U(VI) (see Sec. II.A.2.c). The Np(VI) and U(VI) results are given in Table II-9 and Fig. II-11.

Table II-9. Distribution Ratios for Np(VI) and U(VI) in TRUEX-NPH at 25°C

	Distribution Ratios			
	Np(VI)[a]			
$[HNO_3]$, M	Second Back Ext.	Forward Ext.	Np(VI)[b]	U(VI)[c]
0.05	37.9	34.3	60	15.5
0.10	51.5	48.8		43.7
0.20	77.2	76.1		107
0.50	210	218		298
1.0	325	362	316	497
2.0	418	446	489	848
3.0	565	395		1.42×10^3
5.0	1.13×10^3	2.49×10^3		-
6.0	-	-		5.41×10^3

[a]Np(VI) prepared by HNO_3-HNO_2 oxidation.

[b]Data read from graph in Ref. 18.

[c]From Sec. II.A.2.c.

4. Remote-Handled Contactors

Over the past several years, we have been making improvements to the ANL centrifugal contactor as needed to accommodate new solvent extraction processes and processing requirements. In FY 1986, the 4-cm centrifugal contactors were redesigned so that they could be used with volatile solvents. In FY 1987, we made further modifications so that the 4-cm contactors can be used in a remote facility with manipulators and an observation window or in a glove box. An eight-stage 4-cm centrifugal contactor was fabricated at ANL by the end of September. The finished remote-handled 4-cm contactor with eight stages is shown in Fig. II-12.

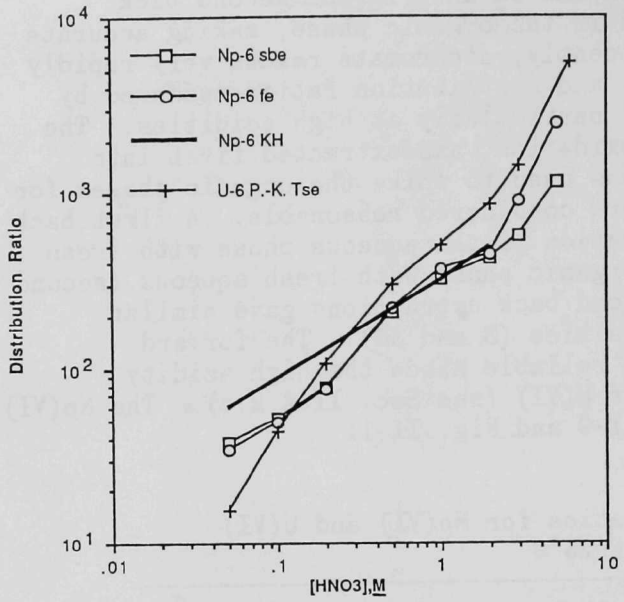

Fig. II-11.

Np(VI) and U(VI) Distribution Ratios between Nitric Acid and TRUEX-NPH. "Np-6 sbe" is second back extraction, and "Np-6 fe" is forward extraction, this study; "Np-6 KH" is from Ref. 18; "U-6 P.-K. Tse" is from Sec. II.A.2.c.

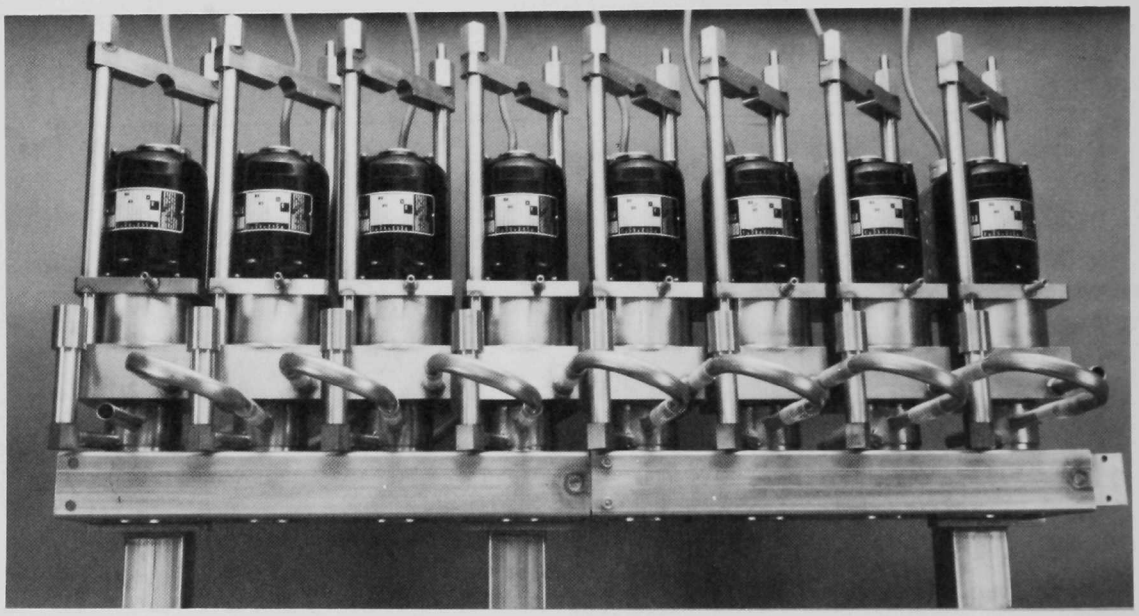

Fig. II-12. Remote-Handled 4-cm Contactor with Eight Stages

In FY 1988, this remote-handled contactor will be evaluated in a glove box and in a remote facility to determine if it meets all performance criteria. The unit will then be used in flowsheet studies required for the TRUEX Technology-Base Development Program.

5. Electronic Worksheet Development

An electronic worksheet, called SASSE (Spreadsheet Algorithm for Stagewise Solvent Extraction), is being developed to allow detailed evaluation

of proposed flowsheets in the TRUEX Technology-Base Development Program. In addition, the SASSE worksheet (spreadsheet) can be used to identify key points for process monitoring and control. An early version of SASSE was used to assist Westinghouse Hanford Company in countercurrent testing of the TRUEX flowsheet using actual Plutonium Finishing Plant wastes. Work is now being done on an Excel macro that will allow both the number of stages in a section and the number of sections in a proposed flowsheet to be changed.

The Excel macro is broken into two parts. The first part generates the template for the SASSE worksheet based on the following information: number of sections, number of stages in each section, number of feed components, and number of rows in the spreadsheet needed to calculate the D value for each component. Once the template is created, the user enters additional information on the worksheet. This part of the Excel macro is completed. The second part of the macro is now being written. This part of the macro generates the formulas for the various sections of the worksheet so that stages and sections can be easily added to, or deleted from, the original worksheet template.

B. PUREX-TRUEX Processing of Chloride Salt Wastes

(L. Reichley-Yinger, R. A. Leonard, G. F. Vandegrift, and C. A. Soto*)

Los Alamos National Laboratory (LANL) is testing PUREX-TRUEX flowsheets for the extraction of Pu and other TRU elements from acidic chloride-containing wastes. These wastes are generated during plutonium-metal production, e.g., Direct Oxide Reduction (DOR), Electrorefining (ER), and Molten Salt Extraction (MSE). In FY 1987, we were funded to support these efforts with flowsheet development, which included laboratory and computer simulation studies. Flowsheets were designed (1) to remove Pu and Am from the feed to make the solution more easily disposable, as nonTRU waste, (2) to separate a purified Pu stream that is acceptable for Pu-metal production, and (3) to accomplish these objectives in a 16-stage centrifugal contactor contained in a glove box.

1. Flowsheet Chemistry

A two-cycle flowsheet is envisioned for processing of chloride solutions: the first cycle to recover purified plutonium from the solutions and the second to provide nonTRU waste disposal.

a. PUREX-TCE Cycle

The apparent fifth-order dependence of the Pu(IV) distribution ratio on $\{Cl^-\}$, measured previously,[21] suggested that protonated Pu(IV)-chloride species, such as $HPuCl_5$ and H_2PuCl_6, were being extracted by TBP. To determine the effect of $\{H^+\}$ on Pu(IV) extraction, distribution ratios for Pu(IV) were measured at 25°C between 25% TBP in TCE and acidic calcium chloride solutions, which had chloride activities of 30 but different hydrogen ion activities (6.36 and 24.0). The solid symbols in Fig. II-13 show the plot of the results. Distribution results obtained[21] previously from HCl only and acidic chloride salt solutions are also plotted for comparison. The acidic calcium chloride solution containing less HCl and having a lower

*Student Research Participant.

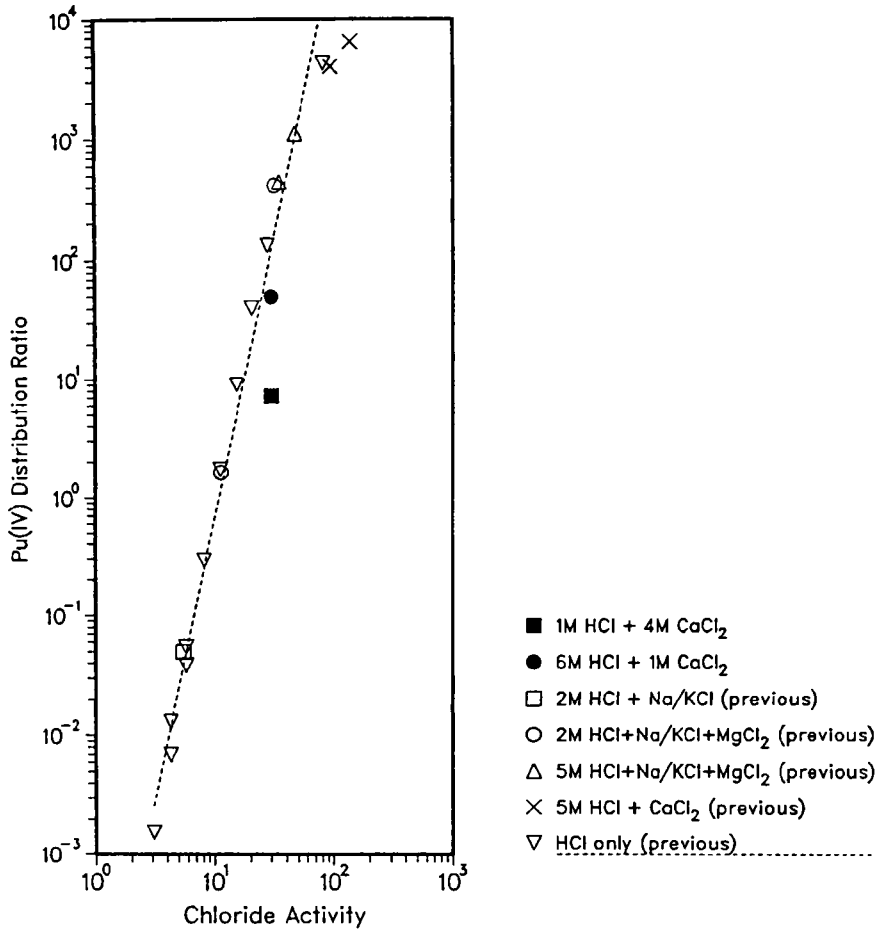

Fig. II-13. Pu(IV) Distribution Ratios between 25% TBP in TCE and Acidic Chloride Solutions at 25.0°C

hydrogen ion activity (1M HCl + 4M $CaCl_2$) was found to have the lower distribution ratio. These results seem to corroborate the belief that protonated Pu(IV)-chloride species are being extracted.

To determine the solvent dependency of HCl extraction, HCl distribution ratios between aqueous phases containing 6 or 7M HCl and TBP in TCE solutions were measured at 25°C. The distribution results for both series of experiments are plotted in Fig. II-14 as functions of the total TBP concentration. Although the distribution ratios measured for 7M HCl are greater than those for 6M HCl, the slopes of the two curves are not the same. The slope is ~3 for the 6M HCl study and ~2 for the 7M HCl study. This decrease in the slope with an increase in $[HCl]_{aq}$ indicates that fewer TBP molecules are associated with each HCl in the organic phase as the organic-phase [HCl] increases.

Experiments measuring the Fe(III) distribution ratios between 25% TBP in TCE and (1) acidic chloride solutions at 25°C and (2) 2.0 and 4.0M HCl at 40°C were done to determine the effects of salts and temperature on the distribution ratio. Figure II-15 shows the results for various acidic chloride salt solutions at 25°C. The results for HCl-only solutions are also

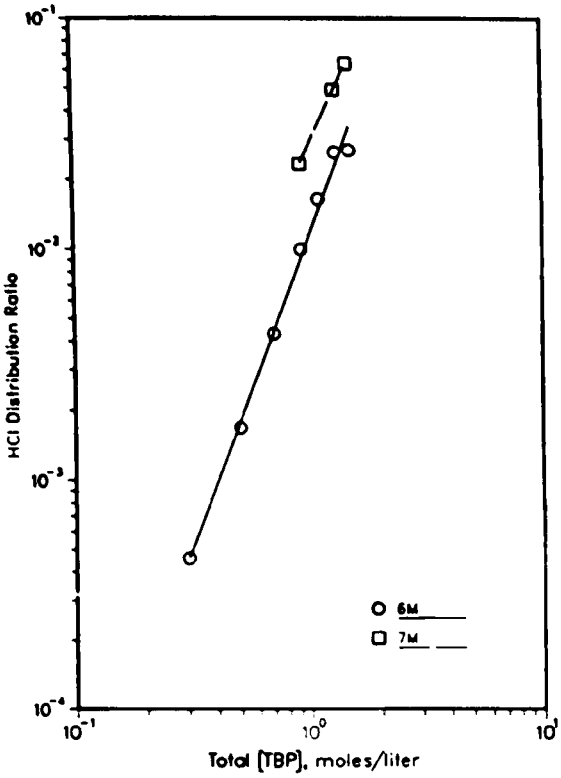

Fig. II-14.

HCl Distribution Ratios between Aqueous Phases Containing 6 or 7M HCl and 25% TBP in TCE at 25.0°C

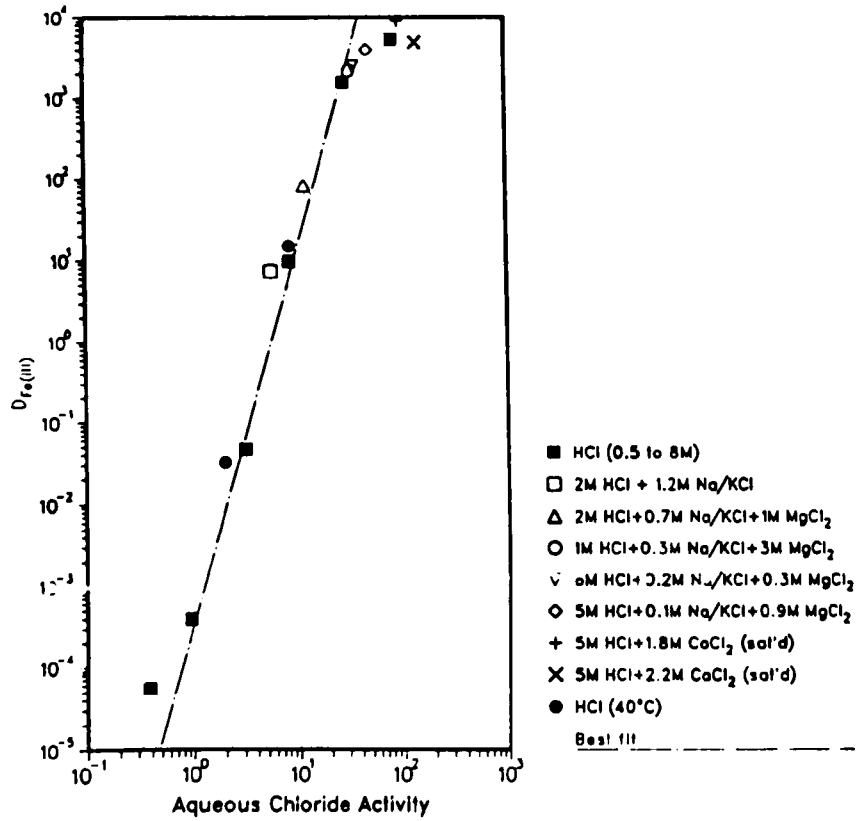

Fig. II-15. Fe(III) Distribution Ratios between 25% TBP in TCE and Acidic Chloride Solutions at 25.0 and 40.0°C

shown (solid symbols) for comparison. Of the seven distribution ratios measured for the acidic chloride salt solutions, five of them are $>10^3$. The two lowest distribution ratios for these salt solutions fall close to (but not on) the line which best fits the HCl-only data and has a slope of 3.6. These results indicate that 25% TBP in TCE extracts Fe(III) very well ($D \geq 10$) from acidic chloride salt solutions that simulate MSE, ER, or DOR salt wastes dissolved in either 2 or 6M HCl. Two Fe(III) distribution ratios measured at 40°C with HCl are also shown in Fig. II-15. These results indicate that the Fe(III) extraction equilibria have only a slight, if any, temperature dependence.

The TBP dependency of the Fe(III) distribution ratios was measured at 25°C between 6M HCl and 0.1 to 1.5M TBP in TCE, and the results are given in Fig. II-16. The best-fit curve has a slope of 3.5. This slope suggests that three or possibly four TBP molecules are involved in the extraction of Fe(III).

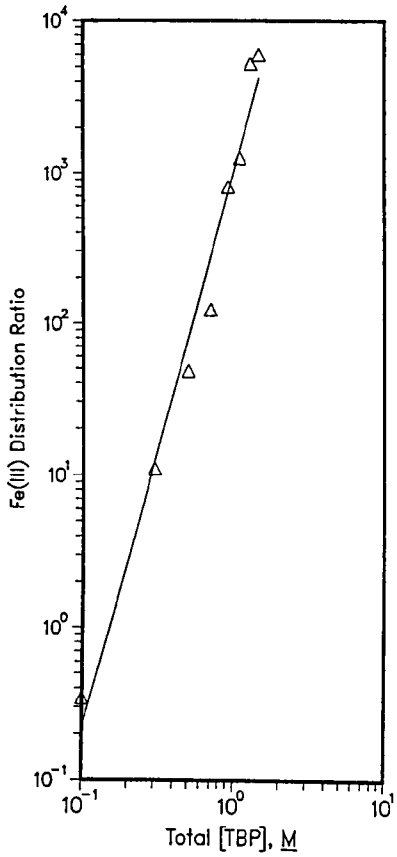

Fig. II-16.

Fe(III) Distribution Ratios between 6M HCl and TBP in TCE Solutions at 25°C.

Some chloride salt wastes contain significant amounts of metallic zinc. Although these wastes will probably not be processed by dissolving the wastes in HCl, which would produce H_2, wastes containing Zn^{2+} may eventually be processed through the PUREX-TRUEX flowsheet. Zinc(II) distribution ratios have been measured at 25 and 40°C as a function of the aqueous phase composition to determine the effects of salts and temperature on the extraction of Zn(II). The distribution ratios measured between 25% TBP and TCE and

acidic chloride salt solutions at 25°C are plotted as a function of aqueous-phase chloride activity in Fig. II-17, along with the HCl-only results. The seven data points for the salt solutions fall below the line that best fits the HCl-only results and has a slope of 0.7. Clearly, Zn(II) extraction is not only affected by chloride ion, but increases in hydrogen ion activity also increase its extraction.

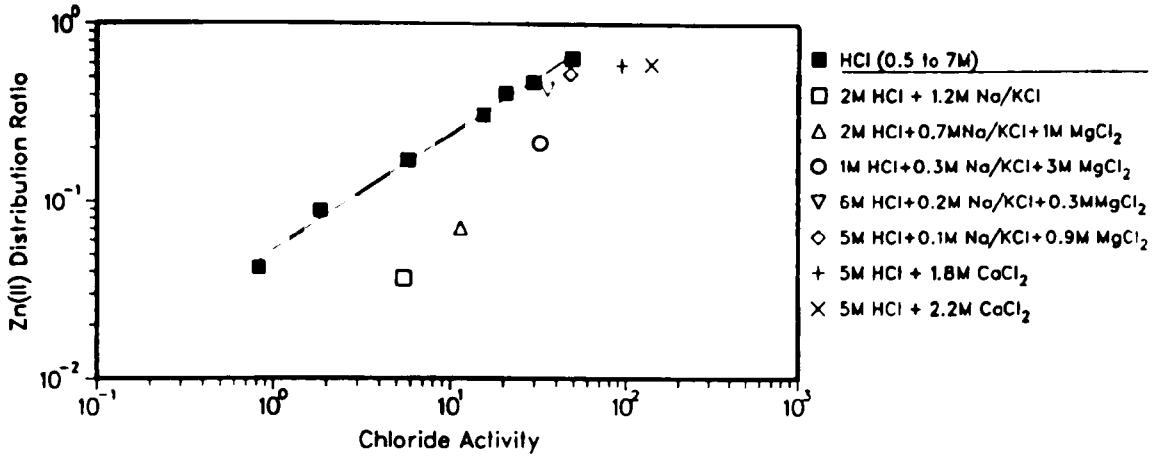

Fig. II-17. Zn(II) Distribution Ratios between 25% TBP in TCE and Acidic Chloride Solutions at 25.0°C. (Curve represents best fit of HCl-only data.)

The Zn(II) distribution ratios measured at 40°C between 25% TBP in TCE and 2-8M HCl were also found to be lower, by approximately 30%, than the HCl-only values measured at 25°C. According to these results, the recovery of Pu(IV) from an acidic chloride solution containing Zn(II) should be possible.

Distribution ratios for Zn(II) were measured between 6M HCl and 0.5 to 1.5M TBP in TCE to determine the TBP dependency of the distribution ratio at 25°C. The results are presented in Fig. II-18. The data points yield a straight line with a slope of 3.4. This slope suggests that Zn(II)-chloride complexes are extracted with three or possibly four TBP molecules.

Distribution ratios for Am(III) between 25% TBP in TCE and HCl-only solutions (4-8M) were found to be $<10^{-2}$. To determine the extent that the presence of NaCl, KCl, and $MgCl_2$ salts would enhance the extraction of Am(III) and to verify the use of chloride activity calculations, distribution ratios from acidic chloride salt solutions were also determined. For salt solutions having chloride activities between 4 and 140, the Am(III) distribution ratios were found to be less than 10^{-2} and verified calculations based on chloride activity.

Distribution ratios for Ca(II) and Ce(III) between 25% TBP and TCE and 2 to 8M HCl were measured at 25°C to determine if either of these two metal ions might interfere in the extraction of Pu(IV) by TBP. The measured

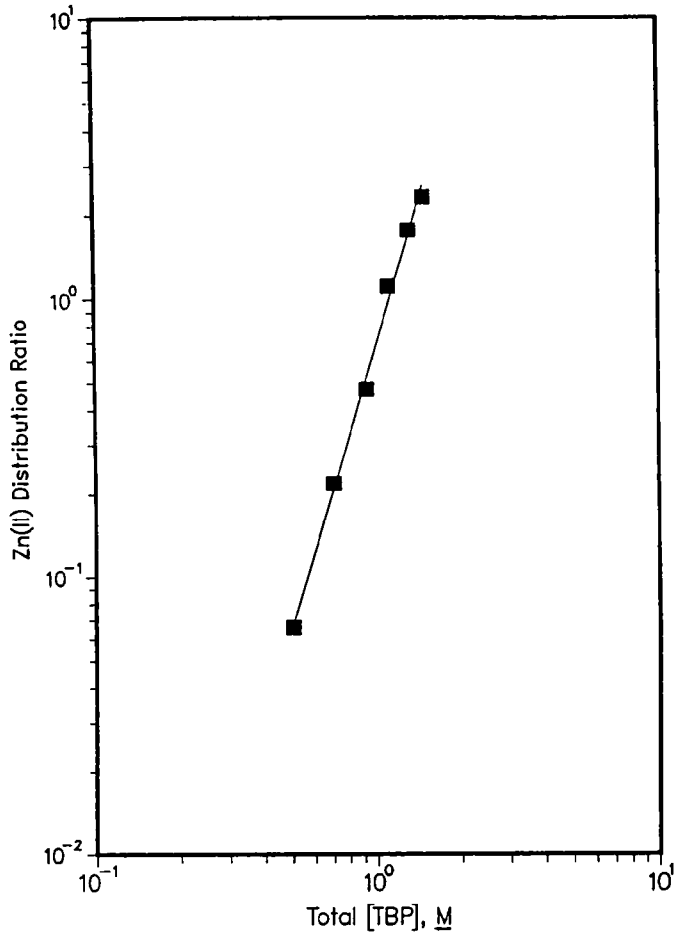

Fig. II-18. Zn(II) Distribution Ratios between 6M HCl and TBP in TCE Solutions at 25.0°C

distribution ratios were less than 10^{-2} for both metal ions; thus, neither of them should interfere in the extraction of Pu(IV).

b. TRUEX-TCE Cycle

Distribution ratios for Am(III) between 0.5M CMPO in TCE and acidic chloride solutions simulating dissolved MSE, ER, and DOR salt wastes have been measured to determine the effects of NaCl/KCl/$MgCl_2$ mixtures and $CaCl_2$ on the extraction of Am(III) at 25°C. A plot of the results is presented in Fig. II-19. For comparison, the distribution ratios for aqueous phases containing only HCl at 25 and 40°C were also measured and are shown (solid symbols) in the figure. Extraction of Am(III) as a complex with two or three CMPO molecules is suggested by the slope of 2.6 for the line derived from the HCl-only data. The Am(III) distribution ratios for the NaCl/KCl/$MgCl_2$ solutions are all higher than those for the HCl-only solutions; this indicates, as expected, that the presence of NaCl/KCl/$MgCl_2$ enhances Am(III) extraction in a way predictable by the use of chloride activities. On the other hand, the Am(III) distribution ratio measured for one $CaCl_2$ solution is less than predicted. It thus appears that the activity calculations for chloride in mixed HCl/$CaCl_2$ solutions are not accurate. As expected, an increase in temperature decreased the Am(III) distribution ratio.

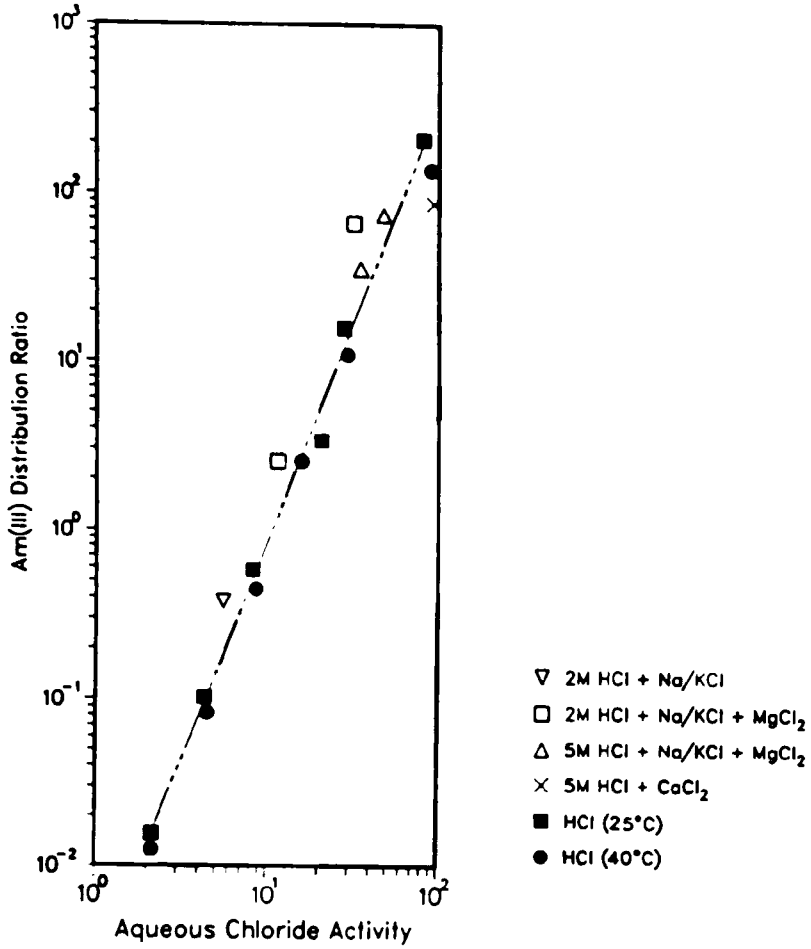

Fig. II-19. Am(III) Distribution Ratios between 0.5M CMPO in TCE and Acidic Chloride Solutions at 25.0 and 40.0°C. (Curve represents best fit for HCl-only results.)

The effect of NaCl, KCl, $MgCl_2$, and $CaCl_2$ salts on the extraction of HCl by CMPO was determined by equilibrating the acidic chloride salt solutions with 0.5M CMPO-TCE and measuring the HCl extracted at 25°C. A plot of the HCl concentration in the organic solution versus the aqueous HCl activity is presented in Fig. II-20 along with the HCl-only results which were obtained by Horwitz et al.[8] Two of the three points measured with the chloride salts fall on the curve defined by the HCl-only data, while the third point, for the acidic calcium chloride solution, falls away from the curve. These results indicate that the [HCl] in the organic phase can be predicted from the aqueous {HCl}, defined as $\{H^+\}\{Cl^-\}$ in HCl solutions containing NaCl, KCl, and $MgCl_2$. Again, it appears that the chloride activity for the mixed $HCl/CaCl_2$ solutions is over-calculated.

2. Contactor Operation

An eight-stage centrifugal contactor with 4-cm rotor was designed in CMT for use in processing HCl/brine waste solutions at LANL. Corrosion of the Hastelloy C-276 contactor was observed, as expected, and appeared to be enhanced by the presence of $NaClO_2$. To overcome this problem, a proposal to

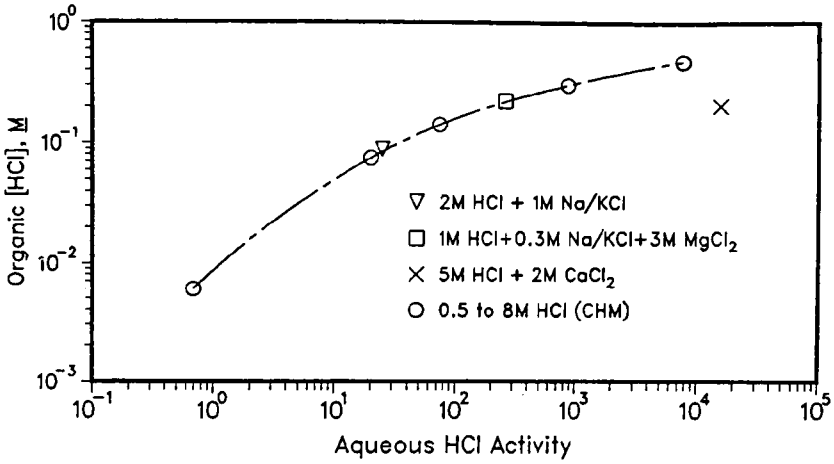

Fig. II-20. HCl Extraction by 0.5M CMPO from Acidic Chloride Solutions at 25°C. Results for 0.5 to 8M HCl are from Ref. 8.

develop a 4-cm contactor made of corrosion-resistant fluorocarbon material such as Kynar was prepared. As part of this work, either an 8-stage or 16-stage contactor would be built and tested. In this contactor, all surfaces that would come in contact with the process liquid would be a fluorocarbon material with one or two possible exceptions, where Hastelloy C-22, which is much more corrosion resistant than Hastelloy C-276, might be used.

3. Model for the Extraction of Pu(IV) in the PUREX-TCE Cycle

Work was initiated on a model to permit optimization of the conditions for the PUREX part of the PUREX-TRUEX flowsheet according to the composition of the feed solution. From the distribution measurements made for HCl and Pu(IV) and the Pu loading results, we concluded that, to a first approximation, the extraction of Pu(IV) from an acidic chloride medium is described by

$$Pu^{4+} + H^{+} + 5\ Cl^{-} + 3\overline{TBP} = \overline{(PuCl_4 \cdot 3TBP) \cdot HCl} \qquad \text{(II-32)}$$

$$HCl + 3\overline{TBP} = \overline{HCl \cdot 3TBP} \qquad \text{(II-33)}$$

These two equations are being used as starting points for the development of a Pu(IV) extraction model.

C. Plutonium Finishing Plant Processing
(L. Burris, G. F. Vandegrift, R. A. Leonard, D. J. Chaiko, D. B. Chamberlain, D. R. Fredrickson, and J. E. Stangel*)

In our cooperative effort with Westinghouse Hanford operations and members of the Chemistry Division, ANL is providing the technical support that

*Co-op student from Georgia Institute of Technology.

is required to implement TRUEX processing of the waste streams in the Plutonium Finishing Plant (PFP) at Westinghouse Hanford. Major tasks include (1) providing a 4-stage 10-cm centrifugal contactor for Westinghouse Hanford, (2) establishing a reference procedure for cleanup of TRUEX process solvent, (3) establishing and documenting specifications for SX-grade CMPO, (4) assisting Westinghouse Hanford in countercurrent testing of the flowsheet using actual Plutonium Recovery Facility waste, (5) identifying key points and appropriate instrumentation for process monitoring and control, and (6) documenting progress with monthly and year-end reports. We have been cooperating with Hanford on site-specific implementations of TRUEX processing for four years.

1. TRUEX Flowsheet

Based on an earlier evaluation of the extraction, scrub, and strip sections[22] and on the solvent cleanup results obtained in FY 1987, a reference flowsheet for the TRUEX processing of PFP waste was developed (see Fig. II-21). This flowsheet gives the complete solvent extraction process, including the solvent cleanup stages. An early version of the SASSE (Spreadsheet Algorithm for Stagewise Solvent Extraction) worksheet being developed as part of the TRUEX Technology Base Development Program (Sec. II.A) was used to (1) evaluate the operation of the extraction, scrub, and two strip sections of this TRUEX flowsheet, (2) guide initial countercurrent tests at Westinghouse Hanford with actual PFP waste, and (3) evaluate process control requirements.

This reference flowsheet for TRUEX processing of PFP waste has been given to Westinghouse Hanford, which has begun countercurrent tests using 4-cm centrifugal contactors of the Argonne design. We have provided technical assistance for these tests. The first two hot tests with actual waste from PFP were run in September 1987; and both the contactors and the TRUEX flowsheet worked well. The microfiltration unit for the TRUEX (DF) feed was found to be the step which limits process throughput. While analytical results are not yet complete, initial radiation counts of the aqueous raffinate (DW) and the exiting solvent indicate that they have the very low levels of Am and Pu that were expected. Before more tests are made, eight contactor stages will be added to the eight stages already being used. These additional stages, built at Hanford following the Argonne design, will simplify tests planned at Westinghouse Hanford in FY 1988.

2. Testing of Prototype Centrifugal Contactors

Construction of a prototype 4-stage 10-cm centrifugal contactor for Westinghouse Hanford was completed, the unit was tested at ANL, the need for several modifications was identified and made, and the fully operational unit (see Fig. II-22) was shipped so that it arrived at Hanford by the end of FY 1987.

Modifications to the 10-cm contactor were required to eliminate excessive vibrations. To assist us in making the appropriate modifications and to develop our ability to overcome such problems in the future, Professor Larry D. Mitchell, Department of Mechanical Engineering, Virginia Polytechnic Institute and State University (VPI&SU), was hired as a consultant. He made two visits here, developed a computer model for the initial design so that its operation could be understood more fully, and trained us in the use of the

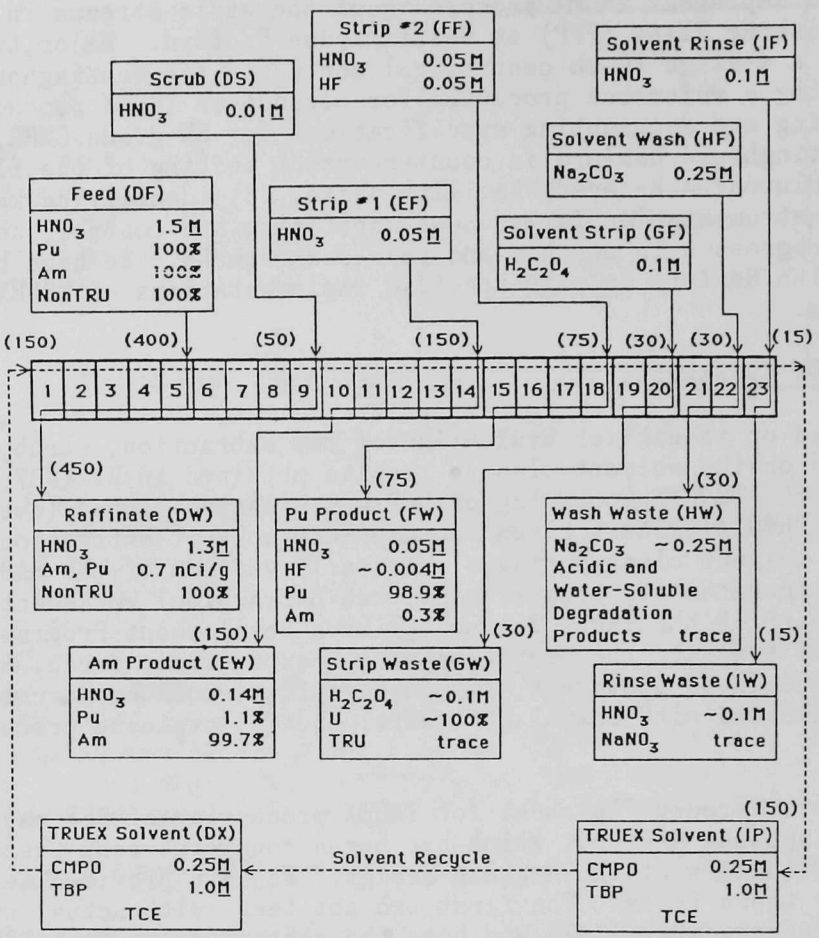

Fig. II-21. Reference Flowsheet for TRUEX Processing of PFP Waste

BEAM IV computer program that was used to do the modeling. As a part of our agreement with Dr. Mitchell, we now have a site-wide license to use this program, which will be set up on the CMT VAX where it can be accessed for use in future contactor designs using a Macintosh computer with a Tektronix terminal emulator (VersaTerm).

To achieve contactor operation with an acceptably low level of vibration, we had to replace the original 1/6-hp motor with a 1-hp Baldor motor (Model VL3510T). With the model developed at VPI&SU using BEAM IV, we were able to determine that the smaller motor could not be used because of its small shaft diameter, 3/8-in. (~1 cm). The 1-hp motor has a 7/8-in. dia (~2 cm) shaft which is stiff enough to control contactor vibrations.

In addition, based on our discussions with Dr. Mitchell, we eliminated the use of vibrational velocity for our vibration specification because it is a relative test rather than an absolute test; that is, the vibrational velocity will vary depending on where the measurement is made. In its stead, we measured the movement of the motor shaft near the motor bearing relative to the motor housing. If this movement is within the motor manufacturer's specifications, then the stress on the bearings will be acceptable

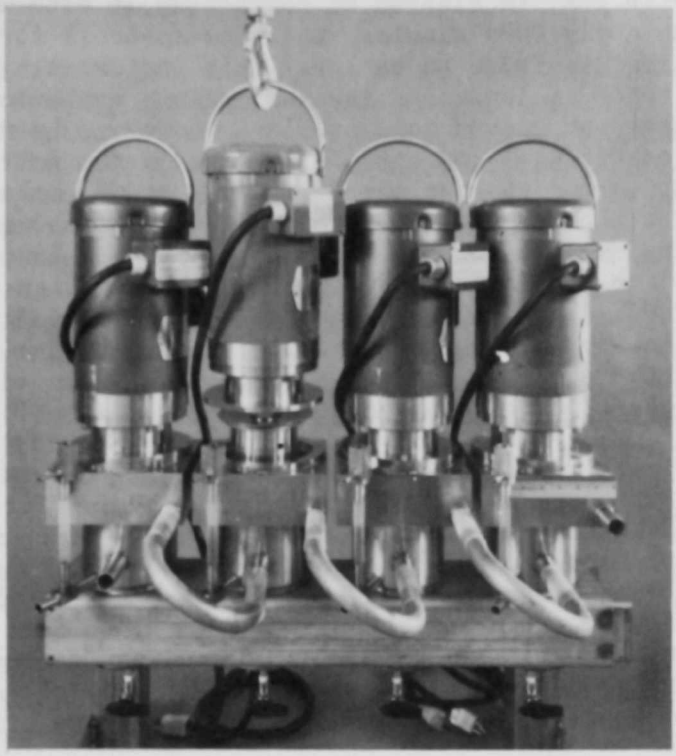

Fig. II-22. Photograph of Prototype 10-cm Contactors

and one can expect a long life for the bearings and, as a result, the satisfactory operation of the contactor stage. Following a procedure outlined by Dr. Mitchell, we made these measurements to be sure that total shaft movement did not exceed the specifications set by the motor manufacturer of 3.9 mils (99 μm). In all four stages, total shaft movement was found to be within the 3.9-mil limit. This movement was found to increase as the density of the solution in the contactor rotor increased from a relative movement of 0.9 mils (23 μm) with the rotor empty to 1.9 mils (48 μm) when filled with water (1000 g/L density) to 2.9 mils (74 μm) when filled with 1.1M TBP in TCE (1421 g/L density) to 3.8 mils (96 μm) when filled with pure TCE (1614 g/L).

The final mechanical test was to operate the unit with all four stages running and check that no interactions occurred between the stages. Such interactions might cause unacceptable operation even when each single stage operates satisfactorily. This problem did not materialize.

After the design changes were completed, hydraulic tests were made to check that (1) all the rotors held the same volume of liquid and did not leak, (2) the lighter and heavier phases flowed through the contactor in the appropriate directions, and (3) single-phase liquid flow in the contactor followed a previously developed contactor model. A few minor problems were found and corrected. The completed unit, now satisfactory, was shipped to Westinghouse Hanford.

One final question concerns the use of centrifugal contactors for TRUEX processing in that flowsheet section where the TRUEX-TCE solvent (0.25M

CMPO and 0.75M TBP in TCE) is cleaned by contacting it with a 0.25M Na_2CO_3 solution. For some early CMPO samples, the time-to-break for the solvent with 0.25M Na_2CO_3 solution was found to be low. This indicates a low dispersion number (ND_i) and, hence, a low value for the maximum contactor throughput. Recent CMPO lots have not caused this problem. However, by making actual tests in the 4-cm centrifugal contactor with some of the poor CMPO, we were able to demonstrate that contactor operation with Na_2CO_3 solution is still possible with poor-quality CMPO. To do this, the O/A flow ratio in the solvent wash (Na_2CO_3) section of the flowsheet has to be low, in the range from 0.33 to 1.0. For the recent CMPO lots, which have high dispersion numbers with all TRUEX feeds including the solvent wash, any O/A flow ratio can be used, even in the solvent wash section.

3. Instrumental Control and Monitoring

Together with Oak Ridge National Laboratory, ANL is to provide assistance to Westinghouse Hanford in setting up a system for monitoring and controlling the TRUEX process for PFP waste. The ANL effort includes two main items. First, the composition of each incoming and outgoing process stream was reviewed with Westinghouse Hanford personnel. Based on this review, a sensitivity analysis of pertinent process parameters was done with the SASSE worksheet and, from this, the basic process control needs were identified. Second, solvent density was correlated with solvent composition so that solvent density can be used to monitor TCE losses from the process.

a. Process Control

The effect of the various operating parameters that control the TRUEX process was analyzed using SASSE. With the help of SASSE, the key parameters that need to be monitored were identified, along with an estimate of how closely each parameter has to be measured to control the process.

For Am and Pu, their concentrations need to be monitored in the DF feed and the DW raffinate to determine whether the extraction section is operating effectively. It is desirable, but not absolutely necessary, to measure the Am concentration (1) in the FW effluent to determine how much Am is getting through the first strip section and (2) in the first three stages of the first strip section to determine how it is performing. In addition, the Pu concentration in the EW effluent should be measured to determine how much Pu is being removed with the Am in the first strip section. Finally, one should monitor the organic effluent from the solvent cleanup section to check that Am and Pu are being effectively removed.

Sensitivity analysis also shows that the CMPO concentration needs to be monitored within fairly close limits so that both the extraction and strip sections work well. For this reason, the use of solution density to monitor the CMPO concentration can be very useful for day-to-day operation. These measurements should be backed up by more complex analytical techniques to determine that the ratio of TBP to CMPO is not changing.

Finally, the flow rates of the various feed streams need to be controlled based on how their variation would affect process operation. The effect of flow rate variations is determined using (1) sensitivity analysis and (2) plant limits set for Am concentrations in the various effluents.

b. Density Measurements

As a part of our program to develop and implement process control schemes, density was measured and correlated as a function of the TCE, TBP, and CMPO concentration, the temperature, and equilibration with various aqueous phases. The specific aqueous solutions chosen are those that, most typically, are in contact with the solvent just before it exits from a centrifugal contactor after the TRUEX processing of PFP wastes. An overview of the data and correlations is given here.

The density correlation was generated in two stages. First, a correlation that calculates the dry density of solutions containing CMPO, TBP, and TCE was developed. By "dry density," we mean that the organic phase has not been contacted with any aqueous solutions. Second, a correlation was developed to predict the solvent density following equilibration with five different aqueous solutions.

One assumption made in the development of a density correlation was that the TBP/CMPO ratio remains constant. Over a period of several weeks, this is a good assumption because the loss of CMPO or TBP in comparison to the TCE will be very small, and any density changes will be due to the loss of TCE. It is recommended that an analytical technique for measuring the concentration of CMPO and TBP in the solvent should be used occasionally to verify that the TBP/CMPO ratio has not changed.

To collect data for the dry density correlation, densities of one-, two-, and three-component organic solutions of CMPO, TBP, and TCE were measured at 20, 25, and 30°C using a Mettler/Parr DMA-46 density meter that is accurate to 0.1 g/L. Using these data, we developed a model which attributes the difference between the actual molar volume and the ideal molar volume to an excess molar volume. Equations were developed to relate the excess molar volume to the mole fractions of each component in the organic solution.

Based upon this correlation, it was found that the excess molar volumes were small and affect only the fourth significant figure of the molar volume and, hence, of the solution density. Thus, the interaction of the various solvent components is small, and the actual molar volume is almost the same as the ideal molar volume.

Using the dry density correlation for solutions of CMPO, TBP, and TCE, we plotted the calculated density as a function of the measured density (Fig. II-23). (A compilation of the wet density data is also shown in this figure; details on these data are given below). For the calculated densities, the mass of each component measured during solution preparation was used to calculate the solution density. Since the diagonal line indicates perfect agreement between the calculated and measured densities, the dry density correlation accurately predicts the solution density.

The second part of the correlation development was to model the density changes that occur when an organic phase is equilibrated with an aqueous phase.[23] This density change is due to the extraction of various components from the aqueous phase. To generate data for this correlation, TBP-TCE and CMPO-TCE solutions were prepared and equilibrated at 25°C with five aqueous solutions (0.05M HNO_3, 2M HNO_3, 0.05M HF-0.05M HNO_3, 0.25M Na_2CO_3, and water). From the measured densities, the change in density was

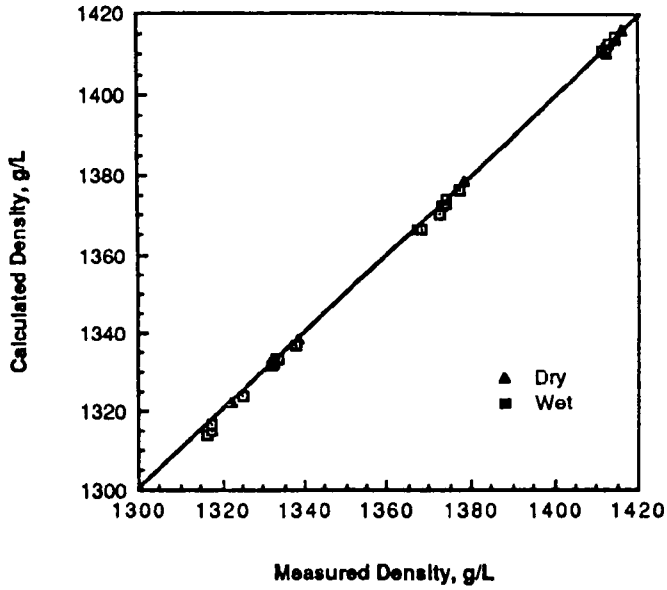

Fig. II-23. Calculated vs. Measured Densities for Solutions of CMPO, TBP, and TCE

plotted as a function of the TBP (or the CMPO) mole fraction. Using a least squares routine, equations were fit to this data. The measured and the calculated densities are plotted in Fig. II-23. The calculated and measured CMPO concentrations agree to within 10.002M, which is adequate for the PFP process.

Two Excel spreadsheets were developed from the dry and wet density correlation. One spreadsheet uses the concentration of both the CMPO and TBP (and the aqueous solution that the organic has been in contact with, if any) to calculate the density of the organic phase and the TCE concentration. The second spreadsheet uses the TBP/CMPO mole ratio, the solution density, and information on whether the solvent had been equilibrated with an aqueous solution to calculate the CMPO, TBP, and TCE concentrations.

D. Production and Separation of ^{99}Mo from LEU
(J. D. Kwok and G. F. Vandegrift)

1. Introduction

Technetium-99m ($t_{1/2}$ = 6.02 h) is the most widely used radionuclide in diagnostic nuclear medicine. It is the decay product of ^{99}Mo ($t_{1/2}$ = 66 h), which is produced in research from the fissioning of ^{235}U or from neutron capture in ^{98}Mo. This effort is concerned with the currently preferred method of producing high specific activity ^{99}Mo from the fissioning of ^{235}U. Presently, ^{99}Mo is produced using a variety of target designs that contain HEU (Highly Enriched Uranium, ~93% ^{235}U). However, safeguard and proliferation concerns have moved the U.S. government to consider prohibiting the export and internal commercial use of HEU. The purpose of this study is to assess the effect on chemical processing of substituting low-enriched

uranium (LEU, <20% ^{235}U) for HEU in targets for production of fission-product ^{99}Mo.

Conversion of present HEU to LEU targets calls for a 5-6 fold increase in total uranium content to produce equivalent ^{99}Mo yields. The incorporation of this larger concentration of uranium in current target geometries will require denser uranium composition. Uranium silicides show promise for use in curved fuel plates because of their relatively higher densities compared to the uranium aluminide currently used. However, because of (1) the different chemical forms of uranium (e.g., U_3Si_x vs. UAl_x) and (2) the need for harder cladding (e.g., A16061 alloy vs. pure aluminum), modifications in the current commercial processes for ^{99}Mo recoveries are necessary.

The process used by the Institut National des Radioelements (IRE) in Belgium involves a basic dissolution of the target in 3M NaOH-4M $NaNO_3$ to precipitate hydroxides of U and dissolve Al and Mo species. Xenon-133 gas is collected during this step. After filtration of the hydroxide precipitate, concentrated HNO_3 is added to the supernatant, and the solution is heated to allow escape of ^{131}I. The IRE process then calls for column separations to purify the Mo-99 product. There are potential problems with the precipitation of silica and/or alumina silicates during the acidification, requiring another filtration and possibly co-precipitating of Mo. We have studied the effect of the presence of dissolved silica, acid concentration, and possibly some uranium on the column separations. The harder A16061 cladding may introduce further radiochemical impurities due to minor metals being present.

2. Dissolution and Precipitation

Based on an analogy to uranium metal dissolution and on our experience in the laboratory with uranium silicides, a strong oxidizing agent such as H_2O_2 is necessary to dissolve the silicides in base. Therefore, it should be feasible to dissolve the A16061 cladding in NaOH while leaving the dense silicides behind. A NaOH dissolution of the cladding avoids problems with contamination by trace metals in the cladding and also avoids precipitation of silica. The decladding solution is separated from the uranium silicide and is discarded. The uranium silicide is dissolved in 1:1 3M NaOH/30% H_2O_2, with the uranium remaining in solution as a peroxide complex. Molybdenum, in the presence of peroxide, should exist as $Mo_2O_{11}^{2-}$. If the pH is lowered at this point to release iodine, the uranyl peroxide will precipitate. In addition, peroxide in solution may destroy the alumina column used to separate the molybdenum. Therefore, destruction of the peroxide while the solution is basic is important. This will also allow the uranium to precipitate as a hydrated oxide for separation from the solution.

Heating will destroy the peroxide, but because the reaction is slow, other methods were tried. Hydroxylamine hydrochloride will speed the reduction of H_2O_2 but it also complexes uranium. Dissolution was also tried with potassium permanganate. This reaction was very quick and complete, yielding a brown precipitate and clear solution. No significant rate increase in the peroxide reaction was noted with the addition of silver metal or iron filings. However, a dilute ferric nitrate solution significantly accelerated the reaction. Apparently, Fe^{3+} initiates a chain reaction involving OH radicals, which destroys hydrogen peroxide.[24] The rate of this reaction drops off when the concentration of peroxide becomes too low to sustain the chain

reaction. At this point, several drops of 0.5M $KMnO_4$ are enough to complete the reaction and allow all the uranium to precipitate. Our original intentions were to avoid permanganate because of the possible interference of manganese, but this may not be a serious problem. Although a large amount MnO_2 precipitate formed, it can be filtered out with the uranium hydroxides.

This process was then tested on compatibility study plates left over from RERTR (Reduced Enrichment for Research and Test Reactor Program) testing of silicide fuel (one quarter used for test). These plates have a similar geometry, on a smaller scale, to that of the targets. The Al6061 cladding was dissolved in approximately 150 mL of 3M NaOH, resulting in a significant amount of black precipitate. The resultant solution and the suspended precipitate were poured off, leaving uranium silicide behind. The uranium silicide was then dissolved in 100 mL of 1:1 3M $NaOH/30\%H_2O_2$. This resulted in the familiar orange uranium peroxide solution, which was heated until uranium hydroxide precipitated. Silica and molybdate should remain in solution. This solution is filtered before being used for experiments that sorb molybdenum on alumina columns.

3. Alumina Column Separations

The alumina column separates ^{99}Mo from the bulk of the impurities, including aluminum. Experiments were performed using tracer quantities of ^{99}Mo on alumina columns to determine the effect of silica, acid concentration, and uranyl ion (present only minimally after precipitation) on the yield of molybdenum. Because results from alumina columns were inconsistent, these parameters were explored with batch studies using ^{99}Mo. During the course of the experiments, temperature, pre-equilibration, molybdenum concentration, amount of alumina, and kinetic effects were also studied. Results are shown in Table II-10.

Table II-10. Experimental Conditions and Results from Alumina-Column Experiments Using ^{99}Mo Only

Run	Temp., °C	Loading $[HNO_3]$, M	Flow Rate, mL/min	FWHM,[a] mL	% ^{99}Mo in Effluent	% Yield ^{99}Mo
1	25	0.5	1.2	-	0.12	144[b]
2	25	0.5	0.67	2.3	0.025	104
3	25	0.5	1	4.5	0.031	102
4	25	0.5	1.2	2.4	-	96
5	25	1	1.2	5	0.89	108
6	50	1	1.2	4	-	104

[a]Full width at half maximum.

[b]High yield probably due to counting interference with ^{99m}Tc peak.

Molybdenum aqueous chemistry is highly dependent on both acid and molybdenum concentration and can be very complicated because of polymer formation. However, if $[MoO_4^{2-}] < 0.001M$, then Mo should remain monomeric.[25]

In acid form, alumina adsorbs negative species, especially divalent anions. It does not adsorb well monovalent anions such as chloride and nitrate.[26] Therefore, TcO_4^- should not be as well adsorbed as is MoO_4^{2-}. Under acidic conditions Si, present as $Si(OH)_4$, and UO_2^{2+} should not adsorb at all.

Problems with reproducibility in results from the batch studies led us to explore other parameters that may affect Mo adsorption. These results are summarized in Table II-10. An increase in contact time between the pre-equilibrating acid solution and alumina increased the adsorption coefficient (K_d) so that more Mo was adsorbed.

Equilibration between Mo and alumina is slow, as evidenced by an increase in K_d values with time. Kinetic factors explain the large increase in K_d with a temperature increase to 50°C; equilibrium is approached faster at higher temperatures.

The ^{99}Mo used was produced from ^{98}Mo and had a low specific activity. Therefore, as the ^{99}Mo decayed, the relative amounts of stable Mo to ^{99}Mo increased. Molybdenum concentration was found to affect K_d values, most likely because of the complicated molybdenum polymer chemistry. Under the conditions that we are interested in, ^{99}Mo concentration should be <0.001M, where Mo should exist as the monomer, MoO_4^{2-}. Therefore, Mo concentration should not have a significant effect.

Acid concentration of the loading solution is very important. At high Mo concentration, increasing acid induces polymerization and protonation of the molybdenum and, therefore, reduces its ability to adsorb on alumina. At low Mo concentrations (<0.001M), the monomer probably protonates and does not adsorb well. We found that above 0.5M HNO_3, K_d values decreased significantly, but below 0.5M HNO_3 they increased. It may benefit the IRE process to acidify to 0.1-0.5M HNO_3 instead of to 1M HNO_3.

Because it inhibits adsorption of MoO_4^{2-} on alumina, uranyl ion seems to interact with MoO_4^{2-}. This reinforces the importance of removing uranium prior to the column separation. Silica also has a negative effect on Mo adsorption, probably because of interaction in solution of silica with molybdenum, since silica itself should not adsorb an alumina. This problem is not critical and is probably most easily circumvented by increasing the amount of alumina.

4. Conclusions

Substitution of uranium silicides for the uranium-aluminum alloy or uranium aluminide dispersed fuel used in current target designs will allow the substitution of LEU for HEU in these targets with equivalent ^{99}Mo yield per target and no change in target geometries. However, this substitution will require modifications in current processing steps due to (1) the insolubility of uranium silicides in alkaline solutions and (2) the presence of significant quantities of silicate in solution. The process envisioned now is derived from the experimentation just described. The cladding is dissolved in basic solution, followed by dissolution of the uranium silicide in a basic peroxide solution. The peroxide is then destroyed by heating, with the addition of permanganate if necessary, resulting in the precipitation of the uranium. After separation of the uranium precipitate, the molybdenum-containing

solution is diluted to avoid silicate precipitation and acidified prior to loading onto the alumina column. The adsorbed ^{99}Mo is eluted with ammonium hydroxide and further purified. With these modifications, it is likely that yield and purity of the ^{99}Mo from the processing of LEU-silicide targets will not vary significantly from those of current processing of HEU targets. In FY 1988, we will irradiate uranium silicide to obtain information on the effect of these changes in processing on the purification and yield of ^{99}Mo.

REFERENCES

1. D. J. Chaiko and G. F. Vandegrift, "A Thermodynamic Model of Nitric Acid Extraction by Tri-n-Butyl Phosphate," Nucl. Technol. 82, 152 (1988).

2. E. Hesford and H. A. C. McKay, "The Extraction of Nitrates by Tri-n-Butyl Phosphate (TBP). III," Trans. Faraday Soc. 54, 573 (1958).

3. T. J. Collopy and J. H. Cavendish, "Equilibrium Constants for the System Tri-n-Butyl Phosphate-Water-Nitric Acid," J. Phys. Chem. 64, 1328 (1960).

4. W. Davis, Jr., "Thermodynamics of Extraction of Nitric Acid by Tri-n-Butyl Phosphate-Hydrocarbon Diluent Solutions. I. Distribution Studies with TBP in Amsco 125-82 at Intermediate and Low Acidities," Nucl. Sci. Eng. 14, 159 (1962).

5. J. M. Schaekers, "Estimation of Equilibrium Constants for the Extraction of Nitric Acid by TBP/Kerosene Mixtures," Proc. ISEC '86, DECHEMA, FRG, Vol. I, p. 185 (1986).

6. P. J. Ly, "Contribution à la modelisation des systemes d'extraction liquide-liquide," Rev. Gen. Nucl. 3, 211 (1985).

7. J. C. Mailen, "An Empirical Equation for Estimating Nitric-Acid Extraction by Tri-n-Butyl Phosphate from Nitric Acid and Nitric-Acid/Sodium-Nitrate Solutions," Nucl. Technol. 52, 310 (1981).

8. E. P. Horwitz, H. Diamond, K. A. Martin, and R. Chiarizia, "Extraction of Americium(III) from Chloride Media by Octyl(phenyl)-N,N-diisobutylcarbamoylmethyl-phosphine Oxide," Sol. Extr. Ion Exch. 5(3), 419-446 (1987).

9. J. A. Rand et al., "Isopiestic Determination of the Activity Coefficients of Some Aqueous Rare Earth Electrolyte Solutions at 25°C. 3. The Rare Earth Nitrates," J. Chem. Eng. Data 22, 337 (1977).

10. D. F. Peppard, G. W. Mason, and I. Hucher, J. Inorg. Nucl. Chem. 24, 581 (1962).

11. M. J. Steindler et al., Nuclear Technology Programs Semiannual Progress Report, October 1986-March 1987, Argonne National Laboratory Report ANL-88-28, p. 74 (1988).

12. J. M. Fletcher, "Complexes Derived from RuNO(III) and Ru(IV)," J. Inorg. Nucl. Chem. 8, 277 (1958).

13. J. J. Katz, G. T. Seaborg, and L. R. Morss, The Chemistry of the Actinide Elements, 2nd ed., Vol. 1, Chapman and Hall, London (1986).

14. R. M. Smith and A. E. Martell, Critical Stability Constants, Vol. 4, Plenum Press, New York (1976).

15. D. A. Orth, R. M. Wallace, and D. G. Karraker, "Solvent Extraction Reactions and Mechanisms," in Science and Technology of Tributyl Phosphate, Vol. I, Synthesis, Properties, Reactions and Analysis, W. W. Schulz, J. D. Navratil, and A. E. Talbot, eds., CRC Press, Boca Raton, FL (1984).

16. L. Reichley-Yinger and G. F. Vandegrift, "Recovery of Plutonium and Americium from Chloride Salt Wastes by Solvent Extraction," Sep. Sci. Technol. 23(12&13), 1409-1421 (1988).

17. J. M. Cleveland, The Chemistry of Plutonium, American Nuclear Society, La Grange Park, IL (1979).

18. Z. Kolarik and E. P. Horwitz, "Extraction of Neptunium and Plutonium Nitrates with n-Octyl(Phenyl)-N, N,-diisobutylcarbamoylmethylphosphine Oxide," Sol. Extr. Ion Exch. 6, 247 (1988).

19. G. A. Burney and R. M. Harbour, Radiochemistry of Neptunium, Report NAS-NS-3060, Office of Technical Information, U.S. Atomic Energy Commission (1974).

20. I. L. Jenkins, "Factors Governing the Choice of a $^{237}Np/^{238}Pu$ Separation Process," in Actinide Review 1, 187-211 (1969).

21. M. J. Steindler et al., Nuclear Technology Programs Semiannual Progress Report, October 1986-March 1987, Argonne National Laboratory Report ANL-88-28, p. 96 (1988).

22. R. A. Leonard et al., unpublished information (1987).

23. R. A. Leonard, G. F. Vandegrift, D. G. Kalina, D. F. Fischer, R. W. Bane, L. Burris, E. P. Horwitz, R. Chiarizia, and H. Diamond, The Extraction and Recovery of Plutonium and Americium from Nitric Acid Waste Solutions by the TRUEX Process--Continuing Development Studies, Argonne National Laboratory Report ANL-85-45 (1985).

24. W. C. Schumb, C. N. Satterfiled, R. L. Wentworth, Hydrogen Peroxide, ACS Monograph Series, Reinhold Publishing, New York (1955).

25. J. Steigman, "Chemistry of the Alumina Column," Int. J. Appl. Radiat. Ist. 33, 829 (1982).

26. S. M. Karagiozova, "Study of the Polymerisation of Mo(VI) in Weakly Acidic Concentrated (10^{-2}M) Paramolybdate Solutions Using the Mo/Fe Atomic Ratio of the Equilibration Iron Molybdate Precipitates," Mat. Res. Bull. 20 (1985).

III. HIGH LEVEL WASTE/REPOSITORY INTERACTIONS
(J. K. Bates)

A. Nevada Nuclear Waste Storage Investigations

The Nevada Nuclear Waste Storage Investigation (NNWSI) Project is investigating the tuff beds of Yucca Mountain, Nevada, as a potential location for a high-level radioactive waste repository. As part of the waste package development portion of this project, which is directed by Lawrence Livermore National Laboratory, we are performing experiment to study the behavior of the waste form under anticipated repository conditions. This effort includes (1) the development and performance of a test to measure waste form behavior in unsaturated conditions, (2) the performance of experiments designed to study the behavior of waste package components in an irradiated environment, and (3) the performance of experiments to investigate the reaction of glass with water.

1. NNWSI Glass Waste Form Testing
(J. K. Bates and T. J. Gerding)

Efforts this period have focused on analyzing components from the N2 Unsaturated Test series (a topical report is being prepared on the N2 test results) and performing the N3 Unsaturated Test series using ATM-10 glass.

The Unsaturated Test apparatus provides for collection and containment of liquid and support of the waste package. The waste package assemblage consists of the waste form and a metallic holder having perforated retainers (one above the waste form, the other below) welded to two pins. The waste form holder is presensitized by heating at 550°C for 24 h, then slowly cooling to room temperature. A solution feed system injects test water (EJ-13 well water) into the test apparatus at 90°C. The N3 Unsaturated Test material is ATM-10 glass (simulated West Valley glass containing actinides plus ^{99}Tc) that was received from the Materials Characterization Center (MCC).

Since the ATM-10 glass as received from the MCC had to be remelted to cast the waste form specimens, the composition and redox state may be different from the reported values.[1] The physical properties of the glass are being remeasured, and comparative leach tests were performed to determine whether there is any difference in reactivity between the as-received and cast glass. A core was taken from bar ATM-10-2 (as-received glass) and cut into ten glass disks, and a core was taken from sample 20-5 (cast glass) and cored into nine glass disks. Then, MCC-1 type leach tests were initiated using deionized water at 90°C. Tests were run in duplicate for periods of 56 and 91 days. The test matrix is given in Table III-1, and the results of transuranic release and weight loss (only analyses performed) are given in Table III-2.

The weight loss values and normalized releases of Np, Pu, and Am for the ATM-10 (as received) and ATM-10 (recast) glasses are identical except for the 91-day value for $(NL)_{Am}$, which is less for the recast glass. These data indicate that the recasting process has resulted in no major change in glass performance.

Table III-1. Comparative MCC-1 Leach Tests for ATM-10 Glass

Glass Type	Expt. No.	Sample No.	Expt. Dur., days	Glass Thick., mm	Glass Dia., mm	Glass SA,[a] mm^2	Total SA[a] of Vessel, mm^2	Glass Mass, g In	Glass Mass, g Out	Δ Mass, μg	$(NL)_{wt}$, g/m^2	Leachate pH In	Leachate pH Out	Mass EJ-13 In, g	Mass Total In	Mass, g Out	Δ Mass, g	LPB[b] Mass, g
As-Received ATM-10	C-567	1000	56[c]	1.41	10.93	236.1	472.65	0.35120	0.34838	2840	1.15	5.56	10.09	47.17	155.26	154.64	0.62	46.21
		1001		1.43	10.91	236.8		0.35887	0.35629	2586								
ATM-10-2	C-568	1002	56[c]	1.48	11.11	245.5	481.48	0.35968	0.35698	2700	1.12	5.56	10.11	48.17	156.27	155.70	0.57	47.16
		1003		1.44	10.96	235.9		0.36464	0.36194	2700								
	C-569	1004	91[d]	1.51	10.99	241.9	477.88	0.36289	0.35963	3260	1.37	5.56	10.05	47.78	156.13	155.19	0.97	46.29
		1005		1.44	10.96	235.9		0.35986	0.35657	3290								
	C-570	1006	91[d]	1.28	11.32	246.1	483.20	0.31144	0.30798	3460	1.42	5.56	10.05	48.37	156.73	155.81	0.92	46.93
		1007		1.44	10.89	237.1		0.36321	0.35979	3420								
	Archive	1008						0.36893										
	Archive	1009						0.41898										
Once-Cast ATM-10	C-571	1010	56[c]	1.44	10.94	237.5	476.94	0.35745	0.35473	272	1.15	5.56	10.12	47.58	155.74	155.64	0.70	46.46
		1011		1.48	11.06	238.5		0.34722	0.34449	273								
#20-5	C-572	1012	56[c]	1.42	10.97	238.0	473.48	0.35147	0.34869	278	1.14	5.56	10.11	47.34	155.49	154.94	0.55	45.94
		1013		1.36	10.96	235.5		0.34845	0.33782	263								
	C-573	1014	91[d]	1.42	11.02	239.9	477.59	0.35799	0.35446	353	1.44	5.56	10.02	47.76	156.02	155.12	0.90	46.19
		1015		1.48	10.98	237.7		0.34364	0.34031	333								
	C-574	1016	91[d]	1.42	11.12	243.8	487.81	0.36639	0.36301	338	1.39	5.56	9.90	48.76	156.99	156.09	0.90	47.36
		1017		1.64	10.93	244.0		0.39253	0.38914	339								
	Archive	1018						0.34836										

[a]SA = surface area.

[b]LPE = liquid polyethylene containers.

[c]Date in: 7/29/87; date out: 9/23/87.

[d]Date in: 7/29/87; date out: 9/30/87.

Table III-2. Actinide Release from ATM-10 Glasses

Glass Type	Experiment Duration, days	Normalized Release, g/m^2 $(NL)_{Np}$	$(NL)_{Pu}$	$(NL)_{Am}$	Wt. Loss, g/m^2
ATM-10	56	3.1	9E-4	3.0E-3	1.14
ATM-10 (recast)	56	3.0	1.1E-3	3.2E-3	1.15
ATM-10	91	3.6	7E-4	4.1E-3	1.40
ATM-10 (recast)	91	3.6	7E-4	2.0E-3	1.42

The N3 test was started July 6, 1987 according to the standard Unsaturated Test matrix and has been completed through the 26-week sampling period. The results of cation and transuranic release are shown in Figs. III-1 to -4. Post-test examination revealed that the glass and the retainer sections are not covered with rust-colored precipitates, as observed in the N2 Test series (SRL 165 glass), but look relatively unreacted. This is despite the moderate degree of sensitization known to have been imparted to the retainer sections during the heat treatment process. While complete interpretation of the results is not possible until the test components have been examined, it appears that ATM-10 glass is reacting at about the same rate as the SRL 165 glass when accelerated stainless steel/glass breakdown occurs for the SRL glass, but at a faster rate than when no accelerated reaction occurs in the SRL glass.[2]

The release of plutonium from the glass is difficult to measure due to the relatively small amount of it in the glass. Americium release is easily measured, but the final values are likely to depend strongly on the acid strip component and will be discussed in future reports.

2. NNWSI Parametric Experiments
(J. K. Bates)

Because the NNWSI Unsaturated Test rigidly sets many of the test parameters, the effect that each parameter may have on the final radionuclide release needs to be studied. This is being done in parametric experiments. A description of the parametric experiments in progress, along with their purpose and status, is given in Table III-3. Each of the ongoing experiments has been discussed in detail previously[3-7] and is continuing as scheduled.

The P-VI series of experiments is being done with nonirradiated UO_2 pellets encased in Zircaloy cladding. The Unsaturated Test protocol is being followed except for variations in drop size and interval between water additions. The fuel was in the form of either crushed or individually stacked disks. Two liquid flow rates were used: that normally used in the Unsaturated Tests (0.075 mL, once every 3.5 days) and a low-volume flow (0.075 mL, once every 14 days). The total U released in the experiments to date is shown

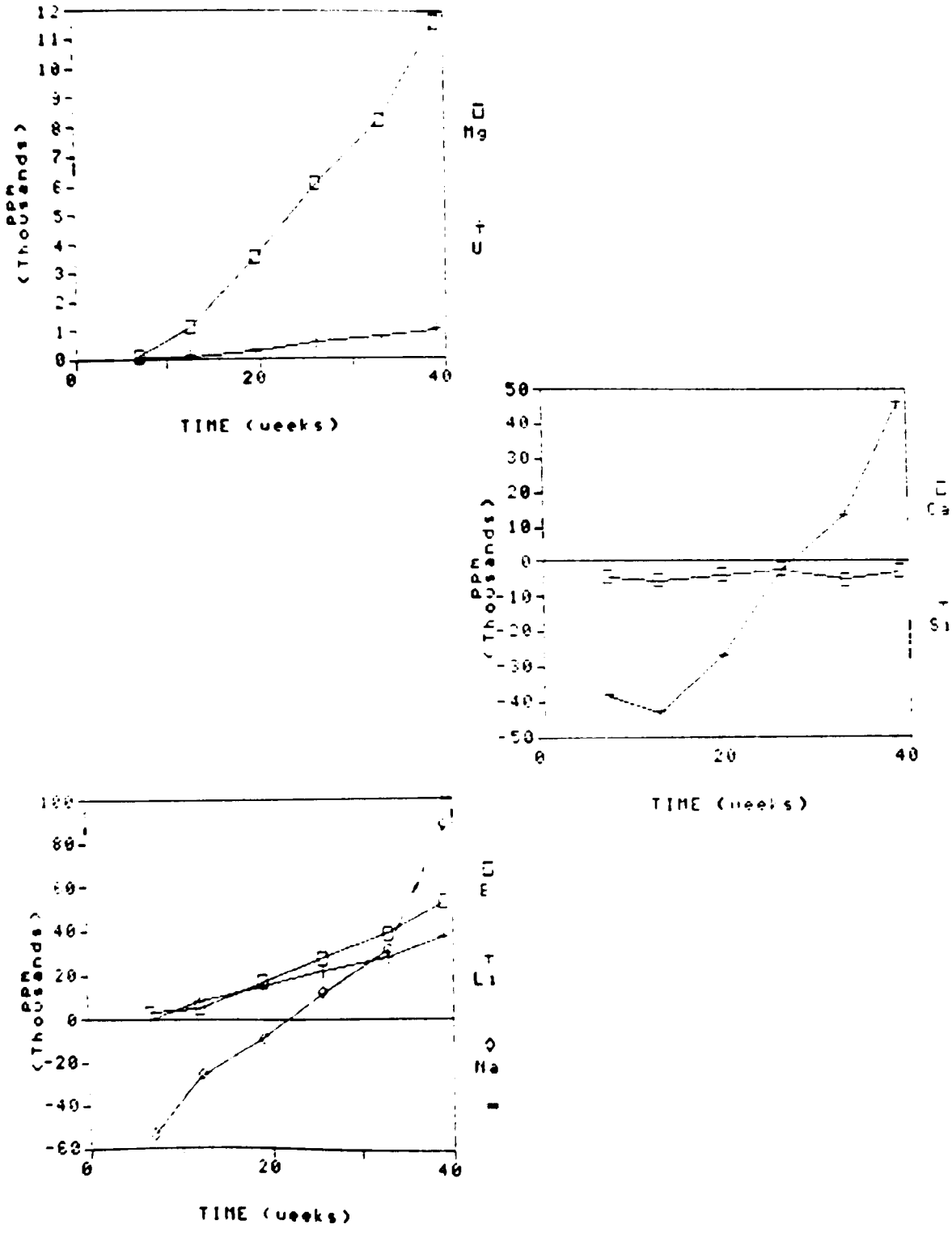

Fig. III-1. Cation Release from the N3 Test Series, No. N3-9

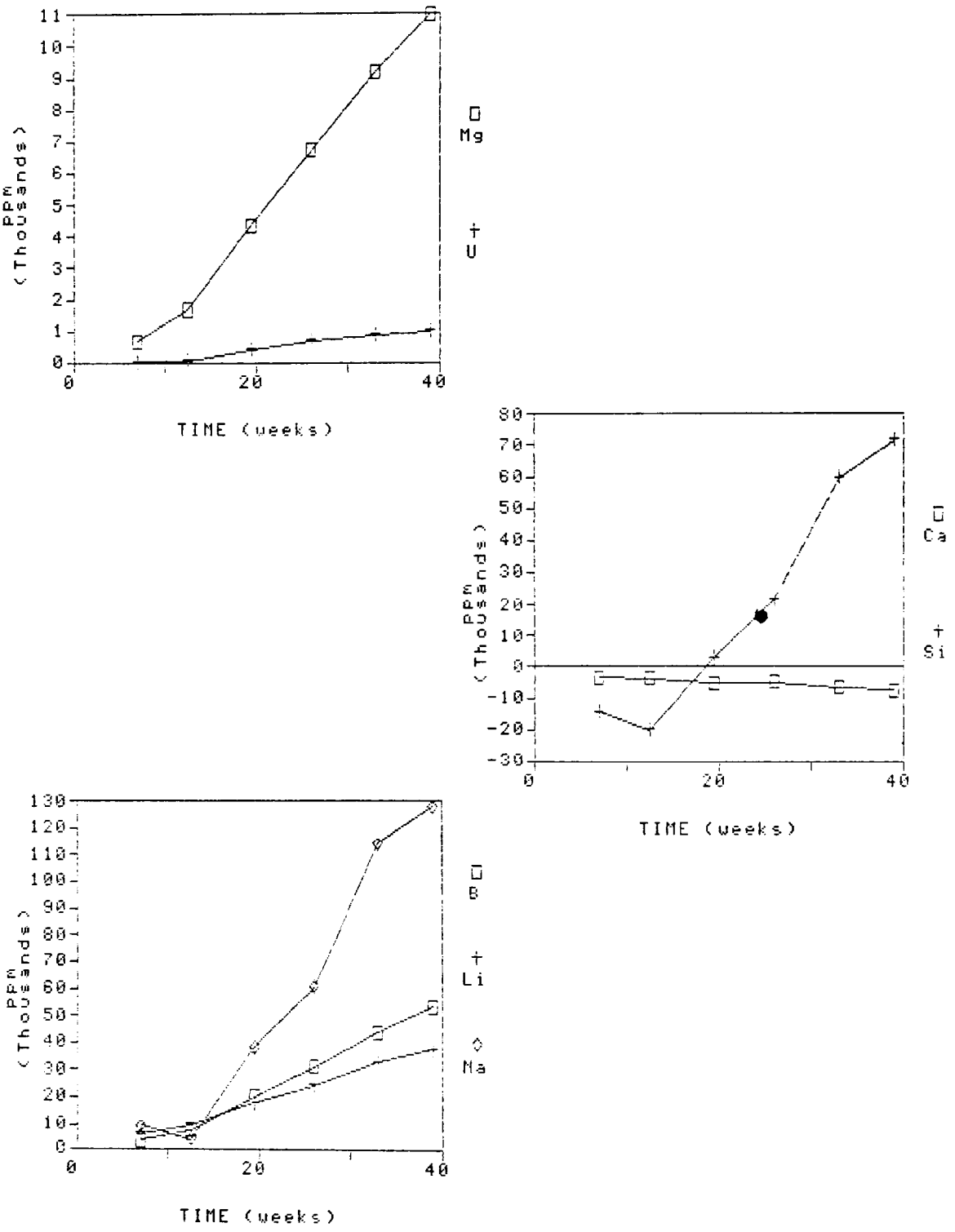

Fig. III-2. Cation Release from the N3 Test Series, No. N3-10

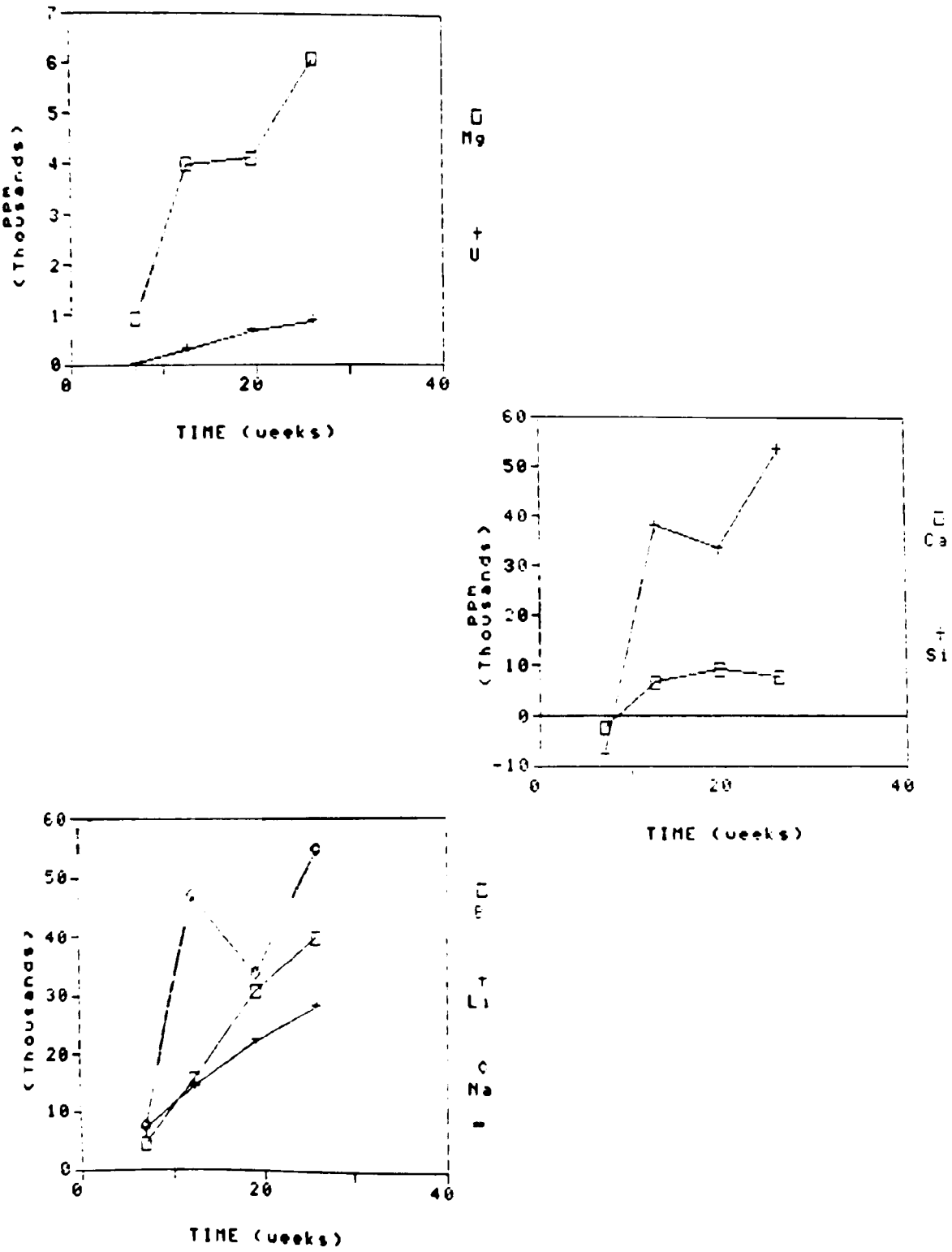

Fig. III-3. Cation Release from the N3 Test Series, No. N3-12

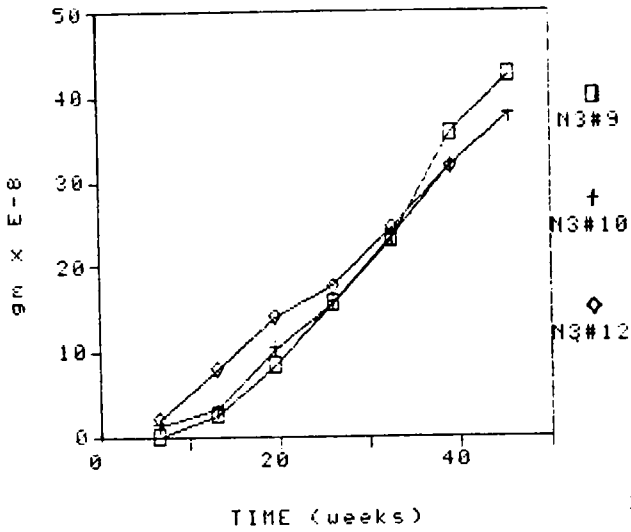

(a)

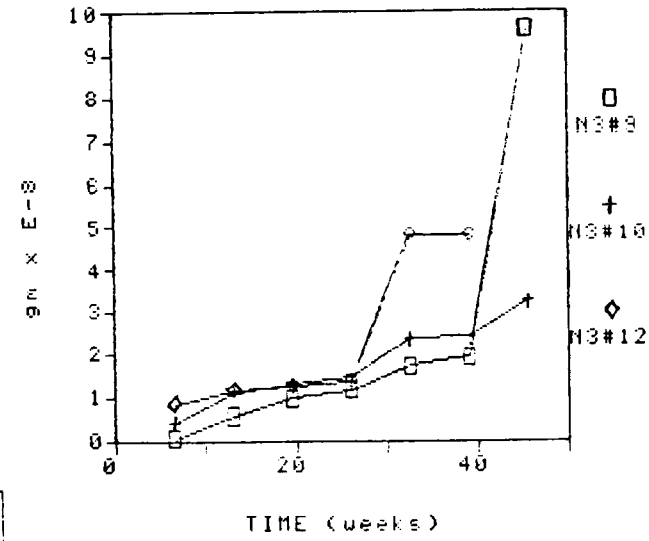

(b)

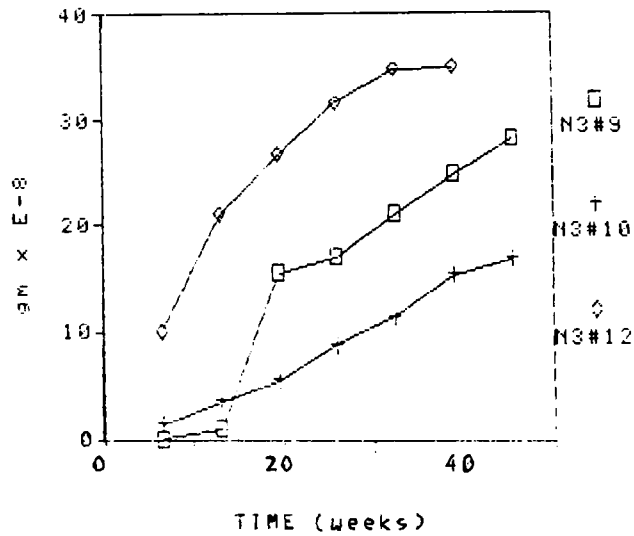

(c)

Fig. III-4. Transuranic Release from the N3 Test Series: (a) Neptunium Release, (b) Plutonium Release, (c) Americium Release

Table III-3. Description, Purpose, and Status of Parametric Experiments

Experiment No.	Description	Purpose	Status
P-II	Regular-sized glass waste form, no SS holder, 0.075 mL J-13/ 3.5 days, continuous and batch expts	To study the release from glass only	Initiated 2/20/84. Batch expts completed 2/18/85. Continuous expts in progress.
P-III	Half-sized glass waste form, SS holder, 0.075 mL and EJ-13/ 3.5 days, continuous and batch expts	To study the effect of waste form surface area by reducing the as-cast surface area by half	Initiated 12/6/84. Batch expts completed 12/5/85. Continuous expts in progress.
P-IV	Half-sized glass waste form, SS holder, 0.0375 mL and EJ-13/ 3.5 days, continuous and batch expts	To study the effect of drop size by reducing the amount of water added and the as-cast surface area by half	Initiated 2/18/85. Batch expts completed through one year. Continuous expts in progress.
P-V	Regular-sized glass waste form, SS holder, 0.075 mL and EJ-13/ 14 days, continuous and batch expts	To study the effect of lengthening the time interval between water additions	Initiated 6/10/85. Batch expts completed through one year. Continuous expts in progress.
P-VI	Pressed and sintered UO_2 pellets in various forms, Zircaloy holder, 0.075 mL and EJ-13/ 3.5 days and 0.0375 mL/7 days, continuous expts	To study the release of U from nonreacted fuel pellets under Unsaturated Test conditions	Initiated 4/25/85. Selected expts terminated to investigate reaction products, the remaining continuous expts in progress.
P-VII	UO_2 pellets soaking in EJ-13 water at ambient temperature, batch expts	To look for reaction product formation	Three- and nine-month batch test terminated.

(Contd)

Table III-3 (Contd)

Experiment No.	Description	Purpose	Status
P-VIII	Regular-sized glass waste forms in presensitized SS holders, 0.075 mL EJ-13/3.5 days, continuous and batch expts	To study the effect of presensitizing the SS waste form holder	Initiated 2/27/86. Batch expts completed through one year. Continuous expts in progress.
P-IX	A variety of glasses (polished, as-cut, powdered) in a controlled atmosphere chamber	To study the effect of the degree of water saturation or glass reaction	Initiated 10/3/86. Selected samples terminated after ~five months and one year, remaining expts still in progress.
P-X	Basaltic and SRL 165 glass vapor hydration expts	To study the use of vapor phase hydration and natural analogues in projecting long-term glass reaction	Review of existing samples and literature initiated, some preliminary expts in progress.
P-XI	SRL 165 U/A glass, WV U/A glass, and ATM-1c/8 vapor hydration	To study the effect of time and temperature on the hydration of nuclear waste glasses under saturated conditions	Sample preparation completed, preliminary matrix completed, additional preliminary expts are in progress.
P-XII	Regular-sized glass waste forms in variously sensitized SS holders, 0.075 mL EJ-13/3.5 days, continuous only	To verify the effect of sensitization on glass reaction	Initiated 11/19/87.

in Fig. III-5. As can be seen, there was little release for about the first 39 weeks, after which the total U released increased dramatically. It appears that neither the drop interval nor form of the UO_2 affects the release dramatically.

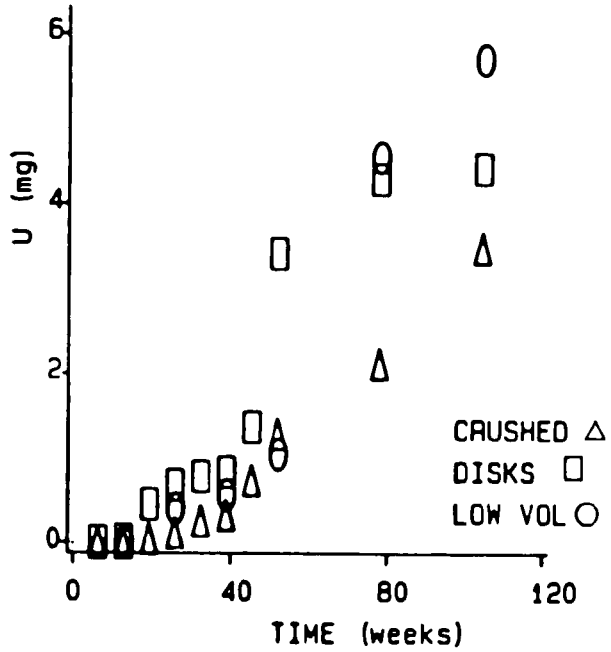

Fig. III-5.

Total Uranium Release from UO_2 Pellets in the P-VI Parametric Experiments

Experiment P-VI, No. 7, was terminated after about two years so that the reacted phase present on the sample surface could be examined. The sample has been studied using optical microscopy, laser Raman microprobe, and X-ray diffraction (XRD).

Optical microscopy indicated the surface was covered with a thick assemblage of reaction products. These products were catalogued according to appearance and position on the sample surface (as identified in photographs). A small portion of the surface was removed for XRD analysis, which yielded the pattern shown in Table III-4. The only identifiable phase was hydrated UO_3 (Fig. III-6). This sample was also subjected to laser Raman microprobe analysis, and the results are discussed in Section III.A.5.

3. Relative Humidity and Simple Glass Experiments
(B. M. Biwer)

The NNWSI repository in Yucca Mountain, Nevada, is located in a hydrologically unsaturated zone. The primary corrosion mechanism for glassified waste forms in such an environment is expected to be one due to vapor phase hydration. Heat generated by such waste containers is expected to drive away any liquid which might be present for a large fraction of the estimated confinement period.

These experiments were designed to (1) probe the dependence of hydration rate on humidity; (2) test the effect of different glass compositions on item (1); and (3) compare the hydration products formed on the

Table III-4. XRD Patterns of Crystalline Phases Formed on UO_2 Surface

Observed XRD Pattern		$UO_3 \cdot (0.8H_2O)$ JCPDS 10-309	
I	d	I	d
60	5.05	100	5.11
		80	3.45
100	3.43	100	3.43
40	2.85	60	2.857
15	2.545	40	2.557
50	2.485	60	2.487
20	2.14	40	2.138
25	2.049	40	2.053
60	1.98	60	1.986
		40	1.971
15	1.82	30	1.817
50	1.78	10	1.782
40	1.74	40	1.740
		20	1.721
30	1.715	30	1.712
30	1.705	20	1.704
		30	1.641
30	1.635	30	1.632
20	1.525	20	1.528

various glasses.[6,7] The glasses under study are the nuclear waste glasses SRL 131, SRL 165, and PNL 76-68 along with the natural glasses obsidian and basalt. The compositions of these glasses are given in Table III-5. Such tests are necessary to gain an understanding of the glass corrosion process. Without this knowledge, reliable lifetime estimates for the integrity of the waste form packages in such an environment as the NNWSI repository cannot be calculated.

All samples have been reacted at a temperature of 75°C in a relative humidity (RH) of 60%, 95%, or 100%. The samples reacted at 60% RH were contained in a Blue M humidity chamber, with all samples exposed to the same atmosphere. Standard operating procedures result in some condensation on the top and sides of the bell jar, and it is possible, although unlikely, that condensed drops could fall on a sample. However, no standing water has been observed on the samples at the termination of any of the experiments, and none of the removed samples has shown signs of being watermarked by such an occurrence.

(a)

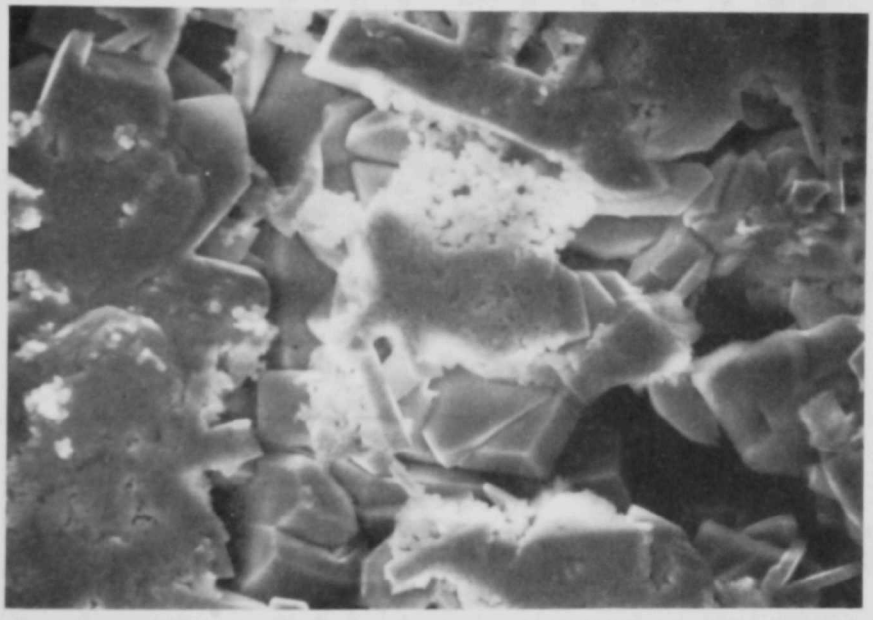

(b)

Fig. III-6. General Surface of UO_2 Pellets Reacted Using the Unsaturated Test Protocol: (a) 200X and (b) 2,000X of Yellow Precipitate Covering the Crystalline $UO_3 \cdot 0.8H_2O$

Table III-5. Glass Compositions for Vapor Hydration Experiments

Glass Type	Composition, Oxide Weight %												
	Al_2O_3	B_2O_3	CaO	Fe_2O_3	K_2O	Li_2O	Na_2O	MgO	MnO	NiO	SiO_2	TiO_2	Other
SRL 165[a]	4.1	6.8	1.6	10.7	0.2	4.2	11.0	0.6	2.8	0.9	53.4	0.2	3.8
SRL 131	3.5	10.9	1.4	14.3	-	4.2	13.7	1.6	3.1	1.8	44.0	0.7	0.8
PNL 76-68	0.6	9.1	2.2	8.7	0.7	-	10.5	0.2	-	0.2	41.2	2.8	23.8
Obsidian	12.5	0.0	1.4	5.4	5.1	0.0	1.4	0.2	0.1	0.0	73.6	0.9	-
Basalt[b]	13.2	-	10.2	11.2	0.6	-	4.5	5.9	0.2	-	49.3	1.70	-

[a]SRL black frit--composition based on the analysis of SRL U glass and the analysis sheet provided by Savannah River Laboratory.

[b]Determined by complete dissolution and inductively coupled plasma/chemical analysis.

The samples exposed to 95% RH were hydrated in a Blue M humidity chamber which does not have the above potential condensation problem, and all of these samples have been exposed to the same atmosphere. The samples reacted at 100% RH were suspended over water in their self-contained Teflon test vessels; additional samples were placed under the deionized water at the bottom of each test vessel for a companion leach test. Each 100% RH test (e.g., V141), therefore, has a corresponding leach test (e.g., L141) associated with it. Some of the samples in the 100% vapor tests were contacted by periodic dripping, as evidenced by their appearance. Improvements have been made in the experimental design to reduce the intermittent dripping.

The vapor hydration experiments are now in their second year, with samples removed after 157 days and 365 days for study. Table III-6 lists the samples removed for study.

Table III-6. Vapor Hydration Samples Available for Study

	157 Day Exposure			365 Day Exposure		
	60% RH	95% RH	100% RH	60% RH	95% RH	100% RH
SRL 165	V126	V104	V141 L141	V127	V105	V142 L142
SRL 131		V108		V129	V109	V144 L144
PNL 76-68		V112		V130	V113	V145 L145
Obsidian		V116		V131	V117	V146 L146
Basalt		V120		V132	V121	V147 L147

All vapor phase samples were weighed after removal from test conditions. No significant gain or loss in mass was observed. The samples were then examined under an optical microscope and photographed. If a significant amount of reactive product is observed on the sample surface, the product is removed for XRD analysis. The 157-day 95% RH samples for SRL 165 (V104), SRL 131 (V108), obsidian (V116), and basalt (V120) were taken directly by F. Ryerson (Lawrence Livermore National Laboratory) for H-profiling as a means of determining the depth of hydration. Unfortunately, the Li concentrations in the SRL 165 and SRL 131 interfered with the H signal, which gave anomalous results. Infrared reflectance measurements subsequently made on the 157-day 95% RH samples indicated that they had become covered with an organic substance, which could also be seen by the naked eye. The samples were then returned to ANL for secondary ion mass spectrometry (SIMS) analysis. Even if

degreased, each sample was seen to have a Si-rich overlayer, which obscured the profiles for the underlying reacted glass. All elements appeared to be depleted with respect to Si. The SIMS data obtained for the 95% RH 157-day samples are not considered valid as a consequence.

The 365-day samples that were not covered by reaction products were analyzed using SIMS. These include all the samples listed in Table III-6 except for the 365-day 95% RH samples (not including obsidian, V117) and the 100% RH nuclear waste glasses (V142, V144, and V145). Scanning electron microscopy (SEM) is being used to examine those samples not amenable to SIMS profiling. Since duplicate samples were reacted for 365 days, one sample for each remains to be studied using techniques yet to be determined. Of interest is the hydrogen profile and the form of water in the hydrated layer of a sample. Hydrogen can be profiled with the existing SIMS if modifications are made to reduce the background water pressure in the system. Infrared and Raman spectroscopies are also possible surface probes.

The SIMS data will be presented separately for each glass type. For reference, Table III-7 presents the sputtering conditions used and the apparent hydration depth as determined by SIMS for all the glasses profiled. When possible, a Dektak profilemeter was used to determine the sputter depth after each profile. Representative SIMS spectra are displayed in Fig. III-7.

Table III-7. Sputter Conditions and Sample Hydration Depth Determined by SIMS Analysis

			Sputter Conditions		
Glass Type	Sample	Hydration Depth, Å	Ion	Voltage, keV	Pressure, torr
SRL 165	V126	750	Ne	2	1.2×10^{-6}
	V141	13,000	Ne	4	2×10^{-6}
	L141	>10,000[a]	Ne	4	2×10^{-6}
	V127	750	Ne	2	1.2×10^{-6}
	L142	40,000	Ar	4	2×10^{-6}
SRL 131	V129	750	Ne	2	1.2×10^{-6}
	L144	>12,250[a]	Ne	4	2×10^{-6}
PNL 76-68	V130	750	Ne	2	1.2×10^{-6}
	L145	45,000	Ar	4	2×10^{-6}
Obsidian	V131		Ar	2	5×10^{-7}
	V117		Ar	2	5×10^{-7}
	V146		Ar	2	5×10^{-7}
	L146		Ar	2	1.2×10^{-6}
Basalt	V132	250	Ne	2	5×10^{-7}
	V147	330	Ne	2	1×10^{-6}
	L147	4500	Ar	2	2×10^{-6}

[a]Total profile not completed.

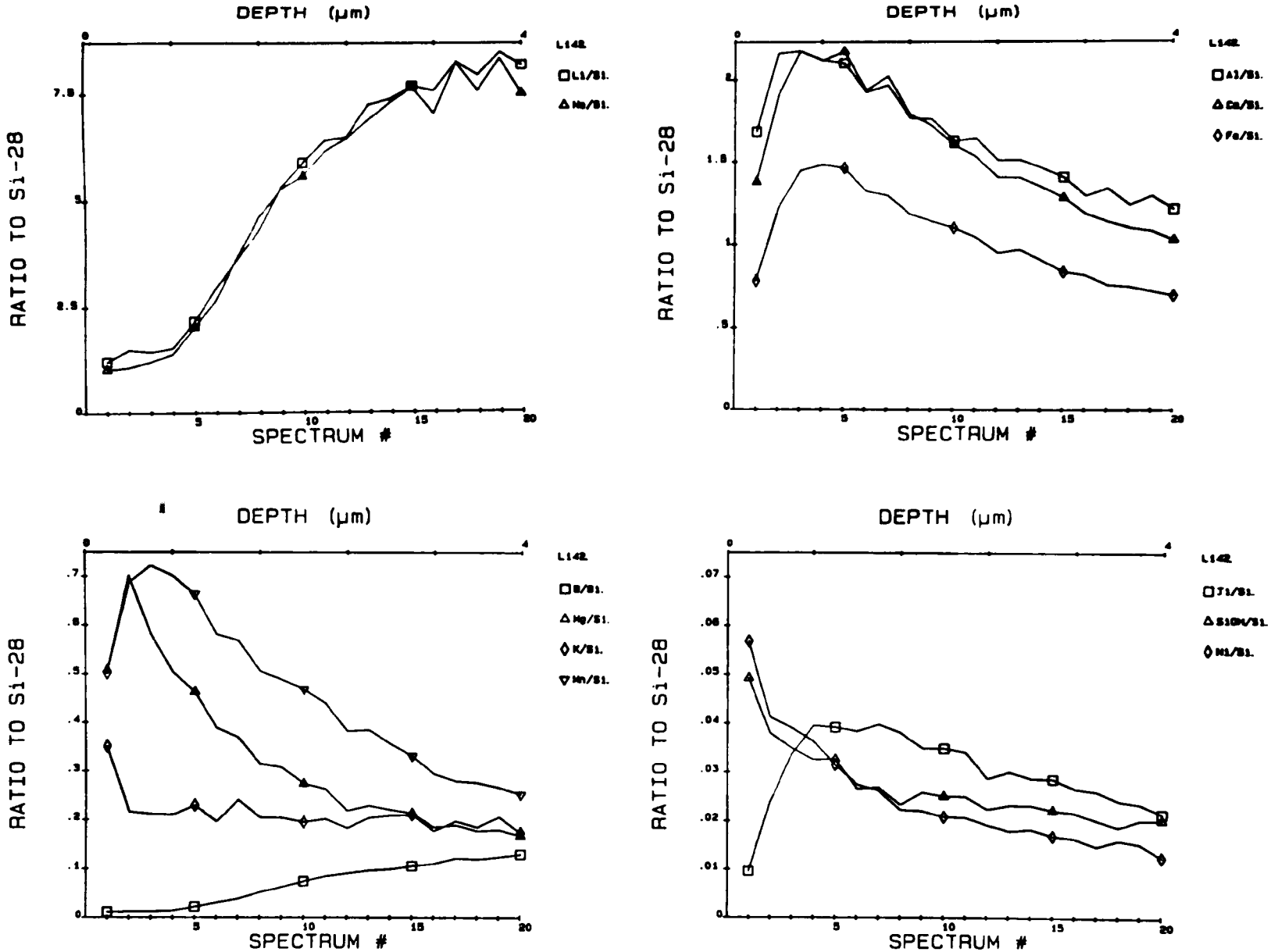

Fig. III-7. SIMS Profiles of SRL 165 Glass (L142) Exposed to Liquid Water at 75°C for 365 Days

a. SRL 165 Glass

The 157-day 60% RH sample (V126) had some surface enrichment of Li and K within the first 100 Å. Possible depletion with respect to Si in the first 300 Å is noted for Al, Fe, Ca, B, and Na. Titanium, Ni, Mg, and Mn all appear to be constant through the hydration layer and into the sample bulk. The hydration layer itself is taken to end at the point where most elements level off to the value observed in the bulk.

The 100% RH sample for 157 days (V141) shows a large depletion of Li, Na, and B in the first 5000 Å and an apparent enrichment of Al, Ca, Fe, and Mn near the surface. Depletion of Li and Na is characteristic of leached samples, since these elements become dissolved in solution after migrating to the surface. In the 100% RH experiments, as the elements migrate toward the glass surface, they should become enriched in the near-surface region. No such enrichment was observed, which suggests that condensation in the 100% RH test vessel could have rinsed the segregated alkalis away from the surface.

The SIMS intensities for each element are plotted relative to the Si-28 signal since Si is the major bulk material. This ratioing is done to minimize effects due to slight scan-to-scan instability of absolute intensity in the system. Enrichment of the Al, Ca, Fe, and Mg is likely due to dissolution of the silicate network whereby these elements are left behind and not segregated to the surface. The samples from higher RH tests had a deeper hydration layer. The 157-day leached sample (L141) shows an even deeper, >10,000 Å, depletion of Li, Na, and B with a near-surface enrichment of K and Al.

After 365 days, the 60% RH sample (V127) shows an even stronger enrichment of the alkalis Li, Na, and K at the surface than was seen after 157 days (V126). Depletion of B and Ca is seen after both test periods. With the strong segregation of the alkalis to the surface, the initial Si intensity is low, thereby giving the initial values of the other elements artificially high ratios. The depletion depths of Ca and B for the two 60% RH samples are both about 750 Å. The cause of these trends, i.e., Li and Na enriched at the surface but not strongly depleted in the subsurface region, and B and Ca depleted in the subsurface region but not enriched on the surface, bears further study. It will be interesting to see whether these trends are observed for the longer term 60% RH samples.

The sample leached for 365 days (L142) exhibits the thickest hydration layer, 40,000 Å, as might be expected. Leaching of Na, Li, and B is observed along with enrichment of the other elements at the surface due to the dissolution of the silica network into the solution.

b. SRL 131 Glass

After 365 days at 60% RH, SRL 131 glass shows strong segregation of Na and Li to the surface within the first 100 Å (V129). Again, the intensities for the other elements are artificially high as a result of the Si concentration being low initially. Most of the other elements would then be constant in concentration through the hydration layer of 750 Å and into the

bulk. Aluminum and boron appear to be depleted in the hydrated layer. A much thicker hydration layer (>12,250 Å) is observed on the 365-day leached sample (L144). Lithium and sodium are depleted in the surface region in addition to Al, Ca, Fe, B, Mg, Mn, and Ti.

c. PNL 76-68 Glass

The PNL 76-68 glass shows high enrichment of Na and Ca at the surface after 365 days at 60% RH and 75°C (V130). Apparent enrichment of K, Fe, and Mg is also observed. Strong depletion of B is observed for the first 400 Å. Aluminum and titanium maintain constant concentrations through the hydration layer (750 Å) and into the bulk. The 365-day leach sample (L145) shows depletion in the hydrated layer of most of the elements present: B, Na, Al, Ca, Ti, and Fe. Possible enrichment of K was noted, with Mg and Ti maintaining constant levels into the bulk.

d. Basalt

The natural glass basalt sample hydrated at 60% RH for 365 days (V132) had a relatively low Si concentration at the surface due, in part, to complementary Na segregation to the surface. The elements Mg, K, Ca, Mn, and Fe were enriched at the surface with respect to Si. The affected region is approximately 250 Å thick and not well defined. The hydration layer for the basalt sample in 100% RH for 365 days (V147) has about the same depth as that for V132. The major difference between the two is the amount of Na at the surface. Buildup of segregated Na on the 100% RH sample is prevented by the condensation in the test vessel rinsing away some of the alkali from the surface. Only a slight surface enrichment of Na and K is present as compared to the 60% RH sample. As a result, the surface concentration of Si is not "depleted," and no "enrichment" of the other elements is observed for V147 or V132. Instead, it is apparent that Al, Ca, Mg, and Fe are all depleted in the first 125 Å. Titanium and nickel maintain constant concentrations through the hydrated layer and into the bulk.

Sodium, K, Ca, and Mg were found to be depleted in the first 1000 Å of L147, the 365-day leached sample. The hydration depth of the leached sample is itself 4500 Å. Aluminum, Fe, and Ti are enriched at the surface; this could indicate dissolution of the silicate network, leaving undissolvable species at the surface. As observed for the other glasses studied, the hydration depth is deeper with increasing humidity:
60% < 95% < 100% < leached.

e. Obsidian

Four obsidian samples were removed from the reaction chambers after 365 days and were analyzed in the optical microscope and with SIMS. All samples appeared nonreacted in reflected light. Thin sections will be prepared for examination using transmitted light at a later date. All of the samples have been examined using SIMS.

Samples V131, V117, and V146 were exposed at relative humidities of 60, 95, and 100%, respectively, while sample L146 was leached in deionized water. The SIMS profiles for sample V131 show a marked absence of

Si on the sample surface. This Si-poor region is about 300 Å thick, after which the Si profile is constant. In the same region where Si is depleted, Ca, Na, Li, and Mg show a clear enrichment. The profiles of Li and Na level off after 300 Å, while the profile for Ca and, perhaps, Mg shows that the enrichment of these elements on the surface corresponds to a depletion in the near-surface region that extends to about 1500 Å. Potassium shows, perhaps, a slight enrichment near the surface, while Al, Fe, and Ti show a flat profile compared to Si.

The overall picture is one where Na, Li, Ca, and Mg form a ~300-Å thick salt layer on the glass surface. Calcium and magnesium are removed from the near-surface region, which results in a measurable depletion of the elements from the first 1500 Å. Sodium and lithium show no such depleted region and are presumably depleted to a lesser degree than Ca and Mg in the near-surface region. While, at this time, the H profile has not been obtained or the penetration of water into the glass has not been measured, it is reasonable that the hydration depth (diffusion of H_2O into the glass) is greater than 1500 Å, and that the observed profiles are part of a process that is occurring separately from the more rapid diffusion of water into the glass.

For sample V117, which was reacted at 95% RH, the Si profile is quite constant, but there is enrichment of Na, Mg, and, perhaps, K on the surface. The enrichment layer is only about 200 Å thick. Sodium shows additional depletion that extends about 700 Å into the glass. Calcium also shows depletion extending >1500 Å into the glass.

For sample V146, there is a slight enrichment of Na and Li on the glass surface and a corresponding slight depletion of Si. For this sample the outer salt layer is only about 50 Å thick. The near-surface region is depleted in Na, reaching the bulk level at about 300 Å. Calcium also shows a near-surface depletion that extends about 1500 Å into the glass. The other elements behave similarly to Si. Thus, for all obsidian samples reacted in vapor, an enrichment of alkalis and alkaline earths is found on the glass surface. The sample reacted in 100% relative humidity shows a more pronounced depletion of Na and Ca.

For the obsidian sample leached in water, L146, there is a depletion of Na or Ca on the surface, which for Na extends about 1100 Å into the glass and for Ca about 2900 Å. However, Si shows marked depletion at the surface, which is compensated by an enrichment of Al, Ti, and Fe. The implication is that, during the leaching process, some dissolution of Si from the glass occurred and left behind residual Al, Fe, and Ti.

Also, it is likely that hydrolysis of the glass matrix is occurring and results in the release of Na and Ca from the glass. The release is greater in liquid water than in vapor and is faster for Ca than for Na.

4. Gamma Irradiation Experiments
(W. L. Ebert and J. K. Bates)

The NNWSI Project has been evaluating the volcanic tuff beds of Yucca Mountain, Nevada, as a potential repository site for the permanent

storage of high-level nuclear waste. Characterising the repository environment many hundreds of years after waste emplacement requires a thorough understanding of the materials interactions which will occur. Radiation fields produced by the waste itself will likely affect the repository performance, and the effects of radiation on the material interactions must be known to accurately predict the repository environment hundreds of years after waste emplacement.

The gamma irradiation of moist air produces nitrogen oxides, which, when dissolved into an aqueous solution, form nitric and nitrous acids that acidify the solution.[8] The waste is planned to be encapsulated in borosilicate glasses, which are known to be more unstable in acidic solutions than in near-neutral solutions.[9] Irradiation of the repository may, therefore, produce small pockets of acidic groundwater in which the waste may be more reactive than in natural groundwater. To understand the repository environment after waste emplacement, it is necessary to first understand how the groundwater is affected by the radiation fields.

The experiments performed were not designed to simulate any one repository scenario, but were designed to monitor waste/repository interactions. Experiments were performed (1) without glass present to determine the effect of radiation on the groundwater alone and (2) with glass present to determine the effect of the irradiated solution on the glass reaction. The series of experiments has been concluded, and the results are summarized below.

Experiments were performed using EJ-13 groundwater and synthetic nuclear waste glass formulations SRL 165, ATM-1c, and ATM-8 under the influence of penetrating gamma irradiation at 90°C. Exposure rates of about 0, 1×10^3, 1×10^4, and 2×10^5 R/h were used in an effort to elucidate the effects of the total gamma radiation exposure on the reaction. Experiments were performed with stainless steel vessels of approximately 22 mL volume. Synthetic waste glass, groundwater, air, and, in some cases, a tuff wafer were placed in the reaction vessels. The amount of groundwater added to a vessel was adjusted to provide an air/liquid volume ratio near 0.3 and a glass surface area/liquid volume ratio near 0.3 cm^{-1}. The vessels were sealed and placed in an oven in the appropriate gamma radiation field and allowed to react for times up to 365 days. After the experiments were terminated, analyses of the leachates and the reacted glass surfaces were performed to characterize the reaction. The results of experiments performed under exposure rates of 2×10^5 and 1×10^4 R/h have been reported previously.[10,11] The results of experiments performed under exposure rates of 0 and 1×10^3 R/h will be reported in detail in a future ANL report.

Irradiation was seen to acidify the EJ-13 groundwater from its initial pH value near 8; however, the high bicarbonate content of the water (~120 ppm) acted to buffer the solution to a pH near 6.4 under all conditions tested. Actual repository conditions wherein liquid groundwater may be present in very small quantities (relative to the volume of air) could possibly become more acidic than the leachates in these experiments because of the limited buffer capacity. The advantage of the tuff repository horizon is that it lies above the water table in the unsaturated zone, and with the scarcity of liquid groundwater, the probability of groundwater contacting the waste and transporting radionuclides away from the repository site is low.

The major influence of penetrating gamma radiation appears to be through acidification of the leachate and lowering of the Eh. Our results have shown the extent of glass reaction to be similar in irradiated and nonirradiated experiments, probably because the release of highly leachable components such as Li, Na, B, or Mo from the glass is not strongly dependent on pH in the range 6.5-9.5. The behavior of some species released from the glass during reaction was influenced by the leachate pH and Eh differences; most noticeably affected were the actinide elements. The solubilities and speciation of the actinides are known to be very pH and Eh sensitive. The distribution of the released actinides between dissolved, suspended, and adsorbed phases was seen to vary slightly at different pH's.

The concentration profiles of elements in the near-surface region of the reacted glasses were obtained using SIMS. The profiles of lithium, sodium, and boron showed these elements to be depleted to the greatest depths and to have sigmoidal profiles consistent with diffusionally controlled release. Other elements having more limited solubilities were seen to be enriched on the outer surface of the glass relative to their bulk concentrations. Figure III-8 shows the SIMS profiles of Li, Al, Fe, B, and Mg for an SRL U sample reacted 91 days in a 1 x 10^3 R/h radiation field at 90°C. The intensities plotted are the measured peak heights divided by the silicon 28 peak height. The sputter.depth is given on the upper horizontal axis. Lithium and boron are depleted to a depth of about 1 μm, while Mg, Al, and Fe are enriched in the outer 0.5 μm of the sample. An altered layer (i.e., a region of different composition) could be seen in the polished cross sections of glasses reacted 91 days or longer using SEM. The SIMS analyses indicate that similar alteration phases form after shorter reaction times but are too thin to be observed in cross sections. The thickness of this layer increased

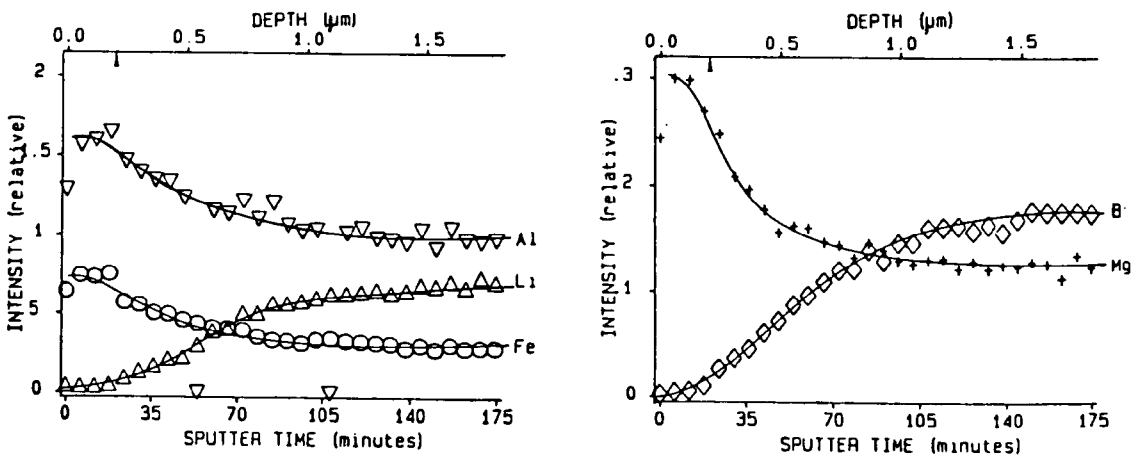

Fig. III-8. The SIMS Profiles of (a) Li-6, Al-27, and Fe-56, and (b) B-11 and Mg-23 for Sample 332. (SRL U glass reacted 91 days at 90°C under 1 x 10^3 R/h gamma radiation. Intensities are normalized to Si-28.)

with reaction time in a nearly parabolic manner. Semiquantitative analysis of this layer showed it to have a composition very similar to nontronite, an iron-rich smectite clay. Similar clays form on reacted natural glasses.[10] The appearance of the altered phase in cracks present in the glass as seen in the polished cross sections suggests that the glass (or the alteration layer) etches to a small extent. This is inferred from the fact that the alteration layer does not completely fill the crack, although the densities of the unreacted glass and the alteration layer are very similar. Such etching is consistent with the silicon concentrations measured in the leachates.

Of particular interest in the repository environment is the behavior of the actinide elements released via glass reaction. Uranium and neptunium were shown by ion microprobe analysis to be depleted in the alteration layer. The uranium was found to be both adsorbed onto the surface of the stainless steel test vessel and fixed in precipitates (as yet unidentified) in both irradiated and nonirradiated experiments. Neptunium was not contained in any surface precipitate but did exist in a suspended phase in the leachate, perhaps being adsorbed onto iron-silicate colloids. A significant amount of neptunium was found in a nonfilterable form as well.

Plutonium was not depleted in the near-surface area of the reacted glass but had a rather flat SIMS profile, similar to that of silicon, although plutonium adsorbed onto the stainless steel vessel surface. Very little plutonium was found in the leachate. Americium was enriched on the outer surface of the alteration phase but showed similar concentrations in the alteration phase and the glass. A small amount of americium was also present on the stainless steel vessel surface.

Uranium and neptunium are thought to be released by a mechanism similar to boron release, while plutonium and americium are released by etching at the alteration layer/leachate interface. Early in the reaction, water infiltrates the glass and an ion-exchange reaction occurs where protons from the water exchange for sodium or lithium in the glass. This raises the pH in the vicinity. A subsequent reaction occurs between boron (or uranium or neptunium) in the glass and a water species, freeing a species containing boron (or uranium or neptunium) from the glass network. This species can then enter solution. The latter reaction may be catalyzed by hydroxide ions because it occurs preferentially under alkaline conditions.

As water continues to infiltrate the glass, glass components are released at various rates to yield a layer having a composition that may vary with depth, the so-called alteration layer. Species at the surface of the alteration layer may become totally dislodged from the residual glass network in the layer and become solvated. In this way, the alteration layer etches. Other species such as Al, Am, and Fe may become enriched at the surface of the alteration layer as the surface etches because of low solubilities. The presence of these insoluble species on and in the alteration layer may, under certain conditions,[12] restrict the flow of water into the glass and thereby slow the reaction.

5. Development of a Laser Raman Microprobe System (W. L. Ebert)

A laser Raman microprobe (LRM) system is being developed to analyze microcrystalline precipitates which form during the hydration of nuclear waste glass. By use of standard microscope objectives, an argon ion laser can be focused to a beam diameter less than 2 μm. This allows spectra to be collected from very small samples without interference from the surrounding substrate. X-ray emission spectroscopy (both energy dispersive and wavelength dispersive), available on the SEM, can be used to analyze the sample. The Raman spectra of compounds having compositions consistent with the unknown can then be consulted for comparative identification. The LRM should be particularly useful in analyzing samples that are too small to be removed from the surface and studied by X-ray diffraction.

The current effort is to obtain spectra of pure compounds to use as standards for comparative identification. Figure III-9 shows the Raman spectra of three uranyl silicates obtained with the LRM. Although the quality

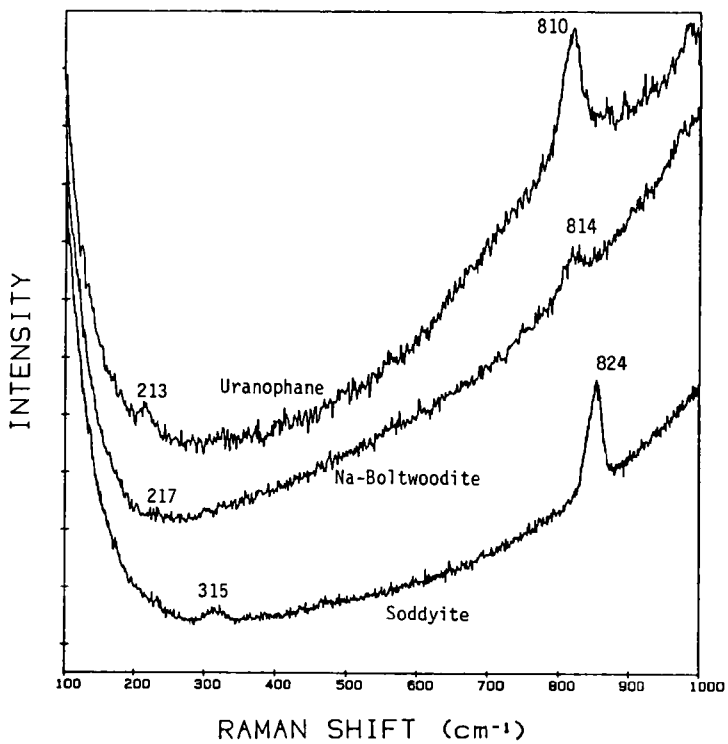

Fig. III-9. Raman Spectra of Uranophane, Sodium Boltwoodite, and Soddyite Obtained Using the Laser Raman Microprobe. Typical power density at sample: 0.1 W/μm^2; spot size: ~80 μm^2; incident beam: 514.5 nm argon.

of the spectra suffers due to the weakness of the collected signals, Raman peaks can be clearly seen to distinguish these compounds. These spectra were collected using an argon ion laser tuned to the 514.5 nm green line. The laser power at the sample is typically 50 mW or less, with a spot size of about 70-80 μm. A large spot size was used in these spectra to collect scattered light from more crystallites and thereby avoid crystal orientation effects. The alignment of the electric field of the incident beam and the polarisation field of the vibration affect the Raman scattering efficiency. Moderate laser power was used to obtain the uranyl because the samples tended to vaporise at higher powers. These uranyl silicates have similar compositions, as shown below:

uranophane	$Ca(UO_2)_2(SiO_3)_2(OH)_2 \cdot 5H_2O$
boltwoodite	$(K,Na)_2(UO_2)_2(SiO_3)_2(OH)_2 \cdot 5H_2O$
soddyite	$(UO_2)_5(SiO_4)_2(OH)_2 \cdot 5H_2O$.

They also have very similar infrared spectra. Raman microprobe analysis provides a convenient method for identifying these compounds.

6. Basalt Analog Experiments (J. J. Maser)

Hydrothermal leaching and vapor phase hydration experiments have been performed using two synthetic basalts and one SRL glass (see Table III-8) and deionised water. A discussion of these experiments has been presented in a previous ANL report.[11] While these experiments were completed under a different sponsor, they provide a wealth of samples and data that still require analysis and interpretation, where the synthesized information will be of use to the NNWSI program. For this reason, work is continuing with these samples.

Table III-8. Compositions of the Three Glasses Used in Experiments of Byers[13]

	Stoichiometry		
	SRL 165	Hawaiian Basalt	Mg-rich Hawaiian Basalt
Li	2.53	-	-
B	1.75	-	-
Na	3.18	1.40	1.37
Mg	0.16	1.43	1.57
Al	0.73	2.52	2.18
Si	8.00	8.00	8.00
K	-	0.13	0.13
Ca	0.26	1.77	1.79
Ti	-	0.21	0.23
Mn	0.29	0.02	0.02
Fe	1.33	1.51	1.55
Ni	0.10	-	-
Zr	0.05	-	-
O	25.77	26.48	26.24

Two test matrices were completed by Byers et al.[13]; in one matrix the glasses were leached at temperatures ranging from 90°C to 187°C for times up to 546 days, and in the second the glasses were vapor hydrated at temperatures ranging from 122°C to 240°C for up to 150 days. The solutions were analyzed for the cation concentrations, and the surfaces of the reacted glasses were characterized to identify mineral phases that had formed. The reacted glasses are being quantitatively analyzed with respect to the layer composition and growth kinetics of the layer.

We obtained quantitative measurements on layer composition for basalt samples hydrothermally leached at 90, 150, and 187°C for varying lengths of time; for a basalt sample that was vapor hydrated at 240°C for 91 days; and for an SRL 165 glass sample leached at 187°C for 183 days. Quantitative analyses were made using a scanning electron microscopy/energy dispersive X-ray spectroscopy (SEM/EDS) system with Princeton Gamma Tech (PGT) System IV software. Spectra were collected from many points on each cross-sectioned sample. Five spectra were collected from the unreacted center of each sample, and these bulk glass spectra were averaged to create a "standard" for the analyses of each sample.

Analysis of reacted layers produces several additional considerations. These types of experiments result in hydrated layers on the glass surface and, since the SEM/EDS system is not sensitive to H_2O, it is assumed that the difference between 100% and the total weight percent determined with this system is due to water in the reacted layer. Analysis of thin layers (<3 μm) also included X-ray examination of bulk glass and the mounting resin. The probed volume was approximately 1 μm^3, depending on the probe current, accelerating voltage, and the density of the material. Consequently, the analyses of the thin layers may vary in total weight percent, but the stoichiometric ratios should be similar if the layer composition is similar. For this reason, results of quantitative analyses are presented in terms of total weight percent of the layer (an indication of the amount of H_2O in the layer) and the stoichiometric ratios of the layer normalized to eight Si atoms (Tables III-9 and III-10). Boron and lithium present in SRL-165 glass cannot be measured with our present SEM/EDS system. Therefore, the analysis of the SRL 165 glass layer assumes that B and Li are not present.

The results in Table III-9 and III-10 are the averages of many (usually ≥10) spectra collected from reacted layers on a sample. In general, the compositions of the layers did not vary significantly. When individual elements did vary, the change did not appear to follow a systematic trend.

The composition of the reacted layer seems to be similar between points on a particular sample and between different samples. The stoichiometries of the analyses are consistent with that of a smectite clay, $(1/2Ca,Na)_{0.7}(Al,Mg,Fe)_4[(Si,Al)_8O_{26}](OH)_4 \cdot nH_2O$. While not an ideal end member, the composition is probably some sort of intermediate clay between nontronite (Fe rich) and saponite (Mg rich). Variations in analyses are more likely due to composition variety than to analytical error and may have resulted from more than one mineral phase being present. Before more definitive discussion is made regarding these layers, further analyses will be made.

Table III-9. Stoichiometric Ratios[a] and Total Weight Percents for Reaction Layer on Hawaiian Basalt Leached at 90-187°C

	Hawaiian Basalt					
	187°C			90°C	150°C	
	#857 (93 days)	#859 (183 days)	#860 (364 days)	#827 (91 days)	#559 (183 days)	#561 (364 days)
Na	0.29 ± 0.10	0.30 ± 0.12	0.40 ± 0.08	0.33 ± 0.33	0.31 ± 0.10	0.51 ± 0.06
Mg	3.64 ± 0.61	4.05 ± 0.53	3.68 ± 0.85	2.32 ± 0.87	0.31 ± 0.97	3.46 ± 0.55
Al	4.42 ± 0.30	4.58 ± 0.17	3.96 ± 0.30	4.13 ± 0.50	4.16 ± 0.29	4.05 ± 0.20
Si	8.00 ± 0.00	8.00 ± 0.00	8.00 ± 0.00	8.00 ± 0.00	8.00 ± 0.00	8.00 ± 0.00
K	0.02 ± 0.01	0.01 ± 0.01	0.03 ± 0.03	0.12 ± 0.04	0.03 ± 0.02	0.09 ± 0.03
Ca	2.07 ± 0.14	2.12 ± 0.12	1.94 ± 0.23	1.36 ± 0.24	1.82 ± 0.49	1.51 ± 0.20
Ti	0.61 ± 0.05	0.63 ± 0.07	0.62 ± 0.11	0.97 ± 0.10	0.75 ± 0.13	0.51 ± 0.04
Mn	0.04 ± 0.03	0.04 ± 0.03	0.05 ± 0.02	0.16 ± 0.11	0.02 ± 0.01	0.12 ± 0.09
Fe	4.37 ± 0.31	4.69 ± 0.48	4.82 ± 0.88	5.95 ± 0.90	4.97 ± 1.10	3.90 ± 0.43
O	36.34 ± 1.00	37.56 ± 1.34	36.33 ± 0.57	37.29 ± 1.76	36.43 ± 2.52	34.48 ± 1.40
TOTAL wt %	85.23 ± 2.89	89.85 ± 1.58	86.41 ± 2.67	72.30 ± 0.91	92.92 ± 3.14	86.17 ± 2.34

[a]Normalized to eight Si atoms.

Table III-10. Stoichiometric Ratio[a] and Total Weight Percent for Reaction Layer on Mg-rich Hawaiian Basalt Leached at 90-187°C, Hawaiian Basalt Hydrated at 240°C, and SRL 165 Leached at 187°C

	Mg-rich Hawaiian Basalt Leached			Hawaiian Basalt Vapor Hydrated		SRL 165 Leached
	at 90°C	at 187°C		at 240°C		at 187°C
	#811 (546 days)	#889 (Inner) (91 days)	#889 (Outer) (91 days)	#40 (91 days)		#159 (183 days)
Na	0.48 ± 0.06	0.79 ± 0.20	0.35 ± 0.06	0.51 ± 0.12	Na	0.87 ± 0.19
Mg	1.78 ± 0.67	1.05 ± 0.76	3.49 ± 0.08	2.58 ± 0.54	Mg	0.32 ± 0.06
Al	3.85 ± 0.29	3.47 ± 0.39	1.99 ± 0.09	2.38 ± 0.54	Al	1.24 ± 0.14
Si	8.00 ± 0.00	8.00 ± 0.00	8.00 ± 0.00	8.00 ± 0.00	Si	8.00 ± 0.00
K	0.08 ± 0.03	0.25 ± 0.08	0.00 ± 0.00	0.14 ± 0.10	Ca	0.43 ± 0.07
Ca	2.63 ± 0.19	3.31 ± 0.38	0.25 ± 0.15	2.05 ± 0.26	Mn	0.66 ± 0.38
Ti	0.64 ± 0.07	0.67 ± 0.15	0.00 ± 0.00	0.48 ± 0.10	Fe	2.69 ± 0.35
Mn	0.14 ± 0.10	0.00 ± 0.00	0.03 ± 0.03	0.08 ± 0.05	Ni	0.11 ± 0.02
Fe	4.82 ± 0.26	5.26 ± 1.08	0.17 ± 0.05	2.21 ± 0.30	Zr	0.07 ± 0.02
O	34.94 ± 1.00	35.32 ± 1.61	23.21 ± 0.22	28.96 ± 0.66	O	24.77 ± 1.39
TOTAL wt %	88.06 ± 2.86	90.65 ± 4.95	65.34 ± 3.38	79.10 ± 11.61	TOTAL wt %	85.05 ± 3.67

[a]Normalized to eight Si atoms.

B. Spent Fuel Leach Tests
(E. Veleckis and J. C. Hoh)

A study is underway to determine radionuclide release rates from spent fuels immersed in site-specific groundwater at the ambient hot cell temperature. The study is a part of the NNWSI project. Spent fuel leaching (SFL) tests are designed to simulate a possible condition in which groundwater may collect in the bottom of a breached waste form canister during the post-containment period. Recent SFL work carried out at Hanford Engineering and Development Laboratory (HEDL) was discussed in the previous semiannual report. The current tests will constitute Series 5 of that part of the NNWSI project.

The SFL tests to be performed at ANL will require elaborate preparations: (1) documentation must be issued for NNWSI approval of all procedures that are related to the tests, analytical services, and quality assurance, (2) equipment must be set up for handling highly radioactive fuel and for preparing a large number (>1000) of leachate samples, and (3) the principal test components, namely, spent fuel, test vessels, and J-13 water must be acquired.

Leaching tests will be conducted at room temperature in 304 L stainless steel vessels on bare fuel specimens submerged in 250 mL of J-13 water. The fuel originates from two reactors: six specimens from the H. B. Robinson PWR (30 MWd/kg U burnup) and two specimens from the Calvert Cliffs PWR (30 and 43 MWd/kg U burnup, respectively). The experimental apparatus is shown in Fig. III-10. The tests will be carried out in two consecutive cycles. During the first cycle (63 days), the initial rapid release of certain radionuclides from the fuel/cladding gap and grain boundaries should be completed. At the start of the second cycle (180 days), the fuel specimens are rinsed and placed in fresh leachants. This cycle is expected to show greatly reduced, steadier release rates. The need for additional cycles will be evaluated at a later date. Leachate samples (15-25 mL) will be taken at predetermined intervals for radiochemical and solution analysis. The volumes removed will be immediately replenished with equal amounts of J-13 water.

Approximately 700 g of spent fuel and associated cladding was received from MCC in September 1987. Total activity in the shipment was estimated to be 214 Ci. The fuel is presently stored in a shielded cask within a hot cell until the start of the tests. Stainless steel vessels were delivered from Pacific Northwest Laboratory in September 1987. They are of two types: those that can be sealed with threaded caps and threaded sampling-port plugs (Fig. III-10), and those that have loosely fitting, unthreaded caps and sampling port plugs. The latter type is intended to simulate more closely the ventilated conditions expected in the repository.

Experimental procedures for SFL tests can be divided into two categories: (1) collection and preparation of leach samples for radiochemical and solution analyses and (2) the analyses of these samples. The latter is to be performed by the Analytical Chemistry Laboratory at ANL. For the first category, procedures were written on the subjects of cycle start, periodic sampling, cycle termination, and sample preparation for analysis. For the second category, 14 procedures were written on the radiochemical analyses of U(total), ^{137}Cs, $^{239,240}Pu$, ^{241}Am, ^{237}Np, ^{99}Tc, ^{90}Sr, ^{14}C, ^{129}I, and ^{79}Se, as well as on the

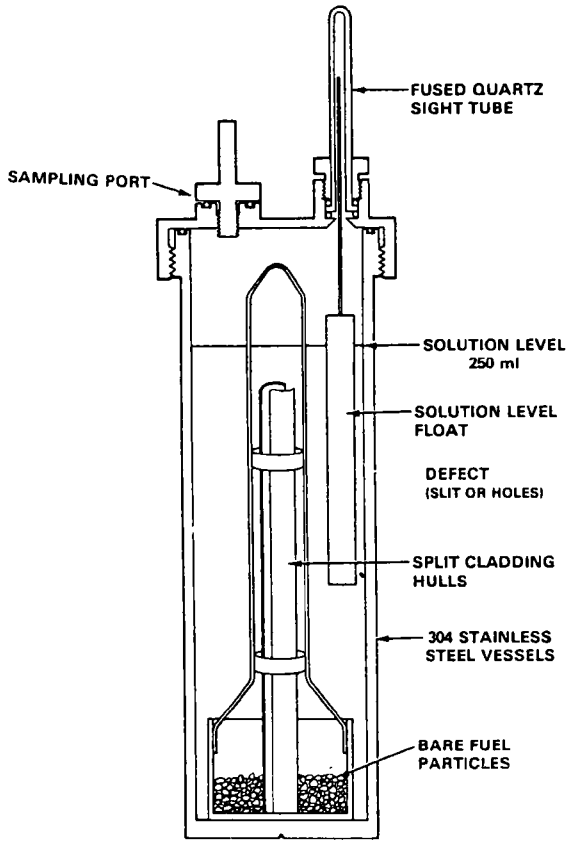

Fig. III-10.

Schematic Diagram of Experimental Apparatus for SFL Tests

inductively coupled plasma and ion chromatographic analyses for the solution chemistry. Other documents prepared during this period were "QA Implementing Procedures" and "NNWSI Spent Fuel Leaching Test Plan."

The NNWSI reference water to be used in SFL tests originates from well J-13 near Yucca Mountain and has a chemistry that approximates the repository pore fluid. Recently, the collection and storage of J-13 water have been subjected to revised technical procedures; as a result, its delivery to ANL has been postponed, thereby causing delays in initiating the SFL work.

C. Speciation of Radionuclides in Natural Groundwaters
(D. T. Reed)

The United States Government is committed to building a repository for the permanent disposal of high-level nuclear waste. One aspect of this effort is to gain an understanding of the chemical behavior of radionuclides in groundwaters in the immediate vicinity of the high-level waste container. Such information is needed to determine radionuclide release rates from the waste package and to make long-term projections of repository performance.

To help accomplish the above objective, two ultrasensitive laser techniques, laser photoacoustic spectroscopy (LPAS) and laser-induced fluorescence (LIF), are being developed for the detection and speciation of trace levels of actinides in solutions typical of those expected in a repository. These studies have been in progress for about 1-1/2 years and extend spectroscopic techniques into the nanomolar and sub-nanomolar regime. Once developed, these techniques will provide a powerful investigative tool for nondestructively monitoring and investigating the chemistry of actinides in typical groundwaters.

The two primary objectives of the actinide speciation work are to study (1) the complexation of actinides with complexants present in typical groundwaters and (2) the speciation (predominant chemical species) of actinides under the conditions expected in the vicinity of the waste package. In this report period, work toward meeting these objectives has been completed for uranyl, Pu^{4+}, Am^{3+}, and Cm^{3+} systems. The early results were presented at the Materials Research Society meeting in 1986[14] and a 1987 meeting in Munich.[15]

The complexation of actinides, both inorganic and organic, relates to the issue of radionuclide release from the high-level waste package. Understanding complexation under repository-relevant conditions would help in determining the sensitivity of radionuclide solubility and mobility to changes in the groundwater chemistry. This determination is particularly important since there is much discrepancy in the literature over the formation constants for actinide complexation, and predicted solubilities based on published values for the formation constants are much higher than those observed in solubility studies. Covering a broad range of complexants and complexant concentrations ensures that both anticipated and unanticipated conditions can be accounted for during the licensing procedure.

The speciation of actinides, or more precisely the identity of the aqueous and therefore mobile actinide species, also relates to the issue of radionuclide release from the waste package. The identification of these species is a necessary step in accurately modeling actinide behavior in a repository environment. Information on the partitioning of actinides between colloidal species and those that are truly in solution will provide additional input to modeling release from the waste package.

During this report period, significant progress was made in the development of both LPAS and LIF and their application to the detection and speciation of radionuclides in simplified transuranic systems relevant to a high-level waste basaltic repository. For the most part, the technique-development effort was completed, although continued improvement to maximize sensitivity is planned. The major objectives during FY 1987 were as follows: (1) acquire and develop a laser photoacoustic system for actinide speciation and detection, (2) extend the LPAS technique to high temperatures, (3) determine the relative sensitivity of LPAS, as well as its specific sensitivity to Am(III) and Pu(IV) species, and (4) investigate the feasibility of LIF studies on transuranic species.

The major accomplishments in FY 1987 on LPAS development were as follows:

- A facility to house the LPAS system and accommodate radioactive samples was constructed.

- An LPAS system designed to analyze radioactive samples at above ambient temperatures was assembled. The system was designed to maximize the potential for high-sensitivity applications.

- Detection and sample holding systems were modified to accommodate temperatures up to 90°C. Preliminary work was completed on a system design that would extend the temperature to 150°C.

- The sensitivity of the LPAS system was pushed to 3×10^{-7} absorbance units per centimeter at a signal-to-noise ratio (S/N) of one. This exceeds published limits by a factor of 10. Increasing the temperature of the system increased its sensitivity.

- Spectra of Am^{3+} in 1M carbonate media were obtained as a function of temperature. This is the first reporting of americium spectra at elevated temperatures. The current LPAS system is sensitive to the tris-carbonato complex of americium at 3×10^{-9}M. Greater sensitivity may be possible using laser-induced fluorescence.

- Americium (III) was prepared and analyzed in dilute sodium chloride solution. The spectrum indicated the presence of colloids. Further work is needed before conclusions can be made.

- Initial spectra of Pu(IV) in high carbonate media were obtained. Further work is needed to fully establish the sensitivity of the LPAS technique.

The emphasis of the work in FY 1987 was on the development and application of LPAS to transuranic speciation. The importance of LIF, however, was soon recognized and has become an important part of the overall speciation effort. Since an existing LIF system was available, the focus of the work was on analyzing two actinide systems relevant to speciation in high-level waste disposal conditions. The following is a summary of accomplishments in FY 1987:

- Work on the uranyl system in GR-4 groundwater, started in FY 1986, was continued. The fluorescence spectrum indicated the presence of up to four uranyl species.

- The sensitivity of LIF to uranyl could not be established with the present system because the observed fluorescence was due to multiple species. Further work on this system is needed and will require substantial capital investment.

- The fluorescence spectra of Cm^{3+} in a dilute perchloric acid medium and simplified basaltic groundwater were obtained. These are the first fluorescence spectra obtained under these conditions.

- The observed sensitivity of LIF to the Cm^{3+} species was 1.8×10^{-11}M. This corresponds to a curium concentration that is considerably lower than the expected solubility in basaltic systems.

REFERENCES

1. G. D. Maupin, W. M. Bowen, and J. L. McDaniel, Pacific Northwest Laboratory, unpublished information (1987).

2. J. K. Bates and T. J. Gerding, "The Performance of Actinide-Containing SRL 165 Type Glass in Unsaturated Conditions," presented at Symp. for Scientific Basis for Nuclear Waste Management, Materials Research Society Meeting, Boston, MA, December 1-4, 1987.

3. M. J. Steindler et al., Nuclear Technology Programs Quarterly Progress Report, January-March 1984, Argonne National Laboratory Report ANL-84-37 (1984).

4. M. J. Steindler et al., Nuclear Technology Programs Quarterly Progress Report, April-June 1984, Argonne National Laboratory Report ANL-84-57 (1985).

5. M. J. Steindler et al., Nuclear Technology Programs Quarterly Progress Report, July-September 1984, Argonne National Laboratory Report ANL-84-91 (1985).

6. J. K. Bates et al., NNWSI Waste Form Testing, Semiannual Report, July-December 1986, Lawrence Livermore National Laboratory Report, in press.

7. J. K. Bates et al., NNWSI Waste Form Testing, Semiannual Report, January-June 1987, Lawrence Livermore National Laboratory Report, in preparation.

8. W. G. Burns et al., J. Nucl. Mater. 107, 245 (1982).

9. M. J. Plodinec, G. G. Wicks, and N. E. Bibler, An Assessment of Savannah River Borosilicate Glass in the Repository Environment, Savannah River Laboratory Report DP-1629 (1982).

10. J. K. Bates, D. F. Fischer, and T. J. Gerding, The Reaction of Glass during Gamma Irradiation in a Saturated Tuff Environment, Part 1: SRL 165 Glass, Argonne National Laboratory Report ANL-85-62 (1986).

11. T. A. Abrajano, Jr., J. K. Bates, T. J. Gerding, and W. L. Ebert, The Reaction of Glass during Irradiation in a Saturated Tuff Environment, Part 3: Long-Term Experiments at 1 x 10^4 rad/hour, Argonne National Laboratory Report ANL-88-14 (1988).

12. G. G. Wicks, B. M. Robnett, and D. Rankin, "Chemical Durability of Glass Containing SRP Waste - Leachability Characteristics, Protective Layer Formation, and Repository System Interactions," in Scientific Basis for Nuclear Waste Management, V. W. Lutze, ed., North-Holland, New York, NY, p. 15 (1982).

13. C. D. Byers, M. J. Jercinovic, and R. C. Ewing, A Study of Glass Analogues as Applied to Alteration of Nuclear Waste Glass, Argonne National Laboratory Report ANL-86-46 (1987).

14. M. M. Doxtader, J. V. Beitz, and V. A. Maroni, "Laser Photoacoustic Spectroscopy for the Trace Level Detection of Actinides in Groundwater," in Scientific Basis for Nuclear Waste Management X, J. K. Bates and W. B. Seefeldt, eds., Materials Research Society, Pittsburgh, PA, Vol. 84, p. 173 (1987).

15. J. V. Beitz, D. L. Bowers, M. M. Doxtader, V. A. Maroni, and D. T. Reed, "Detection and Speciation of Transuranium Elements in Synthetic Groundwater via Pulsed Laser Excitation," Radiochim. Acta 44&45, 87-93 (1988).

Distribution for ANL-88-49

Internal:

T. A. Abrajano
J. P. Ackerman
J. D. Arntsen
C. C. Baker
J. K. Bates (5)
J. E. Battles
J. V. Beitz
B. M. Biwer
P. E. Blackburn
R. A. Blomquist
S. S. Borys
D. L. Bowers
R. L. Breyne
D. J. Chaiko
D. B. Chamberlain
Y. Chang
W. L. Ebert
P. A. Finn
A. K. Fischer
D. R. Fredrickson
T. J. Gerding
L. R. Greenwood
J. E. Harmon
J. C. Hoh
E. P. Horwitz
C. E. Johnson (5)
I. Johnson
J. P. Kopasz
J. Laidler
L. Leibowitz
R. A. Leonard
M. A. Lewis
V. A. Maroni
F. C. Mrazek
P. A. Nelson
P. A. G. O'Hare
D. T. Reed
L. Reichley-Yinger
R. T. Riel
M. F. Roche
W. B. Seefeldt
J. L. Settle
J. E. Stangel
M. J. Steindler
N. C. Sturchio
S.-W. Tam
I. R. Tasker
C. E. Till
L. E. Trevorrow
P.-K. Tse
G. F. Vandegrift (10)
E. H. Van Deventer
E. Veleckis
S. Vogler
L. C. Walters
ANL Patent Dept.
ANL Contract File
ANL Library (2)
TIS Files (3)

External:

DOE-OSTI, for distribution per UC-523, UC-711, UC-510, and UC-516 (339)
Manager, Chicago Operations Office, DOE
D. T. Goldman, DOE-CH
J. Haugen, DOE-CH
S. A. Mann, DOE-CH
A. L. Taboas, DOE-CH/AAO
Chemical Technology Division Review Committee Members:
S. Baron, Brookhaven National Laboratory, Upton, NY
N. Jarrett, Noel Jarrett Associates, Lower Burrell, PA
L. Newman, Brookhaven National Laboratory, Upton, NY
J. Stringer, Electric Power Research Institute, Palo Alto, CA
J. B. Wagner, Arizona State University, Tempe, AZ
R. G. Wymer, Oak Ridge National Laboratory, Oak Ridge, TN
E. B. Yeager, Case Western Reserve University, Cleveland, OH
M. G. Adamson, Lawrence Livermore National Laboratory, Livermore, CA
J. T. Bell, Oak Ridge National Laboratory, Oak Ridge, TN
S. E. Berk, USDOE, Office of Fusion Energy, Germantown, MD
D. F. Bowersox, Los Alamos National Laboratory, Los Alamos, NM
L. Brewer, University of California, Berkeley, CA
K. A. Chasey, USDOE, Defense Waste & Transportation Manage., Germantown, MD
M. Coops, Lawrence Livermore National Laboratory, Livermore, CA
D. Cubicciotti, Electric Power Research Institute, Palo Alto, CA
H. T. Davis, University of Minnesota, Minneapolis, MN
M. Dinehart, Los Alamos National Laboratory, Los Alamos, NM

M. M. Doxtader, George R. Harrison Spectroscopy Laboratory, Cambridge, MA
M. Duff, USDOE, Defense Waste & Transportation Management, Germantown, MD
W. S. Groenier, Oak Ridge National Laboratory, Oak Ridge, TN
T. B. Hindman, USDOE, Defense Waste & Transportation Manage., Germantown, MD
R. R. Hobbins, EG&G Idaho, Inc., Idaho Falls, ID
J. O. Honeyman, Rockwell Hanford Operations, Richland, WA
S. Howell, Los Alamos National Laboratory, Los Alamos, NM
L. J. Jardine, Los Alamos National Laboratory, Los Alamos, NM
J. J. Jicha, USDOE, Defense Waste & Transportation Management, Germantown, MD
R. T. Jubin, Oak Ridge National Laboratory, Oak Ridge, TN
M. Levenson, Bechtel National, Inc., San Francisco, CA
T. B. Lindemer, Oak Ridge National Laboratory, Oak Ridge, TN
A. Malinauskis, Oak Ridge National Laboratory, Oak Ridge, TN
Los Alamos National Laboratory, Director, Los Alamos, NM
F. Marsh, Los Alamos National Laboratory, Los Alamos, NM
W. H. McVey, USDOE, Division of LMFBR Fuel Cycle Projects, Germantown, MD
A. C. Muscatello, Los Alamos National Laboratory, Los Alamos, NM
A. J. Naser, Rockwell Hanford Operations, Richland, WA
L. Nelson, Sandia Corporation, Albuquerque, NM
M. O'Hara, Martin Marietta Energy Systems, Y-12 Plant, Oak Ridge, TN
D. R. Olander, University of California, Berkeley, CA
A. L. Olson, Westinghouse Idaho Nuclear Co., Inc., Idaho Falls, ID
D. A. Orth, Savannah River Laboratory, Aiken, SC
V. M. Oversby, Lawrence Livermore National Laboratory, Livermore, CA
M. Palmer, Los Alamos National Laboratory, Los Alamos, NM
G. Pfennigworth, Martin Marietta Energy Systems, Y-12 Plant, Oak Ridge, TN
R. L. Ritzman, Electric Power Research Institute, Palo Alto, CA
M. W. Shupe, USDOE, Idaho Operations Office, Idaho Falls, ID
D. W. Tedder, Georgia Institute of Technology, Atlanta, GA
T. A. Todd, Westinghouse Idaho Nuclear Co., Inc., Idaho Falls, ID
USDOE, Office of Basic Energy Sciences, Washington, DC
S. Yarbro, Los Alamos National Laboratory, Los Alamos, NM

U.S. GOVERNMENT PRINTING OFFICE 1989—643-177/0001